

# Phasonic Degrees of Freedom in Quasicrystals

Phasonische Freiheitsgrade  
in Quasikristallen

Der Naturwissenschaftlichen Fakultät  
der Friedrich-Alexander-Universität  
Erlangen-Nürnberg

zur

Erlangung des Doktorgrades Dr. rer. nat.

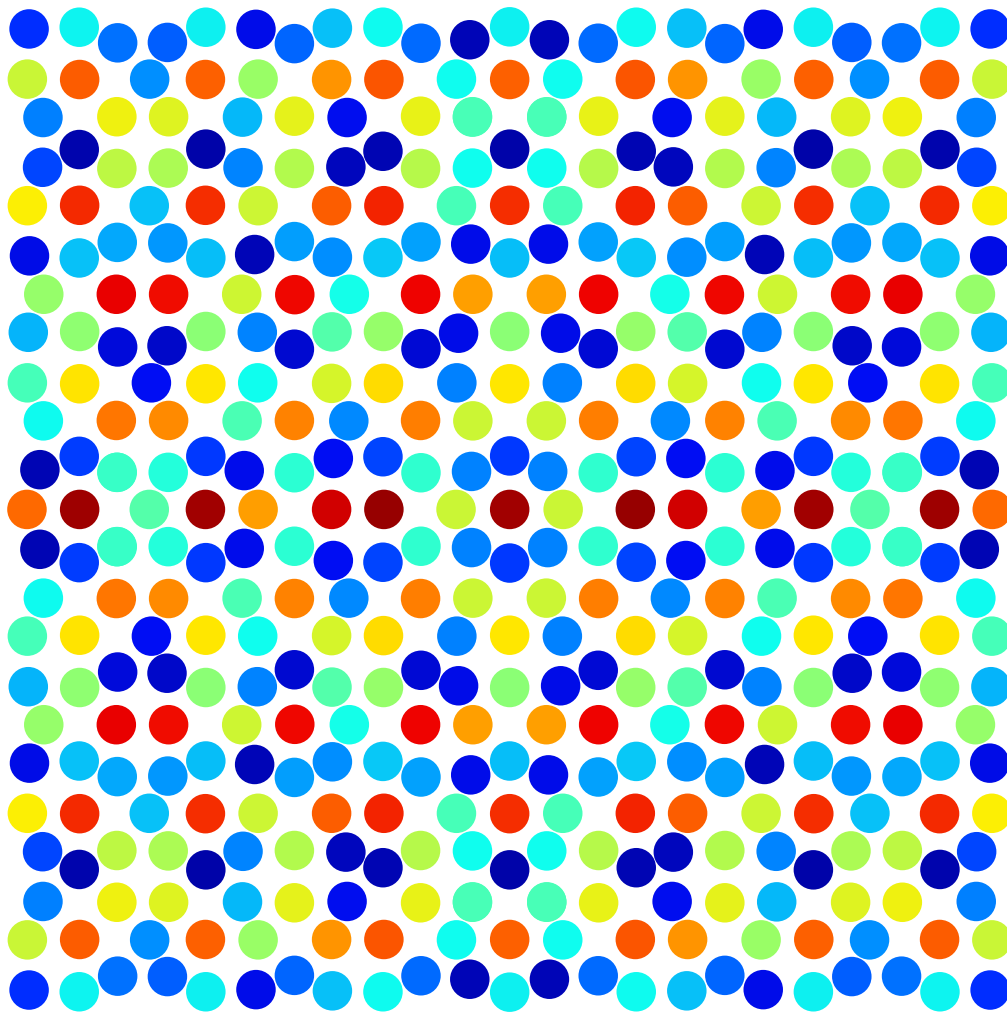
vorgelegt von

Miriam Martinsons

aus Mönchengladbach

Als Dissertation genehmigt  
von der Naturwissenschaftlichen Fakultät  
der Friedrich-Alexander-Universität Erlangen-Nürnberg

Tag der mündlichen Prüfung: 24. Oktober 2019  
Vorsitzender des Promotionsorgans: Prof. Dr. Georg Kreimer  
Gutachter: Prof. Dr. Michael Schmiedeberg  
Prof. Dr. Michael Engel



# Phasonic Degrees of Freedom in Quasicrystals

Miriam Martinsons



# Abstract

Quasicrystals are remarkable ordered structures without periodic translational symmetry. They can possess any discrete rotational symmetry including those that must not be present in periodic crystals. An important characteristic of quasicrystals is the existence of additional degrees of freedom whose excitations lead to rearrangements of particles. Such rearrangements are called phasonic flips. Several material properties like the elasticity of quasicrystals are affected by phasonic excitations. By now, quasicrystals have been synthesized in experiments and simulations and have even been found in nature.

The aim of this thesis is to contribute to the understanding of the amazing order and properties of quasicrystals. For this purpose we employ computational simulations of two-dimensional colloidal model systems where mesoscopic particles are suspended in a liquid. By implementing appropriate external or internal interactions quasicrystalline order of the colloids can be induced.

Significant new insights into the structural and dynamical complexity of quasicrystals are gained. Our results are essentially different from what is known from periodic crystals. In particular, investigations of the phase behavior of quasicrystals reveal a surprisingly rich phase diagram. Even in the solid, positional order is short-ranged due to excited phasonic degrees of freedom, and the transition to liquid is of first order. Furthermore, we illustrate how the growth of quasicrystals is affected by thermodynamic parameters and phasonic flips. Especially the growth of nearly defect-free quasicrystals is presented. In addition, we focus on the dynamics of quasicrystals. The stability of quasicrystals against phasonic perturbations is investigated. Particles are identified which easily perform phasonic flips, while other ones are rather stable. Phasonic drifts lead to complex trajectories of the particles. Even in intrinsic quasicrystals, which form under internal interactions alone, correlated phasonic flips are found and analyzed.

Our work provides significant progress in theory and simulations of quasicrystals and our results obtained from colloidal model systems are also relevant for other fields in physics, chemistry and material science. We expect that our work motivates further theoretical and experimental research on quasicrystals and might also advance the design of novel applications based on quasicrystals.



# Deutsche Zusammenfassung

Quasikristalle sind bemerkenswerte geordnete Strukturen ohne periodische Translationssymmetrie. Sie können jede beliebige diskrete Rotationssymmetrie besitzen, einschließlich solcher, die in periodischen Kristallen nicht auftreten können. Eine wichtige Eigenschaft von Quasikristallen ist die Existenz von zusätzlichen Freiheitsgraden, deren Anregungen zu Umordnungen von Teilchen führen. Solche Umordnungen werden als phasonische Flips bezeichnet. Verschiedene Materialeigenschaften wie die Elastizität von Quasikristallen werden von phasonischen Anregungen beeinflusst. Mittlerweile werden Quasikristalle in Experimenten und Simulationen hergestellt und sind sogar in der Natur gefunden worden.

Ziel dieser Arbeit ist es, zum Verständnis der erstaunlichen Ordnung und Eigenschaften von Quasikristallen beizutragen. Dazu verwenden wir Computersimulationen von zweidimensionalen kolloidalen Modellsystemen, wobei mesoskopische Teilchen in einer Flüssigkeit suspendiert sind. Die Implementierung von externen oder internen Wechselwirkungen kann eine quasikristalline Ordnung der Kolloide hervorrufen.

In dieser Arbeit werden wesentlich neue Einblicke in die strukturelle und dynamische Komplexität von Quasikristallen gewonnen. Unsere Ergebnisse unterscheiden sich deutlich von den bekannten Eigenschaften periodischer Kristalle. Insbesondere offenbaren Untersuchungen des Phasenverhaltens von Quasikristallen ein überraschend vielseitiges Phasendiagramm. Sogar in der festen Phase ist die Positionsordnung kurzreichweitig aufgrund von angeregten phasonischen Freiheitsgraden, und der Übergang zur Flüssigkeit ist erster Ordnung. Des Weiteren verdeutlichen wir, wie das Wachstum von Quasikristallen von thermodynamischen Parametern und phasonischen Flips beeinflusst wird. Speziell das Wachstum von nahezu defektfreien Quasikristallen wird vorgestellt. Zusätzlich konzentrieren wir uns auf die Dynamik von Quasikristallen. Die Stabilität von Quasikristallen gegen phasonische Störungen wird untersucht. Es werden Teilchen identifiziert, die bereits bei geringen Störungen phasonische Flips ausführen, während andere Teilchen eher als stabil klassifiziert werden. Phasonische Driften führen zu komplexen Trajektorien der Teilchen. In intrinsischen Quasikristallen, die sich allein durch interne Wechselwirkung bilden, werden korrelierte phasonische Flips gefun-

den und analysiert.

Unsere Arbeit stellt einen wesentlichen Fortschritt in Theorie und Simulationen von Quasikristallen dar und unsere aus kolloidalen Modellsystemen erhaltenen Ergebnisse sind ebenfalls für andere Felder der Physik, Chemie und Materialwissenschaften relevant. Wir erwarten, dass unsere Arbeit weitere theoretische und experimentelle Forschungen an Quasikristallen motiviert und zur Entwicklung neuer, auf Quasikristallen basierender Anwendungen beitragen könnte.

# Contents

<b>Abstract</b>	<b>v</b>
<b>Deutsche Zusammenfassung</b>	<b>vii</b>
<b>1 Introduction and outline</b>	<b>3</b>
<b>2 Background</b>	<b>7</b>
2.1 Discovery of quasicrystals . . . . .	7
2.2 Current state of research . . . . .	12
2.2.1 Possible quasiperiodic arrangements . . . . .	12
2.2.2 Quasicrystals synthesized in experiments and simulations . .	13
2.2.3 Quasicrystals in nature . . . . .	20
2.2.4 Stability of quasicrystals . . . . .	21
2.2.5 Properties and applications . . . . .	22
2.3 Quasiperiodic tilings . . . . .	26
2.3.1 Definition of tilings . . . . .	27
2.3.2 Development of quasiperiodic tilings . . . . .	27
2.3.3 The golden ratio . . . . .	29
2.3.4 Examples of quasiperiodic tilings . . . . .	30
2.3.5 Construction methods . . . . .	34
2.3.5.1 Substitution method . . . . .	34
2.3.5.2 Projection and section method . . . . .	36
2.3.5.3 Matching rules . . . . .	38
2.3.6 Local isomorphism . . . . .	40
2.4 Rank . . . . .	41
2.5 Phasons . . . . .	41
2.5.1 Phasonic modes . . . . .	42
2.5.2 Phasonic flips . . . . .	44
2.5.3 Recent findings . . . . .	44
2.6 Topological defects . . . . .	47
2.7 Colloidal physics . . . . .	49

---

<b>3</b>	<b>Numerical techniques</b>	<b>53</b>
3.1	Brownian dynamics simulations . . . . .	53
3.1.1	Langevin equation . . . . .	54
3.1.2	Simulation details . . . . .	57
3.1.3	Extension to rotation moves . . . . .	59
3.2	Monte Carlo simulations . . . . .	59
3.2.1	Theoretical concept . . . . .	60
3.2.2	Realization of the Metropolis algorithm in our simulations .	62
3.2.3	Extension to the $NpT$ -ensemble . . . . .	65
3.3	Event-chain Monte Carlo simulations . . . . .	67
3.3.1	Theoretical concept . . . . .	68
3.3.2	Implementation in simulations . . . . .	70
3.4	General settings of our simulations . . . . .	72
3.4.1	Potentials . . . . .	72
3.4.2	Simulation units and parameters . . . . .	78
3.4.3	Initial configurations . . . . .	78
3.4.4	Boundary conditions and size of simulation box . . . . .	78
3.5	Analyzing tools . . . . .	83
3.5.1	Pair distribution and pair correlation function . . . . .	83
3.5.2	Structure factor . . . . .	84
3.5.3	Angular distribution function . . . . .	85
3.5.4	Order parameters and their correlation functions . . . . .	86
3.5.5	Selective density wave analysis for dislocation detection . . .	88
<b>4</b>	<b>Colloids in two-dimensional quasicrystalline laser fields</b>	<b>91</b>
4.1	Optical tweezing . . . . .	92
4.2	Quasicrystalline interference patterns . . . . .	93
4.3	Stability of particles against phasonic perturbations . . . . .	96
4.3.1	Characteristic displacements and characteristic areas . . . . .	99
4.3.2	Phasonic displacements required for phasonic flips . . . . .	101
4.3.3	Distribution of flipping colloids . . . . .	102
4.4	Colloidal trajectories due to phasonic drifts . . . . .	109
4.4.1	Tetradecagonal laser field . . . . .	110
4.4.2	Characteristic displacements and characteristic areas . . . . .	110
4.4.3	Analyzing colloidal trajectories . . . . .	112
4.4.4	Selected trajectories . . . . .	113
4.5	Conclusion . . . . .	115

---

<b>5</b>	<b>Complex structures in systems of patchy colloids</b>	<b>117</b>
5.1	Patchy colloids . . . . .	118
5.2	Stabilizing quasicrystals composed of patchy colloids . . . . .	119
5.2.1	Simulation setup . . . . .	119
5.2.2	Systems of colloids with ten patches . . . . .	120
5.2.3	Systems of colloids with eight patches . . . . .	123
5.2.4	Support of different length scales . . . . .	125
5.2.5	Formation of quasicrystals from random initial configurations	126
5.3	Conclusion . . . . .	128
<b>6</b>	<b>Growth of two-dimensional colloidal quasicrystals</b>	<b>129</b>
6.1	Growth of decagonal quasicrystals . . . . .	130
6.1.1	Simulation setup and determination of layers . . . . .	131
6.1.2	Influence of surface diffusion . . . . .	134
6.1.3	Bond-orientational order . . . . .	137
6.1.4	Surfaces . . . . .	142
6.1.5	Phasonic flips . . . . .	145
6.1.6	Changes of the parameters of the interaction potential . . . . .	147
6.2	Growth of dodecagonal quasicrystals . . . . .	148
6.2.1	Simulation setup and determination of layers . . . . .	149
6.2.2	Diffusion-limited aggregation . . . . .	150
6.2.3	Observed structures and occurrence of the long length scale	153
6.2.4	Order of the grown quasicrystalline structures . . . . .	155
6.2.5	Dynamics of phasonic excitations . . . . .	158
6.2.6	Lines and regions of flipped particles . . . . .	163
6.3	Conclusion . . . . .	165
<b>7</b>	<b>Phase transitions in two-dimensional colloidal quasicrystals</b>	<b>169</b>
7.1	Melting in two dimensions . . . . .	169
7.2	Event-chain Monte Carlo simulations of decagonal quasicrystals . . . . .	171
7.2.1	System and method . . . . .	172
7.2.2	Phase behavior – overview . . . . .	172
7.2.3	Phase transitions . . . . .	174
7.2.4	Correlation functions . . . . .	177
7.2.5	Dislocations and phason relaxation . . . . .	179
7.3	Conclusion . . . . .	181
<b>8</b>	<b>Mode analysis in hyperspace</b>	<b>183</b>
8.1	Detection of phonon and phason modes in intrinsic quasicrystals . . . . .	183
8.1.1	Quasicrystal synthesis by section method . . . . .	184
8.1.2	Phonons and phasons . . . . .	185

---

8.1.3	Reconstruction of hyperspace embedding . . . . .	186
8.1.4	Brownian dynamics simulations . . . . .	189
8.1.5	Phason amplitudes and numbers of phasonic flips . . . . .	189
8.1.6	Recovery of known phasons from flip pattern . . . . .	190
8.1.7	Creation of excitations by annealing . . . . .	192
8.1.8	Dynamics of synthetic phasons during annealing . . . . .	196
8.2	Conclusion . . . . .	196
<b>9</b>	<b>Conclusions</b>	<b>199</b>
	<b>List of Publications</b>	<b>203</b>
	<b>Bibliography</b>	<b>211</b>
	<b>Danksagung</b>	<b>243</b>

# Chapter 1

## Introduction and outline

Quasicrystals are structures with long-range positional and orientational order but lacking translational symmetry [1, 2]. Quasicrystalline order in atomic systems was firstly discovered in 1982 by Dan Shechtman who investigated the structures of metallic alloys by means of their diffraction patterns [3]. However, it took years of further research until the International Union of Crystallography was convinced by the existence of quasicrystals. In 1992 quasicrystals even caused a redefinition of the term crystal [4]. In 2011 Shechtman was awarded with the Nobel Prize for his outstanding discovery of quasicrystals [5].

Quasicrystals possess interesting features which are essentially different from the ones of periodic crystals. The absence of translational symmetry allows for rotational symmetries which are forbidden in periodic crystals [1, 2, 6]. For instance, quasicrystals with 5-, 8-, 10- or 12-fold rotational symmetry build most easily among aperiodic structures [7, 8]. Furthermore, quasicrystalline structures show at least two incommensurate length scales, i.e. the length scales are no rational multiples. Another characteristic of quasicrystals is their additional degrees of freedom which cause additional hydrodynamic modes, called phasons [9, 10]. Beside phonons, phasons correspond to complex rearrangements of particles [11–14] and do not cost free energy in the limit of long wavelengths. Local rearrangements of single particles correspond to localized phasonic excitations and are called phasonic flips. Phasons affect many features of quasicrystals and are of special interest in this thesis.

By now, atomic quasicrystals were found in numerous metallic alloys of at least two elements [15, 16]. Recently, quasicrystalline structures were also observed in mesoscopic systems, for instance soft-matter quasicrystals [17–22]. Even natural quasicrystals were discovered in rock samples [23].

Quasicrystals are also investigated numerically, e.g. in simulations of colloidal systems. Colloids are particles with a typical size in the range of microns [24]. Suspensions of colloids dispersed in a solvent show many similarities to atomic systems and

are well-suited model systems. On the one hand, interactions between colloids are easily tunable, and on the other hand, colloidal suspensions can be influenced by external fields. In this thesis, we employ different methods and simulation techniques to model two-dimensional colloidal quasicrystals and to investigate their features.

After a detailed background about quasicrystals in Chapter 2 and a presentation of employed simulation techniques in Chapter 3 we present the results of our simulations.

In Chapter 4 we induce two-dimensional quasicrystalline arrangements of colloids by light fields. Interfering laser beams cause light patterns in which colloids are driven towards the highest light intensity [25, 26]. In principle, arrangements with any rotational symmetry can be created. The phasonic displacement can be changed by tuning the phases of the laser beams appropriately [11, 12, 27]. We generate colloidal quasicrystals with decagonal, octagonal and dodecagonal symmetry and calculate characteristic areas of phononic and phasonic displacements which are similar to unit cells in periodic crystals. We map the colloids inside these areas and determine the phasonic displacements which are required for phasonic flips. Furthermore, on the example of quasicrystals with tetradecagonal symmetry we analyze trajectories of colloids exposed to phasonic drifts, i.e. changes of the phasonic displacement with a constant rate in time.

In the presence of appropriate internal interactions colloids can also self-assemble into quasicrystalline structures without any external influences. We employ two different kinds of interaction potentials: An isotropic Lennard-Jones–Gauss pair potential [28, 29] which supports two typical incommensurate length scales, and a modified Lennard-Jones potential with preferred binding angles between the colloids (see, e.g. [30]). The latter one models patchy colloids that are furnished with attractive regions at the surface.

In Chapter 5 we model particles with eight and ten symmetrically arranged patches in two-dimensional Monte Carlo simulations. In extensive studies we explore the influence of the patch width on the assembling structures with the goal to obtain octagonal and decagonal quasicrystals.

In Chapter 6 we model the growth of two-dimensional decagonal colloidal quasicrystals in Brownian dynamics simulations with particles that interact according to a Lennard-Jones–Gauss potential. We sequentially add particles at a free surface which corresponds to the growth out of vapor. We analyze the growing structures for various temperatures and sedimentation rates. In particular, we investigate the contribution of phasonic flips to the growth process. The studies are extended to the growth of dodecagonal quasicrystals. Aside from an isotropic Lennard-Jones–Gauss potential with appropriate length scales, we also model anisotropic interactions between patchy particles which are known to build dodecagonal qua-

quasicrystals. We compare the grown structures regarding their order and phasonic flips.

In Chapter 7 we employ event-chain Monte Carlo simulations in order to model phase transitions in decagonal quasicrystals. The particles interact according to the Lennard-Jones–Gauss potential with typical length scales of decagonal quasicrystals. A phase diagram for various densities and temperatures is determined. We examine the validity of the KTHNY theory [31–35], a defect-mediated melting theory for two-dimensional systems, and the influence of phasons on the melting process of quasicrystals.

In Chapter 8 we synthesize two-dimensional decagonal quasicrystals from structures that are periodic in a higher-dimensional space, called hyperspace [36]. The lattice points within a certain acceptance domain are projected onto a two-dimensional projection plane that corresponds to the physical space. Since phasons are displacements in the complementary space perpendicular to the physical space, we are able to incorporate synthetic phasons into the quasicrystal. Conversely, by embedding intrinsic quasicrystals annealed in physical space into hyperspace, we detect and analyze phason modes.

Finally, in Chapter 9 we give a conclusion of our results presented in this thesis.



# Chapter 2

## Background

In this Chapter a detailed background about quasicrystals is given. We begin with the historical background and the discovery of quasicrystals in Section 2.1. The following Section 2.2 is a brief summary of the research about quasicrystals that developed until today. We also put our work into that context. As a basis for the following Chapters we define quasiperiodic tilings and their properties and present common construction methods in Section 2.3. Furthermore, in Section 2.4 the rank is introduced which is an important quantity especially in terms of quasicrystals. Section 2.5 contains a discussion of phasons which correspond to complex rearrangements of particles in quasicrystals and are of special interest in this thesis. Section 2.6 deals with topological defects with a special focus on defects in quasicrystals. Finally, in Section 2.7 we present the field of colloidal physics in general and put it into the context of quasicrystals as employed in this work.

### 2.1 Discovery of quasicrystals

Before 1982, solid state physics proposed a distinction of solids into two kinds, namely amorphous solids and periodically ordered crystals. The former ones are materials whose components do not build an ordered structure. Consequently, there exists only short-range order between the particles. Amorphous solids are created, e.g. by rapidly cooling a melt or a fluid.

The second kind of material is ordered crystals. At the end of the 18th century the mineralogist René J. Haüy established a mathematical theory of crystallography stating that ordered matter always has to be periodic [37]. Periodicity is a form of translational symmetry and means that moving the structure about a certain distance in a certain direction results in the same structure as in the beginning. Haüy's theory was supported in experimental studies of diffraction patterns of

crystals in the beginning of the 20th century, for instance with the first X-ray diffraction experiment by Max von Laue in 1912.

An ideal periodic crystal is given by identical structural elements called unit cell. A space lattice is obtained by periodically putting together the unit cells in a way that no gaps arise. The vectors that are required for the translation of a unit cell within the lattice are called lattice vectors. In a classification by Auguste Bravais the unit cells are composed of parallelepipeds which are adapted to the symmetry of the structure. Through periodic repetition of such unit cells, the so-called Bravais lattices are obtained which provide all possible lattice systems. The lattice points can be furnished with single atoms or several atoms of different species. In three dimensions there are 14 different Bravais lattices, and in two dimensions five different Bravais lattices are obtained [38, 39].

In a periodic lattice only crystallographic symmetries can be present which are restricted to  $n = 1$ -, 2-, 3-, 4- and 6-fold rotational symmetries [40]. As already found by Johannes Kepler in the 17th century [41] only in these cases one can fill the whole space by one single unit cell that is repeated through translation without gaps or overlaps. Note that generally, a structure with  $n$ -fold rotational symmetry in real space possesses a discrete diffraction pattern in reciprocal space with  $m$ -fold rotational symmetry, where  $m = 2n$  when  $n$  is odd and  $m = n$  when  $n$  is even.

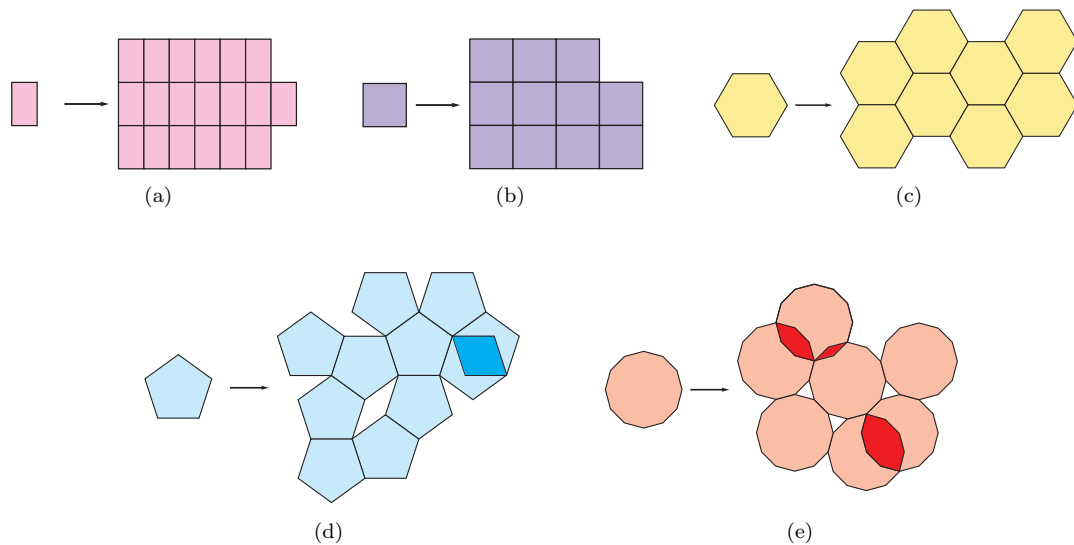


Figure 2.1: (a)-(c) Exemplary unit cells of two-dimensional crystals with 2-, 4- and 6-fold rotational symmetry. Translated copies of the unit cells fill space without gaps or overlaps. (d) and (e) A pentagon or a dodecagon as unit cell cannot fill space by repetition. Gaps (white) or overlaps (high color saturation) occur.

In Figures 2.1 (a)-(c) we illustrate unit cells with 2-, 4- and 6-fold rotational symmetry that fill space by translation. Rotational symmetries with  $n = 5$  and  $n > 6$  are called non-crystallographic symmetries and were explicitly forbidden [39]. A periodic arrangement with non-crystallographic symmetry is not possible which is shown in Figures 2.1 (d) and (e) using the examples of unit cells with 5- and 12-fold rotational symmetry. Note that single molecules with forbidden symmetries have been known, but they are not compatible with translational symmetry.

The assumption that all ordered matter has to be periodic was questioned in 1982 when the Israeli material scientist Dan Shechtman performed diffraction experiments of metal samples at the National Bureau of Standards in Gaithersburg, Maryland [3]. Shechtman produced a solid by rapidly cooling an alloy of aluminum and manganese with composition close to  $\text{Al}_6\text{Mn}$  and recorded electron diffraction patterns along different directions. He found a direction within the solid in which the arrangement of diffraction peaks showed 10-fold rotational symmetry. Furthermore, the peaks did not reveal any periodicity. The diffraction pattern is illustrated in Figure 2.2. Such an arrangement of Bragg peaks can be related to a structure with 5-fold rotational symmetry in real space. In diffraction patterns recorded along further directions within the solid Shechtman observed 6-fold and respectively 2-fold rotational symmetries such that later the symmetry of an icosahedron was revealed (see Section 2.2 for a definition of icosahedra). Thus, the diffraction patterns suggested a structure with long-range positional and orientational order, but no periodicity. Shechtman himself was initially surprised about his discovery which is suggested by three question marks in his transmission electron microscopy logbook [42].

After Shechtman's discovery the existence of ordered structures without translational symmetry was discussed controversially. The majority of the scientific community did not believe in the existence of such structures [42]. Yet, Shechtman stuck to his results and found the material scientist Ilan Blech who was willing to cooperate with him. Blech developed a model in which three-dimensional icosahedra cover space, and the diffraction pattern conformed to Shechtman's findings. In 1984 and 1985, Shechtman and coworkers published their results for the first time [1, 43].

About six weeks after the first publication, the physicists Dov Levine and Paul Steinhardt introduced the term 'quasicrystal' for the discovered structures with long-range positional order but lacking translational symmetry [2]. The term 'quasicrystal' is a short form for quasi-periodic crystal and emphasizes that the translational symmetry is only quasi-periodic.

However, skepticism and criticism remained. Shechtman's main critic was Linus Pauling, a reputable chemist who received two individual Nobel prizes. During an American Chemical Society conference Pauling proclaimed in front of thousands of

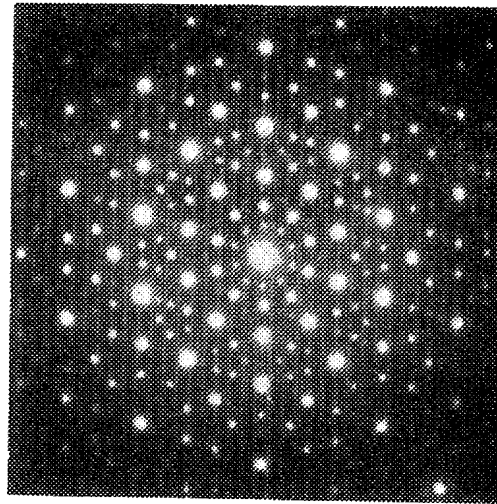


Figure 2.2: Diffraction pattern found by Shechtman with 10-fold rotational symmetry suggesting a structure with 5-fold rotational symmetry in the revealed direction. Adopted figure with permission from [1] (<https://doi.org/10.1103/PhysRevLett.53.1951>). Copyright 1984 by the American Physical Society.

scientists that “there is no such thing as quasicrystals, only quasi-scientists” (see, e.g. [42, 44]). Pauling believed that the non-crystallographic diffraction pattern resulted from multiple twinning of cubic crystals and published his statement in prestigious journals [45–48]. Twinning refers to deformation modes in metals [49–51], in which two independent crystals grow together in a way that they have some lattice points in common at a twin boundary. The diffraction pattern of a twinned crystal does usually not reflect the rotational symmetry of the single crystals since in most cases the two crystals are rotated against each other.

Pauling’s theory was doubted more and more when briefly after Shechtman’s first publication about quasicrystals scientists all over the world tried to produce quasicrystals from metallic alloys, too, and indeed observed structures with 5-fold rotational symmetry without any evidence of twinning (see Subsection 2.2.2). Though Pauling’s assumption was proven wrong (see, e.g. [52]) he kept refusing the existence of quasicrystals. After Pauling’s death in 1994, the main resistance to Shechtman and quasicrystals vanished.

The discovery of quasicrystals even led to a redefinition of the term crystal. Up to 1992, the International Union of Crystallography defined a crystal as “a substance in which the constituent atoms, molecules, or ions are packed in a regularly ordered, repeating three-dimensional pattern” [4] which implied periodicity. With the production of quasicrystalline samples that were large enough to be studied by X-ray microscopy the definition was generalized in 1992: “... By crystal we

mean any solid having an essentially discrete diffraction diagram, and by aperiodic crystal we mean any crystal in which three dimensional lattice periodicity can be considered to be absent” [4]. The redefinition caused a significant paradigm shift [53] concerning the understanding of the structure of solids. Finally, in 2011 ‘quasi-scientist’ Shechtman was awarded with the Nobel prize in chemistry for his discovery of quasicrystals [5].

Let us note that the given new definition of crystals is only a temporary working definition which is applied until crystallinity is better understood [54–56]. In more recent discussions it is argued that the definition is not general enough since it does not include structures with long-range order but lacking sharp Bragg peaks which most people would consider as crystal (see, e.g. [57]). For example, structures that can be obtained by substitution (see Subsection 2.3.5.1) are perfectly deterministic with long-range order. However, such structures do not necessarily possess a discrete diffraction diagram as studied, e.g. in [58–60]. A less explicit definition of crystals was suggested that defines a crystal as “a solid that has long-range positional order” [56, 57]. The topic is still discussed and a further redefinition is expected.

As described, the discovery of quasicrystals was a long time coming. A possible reason for the late discovery of metallic quasicrystals is – according to Shechtman [42] – the usually small size of nanometer scale in samples produced with conventionally applied methods like rapid solidification. The structures could only be observed by an ideal usage of the transmission electron microscopy which has a resolution of about 0.1 nm. However, most crystallographers produced diffraction patterns with X-rays that are only able to resolve larger structures. Another condition for such an outstanding discovery is the belief in oneself and the willingness of complicated research.

Strictly speaking, Shechtman was not the first one who observed a metallic structure with 5-fold rotational symmetry. There must be many researchers who dismissed similar findings as an experimental artifact or who did not have the courage to publish the extraordinary observation. For instance, a student of a European professor found a similar diffraction pattern that Shechtman observed even earlier. However, he did not show his results to his professor since he was not interested in staying in the research field [42].

Note that aside from atomic quasicrystals that started the revolution of solid state physics, macroscopic aperiodic patterns have already been created earlier (see Section 2.3). However, people did not believe to find systems in which particles autonomously arrange to quasiperiodic structures.

## 2.2 Current state of research

By now, quasicrystals have been synthesized in experiments and simulations or by theoretical construction methods. In this Section we first describe possible quasiperiodic arrangements in one, two, and three dimensions before we give a summary of observed synthesized and natural quasicrystals. We discuss the stability of quasicrystals and present their properties and potential applications.

### 2.2.1 Possible quasiperiodic arrangements

Quasicrystals can be realized in several dimensions. A detailed description is presented in [61, 62]. In one dimension, there are numerous ways of arranging two or more unit elements without periodicity. A simple example is the Fibonacci sequence, i.e. a chain composed of two units that are put together aperiodically (see Subsection 2.3.5.1). In case of two-dimensional quasicrystals, the structures can either be quasiperiodic in one dimension with a periodic stacking in the other direction, or quasiperiodicity is given in both dimensions. In the latter case, structures can principally be created with any rotational symmetry, for instance with 8-, 10- or 12-fold symmetry, but also with crystallographic symmetries.

The classification of three-dimensional quasicrystals is similar. First, three-dimensional quasicrystals can be quasiperiodic in only one dimension, e.g. two-dimensional periodic layers are stacked with quasiperiodic order in the perpendicular direction. The second group are structures with quasiperiodicity in two dimensions, e.g. two-dimensional quasiperiodic layers are set periodically one upon the other such that the resulting structure possesses translational symmetry in the third dimension [63]. Such structures are referred to as axial quasicrystals. A schematic illustration is shown in Figure 2.3 (a). As for two-dimensional quasicrystals, the layers can in principle be constructed with arbitrary rotational symmetry.

The only known structure with non-trivial rotational symmetries in at least three directions is the icosahedron. For instance, an icosahedron formed in the metallic alloy investigated by Shechtman [1]. An icosahedron is built from 20 equilateral triangles and possesses 30 edges and 12 vertices. Five edges and respectively surfaces meet in every vertex. An icosahedron possesses six 5-fold rotation axes with each of them passing through opposite corners of the icosahedron, ten 3-fold rotation axes through the centers of opposite surfaces and fifteen 2-fold rotation axes through the centers of opposite edges. Figure 2.3 (b) illustrates an icosahedron from different views along the rotation axes. Note that icosahedra have already been described by Platon (427 - 347 B.C.) who characterized the composition of the world mathematically by Platonic bodies [64]. In his notion the elements of nature are represented by mathematical objects. Among the tetrahedron (fire), octahedron (air) and hexahedron or respectively cube (earth) the icosahedron rep-

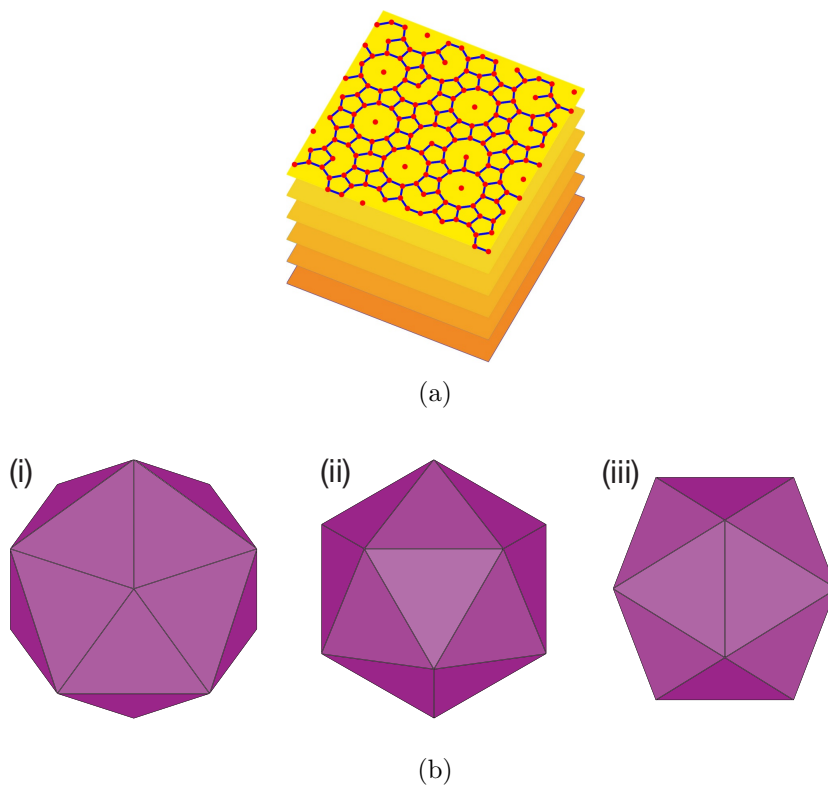


Figure 2.3: Schematic illustration of three-dimensional quasicrystals. (a) Axial quasicrystal composed of periodically stacked two-dimensional quasicrystalline layers with decagonal rotational symmetry. (b) Different views of an icosahedron along (i) a 5-fold, (ii) a 3-fold and (iii) a 2-fold rotation axis.

resents water.

In this thesis we focus on two-dimensional quasicrystals with 8-, 10-, 12-, or 14-fold symmetry.

### 2.2.2 Quasicrystals synthesized in experiments and simulations

Briefly after Shechtman's discovery of metallic quasicrystals, scientists all over the world worked on the fabrication of further synthetic quasiperiodic structures. Most quasicrystals found in experimental studies are composed of metallic alloys. Another field are soft-matter quasicrystals. Also a few quasicrystals are built from other materials. In addition to experimental studies, quasicrystalline structures

have also been obtained numerically in simulations with particles interacting according to appropriate potentials.

In the following we summarize production methods and the current achievements in the field.

### Metallic quasicrystals

The ground state of most metals is often periodic, e.g. usually body-centered cubic (bcc), face-centered cubic (fcc) or hexagonal closed-packed (hcp) [39, 65]. Beside such periodic crystals, meanwhile hundreds of different metallic quasicrystals are known. They possess 5-, 8-, 10- or 12-fold symmetry, which are the symmetries that form most easily among aperiodic structures (see Section 2.4). Numerous quasicrystals consist of ternary alloys, i.e. alloys composed of three different elements, and many alloys include aluminum as a main component.

Two kinds of metallic quasicrystals have been synthesized. They are classified as stable or metastable. The first discovered quasicrystal Mn-Al as well as numerous following examples are thermodynamically metastable which means that they can conform to a crystalline structure with lower energy when temperature is slightly increased. Metastable metallic quasicrystals mostly form through rapid solidification. During that process the thermal energy of a liquid alloy is decreased rapidly with typical cooling rates of  $10^4$  K/s and more, until the desired temperature is reached [66]. Quasicrystals generated with this technique include many defects and are usually only a few microns in size which might be too small for a detailed analysis [67, 68].

After years of research, stable quasicrystals can be produced. Stable quasicrystals offer a well-ordered, almost perfect structure that results from the production with a low cooling rate which typically does not exceed 1 K/s in conventional casting processes [66]. Large areas of single domains with a small amount of defects develop [67, 68].

Further applied production methods of metallic quasicrystals are chemical or physical vapor deposition [69].

Most synthesized metallic quasicrystals show icosahedral symmetry with more than 100 examples known by now [67, 71, 72]. The first stable icosahedral quasicrystal was observed in 1985 by Ball *et al.* with a composition of Al-Li-Cu-Mg [73]. Further quasicrystals were observed by Tsai *et al.* in Al-Cu-Fe ternary systems [70] with a grain size of about  $10\ \mu\text{m}$  as illustrated in Figure 2.4. In 2000 Tsai *et al.* [74] found for the first time stable binary structures with icosahedral symmetry. Binary structures are composed of two elements, which are Ca-Cd and Yb-Cd in Tsai's investigations [74]. The great advantage of binary systems is their increased order which allows a more precise analysis of the structure. Researchers intensely investigate the conditions under which quasicrystals composed of only

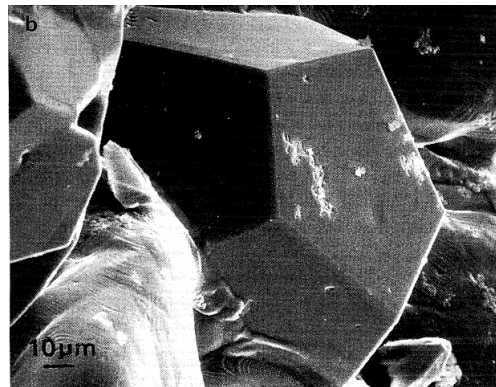


Figure 2.4: Grain of a metallic Al-Cu-Fe quasicrystal with icosahedral symmetry. The structure shows flat surfaces along the symmetry planes. Adopted with permission from [70] (<https://doi.org/10.1143/JJAP.26.L1505>). Copyright 1987 by The Physical Society of Japan and The Japan Society of Applied Physics.

one component may be stable. Single elements with certain preferred bond angles potentially lead to a rotational symmetry of quasicrystals [75].

Since 1988 a few tens of decagonal phases have been observed in alloys. The first stable decagonal quasicrystal Al-Cu-Co was found by He *et al.* [76] and was confirmed by Tsai *et al.* [77, 78]. Dodecagonal metallic quasicrystals are only rarely found. The first structure was observed in 1985 in Ni-Cr [79]. A further example is composed of Ta-Te [80]. Quasicrystals with octagonal symmetry have only been found in metastable alloys. For instance, the ternary alloys V-Ni-Si and Cr-Ni-Si build an octagonal quasicrystal with a size of several nanometers [81].

Up to date progress allowed the production of larger quasicrystalline samples in the range of millimeters to centimeters [82]. Examples are Al-Mn-Pd and Cd-Yb for icosahedral and Al-Cu-Co for decagonal structures.

Metallic quasicrystals have also been designed numerically in many-particle simulations such as molecular dynamics simulations or Monte Carlo simulations. Simulation methods are described in detail in Chapter 3. Interaction potentials are often motivated by the effective pair potential of metals which is well-described by a strong short-range repulsive part followed by a long-range decaying oscillating term [83]. Such oscillations are referred to as Friedel oscillations and are characteristic of interactions between ions [84].

For instance, the Dzugutov potential [85, 86] describes an oscillating potential. It consists of a repulsive core followed by a maximum that covers distances typical of periodic lattices (see Figure 2.5 (a)). The maximum prohibits the formation of the mentioned close-packed periodic structures. Dzugutov obtained icosahedral short-range order in systems of one-component particles [85]. Changing the proto-

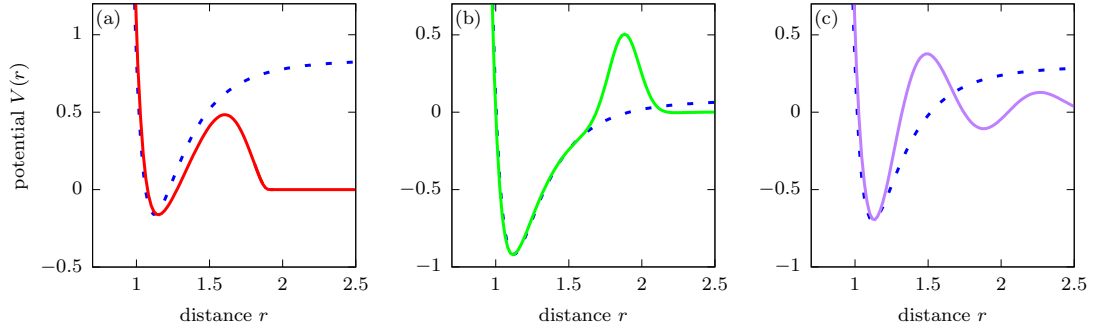


Figure 2.5: Pair potentials which induce quasicrystalline structures. (a) Dzugutov potential which facilitates local icosahedral order. (b) and (c) Variations of the Dzugutov potential which support (b) dodecagonal order and (c) octagonal arrangements. For comparison, the dotted lines illustrate the Lennard-Jones potential shifted about appropriate constants in  $y$ -direction.

col led to an axial quasicrystal with dodecagonal symmetry [86]. However, further investigations revealed the dodecagonal quasicrystal to be metastable [87]. In two-dimensional simulations a variation of the Dzugutov potential, i.e. a potential of the Lennard-Jones type with an additional maximum (see Figure 2.5 (b)), induced planar dodecagonal quasicrystals [88]. Even octagonal arrangements of particles in monatomic liquids were found in case of a short-range repulsive potential with an oscillating tail [89] (see Figure 2.5 (c)).

Further potentials that imitate the interactions in metals are of the Lennard-Jones–Gauss type [28, 29, 90, 91], i.e. the potential is composed of a Lennard-Jones potential with an additional Gaussian term which causes a second minimum. Engel *et al.* stabilized two-dimensional quasicrystals with decagonal or dodecagonal symmetry in systems of identical particles [28, 29, 91]. The Lennard-Jones–Gauss potential is described in detail in Subsection 3.4.1. Moreover, in 2014 Engel *et al.* simulated for the first time three-dimensional icosahedral quasicrystals of identical particles interacting with an isotropic three-well pair potential [92].

A feature that all potentials have in common is the support of two equilibrium distances between nearest neighbors. The equilibrium distances are obtained from the potential minimum at short distance and either the second potential minimum or the distance behind the potential maximum. Two favored lengths are a good starting condition for the stabilization of quasicrystals.

Let us note that even though metallic quasicrystals have been found in experiments as well as in simulations, there is still a gap between both fields. Although the interactions in numerical studies are motivated by interactions in atomic systems, it is difficult or even impossible to realize tunable artificially designed interactions between the particles in experimental atomic systems. In this thesis we employ nu-

merical simulations of colloidal systems to investigate the conditions under which quasicrystals build (see, e.g. Chapters 5 and 6). We compare our results to metallic systems and draw conclusions which conditions support the formation of quasicrystals in metallic alloys.

### Soft-matter quasicrystals

Aside from metallic quasicrystals there are materials that form quasiperiodic structures on the mesoscopic scale. Since 2004 the experimental discovery of quasicrystals in soft condensed matter systems developed. Soft condensed matter is characterized by weak interactions between particles, mesoscopic length scales in the range of nanometers and energy scales in units of  $k_B T$  with the Boltzmann constant  $k_B$  and the temperature  $T$ . Except for one example with octadecagonal (18-fold) symmetry, all soft quasicrystals found so far in experimental systems possess dodecagonal symmetry. Thus, the stabilization mechanism is probably different to the one in metallic quasicrystals. The stabilization of soft-matter quasicrystals seems to be a consequence of entropic effects, while in atomic metallic systems strong attractive interactions exist [93].

Basic tiles in soft quasicrystals possess a length scale of about  $10\text{ nm} - 10\text{ }\mu\text{m}$  which is several orders of magnitude larger than the atomic distances in metallic alloys [94]. Thus, it is possible to observe the dynamics and structure with a light microscope without complicated diffraction experiments [75]. The simple investigation methods may lead to deeper insights into the properties of quasicrystals. As a downside, the high structural imperfection in contrast to nearly perfectly built metallic alloys can cause problems in applications [95].

The first soft quasicrystal was found in 2004 by Zeng *et al.* within liquid crystal dendrimers that assembled to dodecagonal phases [17]. Numerous further examples followed [97]. Since 2005 similar structures were observed in block copolymers [19, 20, 98] as depicted in Figure 2.6 (a). In 2009 and 2013 also binary mixtures of nanoparticles that form structures with 12-fold symmetry were found [96, 99] (see Figure 2.6 (b)). In 2011 Fischer *et al.* observed the self-assembly of colloidal micelles in solution to quasicrystalline structures [21]. The structures provided 12-fold symmetry as well as 18-fold symmetry for the first time. A further soft-matter quasicrystal was observed in 2012 in mesoporous silica [95]. Single grains are shown in Figure 2.6 (c).

In order to approach the question of their formation and stability, soft-matter quasicrystals have been investigated numerically in simulations with potentials that mimic interactions between soft particles. As in simulations of metallic quasicrystals the interactions are chosen to favor two length scales. The first systems were modeled by Jagla *et al.* who applied a hard core potential with an additional soft core in form of a linear ramp [100]. Skibinsky *et al.* used an attractive

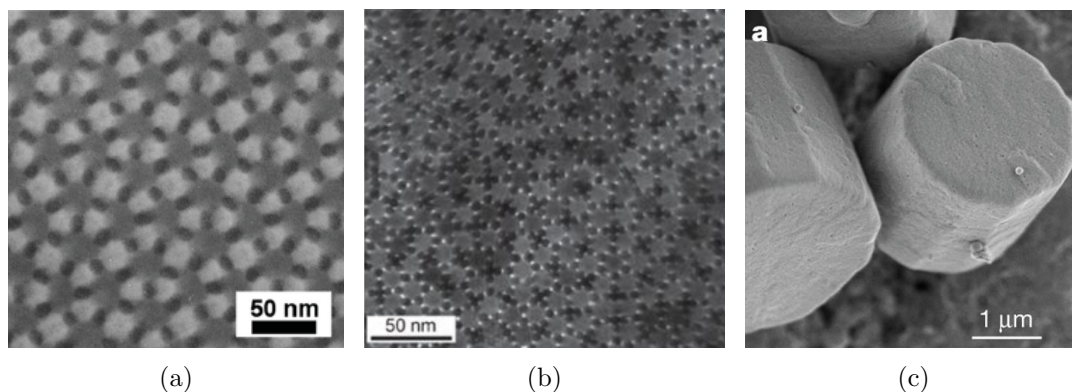


Figure 2.6: Experimental soft quasicrystals with dodecagonal symmetry. (a) TEM (transmission electron microscope) image of block copolymers. Adopted with permission from [20] (<https://doi.org/10.1103/PhysRevLett.98.195502>). Copyright 2007 by the American Physical Society. (b) TEM image of spherical nanoparticles self-assembled to a dodecagonal tiling. Adopted with permission from [96] (<https://doi.org/10.1038/nature08439>). Copyright 2009 by Springer Nature. (c) SEM (scanning electron microscope) image of mesoporous silica illustrating single grains of dodecagonal symmetry. Adopted with permission from [95] (<https://doi.org/10.1038/nature11230>). Copyright 2012 by Springer Nature.

square-well potential [101]. Both methods favor decagonal quasicrystals in two-dimensional systems of one component. Furthermore, Dotera *et al.* [102] simulated two-dimensional disks interacting via a purely repulsive hard-core potential combined with a square-shoulder potential miming a soft shell around a core as found, e.g. in dendritic micelles [17]. Shoulder and diameter of the hard-cores are tunable. Beside decagonal and dodecagonal quasicrystals their potential led to imperfect quasicrystals with 18- and 24-fold symmetry for the first time. Furthermore, interactions between hard electrically charged colloids in a suspension with small polymer coils were modeled [103]. The osmotic pressure of polymers induced a short-range attraction in addition to a repulsive Coulomb interaction. Dodecagonal quasicrystals were obtained for appropriate parameters.

Further simulations employed polydisperse particles. Models of binary systems were applied in two dimensions [104–106] and three dimensions [107]. The ratios of the particles' radii were chosen to prefer decagonal and icosahedral symmetry. Iacovella *et al.* [93] achieved three-dimensional dodecagonal soft-matter quasicrystals and approximants with a potential which models spheres that are functionalized with mobile surface entities to induce structures with low surface contact area. Polydispersity of the building blocks prohibits the formation of close-packed crystals. The models are similar to experiments [17, 21, 108, 109].

Soft quasicrystals have also been modeled with density functional theory. The free energy of the system is expanded in terms of a density field and a minimization of this free energy functional leads to modulations of the density field. E.g. Archer *et al.* [110, 111] applied a soft effective coarse-grained interaction potential that is motivated by features of experimental systems. The potential provides a shoulder resulting in two length scales modeling polymers, dendrimers or micelles. Two-dimensional quasicrystals with dodecagonal symmetry were observed. Similar studies were performed with modified phase field crystal models to investigate Faraday waves [112] or the stability of decagonal quasicrystals [113]. The studies were extended to dodecagonal quasicrystals formed from clusters of particles [114]. Further simulations based on dynamical phase field crystal models investigated the growth of quasicrystals [115, 116]. In an extension to three dimensions a dynamical phase field crystal model was applied to model icosahedral quasicrystals [117]. Another approach for simulations of soft-matter quasicrystals includes patchy particles, i.e. particles with preferred binding angles. A system of two-dimensional particles with five regularly arranged patches is modeled by a Lennard-Jones potential multiplied with an orientational term [118–121]. In such systems quasicrystals with dodecagonal symmetry are observed for appropriate thermodynamic conditions (see also Chapter 5).

A further surprising observation was made in simulations by Haji-Akbari *et al.* [122] who found hard tetrahedra forming dodecagonal structures with a packing fraction that is much larger than for proposed periodic structures. It is the first example of non-spherical hard particles that build a quasicrystalline structure. Since in hard particle systems all allowed configurations possess the same energy, equilibration is governed by entropy maximization. Consequently, only the shape of the particles is enough to generate complex structures. Similar studies were performed with hard triangular bipyramids [123] which assembled to degenerate dodecagonal quasicrystals, and polyhedra [124] which self-assemble to complex structures. Among others, quasicrystals were observed.

In this work we model colloidal quasicrystals in numerical simulations with different internal and external potentials. On the one hand, insights into the formation of soft quasicrystals are given. On the other hand, colloids serve as mesoscopic model systems for atomic systems (see Section 2.7) and we can use our results to make predictions concerning metallic quasicrystals (see previous paragraph).

### Further examples of quasiperiodic structures

Another field of research is quasiperiodic structures induced by external light fields. Appropriately arranged laser beams generate interference patterns with quasicrystalline symmetries in which particles are forced towards the highest intensities. Such systems were investigated in simulations of colloidal particles [8, 11–

13, 27, 125, 126] and hard rods and needles [127, 128]. Experiments [7, 126, 129–131] were mainly realized by Mikhael *et al.* with spheres in the range of microns. In principle, quasicrystals of any desired symmetry can be generated in that way. We will examine colloids in laser fields in detail in Chapter 4.

Two-dimensional quasicrystalline potentials have also been realized for ultra cold atoms, e.g. Bose-Einstein condensates, by one-dimensional optical lattices [132–134] or by two-dimensional optical lattices with octagonal [135, 136] and decagonal [137] symmetry. In further studies [138] also a Fermi gas of ultra cold fermions in a two-dimensional quasiperiodic lattice is investigated. The great advantage of optical lattices is their lack of defects.

Furthermore, quasiperiodic arrangements were included in photonic systems made up of structures composed of areas (e.g. building blocks) with varying refractive indices. The components are arranged with quasicrystalline order. The dimensions of the components possess characteristic length scales in the order of magnitude of optical wavelengths. Like photonic crystals such photonic quasicrystals influence the propagation of photons through the structure [139–142]. Possible applications are described in Subsection 2.2.5.

### 2.2.3 Quasicrystals in nature

Aside from the numerous quasicrystals that have been synthesized in the laboratory or in simulations, also natural quasicrystals are known. In 2009 single grains with icosahedral symmetry were found within a rock sample that was part of a meteorite which built more than about 4.5 billion years ago [143] and fell into earth about 15000 years ago [144]. The rock sample was discovered in Khatyrka, a village in eastern Russia [23, 144–146], and was initially exposed in an Italian natural history museum in Florence under the name khatyrkite. The discovery of the icosahedral grains resulted from further investigations of khatyrkite initiated by Luca Bindi and Paul Steinhardt. The grains show a composition of  $\text{Al}_{63}\text{Cu}_{24}\text{Fe}_{13}$ , have a size of micrometers and remain stable under standard conditions [23, 144–146]. Due to its icosahedral symmetry the discovered quasicrystal was called icosahedrite. In Figure 2.7 a section of khatyrkite with incorporated icosahedrite is depicted.

The discovery shows that quasicrystals can build spontaneously and remain stable under natural conditions. Interestingly, the composition of icosahedrite is nearly the same as in  $\text{Al}_{65}\text{Cu}_{20}\text{Fe}_{15}$  which was the first stable icosahedral quasicrystal synthesized by Tsai *et al.* in 1987 [70].

The second natural quasicrystal was found in the same meteorite again by Bindi and Steinhardt *et al.* [147]. It is the first discovered natural quasicrystal with decagonal symmetry and is composed of  $\text{Al}_{71}\text{Ni}_{24}\text{Fe}_5$ . Laboratory studies found ambient pressure and a narrow temperature range between 1120 K and 1200 K in



Figure 2.7: Sample of khatyrkite in which the dark regions contain icosahedrite, the first discovered natural quasicrystal. Adopted with permission from [23] (<https://doi.org/10.1126/science.1170827>). Copyright 2009 by The American Association for the Advancement of Science.

which the quasicrystal is stable [147]. Decagonal quasicrystals of the same composition were synthesized by Tsai *et al.* in 1989 [148] and are stable within the same temperature range [149].

Both described natural quasicrystals exhibit nearly perfect structural arrangements comparable to the best synthesized samples [147]. The still remaining question is whether quasicrystalline structures may also form under natural conditions on earth, potentially deeper in the mantle of the earth. According to Bindi and Steinhardt, there may even be examples of quasicrystals that have not been observed in the laboratory yet [144].

## 2.2.4 Stability of quasicrystals

So far, it is not yet well understood why certain alloys form quasicrystalline structures and others do not. A basic question is whether the quasicrystalline structures are stabilized by energy or entropy or an interplay of both [150–152].

Energetic stabilization would result in a nearly perfect structure as obtained from construction methods (see Subsection 2.3.5). Due to atomic interactions connected with microscopic forces the structure is forced into an ideal quasicrystal at low enough temperatures. Such structures are referred to as deterministic. However, it is still to be investigated if such forces exist and what their physical origin is. In such a model it is assumed that the system has a quasiperiodic ground state which means that primarily energy stabilizes the structure [2, 153, 154].

Another approach is based on entropic stabilization. Elser and Henley proposed the “random-tiling-model” [104, 105, 155–160] in which the tiles are packed randomly without regarding the matching rules (see Subsection 2.3.5.3). Accord-

ingly, phasons contribute to the stabilization. Phasons are additional hydrodynamic modes that cause complex rearrangements of the particles (see Section 2.5). All possible local configurations are supposed to possess the same energy [104, 105, 157]. The equilibrium configuration is supposed to be the tiling with maximal entropy [155, 161]. In this description, the question remains whether random tilings may provide a ground state of a system [162].

It is shown that entropically stabilized quasicrystals exist [28, 162] and the random tiling hypothesis is also confirmed by Kiselev *et al.* [163] for decagonal quasicrystals.

Apart from the question of the stabilization mechanism of quasicrystals in general, we now want to investigate why synthetic as well as natural quasicrystals prefer certain rotational symmetries. Synthetic metallic quasicrystals possess 5-, 8-, 10- or 12-fold rotational symmetry. Soft quasicrystals mostly show 12-fold symmetry except for one example with 18-fold rotational symmetry. These symmetries are all connected to a low rank (see Section 2.4). More precisely, two-dimensional quasicrystals with 5-, 8-, 10- or 12-fold rotational symmetry possess a rank  $D = 4$ , while quasicrystals with different symmetries have a larger rank. Indeed, there is a connection between the rank of a system and its propensity to build appropriate structures. For instance, the number of incommensurate length scales of a structure increases with its rank. Two-dimensional structures with  $D = 4$  provide two length scales, while a rank  $D \geq 6$  leads to three or more length scales which are difficult to balance within the growth process [115]. Furthermore, structures with a low rank possess rational approximants with only small unit cells which facilitates their formation. Rational approximants are local quasiperiodic structures that fill space by translation. In case of light-induced patterns, quasicrystals with low rank  $D = 4$  build at much lower light intensities than quasicrystals with larger rank  $D \geq 6$  [7]. A possible reason is the number density of symmetry centers that decreases by several orders of magnitude with the rank. Symmetry centers are local motifs in the lattice that obtain the highest possible rotational symmetry and reveal initial sites for quasicrystalline ordering. Consequently, the number density of symmetry centers determines the propensity of a system to build quasicrystals [7, 8]. Additionally, it is expected that in the case of larger ranks the quasicrystalline layers may possess a large amount of defects and impurities which could impede the periodic stacking of layers in three dimensions [7].

### 2.2.5 Properties and applications

Quasicrystals possess many fascinating properties that are completely different from the ones of periodic crystals. Some of these properties make quasicrystals be considered as materials with a great technological potential [75, 164]. In the following we introduce quasicrystals which are possible candidates for applications

and give an overview of their properties. We summarize applications that have already been fabricated or could potentially be realized in the future.

In case of atomic quasicrystals, i.e. quasicrystals composed of metallic alloys, the stable icosahedral alloy Al-Cu-Fe is a quasicrystal with profit-promising features and of commercial interest since it is cheap, easily available and non-toxic [165, 166]. Quasicrystals like Al-Pd-Mn can also be grown as large single grains [167, 168], but the components are quite precious.

Most properties of metallic quasicrystals deviate from the properties that are expected from their constituents [169, 170]. For instance, the mechanical properties of quasicrystals are quite remarkable since quasicrystals are very hard and brittle at room and intermediate temperatures [171, 172], while they become ductile at larger temperatures. In particular, the hardness of quasicrystals based on aluminum is about  $800 - 1000 \text{ kg/mm}^2$  for Al-Cu-Fe at intermediate temperatures [172, 173], which is similar to the hardness of metallic glasses based on iron [174]. As a downside, the intrinsic brittleness of quasicrystals resembles that of ceramics and provides the main limitation for technological applications. The brittleness causes a low fracture toughness and the tendency of the quasicrystal to build out cracks [175]. At high temperatures the transition from brittle to ductile makes the material deform more and more with applied stress [166, 176–178]. Dependent on the material's composition typical transition temperatures to the ductile phase are about  $T_d = 900 - 1100 \text{ K}$ , which means  $T_d > 0.5 T_m$  where  $T_m$  is the melting temperature of the quasicrystal.

The thermal properties of quasicrystals comply even less with the ones of periodic metallic materials. Quasicrystals exhibit a very low thermal conductivity  $\lambda$  which continuously increases with temperature, probably due to an increased contribution of electrons for temperatures larger than  $T = 300 \text{ K}$  [166, 179]. However, within the whole temperature range the thermal conductivity of quasicrystals is separated by one or two orders of magnitude from the thermal conductivity of pure metals [166, 180] (compare, e.g.  $\lambda_{\text{Cu}} = 387 \text{ W/mK}$ ,  $\lambda_{\text{Al}} = 202 \text{ W/mK}$ ,  $\lambda_{\text{Fe}} = 80 \text{ W/mK}$ ,  $\lambda_{\text{Al-Cu-Fe}} = 1.8 \text{ W/mK}$  at room temperature [166]). Such a high thermal resistance is usually known from good thermal insulators or ceramics. Additionally, the higher the structural quality of the quasicrystal is, the lower is its thermal conductivity [181]. Only little deviations from the ideal chemical composition and defects strongly increase the conductivity. A possible reason could be the increased mobility of the atoms in the presence of vacancies, which resembles the behavior of doped semiconductors. Furthermore, the thermal expansion of quasicrystals increases linearly and is similar to the one of iron and steel [166, 182].

The electronic properties of quasicrystals are neither typical of a material consisting of metallic elements. Similar to the low thermal conductivity, a low electric conductivity or respectively a high electric resistance is observed. At low

temperatures, phases that are structurally perfect show an electric conductivity  $\sigma = 100 - 300 \Omega^{-1}\text{cm}^{-1}$  in Al-Cu-Fe or Al-Pd-Mn alloys which is about six orders of magnitude lower than for pure aluminum [178, 183]. The electric conductivity increases with temperature and as well with the amount of defects [178, 183].

Further promising features of quasicrystals are their surface properties, for instance the friction properties. The friction coefficient that results from the friction between two ideal oxide-free quasicrystals is about one order of magnitude below the friction coefficient between pure metals [178]. Some quasicrystalline alloys also show low friction properties when they are in contact with other materials [169, 184, 185]. Additionally, the adhesion energy with water that results from the adhesive force between water and the considered surface is lower for quasicrystals than for common metals, which means that quasiperiodic surfaces do not wet so easily [178]. Furthermore, as proven in experiments with different environmental conditions, quasicrystals are relatively unreactive [165, 186], and other materials do not get stuck so easily on a quasicrystalline surface. Connected to that is the good resistance to oxidation which was first investigated for icosahedral Al-Pd-Mn surfaces [187, 188] and later shown for Al-Cu-Fe alloys [189]. However, note that similar to most metallic crystalline solids the formation of a thin oxide film on the surface when the material is exposed to air or pure oxygen is not completely avoidable for quasicrystals either [178].

Due to their brittleness quasicrystals are unsuitable to build the bulk in most applications. However, two fields of applications are not disturbed by the brittleness, namely applications with reduced thickness, i.e. coatings, and composite materials in which quasicrystalline elements are added to periodic solids.

In the field of thin films, the first product on the market was pans with quasicrystalline coatings. The pans were fabricated by the French company Sitram with the trade name cybernox [190]. Since the adhesion of the quasicrystal is much smaller for many foods compared to a metallic pan, food gets stuck less and the pan is easy to clean. In addition, due to the hardness of quasicrystals the surface is only little destroyed or scratched by metallic kitchen equipment. Furthermore, since quasicrystals become plastic at increased temperatures the quasicrystalline coating can stand the stress at the interface that results from thermal expansion of the bulk material. A further advantage is the low thermal conductivity which results in an even heating of the surface [178, 191]. However, the great problem of such pans with quasicrystalline coatings is that the addition of salt to the food etches the coating, which is the reason why the production was stopped [191].

An alternative application are thin films [192, 193], i.e. solid films in the range of  $10^{-6} - 10^{-9}$  m. For example, quasicrystals are potentially suitable for thermal barrier coatings [178, 192], which are usually applied in engines to protect the metallic part from high temperatures. Due to the low thermal conductivity

a quasicrystalline coating may increase the thermal gradient between surface and bulk. Moreover, quasicrystals can stand the shear stress at the interface with the substrate since they become plastic at high temperatures. An advantage compared to the usually applied zirconia is the larger thermal expansion coefficient of quasicrystals. However, applications are limited because of the rather low melting temperature of quasicrystals. A further general problem of quasicrystalline coatings is the high degree of impurities, which arise during the fabrication. Impurities may increase the propagation of fractures and cause increased wear of the coating. The wear may cause an increased friction coefficient of the coating. A possible way to reduce the wear is the addition of a more ductile alloy to the original coating [178].

The second field of applications comprises composite materials. Small quasicrystalline components in the range of nanometers are added to crystalline metallic alloys to improve their properties [191]. A concrete product on the market produced by the Swedish company Sandvik is steel with additional small quasicrystalline particles. Even though quasicrystals are brittle, in the composite they reinforce the steel in a way that makes it hard, ductile and resistant to corrosion. Already realized applications are razor blades and surgery tools [165, 178, 191]. Quasicrystalline particles stop the motion of dislocations in the steel such that the material becomes harder and stronger. Without quasicrystalline content the dislocations could move freely and the material was easy to bend [191].

Another example is magnesium alloys which are intrinsically of poor corrosion resistance. The addition of Mg-Zn-Nd quasicrystals significantly improves the final resistance of the material against corrosion [194]. Accordingly, the surface remains stable for a longer time, which also enhances the life time of the whole solid. A similar effect is observed for aluminum alloys, copper and low-carbon steel [195]. These materials often suffer from the erosive conditions in their environment which result in wear. With the addition of quasicrystalline particles the wear resistance of such soft alloys is improved due to the hardness of quasicrystals.

Another proposed product is quasicrystalline powder composed of small quasicrystalline balls. With the balls embedded in plastics, the resulting material is suitable for production of gears that do not erode because of the strong quasicrystalline particles that are resistant to wear and friction. An application are ventilators and fans with plastic gears [191].

Further potential applications are in the field of the aviation industry [192]. The addition of lithium to an alloy decreases the density of the alloy due to the reduced atomic weight of lithium which has a positive impact on the fuel consumption. Since at the same time the mechanical properties of quasicrystals are better than the ones of periodic crystals, the adoption of quasicrystals in airplanes is a serious consideration.

Aside from coatings and composites quasicrystals could also have an influence on the chemical industry. In chemical reactions quasicrystals might serve as catalysts because they can rise the efficiency of reactions, such as in the production of hydrogen from methanol [196, 197]. The catalytic activity of quasicrystalline particles could lead to a replacement of conventional expensive materials applied in chemistry.

All in all, metallic quasicrystals possess promising properties. However, the realization of applications is still in an early phase of its development [169]. For instance, it is a challenging task to grow quasicrystals in a way that they can be used in applications. In this thesis we investigate building mechanisms and properties of quasicrystals numerically. We relate our results to metallic quasicrystals with the goal to contribute to a better understanding of their formation which is also required for applications.

Aside from metallic quasicrystals, photonic quasicrystals provide another field of promising applications. Similar as in periodic photonic crystals it is possible to achieve photonic band gaps in quasiperiodic arrangements. In such arrangements the propagation of light is prohibited for certain frequencies [198–200]. These spectral gaps are obtained by destructive interference of scattered photons, i.e. multiple scatterings of photons oppress electromagnetic waves with certain wavelengths. Photonic band gaps have already been found in two-dimensional quasicrystals with 12- and 8-fold symmetries [198, 199] as well as in three-dimensional icosahedral quasicrystals [200].

A possible application of photonic quasicrystals are LEDs [140]. The addition of photonic quasicrystals within the LED could enhance the light emission and, compared to photonic crystals, the direction of illumination could be tuned such that the emitted light shows less directional dependence due to the lack of periodicity in quasicrystals. Accordingly, the far-field pattern is flatter than for periodic photonic crystals. Possible illumination applications are projection displays or flat screen back lighting. Additionally, a wide field of illumination - as required in automotive headlights - may be obtained by tailored quasicrystals [140].

## 2.3 Quasiperiodic tilings

In this Section we describe macroscopic quasiperiodic tilings which were discovered long before the first atomic quasicrystals. The Section gives the theoretical foundation for our studies presented in the following Chapters. We first define the term tiling and summarize the development of aperiodic tilings. Afterwards, we introduce the golden ratio – a number frequently occurring in connection with decagonal tilings. We continue with a selection of quasiperiodic tilings and their construction methods. Finally, the term of local isomorphism is introduced.

### 2.3.1 Definition of tilings

A tiling is a discrete tessellation of space that results from filling space with building blocks, also called tiles, which may be decorated with particles at well-defined positions. Since tilings describe a structure in the discrete picture, they are especially suitable for studying the atomic arrangements and diffraction properties of the structure [10].

Periodic tilings have already been introduced in Section 2.1 (see, e.g. Figure 2.1). A periodic tiling can be constructed from only one single tile or unit cell that is repeated in space through translation. There is an infinite number of tiles of various shapes that build periodic patterns. The construction of a periodic tiling with more than one differently shaped tile is also possible. An interesting approach by the Dutch artist Maurits C. Escher is periodic tilings composed of basic tiles that resemble living objects [201].

Quasicrystals do not possess translational symmetry and therefore cannot be built from translations of one single unit cell. Though, there are other ways to generate aperiodic tilings. For instance, aperiodic tilings may be constructed with two or more differently shaped tiles. The tiles are put together according to certain rules such that the whole space is filled and no gaps or overlaps occur. Rotations and reflections are allowed [201]. Another example is aperiodic tilings built from only one tile with differently marked edges and non-trivial construction rules (see, e.g. [202]). In the following Subsections we give a deeper insight into quasiperiodic tilings.

### 2.3.2 Development of quasiperiodic tilings

The discovery of two-dimensional quasiperiodic tilings started centuries ago. In medieval Islamic architectures quasiperiodic tilings decorated shrines and mosques. Examples were found in Turkey, India, Afghanistan, Iran and Iraq (see Figure 2.8 (a)). The architects were probably not aware of the mathematical background and it is assumed that they found the patterns by trial and error [203–206]. In 1525 the German artist Albrecht Dürer studied the geometry of the plane and found a way to cover space by regular pentagons with the arising gaps filled by rhombs [207, 208]. A reconstruction of one of Dürer's drawings is shown in Figure 2.8 (b). In the beginning of the 17th century the concept was picked up by Johannes Kepler who constructed decagonal tilings during a study of two-dimensional infinite patterns [41].

The probably first deliberately found aperiodic tiling is called Wang dominoes. In 1961 the logician and mathematician Hao Wang developed unit squares with edges marked in certain colors. He assumed that if any set of such Wang dominoes covers space by putting dominoes with the same edge color together, then the resulting

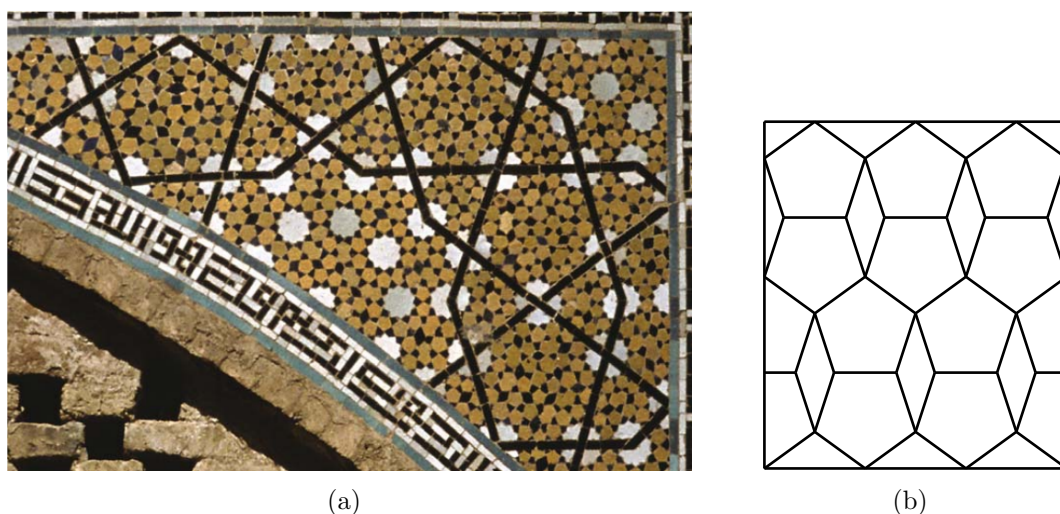


Figure 2.8: Early aperiodic tilings. (a) Photograph of a spandrel from the Darb-i Imam shrine in Isfahan, Iran. The shrine was built in 1453 and is decorated with a decagonal tiling. Adopted with permission from [204] (<https://doi.org/10.1126/science.1135491>). Copyright 2007 by The American Association for the Advancement of Science. (b) One of Dürer's drawings from 1525 (reconstructed from [207]). The tiling consists of regular pentagons and rhombs.

tiling is periodic [209, 210]. However, Wang was proven wrong when in 1966 his student Robert Berger found a set of more than 20000 Wang dominoes that cover space without periodicity [202]. Later, the minimal number of required tiles was reduced to 13 [211]. In 1971, Raphael M. Robinson replaced the dominoes by polygonal tiles with bumps or dents at the edges resulting in jigsaw-like pieces. In that way he generated six tiles that cover space aperiodically when putting appropriate tiles together [212]. It is supposed that six is the minimal number of such square based tiles that is required to fill the plane without periodicity [201]. In 1973 and 1974 Roger Penrose discovered further sets of tiles that cover space without periodicity and which are not based on square tiles. While initially Penrose “wanted to design something interesting for someone who was in hospital to look at” [213] he found an aperiodic tiling that is composed of four basic tiles, namely a pentagon, a pentagram, a tile built from  $3/5$  pentagram and a rhomb. Today it is called the pentagon tiling. In continuing studies Penrose found two further possibilities to describe the tiling by only two basic tiles each. All of his tilings possess 5-fold rotational symmetry identified by Alan L. Mackay who calculated the Fourier transforms of the tilings in 1982 [201, 213, 214].

### 2.3.3 The golden ratio

A characteristic length scale of aperiodic tilings with decagonal rotational symmetry is the golden ratio. In this work we mainly study tilings with decagonal symmetry and hence often face the golden ratio. In the following we introduce the golden ratio and some interesting properties of it.

The golden ratio or golden mean  $\tau$  is an irrational number. Mathematically expressed,  $\tau$  is given by the positive solution of the equation

$$\tau^2 - \tau - 1 = 0 \quad (2.1)$$

which leads to

$$\tau = \frac{1 + \sqrt{5}}{2} = 1.618\dots \quad (2.2)$$



Figure 2.9: Graphical illustration of  $\tau$  as the ratio of two lengths.

In a graphical illustration (see Figure 2.9) the golden ratio can be described as the ratio  $\tau = B/A$  of two segments  $B$  and  $A$  that divide a length in a way that the ratio of the longer segment  $B$  to the shorter one  $A$  correlates with the ratio of the whole length to the longer segment  $B$ , i.e.

$$\frac{B}{A} = \frac{A+B}{B} \Rightarrow \tau = \frac{1}{\tau} + 1 \quad (2.3)$$

which is also obtained by rearranging equation (2.1).

Curiously, the ratio of the shorter segment  $A$  and the difference of the segments  $B$  and  $A$  provides  $\tau$  again, i.e.

$$\frac{A}{B-A} = \frac{B}{A} \Rightarrow \frac{1}{\tau-1} = \tau \quad (2.4)$$

which is again in agreement with equation (2.1).

Since  $\tau$  is an irrational number, the mentioned segments  $A$  and  $B$  are no rational numbers. In particular,  $A$  takes about 0.382 and  $B$  about 0.618 of the whole length. The approximation of  $\tau$  by the lengths  $A$  and  $B$  is quite imprecise. An

alternative approximation is the ratio of two successive Fibonacci numbers (see Subsection 2.3.5.1), i.e.  $\tau = F_{n+1}/F_n$ . The higher the Fibonacci numbers are, the more precise becomes the approximation.

Another approach is the expression of  $\tau$  as a continuous fraction of the form

$$\tau = 1 + \frac{1}{\tau} = 1 + \frac{1}{1 + \frac{1}{\tau}} = \dots = 1 + \frac{1}{1 + \frac{1}{1 + \frac{1}{\dots}}} \quad (2.5)$$

or as the continuous square root

$$\tau = \sqrt{1 + \tau} = \sqrt{1 + \sqrt{1 + \sqrt{1 + \sqrt{1 + \dots}}}} \quad (2.6)$$

Moreover, from trigonometrical considerations one obtains

$$\tau = 2 \cos(\pi/5) = 2 \sin(3\pi/10) \quad \text{and} \quad \frac{1}{\tau} = 2 \sin(\pi/10) = 2 \cos(2\pi/5). \quad (2.7)$$

Apart from quasicrystals the golden ratio appears in several areas of life (see, e.g. [215] for a summary). For example, the golden ratio is found in nature: The numbers of petals in flowers often correspond to Fibonacci numbers. Examples are ordinary daisies with 21 or respectively 34 petals and sunflowers with up to 144 petals. Additionally, in many plants the leaves around a stem are arranged in a golden angle of about 137.5 degrees. This angle is obtained by dividing a circle into two parts in a way that the ratio of the arc lengths corresponds to the golden ratio  $\tau$ . In such an arrangement the space for each leaf and the amount of light that attains each leaf is maximal. Another example is the plant sneezewort (*Achillea ptarmica*). After a first branching after two months, it branches every successive month in a way that the numbers of branches correspond to successive Fibonacci numbers. Also some animals exhibit proportions of the golden ratio. For instance, the diagonals in a regular pentagon build a pentagram with golden proportions that are also present in starfish. Even in the human body the golden ratio is present, for instance as the ratio between forearm and hand. An extensive study of the proportions of the human body was done by Leonardo DaVinci in his work of the vitruvian man from 1490. It is speculated that he incorporated golden proportions in the illustration (see, e.g. [216]).

### 2.3.4 Examples of quasiperiodic tilings

In this Subsection we examine the already addressed tilings discovered by Penrose in detail and give an overview of further quasiperiodic tilings.

### Penrose tilings

The tilings constructed by Penrose belong to the most common tilings with 5-fold rotational symmetry. The rhombus tiling which nowadays is referred to as Penrose tiling [217] consists of two basic tiles in the shape of rhombs, a fat and a skinny one. Although initially found by Penrose, Roger Ammann discovered the rhombus tiling independently in 1976 [201].

Figure 2.10 (a) depicts the single tiles of the Penrose tiling. Geometrical properties are drawn in. In Figure 2.10 (b) a section of a Penrose tiling is shown.

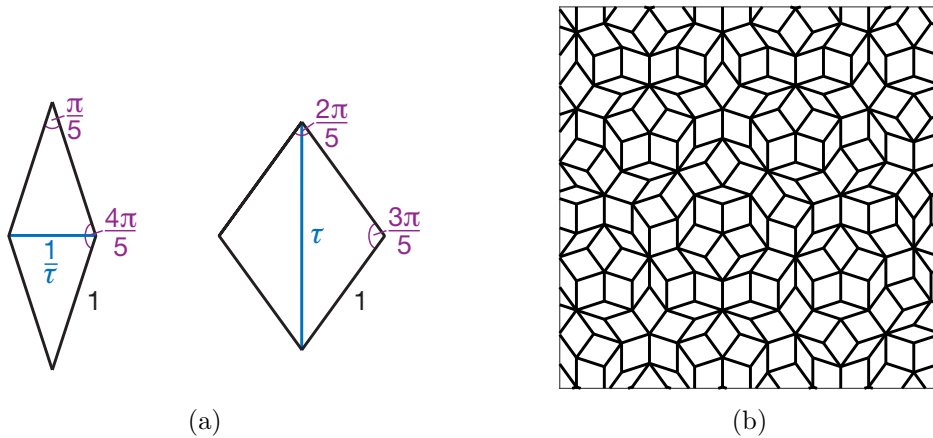


Figure 2.10: (a) Basic tiles of the rhombus tiling: a skinny rhomb (left) and a fat rhomb (right). (b) Section of a rhombus tiling. Data for the positions of the edges obtained by Matthias Sandbrink.

All side lengths of the tiles are equal. A further length scale is provided by the diagonals of the tiles: A fat rhomb with side length  $l_0 = 1$  possesses a long diagonal of length  $l_1 = \tau$ , while in the skinny rhomb the length of the short diagonal is  $1/l_1 = 1/\tau$ . These incommensurate length scales with  $l_1/l_0 = \tau$  are typical of a decagonal quasicrystal. A further characteristic is the ratio of the number of fat and skinny rhombs in a tiling which approaches  $\tau$  for a large number of tiles  $N_{\text{tiles}}$ , i.e.

$$\lim_{N_{\text{tiles}} \rightarrow \infty} \frac{N_{\text{fat}}}{N_{\text{skinny}}} = \tau. \quad (2.8)$$

There are several methods to construct the Penrose tiling, for example by matching rules (see Subsection 2.3.5.3) or as a projection from a higher-dimensional space (see Subsection 2.3.5.2). The Penrose tiling can also be expanded to three dimensions in a way that space is filled aperiodically resulting in an icosahedral quasicrystal (see, e.g. [6, 218, 219]).

Another tiling constructed by Penrose is the kite-and-dart tiling which is also composed of two basic tiles. Their forms resemble a kite and a dart as depicted in Figure 2.11 (a). The denomination was given by John H. Conway who studied the tiling intensely [201]. A section of a kite-and-dart tiling which can be obtained by matching rules (see Subsection 2.3.5.3) is illustrated in Figure 2.11 (b).

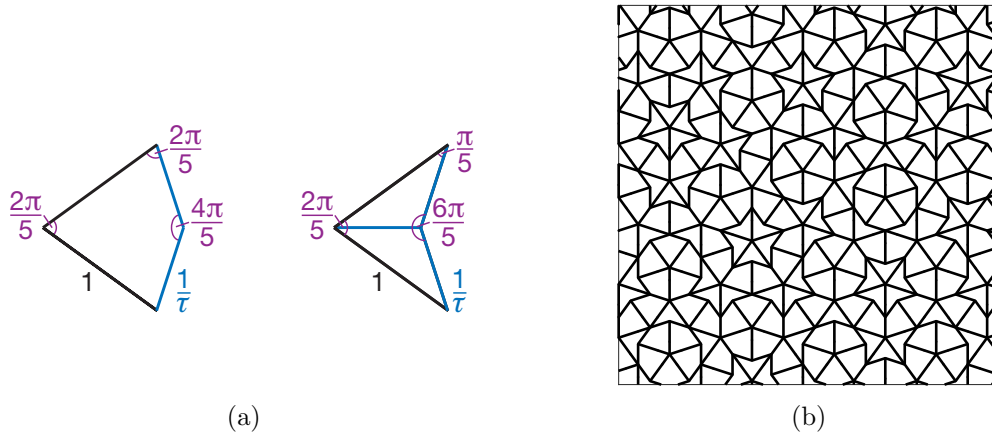


Figure 2.11: (a) Basic tiles of the kite-and-dart tiling: a kite (left) and a dart (right). (b) Section of a kite-and-dart tiling.

As in the rhombus tiling, there are two incommensurate length scales with a ratio  $\tau$ , and the ratio of the number of tiles in a tiling reads

$$\lim_{N_{\text{tiles}} \rightarrow \infty} \frac{N_{\text{kite}}}{N_{\text{dart}}} = \tau. \quad (2.9)$$

### Further quasiperiodic tilings

By now, numerous quasiperiodic tilings with different rotational symmetries are known. The most famous tilings possess 8-fold, 10-fold or 12-fold rotational symmetry, which correspond to the quasicrystalline symmetries that build most easily (see Section 2.4).

An example of a tiling with 10-fold rotational symmetry is composed of Tübingen triangles, i.e. two differently shaped triangles discovered by a group in Tübingen [220]. A further development led to a Tübingen tiling composed of five basic tiles as illustrated in Figure 2.12 (a). The tiling possesses two incommensurate lengths  $l_0$  and  $l_1$  with a ratio  $l_1/l_0 = \tau$ . Common tilings with 8-fold rotational symmetry are the Ammann-Beenker tilings which are composed of rhombs and squares and show two typical length scales with  $l_1/l_0 = \sqrt{2}$ . A section of an Ammann-Beenker tiling is depicted in Figure 2.12 (b). Ammann found the tiling by putting the

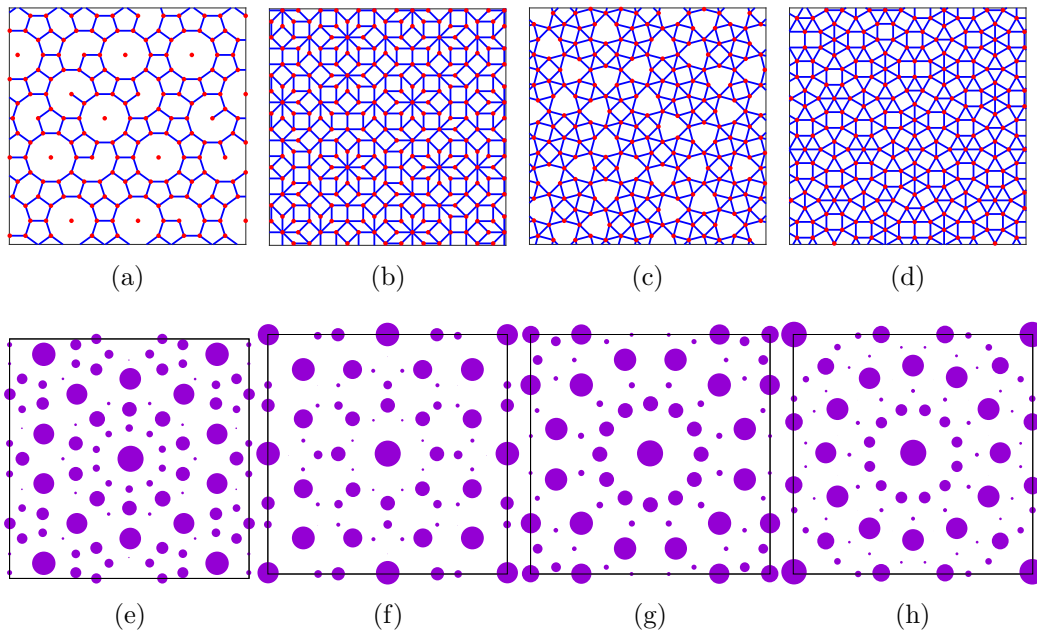


Figure 2.12: (a)-(d) Sections of two-dimensional tilings with different rotational symmetries. (a) Tuebingen tiling with decagonal (10-fold) rotational symmetry, (b) Amman-Beenker tiling with octagonal (8-fold) rotational symmetry, (c) shield tiling and (d) square-triangle tiling each with dodecagonal (12-fold) rotational symmetry. Red dots represent the positions of particles. A tiling is drawn by connecting next neighbor particles. The positions of the Tuebingen tiling, the Ammann-Beenker tiling and the shield tiling are obtained from the minima in a corresponding potential landscape (see Section 4.2). The positions of the square-triangle tiling are obtained from substitution rules (courtesy of Matthias Sandbrink). (e)-(h) Structure factors of the depicted tilings in reciprocal space. Point sizes reveal the intensities of the peaks.

basic tiles together, Beenker discovered it independently by mathematical calculations [221]. Tilings with 12-fold symmetry are provided, for example by the shield tilings, which were discovered by Gähler [222] and are composed of squares, equilateral triangles and tiles in the shape of a shield (see Figure 2.12 (c)). Further tilings with 12-fold symmetry are the square-triangle tilings [223] with appropriate two basic tiles. A section of a square-triangle tiling is illustrated in Figure 2.12 (d). The illustrated dodecagonal tilings offer two typical lengths with a ratio  $l_1/l_0 = \sqrt{3}$ .

All depicted patterns possess two incommensurate lengths. The length scales are given by the reciprocal lattice vectors (see also Subsection 3.4.4). The tilings are usually obtained by connecting nearest neighbor particles with a distance of the

short length scale. An extensive selection of further tilings with two or more incommensurate lengths is presented in [224].

In Figures 2.12 (e)-(h) we show the corresponding structure factors of the depicted tilings. The structure factor is a measure of the particles' positions in reciprocal space and illustrates the rotational symmetry of a system (see Subsection 3.5.2). Perfect quasicrystals possess discrete Bragg peaks of small width. For an improved contrast in the illustration we integrate over the peak intensities. At the positions of the peaks we plot points with a radius that is proportional to the integrated intensities.

In this thesis we investigate systems of particles that arrange to the tilings illustrated in Figure 2.12 in detail.

### 2.3.5 Construction methods

Due to the lack of translational symmetry, the construction of quasiperiodic tilings is more complex than the construction of periodic tilings. In the following, we introduce different convenient methods to generate tilings with quasicrystalline symmetries.

#### 2.3.5.1 Substitution method

The substitution method is based on the repeated replacement of single elements by further elements. For instance, the Fibonacci word sequence which describes a quasicrystal in one dimension can be obtained by substitution. The Fibonacci word sequence is composed of two elements denoted by  $L$  and  $S$ . For its construction we begin with an element  $L$ . In the following steps we substitute  $L \rightarrow LS$  and  $S \rightarrow L$ . By applying the substitution again and again, the Fibonacci word sequence grows. The first five iterations lead to

$$\begin{aligned}
 &L \\
 &LS \\
 &LSL \\
 &LSLLS \\
 &LSLLSLSL \\
 &LSLLSLSLLSLLS.
 \end{aligned}
 \tag{2.10}$$

After  $n$  steps of substitution one obtains  $F_{n+1}$  segments of the species  $L$  and  $F_n$  segments of species  $S$ . The integers  $F_n$  denote the Fibonacci numbers and are given by the recursion formula  $F_n = F_{n-1} + F_{n-2}$  with the first two numbers

$F_1 = F_2 = 1$ . Accordingly, the Fibonacci numbers read

$$1, 1, 2, 3, 5, 8, 13, 21, 34, 55, 89, 144, 233, \dots \quad (2.11)$$

and build the Fibonacci sequence. A curious observation is that the ratio of two consecutive Fibonacci numbers approaches the golden ratio  $\tau$  for large numbers, i.e.

$$\lim_{n \rightarrow \infty} F_{n+1}/F_n = \tau. \quad (2.12)$$

Aside from one-dimensional quasicrystals, one can also construct two-dimensional quasicrystals by substitution: The construction procedure starts with a two-dimensional basic tile of the desired tiling. The tile is expanded by multiplying it with an appropriate inflation factor  $q > 1$ . By following certain substitution rules the expanded tile is decomposed into smaller tiles that correspond to the basic tiles of the desired tiling. Iterations of this process result in an ever growing tiling within the boundaries of the expanded starting tile.

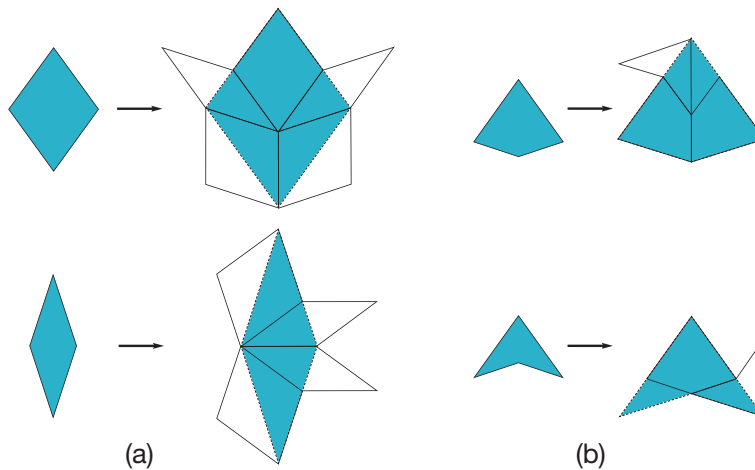


Figure 2.13: Substitution of the basic tiles of (a) the rhombus tiling and (b) the kite-and-dart tiling. The inflated basic tile (blue) is substituted by basic tiles bordered by continuous lines.

In Figure 2.13 we illustrate substitution rules for the basic tiles of the rhombus tiling (see Figure 2.13 (a)) as well as the kite-and-dart tiling (see Figure 2.13 (b)). The inflation factor is the golden ratio, i.e.  $q = \tau$ . Note that in our examples the inflated tiles cannot be completely filled with basic tiles. Certain areas are not covered and at other areas the basic tiles exceed the inflated tile. However, by iterating the depicted substitutions proper tilings without gaps or overlaps are

achieved. The resulting tilings comply with the matching rules (see Subsection 2.3.5.3).

Other tilings can also be constructed by substitution [224]. In tilings with a symmetry different from five, the inflation factor is different from  $\tau$ . For example, the Ammann-Beenker tiling has an inflation factor  $q = 1 + \sqrt{2}$ . There are also known substitution rules for tilings with, e.g. 7-, 9- or 11-fold symmetry [224]. However, the rules may become complicated and the number of required rules increases with the number of basic tiles.

### 2.3.5.2 Projection and section method

Quasicrystals can be constructed from projections or sections of structures in a higher-dimensional space, called hyperspace [36]. While many quasicrystals can be obtained from periodic arrangements in hyperspace, for other quasicrystals the hyperspace structure is rather complicated, e.g. in the form of fractals. In order to obtain a quasicrystal, lattice points in the hyperspace within a certain acceptance domain are projected onto a space of lower dimension. For example, the Penrose tiling can be constructed by projecting a five-dimensional cubic lattice onto a two-dimensional plane [218, 225, 226].

Since it is difficult to depict a five-dimensional hyperspace, we demonstrate the method using the example of a two-dimensional square lattice in which points within the acceptance domain are projected onto a one-dimensional space given by a line (see Figure 2.14). The line is referred to as projection line. The acceptance domain is a rectangle parallel to the considered projection line. In order to achieve an infinitely large structure the rectangle needs to be infinitely long in parallel direction. The height of the acceptance domain is usually defined in a way that it is maximal but no unit cell of the square lattice lies completely inside the acceptance domain, i.e. at most three points on the edges of each unit cell are projected onto the line (see Figure 2.14 (a)). Regarding that condition the height  $h$  of the acceptance domain reads  $h = a(\cos(\alpha) + \sin(\alpha))$  with the lattice constant  $a$  and the angle  $\alpha$  between the  $x$ -axis and the projection line. In our examples the projection line lies within the acceptance domain. Note that we can also shift the line or the acceptance domain independently.

The projected points show long-range positional order. If the slope of the projection line is irrational, we obtain an arrangement of projected points without translational symmetry, i.e. a quasicrystal. In Figure 2.14 we illustrate the special case of the irrational slope  $1/\tau$  with the golden ratio  $\tau$  (see Subsection 2.3.3). For that choice the distances between the projected points build a Fibonacci sequence. Note that the Fibonacci sequence is not the only quasiperiodic lattice that can be obtained by projection. Modifying the slope or acceptance domain can result in further quasiperiodic arrangements. However, even a very small change of the

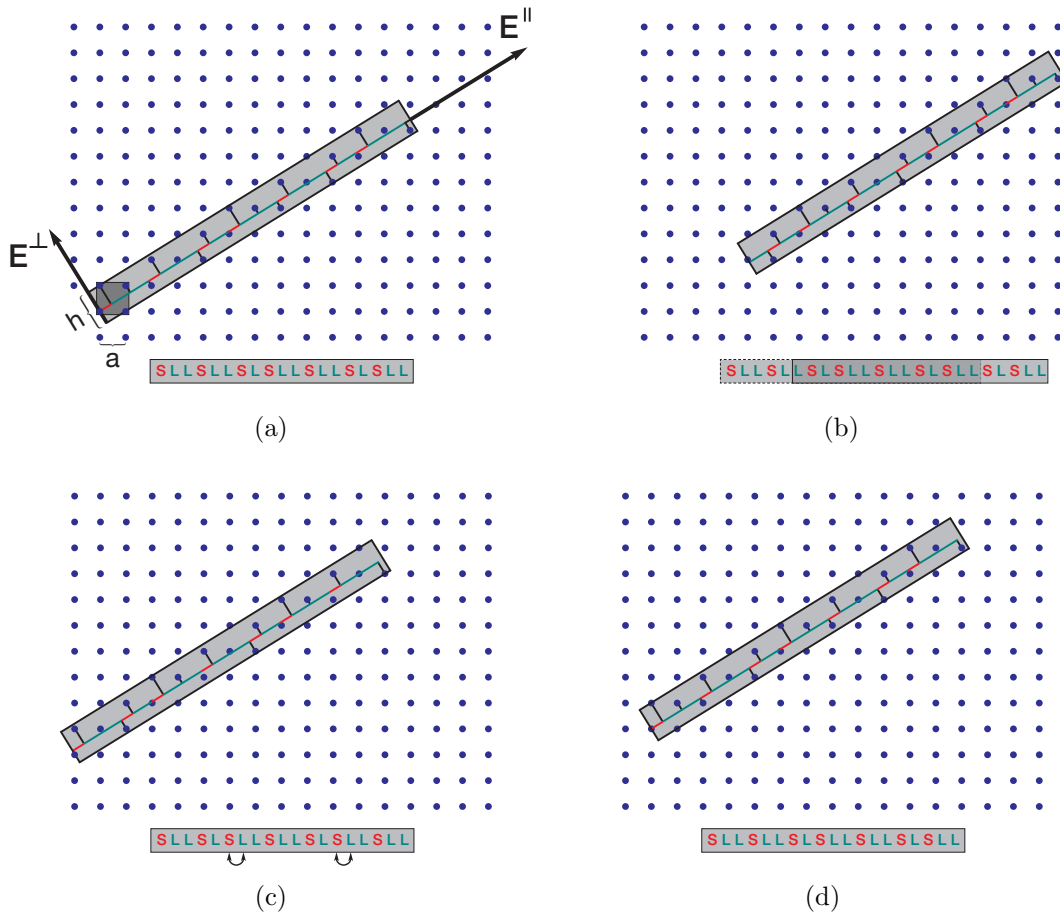


Figure 2.14: Projections of points within a two-dimensional square lattice onto a projection line with slope  $1/\tau$ . The acceptance domain is depicted as a gray rectangle. A Fibonacci sequence of long (L) and short (S) segments is obtained. (a) Determination of the size of the acceptance domain by the outermost vertices of the dark gray unit cell. (b) Shift of the acceptance domain along the physical space  $E^{\parallel}$  resulting in a phasonic displacement. The projected points are shifted about a distance proportional to the displacement of the acceptance domain. (c) Displacement of the acceptance domain along the perpendicular space  $E^{\perp}$  resulting in a phasonic displacement. Some segments of the sequence rearrange which corresponds to phasonic flips indicated by arrows. (d) Combination of displacements in physical and perpendicular direction in a way that the original arrangement does not change.

slope such that it becomes rational leads to a periodic arrangement of projected points.

The subspace in the direction of the projection line is called the physical or real space  $E^{\parallel}$ . The perpendicular direction refers to the mathematical dimension with the subspace  $E^{\perp}$  called perpendicular or complementary space.

A presentation of a quasicrystal as projection of a periodic structure in a higher-dimensional space can be used to detect phononic and phasonic displacements. Phononic displacements correspond to a translation of the acceptance domain in physical direction (see Figure 2.14 (b)). Phasons are characteristic of quasicrystals and are due to additional degrees of freedom that arise as a consequence of the periodicity in hyperspace. Phasons are defined and explained in more detail in Section 2.5. Phasonic displacements can be described by displacements of the acceptance domain along the perpendicular direction. In this case the quasicrystalline structure rearranges as depicted in Figure 2.14 (c). Note that for certain combinations of displacements in  $E^{\parallel}$  and  $E^{\perp}$  the projected points remain at the same positions as without any displacement (see Figure 2.14 (d)). These displacements are called characteristic displacements and correspond to the lattice vectors of the hypercrystal.

A method similar to the described projection method is the section method. Using again the example of a square lattice, line segments of length  $h = a(\cos(\alpha) + \sin(\alpha))$  directed along the perpendicular space  $E^{\perp}$  are put onto the lattice points. The length of the segments corresponds to the width of the acceptance domain in the projection method. Line segments of points close to the projection line divide the line into long and short segments which again provide the Fibonacci sequence in case of  $\alpha = \text{atan}(1/\tau)$ .

In order to construct two- or three-dimensional quasicrystals the procedure has to be generalized. The hyperspace with the embedded periodic structure has to be at least of the dimension  $D$  where  $D$  denotes the rank of the structure (see Section 2.4). For instance, to obtain two-dimensional quasicrystals with decagonal rotational symmetry one needs a hyperspace of at least  $D = 4$  dimensions.

In this thesis we describe the construction of a two-dimensional decagonal quasicrystal that is derived from a five-dimensional integer lattice (see Section 8.1).

### 2.3.5.3 Matching rules

Another method to obtain quasiperiodic tilings is putting together at least two different basic tiles under consideration of matching rules, which enforce perfect quasiperiodic arrangements. Note that a perfect tiling describes the ground state of a system without phasonic flips. In contrast, a random tiling is assumed to form due to entropic effects and phasons can be present [151]. Matching rules allow to

place only certain tiles next to each other whose edges are marked appropriately, for instance by same colors or symbols.

In Figure 2.15 we illustrate the matching rules for the rhombs in the rhombus tiling (see Figure 2.15 (a)) and the kites and darts in the kite-and-dart tiling (see Figure 2.15 (b)). The matching rules are given by arrows at the edges of the tiles. Tiles are allowed to be put together if the direction and number of arrows at touching edges coincide.

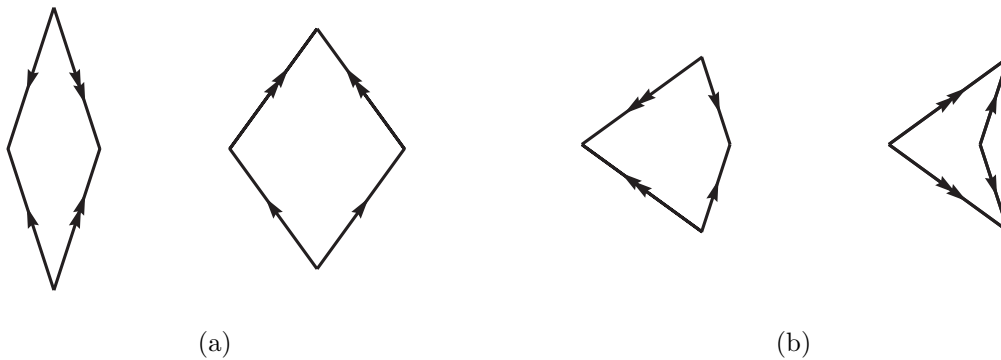


Figure 2.15: Matching rules for Penrose tilings composed of (a) rhombs and (b) kites and darts. Tiles are only allowed to lie side by side if the direction and number of arrows at touching edges coincide.

To construct a tiling it is started with one basic tile. Further tiles are added radially according to the matching rules. At some positions the neighboring tile is unambiguously prescribed. At other positions there is the possibility of attaching several tiles and the choice can lead to contradictions in the further construction. Such contradictions represent defects in the structure. It was believed that the arrangement of distant tiles needs to be known to avoid defects [155], which includes that global, long-range rules are required [227]. However, according to Gardner [201] an infinite tiling may be built by simply first filling prescribed areas. In another approach of Onoda *et al.* [228] additional rules concerning the vertices are required to build a defect-free tiling. In both approaches the matching rules are only local and represent short-range interactions, which contradicts to the assumption that long-range interactions are necessary for the growth of a perfect Penrose tiling as discussed in [229].

Due to not always uniquely prescribed neighboring tiles an infinite number of tilings may arise from the construction according to the matching rules. All these tilings have the same local isomorphism class [152] (see also Subsection 2.3.6). Violations of the matching rules during the construction, i.e. a rearrangement of the tiles, may be interpreted as local phasonic flips and a resulting random tiling.

Note that each tiling which is obtained by substitution rules can be built with finite matching rules [230]. The matching rules are much more complicated in case of tilings different from the Penrose tiling (see, e.g. [231, 232]) and become more and more complex for systems with higher symmetries. In two dimensions, there are no matching rules known for quasicrystals with a rotational symmetry higher than 14 [233].

Let us note that atoms in real quasicrystalline systems are not connected by lines nor arrows. However, one can establish a connection between the described tiling models and atomic quasicrystals [152, 160]: The tiles represent stable clusters that the atoms are supposed to build. Local matching rules correspond to local interactions between the tiles, i.e. interactions of finite range. These interactions represent the atomic interactions between the clusters in metallic alloys that favor quasiperiodic order. I.e. local matching rules represent sufficiently strong atomic interactions to induce a perfect quasicrystal. Violations of the matching rules mean weak atomic interactions that cause a random tiling and can be neglected at high temperatures.

### 2.3.6 Local isomorphism

A large number of quasiperiodic tilings is known which can be completely different or provide certain similarities. Two tilings are completely different if their global and local structures are different. Such tilings are built from different sets of basic tiles. In case of tilings built from the same basic tiles relations may occur: Two tilings are said to be equivalent if a simple translation or rotation of one tiling results in the other one. Furthermore, two tilings are locally isomorphic or of the same local isomorphism (LI) class if the patterns are maybe different concerning the global structure but indistinguishable in any finite region [154]. A proper definition reads: “Two tilings are locally isomorphic if and only if given any point  $\mathbf{P}$  in either tiling and any finite distance  $d$ , there exists a pure translation of the other tiling that causes the two to coincide everywhere in a circle of diameter  $d$  around  $\mathbf{P}$ ” [154].

An example of local isomorphisms is the Penrose tilings. Penrose showed that each finite area in a chosen Penrose tiling is found somewhere in every other Penrose tiling. Even more fascinating is that it is contained infinitely many times in every tiling. Hence, the translational repetition of unit cells in periodic tilings is replaced by a repetition of finite areas in quasiperiodic tilings [201].

Infinite tilings of the same LI class cannot be distinguished by measurements, i.e. they are physically indistinguishable. For instance, their diffraction patterns possess the same wave vectors and even the same intensities of the Bragg peaks.

## 2.4 Rank

Crystals and quasicrystals can be classified according to their rank  $D$ . The rank is defined as the minimal number of basic vectors or respectively linearly independent wave vectors that are required to span the reciprocal lattice of the structure. The rank is always bigger than or as big as the dimension  $d$  of the lattice [56, 234].

For the calculation of the rank we consider the number  $n_i$  of incommensurate length scales, which is given by the number of rationally independent lengths when projecting the wave vectors of the reciprocal lattice on a straight line. In a periodic crystal, there is only one length scale per direction, i.e.  $n_i = 1$ . A quasicrystal can possess two or more incommensurate length scales per direction. The rank is given by  $D = n_i \cdot d$  with the dimension  $d$  of the system. Accordingly, in a periodic structure it is  $D = d$ , and in quasiperiodic structures  $D > d$ .

Mathematically, the rank of a two-dimensional structure can be determined with Euler's phi function  $\varphi(n)$ . For every natural number  $n$  it provides the number of positive integers which are smaller than  $n$  and relatively prime to  $n$ , i.e.

$$\varphi(n) = |\{a \in \{1, \dots, n-1\} | \gcd(a, n) = 1\}| \quad (2.13)$$

with  $\gcd(a, n)$  denoting the greatest common divisor of  $a$  and  $n$ . The rank of a two-dimensional quasicrystal with  $n$ -fold rotational symmetry reads  $D = \varphi(n)$  [8]. The first values of  $\varphi(n)$  are given in Table 2.1.

symmetry $n$	3	4	5	6	7	8	9	10	11	12	13	14	15	16	17	18
rank $D = \varphi(n)$	2	2	4	2	6	4	6	4	10	4	12	6	8	8	16	6

Table 2.1: Values of Euler's phi function  $\varphi(n)$  that provides the rank  $D$  of a two-dimensional structure dependent on its symmetry  $n$ . Table after [8].

The rank of a quasicrystal gives information about the structure. For instance, quasicrystals with a low rank build most easily (see Subsection 2.2.2). Furthermore, the rank gives the minimal dimension of the hyperspace needed for the construction of a quasicrystal (see Subsection 2.3.5.2). The rank also provides the number of hydrodynamic variables in a system (see Subsection 2.5.1).

## 2.5 Phasons

Under the influence of heat there can arise thermal excitations in quasicrystals. One kind of excitation is phonons that are also known from periodic crystals. Particles fluctuate around their steady positions with amplitudes that increase with rising temperature. The collective thermal fluctuations of many particles result in

phononic modes with certain wavelengths. In the case of long-wavelength fluctuations such phonons do not cost free energy [38].

Like phonons, phasons are another kind of thermal excitations that are characteristic of quasicrystals [9, 10]. Phasons correspond to complex rearrangements of the basic tiles that the quasicrystal is built from. Local rearrangements are called phasonic flips [10].

Phasons can arise in different ways. On the one hand, correlated phasonic flips cause phason modes that (like phonons) do not cost free energy in the limit of long wavelengths [10–14, 235]. On the other hand, phasonic flips can also occur in an uncorrelated way. In this case they correspond to excitations of finite wavelength. Phasons arise as a consequence of the quasiperiodicity and the connected additional degrees of freedom in quasicrystals [10]. Their occurrence can be explained either with the description of a quasicrystal as a projection from a regular lattice in a higher dimensional space (see Subsection 2.3.5.2), or in a general continuum description. In the former case a displacement of the acceptance domain along the perpendicular space results in a phasonic displacement (see Figure 2.14 (c) in Subsection 2.3.5.2) and hence local phasonic flips occur. In the continuum description phasons are defined as hydrodynamic modes.

Phasons are of special interest in this thesis. In the following phasonic modes are described in the continuum picture. We continue with examples of possible local phasonic flips in selected quasicrystalline tilings as employed in this thesis. Finally, recent findings in the field of phasons are summarized.

### 2.5.1 Phasonic modes

In the following we describe hydrodynamic modes – especially phasonic modes – in the continuum picture. Hydrodynamic modes are elementary excitations within fluids or – in a coarse-grained view – within continuous structures that do not cost any energy in the long-wavelength limit [10]. Hydrodynamic modes are described by hydrodynamic variables.

In order to explain the additional degrees of freedom in quasicrystals and the consequently arising phasonic modes a free energy density  $f$  of quasicrystals is developed. We briefly depict the deduction of  $f$  similar to Socolar *et al.* [10]. Socolar *et al.* performed a Taylor expansion of  $f$  in terms of the density field  $\rho(\mathbf{r})$  of the structure as order parameter:

$$f = \sum_{k=1}^{\infty} B_k \rho(\mathbf{r})^k. \quad (2.14)$$

The coefficients  $B_k$  are dependent on the properties of the considered system, for example temperature, pressure and atoms. The density field is expressed by its

Fourier transform

$$\rho(\mathbf{r}) = \sum_{j=1}^n \rho_j \exp(-i\mathbf{G}_j \cdot \mathbf{r}). \quad (2.15)$$

The coefficients of the Fourier expansion read  $\rho_j = |\rho_j| \exp(i\phi_j)$  with phases  $\phi_j$ .  $\mathbf{G}_j$  denote wave vectors which are arranged symmetrically and define the rotational symmetry of the system. Appropriate phases and wave vectors are specified in Section 4.2. In a system with  $n$ -fold rotational symmetry the sum is composed of  $n$  terms. With the required powers

$$\rho(\mathbf{r})^k = \sum_{j_1, \dots, j_k=1}^n \exp(-i \sum_{l=1}^k \mathbf{G}_{j_l} \cdot \mathbf{r}) \prod_{l=1}^k \rho_{j_l} \quad (2.16)$$

the energy density becomes

$$\begin{aligned} f &= \sum_{k=1}^{\infty} B_k \sum_{j_1, \dots, j_k=1}^n \exp(-i \sum_{l=1}^k \mathbf{G}_{j_l} \cdot \mathbf{r}) \prod_{l=1}^k \rho_{j_l} \\ &= \sum_{k=1}^{\infty} B_k \sum_{j_1, \dots, j_k=1}^n \delta(\sum_{l=1}^k \mathbf{G}_{j_l}) \prod_{l=1}^k \rho_{j_l} \\ &= \sum_{k=1}^{\infty} B_k \sum_{j_1, \dots, j_k=1}^n \delta(\sum_{l=1}^k \mathbf{G}_{j_l}) \exp(i \sum_{i=1}^n \phi_{j_i}) \prod_{l=1}^k |\rho_{j_l}|. \end{aligned} \quad (2.17)$$

The fact that only wave vectors with a vanishing sum  $\sum_{l=1}^k \mathbf{G}_{j_l} = 0$  contribute to the free energy results in the  $\delta$ -function. All in all, the free energy density is only dependent on the sum of the phases which leads to  $D$  degrees of freedom.  $D$  corresponds to the rank of the system (see Section 2.4). In a  $d$ -dimensional system one obtains  $d$  phononic variables and  $D - d$  phasonic ones.

In this thesis we consider two-dimensional quasicrystals with decagonal, octagonal and dodecagonal symmetry which are all of rank  $D = 4$ . Thus, such systems provide a two-component phononic variable  $\mathbf{u} = (u_x, u_y)$  and a two-component phasonic variable  $\mathbf{w} = (w_x, w_y)$ . We additionally investigate two-dimensional quasicrystals with tetradecagonal symmetry (see Section 4.4) which possess a rank  $D = 6$  and, accordingly, two two-component phasonic variables  $\mathbf{v} = (v_x, v_y)$  and  $\mathbf{w} = (w_x, w_y)$ .

Moreover, regarding the local isomorphism class of a tiling (see Subsection 2.3.6), locally isomorphic tilings exhibit the same free energy density. Since shifts in the phases  $\phi_j$  that preserve the value of  $\sum \phi_j$  do not change the free energy, hydrodynamic modes in the long-wavelength limit do not alter the LI class [10].

## 2.5.2 Phasonic flips

Aside from phasonic excitations with long wavelengths, phasonic excitations with short wavelengths correspond to discrete phasonic flips. In a quasicrystalline tiling a phasonic flip corresponds to a local rearrangement of basic tiles which may lead to violations of matching rules (see Subsection 2.3.5.3). Note that phasonic flips are excitations but no defects. In the following we present an overview of discrete phasonic flips in the decagonal Tuebingen tiling and the dodecagonal shield tiling as investigated in this thesis.

The perfect Tuebingen tiling (cf. Figure 2.12 (a) in Subsection 2.3.4) is composed of five basic tiles which are given by decagons (D), decagons with a kink at one side (U), nonagons (N), hexagons (H) and pentagons (P) [28, 91, 236] as illustrated in Figure 2.16 (a). In a perfect tiling, particles at certain positions have the possibility to rearrange in a way that the resulting tiling is still composed of the five basic tiles. There are five local configurations in which these phasonic flips are possible [91]. Figure 2.16 (b) illustrates the arrangements of particles before and after a phasonic flip.

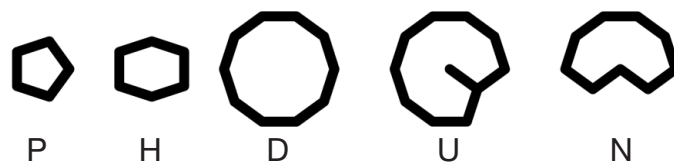
The particles indicated by pink dots flip along the direction of a symmetry axis. The flip distance  $d_{\text{flip}} = d_2 - d_1$  is obtained from geometrical considerations.  $d_1$  and  $d_2$  denote the first and the second peak of the radial distribution function (see Subsection 3.5.1). In case of flip 1 and flip 2 only the local arrangement of the tiles is changed. The potential energy of the system is conserved. In case of flip 3, 4 and 5 the tiles change, but still correspond to the five basic tiles.

The perfect shield tiling (cf. Figure 2.12 (c) in Section 2.3.4) is composed of three basic tiles, namely squares (S), triangles (T) and shield tiles (Sh) as depicted in Figure 2.17 (a). There is one local arrangement in which particles may flip [28] (see Figure 2.17 (b)). After the flip only the local configuration changes, while the tiles are maintained. The flip distance reads  $d_{\text{flip}} = 2 \sin(\pi/12) d_1$  with the nearest neighbor distance  $d_1$ .

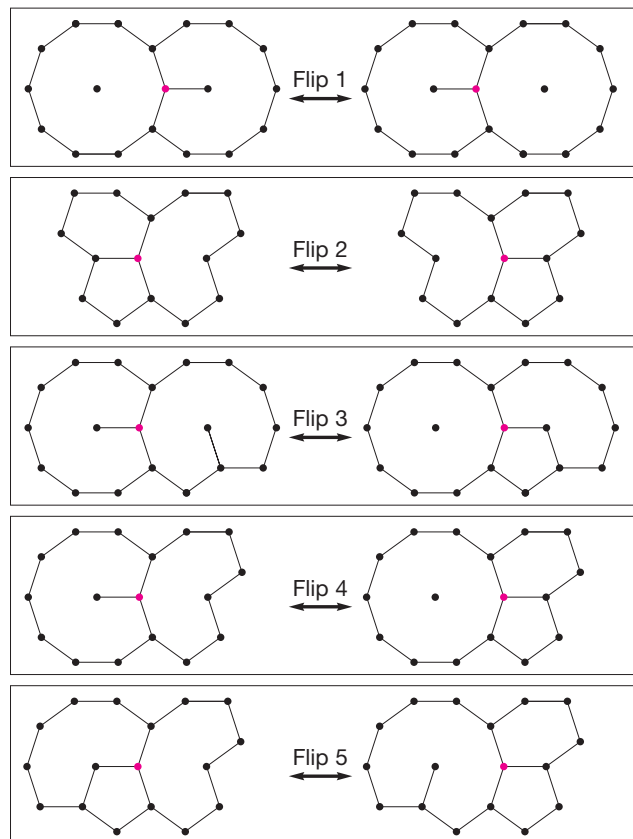
## 2.5.3 Recent findings

Briefly after the discovery of quasicrystals phasons became subject of numerous studies. It is assumed that phasons affect several material properties of quasicrystals. Since phasonic modes can be excited thermally they can possibly explain thermal properties of quasicrystals [11, 237]. For instance, phasons may be responsible for the deviation of the heat capacity from the Dulong-Petit law as examined experimentally in a quasicrystalline Al-Pd-Mn alloy [238]. Furthermore, phasonic contributions to thermal vibrations were investigated in a decagonal quasicrystal [237].

Phasons also play an essential role in the crack propagation which is important for



(a)



(b)

Figure 2.16: (a) Five basic tiles that build a decagonal Tübingen tiling (see also [28, 91, 236]). (b) Local arrangements of particles (dots) in which phasonic flips are allowed due to the geometry (see also [91]). On the left hand side, arrangements before a discrete phasonic flip of a single particle (pink dot) are shown. On the right hand side, the pink particle has flipped. The tiles are obtained by connecting nearest neighbor particles with a distance of the short length scale.

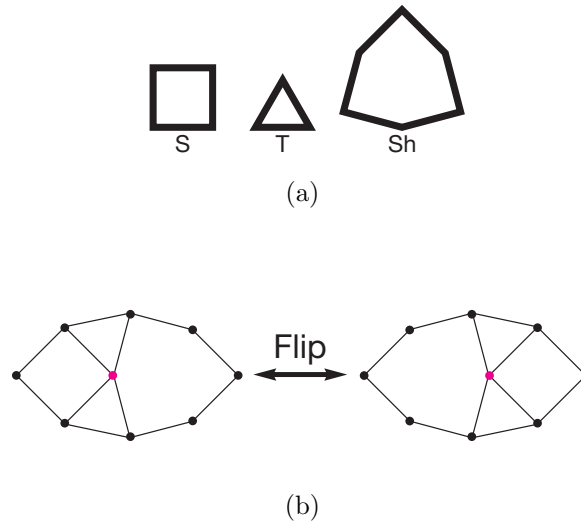


Figure 2.17: (a) Three basic tiles that build the dodecagonal shield tiling. (b) Rearrangement due to a phasonic flip (see also [28]).

understanding the temperature dependence of the brittleness and elasticity of quasicrystals [175, 239]. In recent studies [175] the crack propagation is described as a mechanism influenced by phasons: On the one hand, quasicrystals are composed of stable clusters that serve as obstacles for cracks. Clusters prevent dislocations from propagating and stop plastic deformations. On the other hand, a phason wall follows a dislocation and makes the material break up along that wall. Phason walls as hints of phasonic flips have also been observed experimentally [240]. Another field that is influenced by phasons is the dynamics in quasicrystals. The short-time dynamics is dominated by phasonic flips, over longer times the flips can lead to diffusive motion [29]. The motion of dislocations can also be explained by phasons [10]. In addition, the impact of phasons on elasticity is investigated in [241].

Furthermore, phasons are part of the growth process of quasicrystals and affect the resulting structure. Simulations of the growth from a seed [115] reveal that dependent on the distance from the triple point either stable quasicrystals without defects or metastable random tilings with incorporated flips grow. Moreover, concerning the growth from two seeds, phasonic strain fields arise when the seeds approach and relax later due to phasonic flips [116]. Further studies of the growth of quasicrystals and the impact of phasons are presented in Chapter 6.

In addition, since phasonic flips increase the entropy of a quasicrystalline structure, it is assumed that they contribute to the stability of random tilings [163, 242–244] (see also Section 2.2.4).

In experimental studies [245] phasons have even been observed under the trans-

mission electron microscope. However, many properties of phasons are still a main subject of current research and are discussed intensely (see, e.g. [161, 246]).

## 2.6 Topological defects

Like in periodic crystals, defects in terms of dislocations and disclinations can also occur in quasicrystals. Dislocations are defects in the translational order of a structure. They appear as incomplete lattice lines in an otherwise perfect lattice. The magnitude and orientation of a dislocation is characterized by the Burgers vector  $\mathbf{b}$ : In a perfect lattice, connecting the particles around an arbitrary particle results in a rhomboid with lengths that are multiples of the length of a unit cell. In contrast, when connecting the particles around a dislocation two opposite sides of the rectangle do not exhibit the same length. The additional path that is needed to close the loop is named the Burgers vector. An example of a dislocation and the Burgers vector in a triangular lattice is illustrated in Figure 2.18.

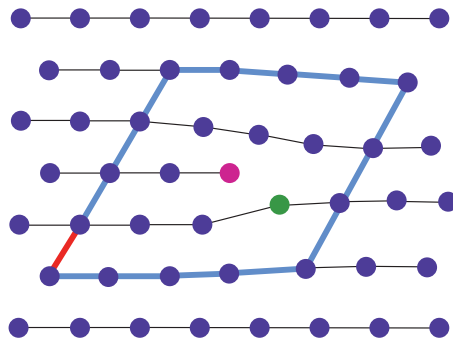


Figure 2.18: Dislocation in a triangular lattice resulting from an interrupted lattice line. The Burgers vector is colored in red. A dislocation consists of a pair of disclinations which is given by a particle (pink) that is surrounded by five nearest neighbor particles and a particle (green) with seven nearest neighbors. A further description of disclinations is given in the text below.

In quasicrystals the formation of a dislocation composed of an interrupted lattice line is more complicated than in periodic crystals. Aside from phononic components, the Burgers vector possesses additional phasonic components [10, 247], i.e. a dislocation is composed of phononic and phasonic displacements. A dislocation in a quasicrystal is shown in Figure 2.19 using the example of a structure with 8-fold rotational symmetry.

Disclinations are another kind of defect and cause a local deviation of single particles from the rotational symmetry of the structure. In periodic structures discli-

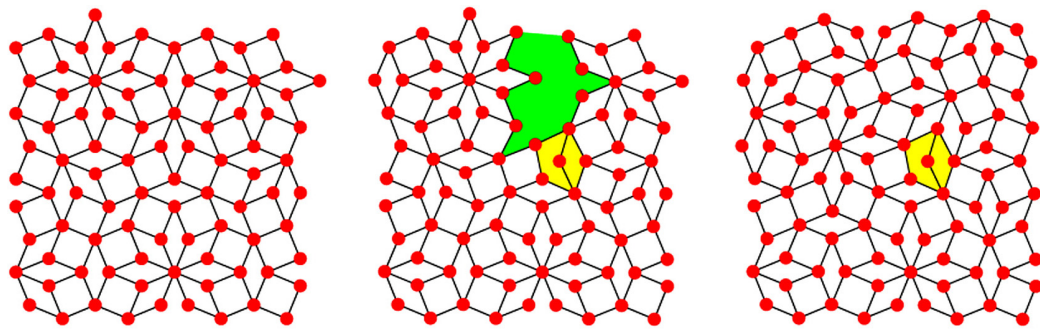


Figure 2.19: Formation of a dislocation in a quasicrystal with 8-fold rotational symmetry. Left: Perfect quasicrystalline lattice. Middle: Removal of a lattice line. The particles cannot arrange to a quasicrystalline lattice by pure phononic motion. Right: The particles fill the vacancies by performing phasonic flips. However, there is still a gap (yellow) that cannot be filled by the basic tiles and describes the dislocation. Adopted with permission from [247] (<https://doi.org/10.1103/PhysRevB.90.064108>). Copyright 2014 by the American Physical Society.

nations can be identified by means of the number of neighboring particles of the lattice particles. In a triangular lattice a particle usually has six nearest neighbor particles. Particles with another number of nearest neighbors, i.e. five or seven, build a disclination. In Figure 2.20 the two kinds of disclinations are illustrated.

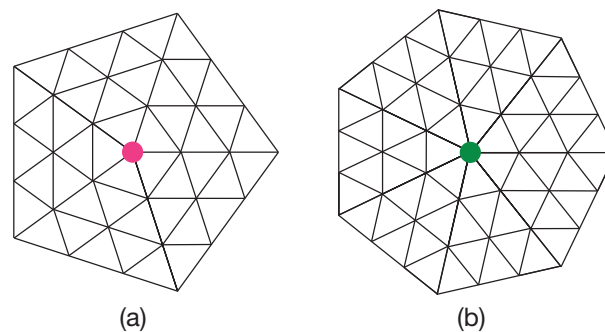


Figure 2.20: Two kinds of disclinations in a triangular lattice. (a) A particle (pink) with five nearest neighbors. (b) A particle (green) with seven nearest neighbors.

Note that a dislocation consists of a pair of disclinations with a distance of a lattice spacing [248]. In Figure 2.18 the last particle of the interrupted lattice line has only five neighbors, while a particle next to it is surrounded by seven nearest neighbors. Furthermore, single disclinations have a significantly larger energy than dislocations (see, e.g. [249]).

In this thesis dislocations and disclinations are relevant concerning the predicted

melting process of quasicrystals (see Chapter 7). In numerical investigations of the melting process of quasicrystals we analyze the assembled structures with regard to dislocations (see Subsection 7.2.5). Furthermore, in Section 6.2.6 we test our grown quasicrystals for dislocations. Since dislocations in quasicrystals are usually hard to observe we introduce a method for their detection in Subsection 3.5.5.

## 2.7 Colloidal physics

In this work we study colloidal systems in numerical simulations. Colloids are particles or droplets as defined, e.g. in [24]. The word colloid is derived from the Greek words “kólla” (glue) and “eidos” (shape), which reflects their muddy consistence. The size of a colloid with a typical length scale of  $10\text{ nm} - 10\text{ }\mu\text{m}$  is about 100-100000 times larger than the size of atoms. Accordingly, in optical experiments colloids can be investigated in real space, for instance by dynamic light scattering or even directly by confocal microscopy. Colloids are usually large enough to be described with classical dynamics, but small enough to undergo Brownian motion (see Section 3.1).

Colloidal systems consist of a dispersed phase in a dispersion medium. Both, dispersed phase and dispersion medium can be solid, liquid or gaseous [24]. For example, the dispersed phase can be composed of particles, droplets or gas bubbles, which are uniformly distributed in the dispersion medium and do not sediment to the ground. Due to their size the components of the dispersed phase can be distinguished from the dispersion medium. Examples of colloidal systems are fog or smoke, in which droplets or particles are distributed in a gas. Foam plastics consists of gas dispersed in a solid, and milk or blood are colloidal systems, in which droplets are distributed in a liquid. Coffee or ink are common examples of colloidal suspensions which are composed of colloidal particles dispersed in a liquid. In this thesis, we usually consider colloidal suspensions.

Interactions between colloids can be described by attractive Van-der-Waals forces that are induced by fluctuating dipoles and increase with decreasing distances between the colloids. In order to prevent aggregation, colloids are kept away from each other when they approach closer than a critical distance. One possibility is to provide each particle with the same charge. This charge stabilization leads to electrostatic Coulomb repulsion. Counter ions in the solvent screen the interaction. The total interaction is described by the DLVO pair potential, named after Derjaguin, Landau, Verwey and Overbeek, and reads [250, 251]

$$V_{DLVO}(r) = \frac{(Ze)^2}{4\pi\epsilon_0\epsilon_r} \left( \frac{e^{\kappa R}}{1 + \kappa R} \right) \frac{e^{-\kappa r}}{r}. \quad (2.18)$$

$r$  denotes the distance between the centers of mass of two colloids,  $Z$  the effective charge on the surface,  $e$  the elementary charge,  $\epsilon_0$  the electric constant and  $\epsilon_r$  the dielectric constant of water.  $R$  is the radius of the colloids and  $\kappa = \sqrt{n_e e^2 / (\epsilon_0 k_B T)}$  describes the inverse Debye screening length with the electron density  $n_e$ , the Boltzmann constant  $k_B$  and the temperature  $T$ .

The characteristic time scale for the movement of particles is  $\tau = \frac{R^2}{6D}$  with the Stokes-Einstein diffusion coefficient  $D = \frac{k_B T}{6\pi\eta R}$ .  $\eta$  describes the viscosity of the medium. Due to the dependence on the radius  $R$ , the characteristic diffusion time for colloids is in the order of seconds, while for atoms it would be in the range of picoseconds. The slow dynamics of colloidal systems allows the investigation in real time and the analysis of dynamical processes like crystallization [252].

Despite their simple pair potential colloids show many remarkable similarities to atomic systems and can be considered as mesoscopic model systems in statistical physics. For instance, colloidal systems are suited to test predictions of statistical thermodynamics and to simulate atomic processes (see, e.g. [253, 254]). In experiments, different possibilities for the design of colloids are given. Commonly applied colloids are often synthesized from PMMA (Polymethylmethacrylate), a transparent plastic. In simulations, interactions between colloids can easily be tuned. There is a whole zoo of interaction potentials that can be modeled in addition to the aforementioned DLVO pair potential present in charge stabilized colloidal suspensions. Accordingly, colloids are used for predictions in many fields. In this work our main interest concerns two-dimensional colloidal systems which represent colloids at an interface, colloids trapped between two plates, or two-dimensional solid monolayer films.

One approach that is applied in this work (see Chapter 5) is patchy colloids [255, 256], i.e. colloids with attractive regions at the surface that represent bonds in metallic alloys. The interactions are usually described by a Lennard-Jones potential multiplied with an additional angular term (see, e.g. [30, 118–121, 257–261]). In previous studies the self-assemblies of patchy colloids to Archimedean tilings [126, 129, 262, 263], rhombic phases [264] or even quasicrystals [119–121] were observed. Another interaction between colloids that is applied in this work is of Lennard-Jones–Gauss type [28, 29]. Two minima with tunable length scales can support periodic structures as well as dodecagonal or decagonal colloidal quasicrystals. In case of quasicrystals phasonic flips can be studied. Furthermore, the growth process [121, 265] and phase transitions in quasicrystalline systems can be studied with colloidal model systems (see also Chapters 6 and 7).

Charged stabilized colloidal suspensions can also be influenced by external fields. For example, the arrangement and dynamics of colloids can be manipulated specifically with interfering laser beams. Aside from colloids trapped in periodic interference patterns [266–268] also quasiperiodic arrangements of colloids are achieved

by external light fields in both, experiments [7, 126, 129–131] as well as simulations [8, 11–13, 27, 125, 126] (see also Chapter 4).

There are numerous further examples of colloidal systems that are not directly connected to this work, for instance binary mixtures of colloids (see, e.g. [269–271]). Furthermore, the aggregation of colloids is investigated concerning the influence of the shape of the particles [272], the sedimentation [273], or a flow field [274, 275]. Further studies contain the crystallization transition [276–280] or even the dynamics in glasses [281, 282]. Over the last years, also the field of active colloids has won great attention (see [283] for a review) and the realization of autonomous applications is discussed [284].



# Chapter 3

## Numerical techniques

In order to study many-particle systems theoretically, for instance the assembly or the dynamics of particles, one can develop models that describe the systems. In these models the interactions between particles are usually given by internal interaction potentials. External influences can be added by an external potential. In many approaches equations of motions have to be solved for each single particle. Since in most cases it is not possible to solve the equations analytically, an alternative method is computer simulations in which the equations of motion are solved numerically. The most frequently used simulation methods concerning the dynamics are molecular dynamics simulations based on Newton's equations and Brownian dynamics simulations as a special case of molecular dynamics simulations which are based on the Langevin equation. The results of these simulations are trajectories of the particles within the simulation time. A different approach which is rather based on stochastic processes and intended to predict statistical properties is Monte Carlo simulations. In Monte Carlo simulations a notion of physical time is missing.

In this work we make use of Brownian dynamics and Monte Carlo simulations, as well as the special case of event-chain Monte Carlo simulations. In this Chapter we describe the basic ideas and the implementations of the employed algorithms (Sections 3.1, 3.2 and 3.3). In Section 3.4 the settings applied in our simulations are presented. Furthermore, in Section 3.5 we give an overview of mathematical tools for analyzing the structures that the particles in our systems adopt.

### 3.1 Brownian dynamics simulations

Brownian dynamics simulations model particles, for example colloids (see Section 2.7), that are dispersed in liquids or gases and perform irregular movements called Brownian motion.

Brownian motion has already been reported in 1784 by Jan Ingen-Housz [285] who observed fluctuations of small particles that were immersed in a fluid. However, he did not find the correct explanation for the dynamics. In 1827 Robert Brown observed the movement of particles in fluids, too [286]. It took about 80 years until in 1905 and 1906 Albert Einstein [287] and Marian Smoluchowski [288] theoretically explained the motion to be caused by the surrounding solvent molecules of the liquid: At finite temperature, the solvent molecules perform thermal fluctuations and frequently hit the immersed particles from all directions. During 1908 and 1913 Jean Baptiste Perrin proved the predictions of Einstein experimentally and could even determine Avogadro's number from detailed analyses [289].

In this Section we introduce Brownian dynamics simulations. The algorithm is derived and details about the simulation and implementation are given. We also present an extension to additional rotation moves.

### 3.1.1 Langevin equation

In the following we derive the algorithm of Brownian dynamics simulations. The motion of a particle is calculated with Newton's equation [290]

$$\mathbf{F} = m \frac{\partial \mathbf{v}}{\partial t}. \quad (3.1)$$

$\mathbf{F}$  describes the total force acting on the particle,  $m$  is the mass and  $\mathbf{v}$  the velocity of the particle. In order to describe the motion of a particle in a liquid, the total force  $\mathbf{F}$  is expressed by

$$\mathbf{F} = \mathbf{F}_{\text{fric}} + \mathbf{F}_{\text{ext}} + \mathbf{F}_{\text{int}} + \mathbf{F}_T. \quad (3.2)$$

$\mathbf{F}_{\text{fric}} = -\gamma \mathbf{v}$  is the friction force with the friction coefficient  $\gamma$  of the particle in the solvent. For spherical particles of radius  $R$  the friction coefficient is determined by Stokes' law  $\gamma = 6\pi\eta R$  with the dynamic viscosity  $\eta$ . A combination of equations (3.1) and (3.2) provides the Langevin equation [291, 292]

$$m \frac{\partial \mathbf{v}}{\partial t} = -\gamma \mathbf{v} + \mathbf{F}_{\text{ext}} + \mathbf{F}_{\text{int}} + \mathbf{F}_T. \quad (3.3)$$

The external force  $\mathbf{F}_{\text{ext}}$  arises from external influences like gravitation, or electric or magnetic fields. Walls or obstacles can cause an external force, too.  $\mathbf{F}_{\text{int}}$  describes internal forces which are usually derived from an interaction potential between the particles. The interaction potentials applied in this thesis are specified in Subsection 3.4.1.  $\mathbf{F}_T$  is the random force on the particles due to collisions with the molecules of the solvent. Since  $\mathbf{F}_T$  is stochastic in nature it is also referred to

as stochastic force. A further denomination is white noise.  $\mathbf{F}_T$  complies with

$$\langle \mathbf{F}_T \rangle = 0 \quad \text{and} \quad (3.4)$$

$$\langle F_{T,j}(t) F_{T,k}(t') \rangle = 2B\delta_{jk}\delta(t-t'). \quad (3.5)$$

Equation (3.4) states that the ensemble average of the random force is zero. It ensures that there is no preferred direction of the force. Equation (3.5) defines the variance of the random force and indicates that it is uncorrelated for different times. Furthermore, each component of the force is independent of the other components.  $B$  is a constant representing the amplitude of the force.

In order to calculate  $B$  the velocity and its mean square is considered. Assuming a constant friction coefficient  $\gamma$  and absence of internal and external forces, equation (3.3) is an inhomogeneous linear differential equation of first order. Via variation of constants one receives the solution

$$\mathbf{v}(t) = \mathbf{v}_0 e^{-\frac{\gamma}{m}t} + e^{-\frac{\gamma}{m}t} \int_0^t dt' e^{\frac{\gamma}{m}t'} \frac{\mathbf{F}_T(t')}{m}, \quad (3.6)$$

where  $\mathbf{v}_0$  denotes the initial velocity. Under consideration of equation (3.4), the mean velocity becomes

$$\langle \mathbf{v}(t) \rangle = \mathbf{v}_0 e^{-\frac{\gamma}{m}t} \quad (3.7)$$

with the characteristic time scale  $m/\gamma$ .

The square velocity reads

$$\begin{aligned} \mathbf{v}^2(t) &= \mathbf{v}_0^2 e^{-\frac{2\gamma}{m}t} + 2\mathbf{v}_0 e^{-\frac{2\gamma}{m}t} \int_0^t dt' e^{\frac{\gamma}{m}t'} \frac{\mathbf{F}_T(t')}{m} \\ &+ e^{-\frac{2\gamma}{m}t} \int_0^t \int_0^t dt' dt'' e^{\frac{\gamma}{m}(t'+t'')} \frac{\mathbf{F}_T(t') \cdot \mathbf{F}_T(t'')}{m^2}. \end{aligned} \quad (3.8)$$

Using equations (3.4) and (3.5), the mean square velocity in  $d$  dimensions results in

$$\begin{aligned} \langle \mathbf{v}^2(t) \rangle &= \mathbf{v}_0^2 e^{-\frac{2\gamma}{m}t} + e^{-\frac{2\gamma}{m}t} \int_0^t dt' e^{\frac{\gamma}{m}2t'} \frac{2dB}{m^2} \\ &= \mathbf{v}_0^2 e^{-\frac{2\gamma}{m}t} + \frac{dB}{\gamma m} (1 - e^{-\frac{2\gamma}{m}t}) \end{aligned} \quad (3.9)$$

which becomes

$$\langle \mathbf{v}^2(t) \rangle = \frac{dB}{\gamma m} \quad (3.10)$$

for large times  $t \gg m/\gamma$ . With the equipartition theorem  $\langle \mathbf{v}^2(t) \rangle = dk_B T/m$  a connection between the amplitude of the thermal fluctuations  $B$ , the Boltzmann constant  $k_B$ , the temperature  $T$  and  $\gamma$  is obtained, i.e.

$$B = \gamma k_B T. \quad (3.11)$$

The relation is a special form of a fluctuation-dissipation relation since stochastic force and friction are connected.

We now calculate the mean square displacement which we later need to determine the values that  $\mathbf{F}_T$  can take in the simulations. The distance vector a particle covers after time  $t$  is the difference between the position  $\mathbf{r}(t)$  of the particle at time  $t$  and the initial position  $\mathbf{r}(0)$ . It is calculated by integrating the velocity:

$$\begin{aligned} \mathbf{r}(t) - \mathbf{r}(0) &= \int_0^t dt' \mathbf{v}(t') \\ &= \int_0^t dt' \mathbf{v}_0 e^{-\frac{\gamma}{m}t'} + \int_0^t dt' e^{-\frac{\gamma}{m}t'} \int_0^{t'} dt'' e^{\frac{\gamma}{m}t''} \frac{\mathbf{F}_T(t'')}{m} \end{aligned} \quad (3.12)$$

With the help of equation (3.10) one finds

$$\langle (\mathbf{r}(t) - \mathbf{r}(0))^2 \rangle = 2 \frac{Bd}{\gamma^2} \left( t - \frac{m}{\gamma} + \frac{m}{\gamma} e^{-\frac{\gamma}{m}t} \right). \quad (3.13)$$

For short times  $t \ll m/\gamma$  a Taylor expansion of the exponential function on the right hand side of equation (3.13) results in

$$\langle (\mathbf{r}(t) - \mathbf{r}(0))^2 \rangle \propto t^2 \quad (3.14)$$

which indicates ballistic motion.

For large times  $t > m/\gamma$  the mean square displacement becomes

$$\langle (\mathbf{r}(t) - \mathbf{r}(0))^2 \rangle = 2 \frac{Bd}{\gamma^2} t = 2d \frac{k_B T}{\gamma} t. \quad (3.15)$$

As normal diffusion with a diffusion constant  $D$  fulfills  $\langle (\mathbf{r}(t) - \mathbf{r}(0))^2 \rangle = 2dDt$ , one gets the Einstein-Stokes relation [293]

$$D = \frac{k_B T}{\gamma}. \quad (3.16)$$

For typical Brownian particles the time  $m/\gamma$  is only about  $10^{-9}s$  such that the term  $m \frac{\partial \mathbf{v}}{\partial t}$  in the Langevin equation (3.3) is much smaller than the other terms.

Thus, we can neglect inertia and the ballistic motion in the beginning and the Langevin equation becomes

$$\gamma \mathbf{v} = \mathbf{F}_{\text{ext}} + \mathbf{F}_{\text{int}} + \mathbf{F}_T. \quad (3.17)$$

In this limit with  $m \rightarrow 0$ , the equation is called overdamped Langevin equation. The overdamped Langevin equation is easier to integrate and sufficient to describe systems of Brownian particles with small  $m/\gamma$ . Using this simplification in simulations speeds up the calculation and enables the investigation of larger systems over longer times.

### 3.1.2 Simulation details

Brownian dynamics simulations are usually performed in the canonical ensemble – also called  $NVT$ -ensemble – in which the number of particles  $N$ , the volume  $V$  and the temperature  $T$  are constant.

Within the simulation the overdamped Langevin equation as presented in equation (3.17) is integrated numerically for each particle in successive time steps  $\Delta t$ . In a discretized form the equation reads

$$\mathbf{r}(t + \Delta t) = \mathbf{r}(t) + \frac{\Delta t}{\gamma} (\mathbf{F}_{\text{ext}}(t) + \mathbf{F}_{\text{int}}(t) + \mathbf{F}_T(t)). \quad (3.18)$$

With this Euler algorithm the displacements and accordingly the trajectories of particles can be modeled when the forces are known.

In our calculation we assume a constant friction coefficient  $\gamma$ . Note that in case of friction coefficients that depend on the position the Langevin equation is not well-defined. In this case there are different methods for numerical integration, for instance the Ito- or Stratonovich integration (see, e.g. [294]).

The internal force  $\mathbf{F}_{\text{int},ij}$  on particle  $i$  due to particle  $j$  is calculated from the negative derivative of the pair potential  $V(r)$  at the particle distance  $r = |\mathbf{r}_j - \mathbf{r}_i|$ .  $\mathbf{r}_i$  and  $\mathbf{r}_j$  denote the positions of the particles. The total internal force  $\mathbf{F}_{\text{int},i}$  on a particle  $i$  is given by the sum of the forces  $\mathbf{F}_{\text{int},ij}$  resulting from the interactions with all other particles  $j$ :

$$\mathbf{F}_{\text{int},i} = \sum_j \mathbf{F}_{\text{int},ij} = - \sum_j \nabla V(r)|_{r=|\mathbf{r}_j - \mathbf{r}_i|}. \quad (3.19)$$

For short-range pair potentials as applied in this thesis the forces become negligible if the distances between the particles are large. Thus, it is sufficient to calculate the forces between two particles with a distance smaller than a given cutoff radius  $r_{\text{cut}}$ . To ensure continuity the value of the force at the cutoff radius is subtracted:

$$\mathbf{F}_{\text{int},ij}(r) = \begin{cases} \mathbf{F}_{\text{int},ij}(r) - \mathbf{F}_{\text{int},ij}(r_{\text{cut}}) & r \leq r_{\text{cut}} \\ 0 & r > r_{\text{cut}}. \end{cases} \quad (3.20)$$

In the following we calculate the values that the amplitude of the random thermal force  $\mathbf{F}_T$  can adopt in a way that the conditions of equations (3.4) and (3.5) are fulfilled. Assuming  $\mathbf{F}_{\text{ext}} = \mathbf{F}_{\text{int}} = 0$  we rewrite the discretized Langevin equation (3.18) to get the particles' displacements at any time  $t$ :

$$\mathbf{r}(t) - \mathbf{r}(0) = \frac{\Delta t}{\gamma} \sum_{j=0}^{t/\Delta t} \mathbf{F}_T(j\Delta t). \quad (3.21)$$

$j\Delta t$  gives the discrete time steps. Since the mean particle displacement equals zero, equation (3.4) is already fulfilled. Furthermore, the mean square displacement reads

$$\begin{aligned} \langle (\mathbf{r}(t) - \mathbf{r}(0))^2 \rangle &= \frac{(\Delta t)^2}{\gamma^2} \left\langle \left( \sum_{j=0}^{t/\Delta t} \mathbf{F}_T(j\Delta t) \right)^2 \right\rangle \\ &= \frac{(\Delta t)^2}{\gamma^2} \frac{t}{\Delta t} \langle \mathbf{F}_T^2 \rangle. \end{aligned} \quad (3.22)$$

When calculating the mean of the squared sum, terms of the form  $\langle \mathbf{F}_T(j\Delta t) \cdot \mathbf{F}_T(k\Delta t) \rangle$ ,  $j \neq k$  are omitted according to equation (3.5) such that only  $t/\Delta t$  terms of the form  $\langle (\mathbf{F}_T(j\Delta t))^2 \rangle$  are left. As the random force is not time-dependent, it is  $\langle (\mathbf{F}_T(j\Delta t))^2 \rangle = \langle \mathbf{F}_T^2 \rangle$ . Finally, combining equations (3.15) and (3.22), one obtains

$$\langle \mathbf{F}_T^2 \rangle = \frac{2d\gamma k_B T}{\Delta t} \quad (3.23)$$

for the mean square of the random force.

Accordingly, to realize the thermal force we need random numbers with an average value of zero and a mean square value of  $2d\gamma k_B T/\Delta t$ . One possibility is Gaussian distributed numbers with a mean of zero and a second moment of  $2d\gamma k_B T/\Delta t$ . An alternative is numbers that are distributed equally. In that case, the random forces in random directions possess amplitudes which are evenly distributed between 0 and  $\sqrt{12\gamma k_B T/\Delta t}$ . The upper limit is calculated such that the condition for the second moment given in equation (3.23) is fulfilled.

In our simulations we employ equally distributed random numbers and use the Mersenne Twister 19937 generator [295] that produces pseudo random numbers. For a discussion on the quality of random number generators we refer to [296, 297]. To test the properness of our random force, we calculate the trajectories that arise when we integrate the discretized Langevin equation (3.18) without external and internal forces in numerical simulations. The mean particle displacement after each step is zero and the mean square displacement conforms to equation (3.15) with the correct free diffusion constant. Thus, the choice of our random numbers is acceptable and the random force is calculated correctly.

### 3.1.3 Extension to rotation moves

Aside from isotropic pair potentials we also model pair potentials  $V_p(r, \theta_k, \theta_l)$  with preferred binding angles (see Subsection 3.4.1). In this case, the particles perform the described displacement moves and additional rotation moves. Similar to the overdamped Langevin equation, the equation for the orientation  $\theta$  of a particle reads

$$\gamma_\theta \frac{d}{dt} \theta = \mathbf{M}_{\text{int}} + \mathbf{M}_T \quad (3.24)$$

with the rotational diffusion  $\gamma_\theta = \frac{4}{3} r_0^2 \gamma$ . The implementation is analog to the implementation of displacement moves. Here, the internal torque of particle  $i$  is given by

$$\mathbf{M}_{\text{int},i} = - \sum_j \frac{\partial}{\partial \theta} V_p(r, \theta_k, \theta_l) |_{r=|\mathbf{r}_j - \mathbf{r}_i|}. \quad (3.25)$$

The thermal torque  $\mathbf{M}_T$  has to comply with

$$\langle \mathbf{M}_T \rangle = 0 \quad \text{and} \quad (3.26)$$

$$\langle M_{T,j}(t) \cdot M_{T,k}(t') \rangle = 2\gamma_\theta k_B T \delta_{jk} \delta(t - t'). \quad (3.27)$$

In the simulations with anisotropic potentials presented in this thesis displacement and rotation moves of all particles are applied in the same amount.

## 3.2 Monte Carlo simulations

Another simulation method applied in this work is Monte Carlo simulations [298–300]. The method was developed by Edward Teller, John von Neumann, Stanislaw Ulam, Robert Richtmyer, Nicholas Metropolis and many coworkers in Los Alamos at the time around the second world war [301, 302]. The simulations were initially tested on one of the first electronic digital computers, called MANIAC (Mathematical Analyzer Numerical Integrator And Computer), that was built under the direction of Metropolis. Nowadays, Monte Carlo simulations provide a good and useful tool for numerous numerical calculations, for example for the simulation of many-particle systems. The name Monte Carlo dates to the casino Monte Carlo in Monaco (see, e.g. [302]) since the simulations are based on random numbers generated by the computer.

We apply Markov-chain Monte Carlo simulations in which Markov chains describe stochastic processes. Within a series of steps, states in a large configuration space are proposed with a certain probability. A new state only depends on the previous state and is independent of earlier states. Also the transition probability is

history-independent. Thus, a random walk through configuration space is modeled in which in principle all states may be reached after sufficient time and ergodicity is ensured. Since Monte Carlo simulations do not model a real temporal evolution of the system, the method is suitable to measure the statistics of a system rather than the dynamics.

In the following we describe the theoretical background and implementation of Monte Carlo simulations in the canonical ensemble and present an extension to the isothermal-isobaric ensemble that are both applied in this work.

### 3.2.1 Theoretical concept

In general, Monte Carlo steps are based on the probabilities of states in phase space. The phase space is composed of points  $\boldsymbol{\pi} = (\mathbf{r}_1, \dots, \mathbf{r}_N, \mathbf{p}_1, \dots, \mathbf{p}_N)$  with the positions  $\mathbf{r}_i$  and momenta  $\mathbf{p}_i$  of the particles  $i = 1, \dots, N$ . Each state of a system is described by a certain point  $\boldsymbol{\pi}$  in phase space. In the canonical ensemble – which is conventionally applied in Monte Carlo simulations and mainly employed in this thesis – the probability of finding a certain state  $\boldsymbol{\pi}$  with a total energy  $E$  provided by the Hamilton operator  $H(\boldsymbol{\pi})$  is  $P(\boldsymbol{\pi}) = e^{-\beta H(\boldsymbol{\pi})}/Z$ . Here,  $e^{-\beta H(\boldsymbol{\pi})}$  describes the Boltzmann factor with the inverse thermal energy  $\beta = 1/k_B T$ , where  $k_B$  denotes the Boltzmann constant.  $Z$  is the partition sum. Since we only need relative probabilities, it is not necessary to calculate  $Z$  explicitly. It is sufficient to notice that a state  $A$  with energy  $E_A$  appears with the probability  $P(A) \propto e^{-\beta E_A}$  and a state  $B$  with energy  $E_B$  occurs with the probability  $P(B) \propto e^{-\beta E_B}$ .

#### Detailed balance and acceptance criterion

In order to find the configurations with the highest probabilities transition probabilities are introduced. The probability to advance from a given configuration  $A$  to a configuration  $B$  is provided by the transition probability  $\pi(A \rightarrow B)$ . The probability for the reverse transition is  $\pi(B \rightarrow A)$ . The transitions are chosen such that they obey detailed balance, i.e. the transition rate from configuration  $A$  to configuration  $B$  needs to equal the transition rate from configuration  $B$  to configuration  $A$ . The transition rate, also referred to as probability flow, reads  $\phi(A \rightarrow B) = P(A) \pi(A \rightarrow B)$ . Accordingly, the detailed balance condition reads

$$P(A) \pi(A \rightarrow B) = P(B) \pi(B \rightarrow A). \quad (3.28)$$

In an ergodic system in which all configurations in configuration space can be reached, the condition of detailed balance ensures a correct probability distribution, i.e. the probability of finding a configuration  $A$  is indeed proportional to  $e^{-\beta E_A}$  in the canonical ensemble.

A proposed configuration  $B$  can either be accepted or rejected. The acceptance probability is termed  $p_{\text{acc}}(A \rightarrow B)$ . Equivalently, the rejection probability is  $p_{\text{rej}}(A \rightarrow B) = 1 - p_{\text{acc}}(A \rightarrow B)$ . For the calculation of  $p_{\text{acc}}(A \rightarrow B)$  we express the transition probability in the following form:

$$\pi(A \rightarrow B) = w(A \rightarrow B) p_{\text{acc}}(A \rightarrow B). \quad (3.29)$$

$w(A \rightarrow B)$  describes the proposal density of a new state. It gives the probability that a configuration  $B$  is chosen as the next trial configuration tested for acceptance. With this notation the condition for detailed balance in equation (3.28) becomes

$$P(A) w(A \rightarrow B) p_{\text{acc}}(A \rightarrow B) = P(B) w(B \rightarrow A) p_{\text{acc}}(B \rightarrow A). \quad (3.30)$$

There are different possibilities for choosing the proposal density  $w(A \rightarrow B)$ . In this thesis we employ the Metropolis algorithm which belongs to the most common Monte Carlo algorithms and was developed by Metropolis *et al.* [303]. In the Metropolis algorithm the proposal density is chosen symmetrically, i.e.  $w(A \rightarrow B) = w(B \rightarrow A)$ . From equation (3.30) one receives a condition for the acceptance probabilities that reads

$$\frac{p_{\text{acc}}(A \rightarrow B)}{p_{\text{acc}}(B \rightarrow A)} = \frac{P(B)}{P(A)}. \quad (3.31)$$

Equation (3.31) is fulfilled for many choices of  $p_{\text{acc}}(A \rightarrow B)$ . Today's simulations commonly apply the acceptance criterion that Metropolis decided for which reads

$$p_{\text{acc}}(A \rightarrow B) = \begin{cases} \frac{P(B)}{P(A)} & \text{if } P(B) < P(A) \\ 1 & \text{if } P(B) \geq P(A). \end{cases} \quad (3.32)$$

By calculating the acceptance probability of the reverse transition  $p_{\text{acc}}(B \rightarrow A)$  and inserting both probabilities in equation (3.31) it can easily be shown that such a choice indeed fulfills the condition. In the considered canonical ensemble the acceptance criterion becomes

$$p_{\text{acc}}(A \rightarrow B) = \begin{cases} e^{-\beta(E_B - E_A)} & \text{if } E_B > E_A \\ 1 & \text{if } E_B \leq E_A \end{cases} \quad (3.33)$$

which corresponds to the original Metropolis algorithm as also implemented in this thesis.

Though the Metropolis acceptance criterion is used most frequently in simulations,

it is not the only possible choice. Another acceptance criterion fulfilling detailed balance is

$$p_{\text{acc}}(A \rightarrow B) = \frac{P(B)}{P(B) + P(A)}. \quad (3.34)$$

Moreover, asymmetric proposal densities as applied, for example in the Metropolis-Hasting algorithm lead to a generalized Metropolis acceptance criterion of the form

$$p_{\text{acc}}(A \rightarrow B) = \begin{cases} \frac{P(B)}{w(A \rightarrow B)} \frac{w(B \rightarrow A)}{P(A)} & \text{if } P(B) < P(A) \\ 1 & \text{if } P(B) \geq P(A). \end{cases} \quad (3.35)$$

### Average of an observable

Monte Carlo simulations can be applied to calculate the average of an observable. The average value of an observable  $A(\mathbf{r}_1, \dots, \mathbf{r}_N, \mathbf{p}_1, \dots, \mathbf{p}_N)$  is defined as

$$\langle A \rangle = \frac{\int d\mathbf{p}^N d\mathbf{r}^N A(\mathbf{r}_1, \dots, \mathbf{r}_N, \mathbf{p}_1, \dots, \mathbf{p}_N) e^{-\beta H(\mathbf{r}_1, \dots, \mathbf{r}_N, \mathbf{p}_1, \dots, \mathbf{p}_N)}}{\int d\mathbf{p}^N d\mathbf{r}^N e^{-\beta H(\mathbf{r}_1, \dots, \mathbf{r}_N, \mathbf{p}_1, \dots, \mathbf{p}_N)}}. \quad (3.36)$$

Since it is hard to evaluate the integrals, one can consult Monte Carlo simulations and sample the phase space for a large number of configurations  $N_{\text{config}}$ .  $A_j(\mathbf{r}_1, \dots, \mathbf{r}_N, \mathbf{p}_1, \dots, \mathbf{p}_N)$  of each configuration  $j$  is determined. In case of configurations that are independent from each other, i.e. that are separated by at least the correlation time, we receive the mean value by the simplified equation

$$\langle A \rangle = \frac{\sum_j^{N_{\text{config}}} A_j(\mathbf{r}_1, \dots, \mathbf{r}_N, \mathbf{p}_1, \dots, \mathbf{p}_N)}{N_{\text{config}}} \quad (3.37)$$

The result corresponds to the expectation value in the canonical ensemble.

### 3.2.2 Realization of the Metropolis algorithm in our simulations

In our simulations we implement different trial moves in which new configurations are proposed in order to sample configurations according to thermal equilibrium. In a system of  $N$  particles, a sequence of  $N$  trial moves is called one Monte Carlo step. Thus, in one Monte Carlo step each particle is proposed to be displaced once on average. In the following we suppose a present configuration  $A$  and describe how to obtain suitable configurations  $B$  to be proposed for the next move.

For the generation of a new configuration  $B$  it is enough to alter the present

configuration  $A$  only slightly since close configurations are favored. However, the deviation should be large enough such that convergence towards the correct probability distribution is reached after a relatively small number of steps. In our simulations we propose the displacement of one randomly chosen particle in each trial move. As in the Brownian dynamic simulations the random numbers are obtained with the Mersenne Twister 19937 generator [295]. The displacement is either local, global or mimics a phasonic flip. Figure 3.1 depicts the employed trial moves which we describe in the following in detail.

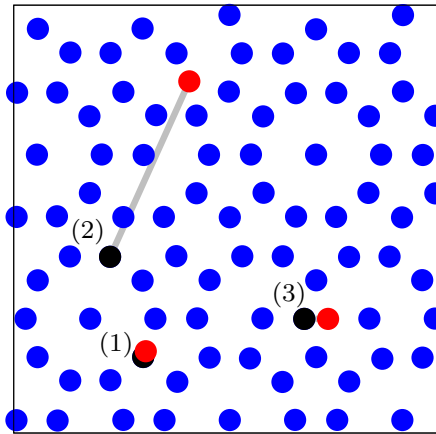


Figure 3.1: Illustration of three different trial moves applied in a system with decagonal order. The black particles are proposed to be displaced in one trial move each. The proposed new positions are colored in red. (1) depicts a local trial move, (2) a global trial move and (3) a phasonic flipping trial move. The gray lines connect the current positions of the particles and the proposed positions and serve as guides to the eyes.

- (1) In a **local trial move** a particle is proposed to be displaced to a random position inside a circle around its original position. In conventional Monte Carlo methods the size of the circle is often chosen in a way that the average acceptance rate  $\langle p_{\text{acc}} \rangle$  of a new configuration is about 50%. The average acceptance rate is the ratio of accepted moves  $N_{\text{acc}}$  out of  $N_{\text{try}}$  trial moves and the number of trial moves, i.e.  $\langle p_{\text{acc}} \rangle = N_{\text{acc}}/N_{\text{try}}$ . If  $\langle p_{\text{acc}} \rangle < 50\%$  we decrease the possible displacement radius since for small displacements the energy difference  $\Delta E = E_B - E_A$  between the configurations is small and causes a higher acceptance probability. If  $\langle p_{\text{acc}} \rangle > 50\%$  we increase the size of the circle. With the chosen acceptance rate of about 50% we are able to sample a large number of configurations with low energies in a short simulation time.

- (2) When only displacing particles locally we may get stuck in a local energy minimum in the energy landscape. In order to explore the landscape beyond a local minimum we also implement **global trial moves** in which a particle is set to a random position within the whole simulation box. These moves are usually proposed with a low probability, e.g. 10%, since their acceptance probability is low.
- (3) The third kind of trial move is **phasonic flipping**, i.e. we displace a particle about the distance  $d_{\text{flip}}$  of a phasonic flip. The direction of the displacement is chosen arbitrarily. Like for global moves the probability of accepting a phasonic flip is rather small since the direction of the displacement is random and not all particles are actually able to flip (see also Subsection 2.5.2).

Note that in case of patchy particles with preferred binding angles (see Section 5.1) we propose additional rotation moves in which the particles are proposed to be rotated about certain angles. The maximal proposed rotation angle is chosen in a way that the acceptance rate is also about 50%.

In order to determine whether configuration  $B$  proposed in a trial move is accepted or rejected we apply the Metropolis acceptance criterion presented in equation (3.33). Dependent on the energies of the configurations there are two possibilities:

- $E_B \leq E_A$ : If the energy of the new configuration  $B$  is lower than or equal to the energy of the previous configuration  $A$ , the new configuration is always accepted.
- $E_B > E_A$ : In case of an increased energy the new configuration is accepted with a probability  $p_{\text{acc}}(A \rightarrow B) = e^{-\beta(E_B - E_A)}$ . Therefore, we compare  $e^{-\beta(E_B - E_A)}$  with a uniform random number  $a \in [0; 1]$ . If  $e^{-\beta(E_B - E_A)} > a$ , the new configuration is accepted and otherwise rejected. If the new configuration is rejected, the trajectory in configuration space is continued with the old configuration  $A$ . Note that if we rejected a proposed configuration with  $E_B > E_A$  directly, we could get stuck in a local minimum.

In our simulations the energy  $E$  of a configuration is provided by the interaction potential  $V(r)$ , i.e.

$$E = \sum_{i=1}^N \sum_{j=i+1}^N V(|\mathbf{r}_j - \mathbf{r}_i|). \quad (3.38)$$

with the positions  $\mathbf{r}_j$ . In this case  $E$  corresponds to the inner energy  $U$  of the system, i.e.  $E = U$ . With the applied pair potentials introduced in Subsection 3.4.1 it is enough to calculate the energy  $U(\mathbf{r}_i) = \sum_{j=1}^N V(|\mathbf{r}_j - \mathbf{r}_i|)$  of the displaced

particle  $i$  before and after the displacement in order to compare the energies of configuration  $A$  and  $B$  in which exclusively one position is altered. The interaction terms without contribution of the displaced particle cancel out within the energy difference.

In case of short-range interactions as modeled in this thesis we apply a cutoff radius  $r_{\text{cut}}$  such that particles with distances  $r > r_{\text{cut}}$  do not contribute to the potential energy. We shift the potential in order to make it continuous, i.e.

$$V(r) = \begin{cases} V(r) - V(r_{\text{cut}}) & r \leq r_{\text{cut}} \\ 0 & r > r_{\text{cut}}. \end{cases} \quad (3.39)$$

The accepted configurations move along a trajectory in configuration space. Figure 3.2 illustrates an energy landscape in configuration space with a trajectory of accepted configurations.

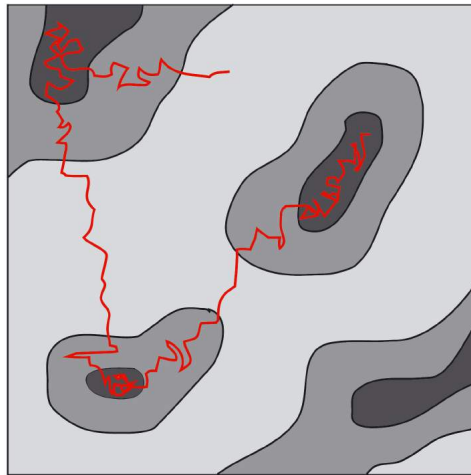


Figure 3.2: Schematic illustration of an energy landscape in configuration space. Areas colored in dark gray possess low energies, lighter gray indicates higher energies. The red line shows a trajectory beginning with a high energy configuration. Local and global displacements as well as phasonic flips make it possible to overcome energy barriers and reach regions of minimal energies in configuration space.

### 3.2.3 Extension to the $NpT$ -ensemble

In the  $NpT$ -ensemble – also called isothermal-isobaric ensemble – the number of particles  $N$  and the temperature  $T$  are constant. Furthermore, an additional

barostat ensures an approximately constant pressure which is realized by volume changes. Many real experiments are performed under these conditions, e.g. systems close to a phase transition of first order. The system is free to expand or contract and a complete conversion into the state with the lowest Gibbs energy is possible.

The first Monte Carlo simulations in the  $NpT$ -ensemble were derived by Wood [304] in 1968 who investigated the properties of hard disks. McDonald [305] developed a simulation method for systems with continuous forces which is widely used up to date.

The thermodynamic potential belonging to the  $NpT$ -ensemble is the free enthalpy, also known as Gibbs energy  $G(N, p, T) = U + pV - TS$  with the inner energy  $U$  and the entropy  $S$ . The free enthalpy is minimal in equilibrium.

In addition to displacements of the particles like described for the canonical ensemble one also needs to sample configurations with varying volumes to achieve a constant pressure  $p$  that is specified in the simulation. Thus, volume fluctuations are added. We select a random value  $\Delta V \in [-\delta V_{\max}, \delta V_{\max}]$  and increase or respectively decrease the total volume of the considered system about  $\Delta V$ , i.e.  $V_B = V_A + \Delta V$ . We scale the simulation box and the positions of the particles appropriately. While in the canonical ensemble the Metropolis acceptance criterion is  $p_{\text{acc}}(A \rightarrow B) = \min[1, \exp(-\beta\Delta U)]$ , i.e. dependent on the difference of the inner energy  $\Delta U$ , in the  $NpT$ -ensemble a volume change configuration is accepted with a probability

$$\begin{aligned} p_{\text{acc}}^{\text{volume}}(A \rightarrow B) &= \min [1, \exp(-\beta\Delta G)] \\ &= \min [1, \exp(-\beta\Delta U - \beta p\Delta V + \beta T\Delta S)], \end{aligned} \quad (3.40)$$

i.e. dependent on the difference of the Gibbs energy.  $\Delta S$  is the change of the entropy due to a change of the volume and is given by  $\Delta S = k_B N \ln(V_2/V_1)$ .

In systems close to a phase transition there may arise large volume fluctuations such that many displacements  $\Delta V$  are needed to obtain the density of the new phase. Therefore, it is convenient to choose the volume change in the logarithmic volume space, i.e. the proposed volume is determined by  $\ln(V_B) = \ln(V_A) + \Delta V$  [306, 307]. The acceptance probability of a trial move is modified to

$$\begin{aligned} p_{\text{acc}}^{\text{volume}}(A \rightarrow B) &= \min \left[ 1, \exp \left( -\beta(U_B - U_A) - \beta p(V_B - V_A) + (N + 1) \ln \left( \frac{V_B}{V_A} \right) \right) \right]. \end{aligned} \quad (3.41)$$

For a derivation of the acceptance probability see, e.g. [307].

We choose the maximal change of volume  $\delta V_{\max}$  in a way that about 50% of the

volume trial moves are accepted.

The ratio of volume trial moves and displacement trial moves is usually determined from the computational costs required for both moves. A displacement move scales with  $N$  while the cost of a volume move is proportional to  $N^2$ . Thus, on average we implement one volume trial move in each Monte Carlo step. To ensure the correct convergence of the Markov chain we do not repeat volume trial moves periodically after  $N$  displacement trial moves. Instead, in each trial move the probability of a volume trial move is given by  $1/N$  [307].

We check the correctness of the algorithm by calculating the virial pressure  $p_{\text{virial}}$  during the simulation. In equilibrium, the virial pressure should adopt the pressure  $p$  that we specified in the simulation. The virial pressure in simulations of many-particle systems reads [307, 308]

$$p_{\text{virial}} = \frac{N}{\Omega_d} k_B T + \frac{1}{d\Omega_d} \sum_{i=1}^N \langle \mathbf{r}_i \cdot \mathbf{F}_i \rangle. \quad (3.42)$$

The first part results from the ideal gas, the second one is due to the interactions between the particles and is referred to as virial.  $\mathbf{F}_i$  describes the force on particle  $i$ .  $\Omega_d$  corresponds to the considered volume in a  $d$ -dimensional system. In our two-dimensional system we set  $d = 2$  and  $\Omega_2 = A = L_x L_y$ . Including pairwise forces between the particles we obtain

$$p_{\text{virial}} = \rho k_B T + \frac{1}{2A} \left\langle \sum_{i=1}^N \sum_{j=i+1}^N \mathbf{F}_{ij} \cdot \mathbf{r}_{ij} \right\rangle \quad (3.43)$$

with the particle density  $\rho$ .  $\mathbf{F}_{ij}$  is the force on particle  $i$  induced by particle  $j$  and  $\mathbf{r}_{ij} = \mathbf{r}_j - \mathbf{r}_i$  is the vector from particle  $i$  to  $j$ . The average is taken over configurations.

### 3.3 Event-chain Monte Carlo simulations

Event-chain Monte Carlo simulations are based on a Markov-Chain Monte Carlo algorithm, i.e. states in a configuration space are proposed and accepted with a certain probability (see Section 3.2). The method was primarily introduced by Bernard *et al.* [309]. In first applications of the algorithm systems of hard particles were investigated [309–313], for example to study the melting in two dimensions [310, 313] or hard sphere polymer melts [311, 312]. In a recent generalization the algorithm was extended to continuous pair interactions between particles [314]. Simulations were performed with purely repulsive pair potentials [315] to study phase transitions in two dimensions. Event-chain Monte Carlo simulations are

usually performed in the  $NVT$ -ensemble and are known to be faster than conventional Monte Carlo algorithms [314].

In the following we introduce the theoretical concept which is based on a factorized Metropolis acceptance criterion combined with a “lifting” concept and infinitesimal displacements resulting in a rejection-free algorithm that fulfills maximal global balance. We also describe the implementation of the algorithm in our simulations.

### 3.3.1 Theoretical concept

#### Factorization of the Metropolis acceptance criterion

The usual Metropolis acceptance criterion presented in equation (3.32) depends on the statistical weights  $P(A)$  and  $P(B)$  of a current state  $A$  and a proposed state  $B$ . In the event-chain Monte Carlo algorithm the acceptance criterion is rewritten in a way that  $P(A)$  and  $P(B)$  are factorized [314]: In a system of  $N$  particles that interact according to a pair potential the energy  $E$  of a state is the sum over all pair energies between two particles  $\langle i, j \rangle$ , i.e.  $E = \sum_{\langle i, j \rangle} E_{ij}$ . Factorization of the Boltzmann factor results in  $e^{-\beta E(A)} = e^{-\beta \sum_{\langle i, j \rangle} E_{ij}(A)} = \prod_{\langle i, j \rangle} e^{-\beta E_{ij}(A)}$  and consequently  $P(A) = \prod_{\langle i, j \rangle} P_{ij}(A)$ . The probability  $P(A)$  is thus a product of the probabilities of all particle pairs  $P_{ij}(A)$ .  $P(B)$  is factorized analogously. According to the Metropolis acceptance criterion the acceptance probability of a single pair of particles  $\langle i, j \rangle$  becomes

$$p_{\text{acc},ij}(A \rightarrow B) = \min \left( 1, \frac{P_{ij}(B)}{P_{ij}(A)} \right) = \min(1, e^{-\beta \Delta E_{ij}(A \rightarrow B)}), \quad (3.44)$$

where  $\Delta E_{ij}(A \rightarrow B)$  denotes the potential difference of the pair  $\langle i, j \rangle$  in configuration  $A$  and  $B$ . Finally, the pairwise factorized Metropolis acceptance criterion – also called Metropolis filter – is the product of the independent acceptance probabilities  $p_{\text{acc},ij}(A \rightarrow B)$  [314, 316, 317]

$$p_{\text{acc}}^{\text{fact}}(A \rightarrow B) = \prod_{\langle i, j \rangle} p_{\text{acc},ij}(A \rightarrow B) = \prod_{\langle i, j \rangle} \min(1, e^{-\beta \Delta E_{ij}(A \rightarrow B)}). \quad (3.45)$$

The factorized Metropolis filter satisfies detailed balance since the same probability flow conditions as in the usual Metropolis acceptance criterion are considered [314]. In case of hard spheres or in systems of only two particles the factorized Metropolis criterion is equal to the usual one. In all other cases, the number of rejected configurations is higher with the factorized filter in case of detailed balance simulations [314, 317].

The factorized Metropolis filter can be applied in two ways: First, one can accept a proposed configuration like in case of the usual Metropolis acceptance criterion,

i.e. we choose a random number  $a \in (0, 1)$  and the proposed trial move is accepted if  $a < p_{\text{acc}}^{\text{fact}}(A \rightarrow B)$ . Alternatively, in our simulations the probability function  $p_{\text{acc}}^{\text{fact}}(A \rightarrow B)$  is not evaluated explicitly. Instead, the single independent probabilities for each pair of particles are considered: Several independent random numbers  $a_{ij} \in (0, 1)$  are chosen and the trial move is only accepted if  $a_{ij} < p_{\text{acc},ij}(A \rightarrow B)$  for all pairs  $\langle i, j \rangle$ . Thus, all pairs need to agree with the trial move to make it be accepted. If at least one pair does not accept the trial move then an event takes place. The idea of events is given in the next paragraph.

The probability of rejecting a displacement trial move is [314]

$$\begin{aligned} p_{\text{rej}}^{\text{fact}}(A \rightarrow B) &= 1 - p_{\text{acc}}^{\text{fact}}(A \rightarrow B) \\ &= 1 - e^{-\beta \sum_{\langle i,j \rangle} \max(0, \Delta E_{ij}(A \rightarrow B))} \\ &\approx \beta \sum_{\langle i,j \rangle} \max(0, \Delta E_{ij}(A \rightarrow B)) \end{aligned} \quad (3.46)$$

where a Taylor expansion of the exponential function  $e^x \approx 1 + x$  is applied in the last step.

### Lifting concept and infinitesimal displacements

Event-chain Monte Carlo simulations make use of a lifting concept as described in [314]. For its realization two additional variables are introduced as an extension of the physical configuration space with points  $\boldsymbol{\pi} = (\mathbf{r}_1, \dots, \mathbf{r}_N)$ . The first additional variable – called lifting variable – defines an active particle  $a$  which is the next one to be displaced. All other particles are referred to as target particles  $t$ . The second additional variable gives the direction of motion in which the active particle is displaced.

On the basis of the factorized Metropolis filter given in equation (3.45) it is determined what happens to the proposed new configuration and the lifting variable.

- If all pairs of particles accept the trial move, the proposed configuration is taken and the lifting variable does not change in the next step.
- If at least one target particle  $t$  or respectively the pair of particles  $\langle a, t \rangle$  does not accept the displacement, then the proposed trial move is rejected. Nevertheless, the proposed new position is taken but in combination with a lifting move. Lifting move means that the lifting variable is transferred to the particle  $t$  that refused the displacement move. Such a lifting move does not result in a change of the physical configuration.

Infinitesimal displacements of the active particle between two configurations effect that the probability of accepting the move approaches one and the probability of

rejecting a move approaches zero. Consequently, there are no multiple rejections caused by multiple particle pairs  $\langle a, t \rangle$  in one displacement move and the lifting variable is unique. For finite displacements there would be the possibility of multiple rejections such that global balance would not be satisfied (see, e.g. [314]). The concept of global balance is explained in the next paragraph. Since there is either a displacement move or a lifting move the algorithm is rejection-free.

### Global balance

The standard Metropolis Monte Carlo algorithm fulfills detailed balance (see equation (3.28)). In event-chain Monte Carlo simulations, however, detailed balance is broken since displacements of particles are irreversible as described in Subsection 3.3.2. In case of a move from configuration  $A$  to configuration  $B$ , i.e.  $A \rightarrow B$ , the reverse move  $B \rightarrow A$  is not proposed. Though, a weaker condition for the transitions between states is fulfilled. The condition is called global balance. In a general Markov-Chain Monte Carlo simulation it is sufficient when global balance is satisfied. Global balance means that the whole probability flow going inside a configuration  $A$  equals the flow that goes out of  $A$  [314, 316]:

$$\sum_B P(B)p_{\text{acc}}(B \rightarrow A) = \sum_B P(A)p_{\text{acc}}(A \rightarrow B) = P(A). \quad (3.47)$$

Here, a symmetric proposal density  $w(A \rightarrow B) = w(B \rightarrow A)$  is supposed. Denoting the probability flow from configuration  $A$  to  $B$  as  $\phi(A \rightarrow B) = P(A)p_{\text{acc}}(A \rightarrow B)$  one gets

$$\sum_B \phi(B \rightarrow A) = \sum_B \phi(A \rightarrow B). \quad (3.48)$$

By including both displacement and lifting moves to the flow into and respectively out of a configuration the event-chain Monte Carlo algorithm fulfills global balance. Even maximal global balance is ensured which means that in addition to equation (3.48) the algorithm is free of rejections, i.e.  $\phi(A \rightarrow A) = 0$  and the flow only goes in one direction, i.e. from  $\phi(A \rightarrow B) > 0$  follows  $\phi(B \rightarrow A) = 0$  (see, e.g. [314]). To prove that maximal global balance is fulfilled the rejection probabilities of a displacement move given in equation (3.46) are considered as probabilities of a lifting move. Then, there are  $N - 1$  lifting moves and one displacement move into a state  $A$ . The flow into  $A$  corresponds to the flow out of  $A$  as proven in [314].

### 3.3.2 Implementation in simulations

Sampling the configuration space is implemented in an event-based algorithm, i.e. an active particle is moved and the collisions - called events - with all other parti-

cles are determined. In case of hard spheres, such collisions occur when particles touch each other [309]. In case of soft particles as considered in this work the determination of events is more tricky as explained below.

A series of successive events is referred to as an event chain. The current length of the chain is the sum of all particle displacements within the chain. The total length of a chain is restricted to a fixed value  $l$ . Furthermore, the cumulative number of events per particle is given in sweeps, i.e. 1 sweep corresponds to  $N$  events.

### Implementation of event chains

As described in [314] a chain is started with an active particle  $a$  that is determined by the random lifting variable. We randomly choose the direction  $\hat{e}$  in which particle  $a$  should move, which is limited to the positive  $x$ - or  $y$ -direction in our case. Particle  $a$  is planned to be moved about the remaining chain length. On the way we need to check whether the particle collides with the surrounding particles. Since we are only interested in the first collision partner, it is not necessary to implement infinitesimal displacements by small time increments. Instead, we determine for each target particle  $t$  the distance  $\Delta s_{at}$  which particle  $a$  can move until a collision occurs. If there are distances  $\Delta s_{at}$  that are smaller than the planned displacement we choose the event partner for which the event happens temporally first. Particle  $a$  is moved about  $\Delta s_{at}$ , i.e.  $\mathbf{r}_a \rightarrow \mathbf{r}_a + \Delta s_{at} \hat{e}$ , and its event partner becomes the new active particle. The process corresponds to a lifting event. The remaining chain length is reduced by the performed displacement  $\Delta s_{at}$ . The described process is repeated for the new active particle. In case of no collisions on the way, particle  $a$  is moved about the planned distance.

When the given chain length  $l$  is reached a new chain is started with a new random particle as initial active particle and a new direction of motion. This procedure ensures that the whole configuration space can be sampled. The simulation is stopped when a given number of chains is reached.

### Determination of event distances in soft particle systems

In our simulations we only search for short-range events which means that only particles within a certain cutoff radius around the active particle are considered as possible event partners. Long-range events may be efficiently computed by the cell veto algorithm [316]. Possible event partners and the corresponding distance  $\Delta s_{at}$  to the event are determined according to the applied pair potential. The procedure is explained according to [314]:

For each target particle we determine the maximal increase in pair energy  $E_{at}^*$  that is allowed before a lifting move occurs. The allowed rise in energy reads  $E_{at}^* = -\ln(\gamma_{at})$  with independent uniform random numbers  $\gamma_{at} \in (0, 1]$  for each

particle pair. The displacement  $\Delta s_{at}$  until the active particle is lifted is (formally) determined from

$$E_{at}^* = \int_0^{E_{at}^*} [dE_{at}]^+ = \int_0^{\Delta s_{at}} \left[ \frac{\partial E_{at}(\mathbf{r}_t - \mathbf{r}_a - s\hat{e})}{\partial s} \right]^+ ds \quad (3.49)$$

with  $[x]^+ = \max(x, 0)$  and accordingly  $[x]^+ \geq 0$ . Target particle  $t$  that requires the smallest distance  $\Delta s_{at}$  is the next active particle.

Since it is often difficult to solve equation (3.49), there is a trick for central potentials with  $E_{ij}(\mathbf{r}_{ij}) = E_{ij}(r_{ij})$  as applied in this thesis. First, the potential is divided into repulsive and attractive regions. In case of our potential with two minima we consider two repulsive and two attractive regions. Events may only occur if the pair energy between the active and the target particle increases after a displacement of the active particle. The allowed pair energy until an event takes place reads  $E_{at}^{\text{lift}} = E_{at}(r_{at}^{\text{now}}) + E_{at}^*$  with the current pair energy  $E_{at}(r_{at}^{\text{now}})$ . By inverting  $E_{at}^{\text{lift}} = E_{at}(r_{at}^{\text{lift}})$  one receives the distance  $r_{at}^{\text{lift}} = E_{at}^{-1}(E_{at}^{\text{lift}})$  between a particle pair  $\langle a, t \rangle$  which leads to an event.  $r_{at}^{\text{lift}}$  corresponds to the probabilistic veto radius. The particular solution in the repulsive or attractive region is picked. The maximal allowed displacement  $\Delta s_{at}$  then is given by the positive solution of  $r_{at}^{\text{lift}} = |\mathbf{r}_t - \mathbf{r}_a - \Delta s_{at}\hat{e}|$ . The allowed displacements are recalculated after each event.

In Figure 3.3 we show the cases in which events take place for particle distances in the repulsive and attractive region of the potential and illustrate how the maximal displacement  $\Delta s_{at}$  is determined.

## 3.4 General settings of our simulations

In the simulations presented in this work we model two-dimensional colloidal systems under conditions which are suitable for the considered problem.

In the following we introduce the interaction potentials which we apply in our simulations and specify simulation units and required input parameters. Furthermore, applied initial configurations of the particles are described. We introduce suitable boundary conditions and determine appropriate simulation box sizes as used in our investigations.

### 3.4.1 Potentials

Particles can arrange to ordered structures if internal or external forces act on them. In case of only internal forces the process is called self-assembly [318]. Internal forces can be derived from internal interaction potentials. In case of the applied colloidal model systems the interactions can easily be altered by changing

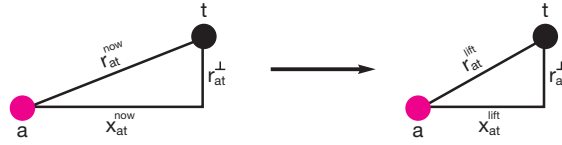
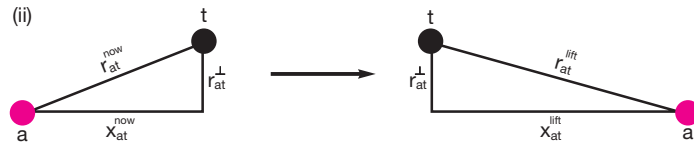
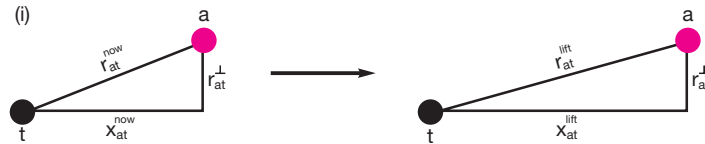
(a) Pair distance  $r_{at}^{\text{now}}$  in the repulsive region of the potential.(b) Pair distance  $r_{at}^{\text{now}}$  in the attractive region of the potential.

Figure 3.3: Configurations that may lead to lifting events and determination of the event distances. (a) The distance between particle  $a$  and  $t$  is in the repulsive part of the potential. An event may only happen if the target particle  $t$  is in front of the active particle  $a$  with respect to the considered direction of motion (here the positive  $x$ -direction). The distance until the lifting event is  $\Delta s_{at} = x_{at}^{\text{now}} - x_{at}^{\text{lift}}$ . (b) Particles with a distance in the attractive range of the potential. (i) The target particle  $t$  lies behind the active particle  $a$ . When  $a$  moves forwards an event occurs at  $\Delta s_{at} = x_{at}^{\text{lift}} - x_{at}^{\text{now}}$ . (ii) The target particle is ahead in the beginning. After  $a$  has come so close to  $t$  that  $r_{at} = r_{at}^{\perp}$  the particle distance becomes larger when  $a$  keeps on moving. After  $a$  has passed  $t$ , an event is possible with  $\Delta s_{at} = x_{at}^{\text{now}} + x_{at}^{\text{lift}}$ .

the potential parameters. We employ two different kinds of potentials that can stabilize quasicrystals.

### The Lennard-Jones–Gauss potential

Previously, Rechtsman *et al.* [319–322] designed Lennard-Jones potentials with an additional Gaussian term in order to stabilize targeted structures via optimization. By choosing Gaussian terms that support or respectively disfavor certain lengths Rechtsman *et al.* found potentials that stabilize two-dimensional square lattices [319] and honey comb lattices [319, 320], as well as three-dimensional cubic lattices [321] and diamond structures [322].

Engel *et al.* [28, 29] picked up the idea of an isotropic Lennard-Jones pair potential with an additional Gaussian term to investigate structures that arise for different potential parameters. The employed Lennard-Jones–Gauss potential reads [28, 29]

$$\frac{V_{LJG}(r)}{\epsilon_0} = \left(\frac{r_0}{r}\right)^{12} - 2\left(\frac{r_0}{r}\right)^6 - \epsilon \exp\left(-\frac{(r - r_G)^2}{2r_0\sigma^2}\right) \quad (3.50)$$

and resembles the effective pair potentials in many metals that consist of a repulsive core and a decaying oscillating tail called Friedel term [86, 323, 324].

$\epsilon_0$  and  $r_0$  give energy and length unit and  $r = |\mathbf{r}_i - \mathbf{r}_j|$  denotes the distance between two particles  $i$  and  $j$ . For most values of the potential parameters  $r_G$ ,  $\epsilon$  and  $\sigma^2$  a double-well potential is induced. The first minimum results from the Lennard-Jones part and is located exactly at  $r = r_0$ . The second minimum is caused by the Gaussian term.  $r_G$  determines its position,  $\epsilon$  its depth and  $\sigma^2$  its width. The two minima provide two supported lengths between the particles. Note that two minima is a good starting condition to model quasicrystals with two incommensurate length scales.

In systems of identical particles that interact according to the Lennard-Jones–Gauss potential Engel *et al.* [28, 29, 91] observed the self-assembly of complex structures. For appropriate potential parameters the authors found decagonal and dodecagonal quasicrystalline arrangements with two incommensurate lengths. Note that the length scales in the assembled quasicrystals do not exactly correspond to the potential minima but are slightly shifted [14]. Farther, periodic structures like triangular, square or honeycomb lattices were observed for further potential parameters [28].

In this thesis, we apply the Lennard-Jones–Gauss potential with parameters that support decagonal and dodecagonal quasicrystals. The former ones are stabilized with the parameters  $r_G = 1.52$ ,  $\epsilon = 1.8$  and  $\sigma^2 = 0.02$  [28, 29]. The corresponding potential is visualized in Figure 3.4 (a). Decagonal quasicrystals are supported for pressure  $p = 0$  and temperatures below the melting temperature  $T_m = 0.56 \pm 0.02$  [29]. Suitable parameters for dodecagonal quasicrystals are  $r_G = 1.95$ ,  $\epsilon = 2.0$

and  $\sigma^2 = 0.02$  [91]. The corresponding potential is depicted in Figure 3.4 (b). With these parameters dodecagonal quasicrystals form at  $p = 0$  and  $T < T_c$  with  $T_c = 0.80 \pm 0.03$  denoting the transition temperature to a hexagonal phase [91]. Since the potential is short-range it is cut and shifted appropriately at a cutoff radius  $r_{\text{cut}} = 2.5$ , which is larger than both length scales of the potentials.

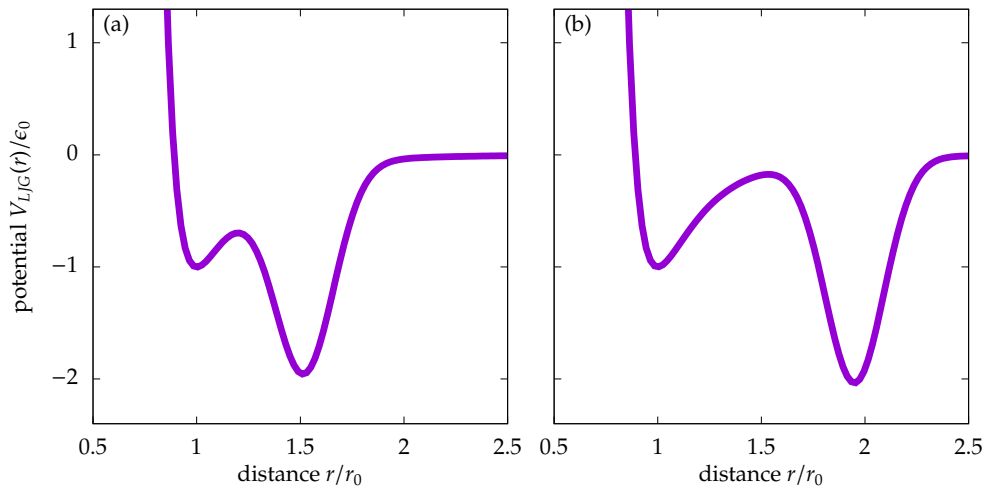


Figure 3.4: Lennard-Jones–Gauss potential with different potential parameters. (a)  $r_G = 1.52$ ,  $\epsilon = 1.8$  and  $\sigma^2 = 0.02$  support decagonal structures. (b)  $r_G = 1.95$ ,  $\epsilon = 2.0$  and  $\sigma^2 = 0.02$  favor dodecagonal structures.

### Pair potential with preferred binding angles

Aside from isotropic interactions between particles we also study patchy colloids with preferred binding angles. Patchy colloids are furnished with regions – called patches – that attract each other (see Section 5.1 for a detailed description of patchy colloids). For realizing the interactions in simulations we modify the Lennard-Jones potential by multiplying it with an additional anisotropic term that depends on the binding angles. Such a potential has been used in previous simulations to study self-assembly and crystallization processes in two- and three-dimensional systems of patchy colloids [30, 118–121, 257–261]. The complete potential is given by

$$V_p(r, \theta_k, \theta_l) = V_{LJ}(r) \cdot V_a(\theta_k, \theta_l). \quad (3.51)$$

The Lennard-Jones potential reads

$$V_{LJ}(r) = \epsilon_0 \left[ \left( \frac{r_0}{r} \right)^{2n} - 2 \left( \frac{r_0}{r} \right)^n \right] \quad (3.52)$$

(see also previous paragraph). Here, the Lennard-Jones exponent  $n$  is variable. It determines the width of the potential minimum which will be adjusted to the simulations.  $r_0$  gives the location of the potential minimum. The angular term is of the form

$$V_a(\theta_k, \theta_l) = \exp\left(-\frac{\theta_k^2}{2\sigma_{pw}^2}\right) \exp\left(-\frac{\theta_l^2}{2\sigma_{pw}^2}\right), \quad (3.53)$$

where  $\theta_k$  or respectively  $\theta_l$  denote the angles between the nearest patch on particle  $i$  or respectively particle  $j$  to the interparticle vector between particle  $i$  and  $j$  (see sketches on the right hand side of Figure 3.5).  $\sigma_{pw}$  models the patch width. For instance, later in this thesis we model particles with five symmetrically arranged patches with a width  $\sigma_{pw} = 0.49$  which are known to form dodecagonal quasicrystals at appropriate thermodynamic conditions [119–121]. The corresponding potential is illustrated in Figures 3.5 (a) and (b).

Dependent on the structure that we want to stabilize we slightly alter the angular term in some simulations. The modified angular term reads

$$V_a(\theta_k, \theta_l) = \exp\left(-\frac{\theta_k^2}{2\sigma_1^2}\right) \exp\left(-\frac{\theta_l^2}{2\sigma_1^2}\right) + \exp\left(-\frac{\theta_k^2}{2\sigma_2^2}\right) \exp\left(-\frac{\theta_l^2}{2\sigma_2^2}\right) \quad (3.54)$$

with two patch widths  $\sigma_1$  and  $\sigma_2$ . Thus, we can model a narrow patch width  $\sigma_1$ , while a superposition with a broad patch width  $\sigma_2$  ensures that the patches still find each other within a reasonable time. We will see in Chapter 5 that narrow patches are required to stabilize octagonal and decagonal quasicrystals. A potential that stabilizes octagonal quasicrystals is shown in Figures 3.5 (c) and (d).

The potentials are truncated at  $r_{\text{cut}} = 3$ . Note that this cutoff radius is larger than the cutoff radius of the Lennard-Jones–Gauss potential. This choice is due to the variable Lennard-Jones exponent  $n$ . For low values of  $n$  the potential minimum is broadened and the potential approaches zero only at larger distances than the Lennard-Jones–Gauss potential.

The complete potential  $V_p(r, \theta_k, \theta_l)$  as given in equation (3.51) models the interaction between particles with patches that extend into the particle core. Alternatively, in recent works [30, 118–120, 257–261] particles are furnished with patches at the surface, i.e. the angular modifications are only present for distances that are larger than the radius of the particles:

$$V_{p,\text{surf}}(r, \theta_k, \theta_l) = \begin{cases} V_{LJ}(r) & r \leq r_0 \\ V_{LJ}(r) \cdot V_a(\theta_k, \theta_l) & r \geq r_0. \end{cases} \quad (3.55)$$

If not stated otherwise, we employ  $V_{p,\text{surf}}(r, \theta_k, \theta_l)$  in our simulations.

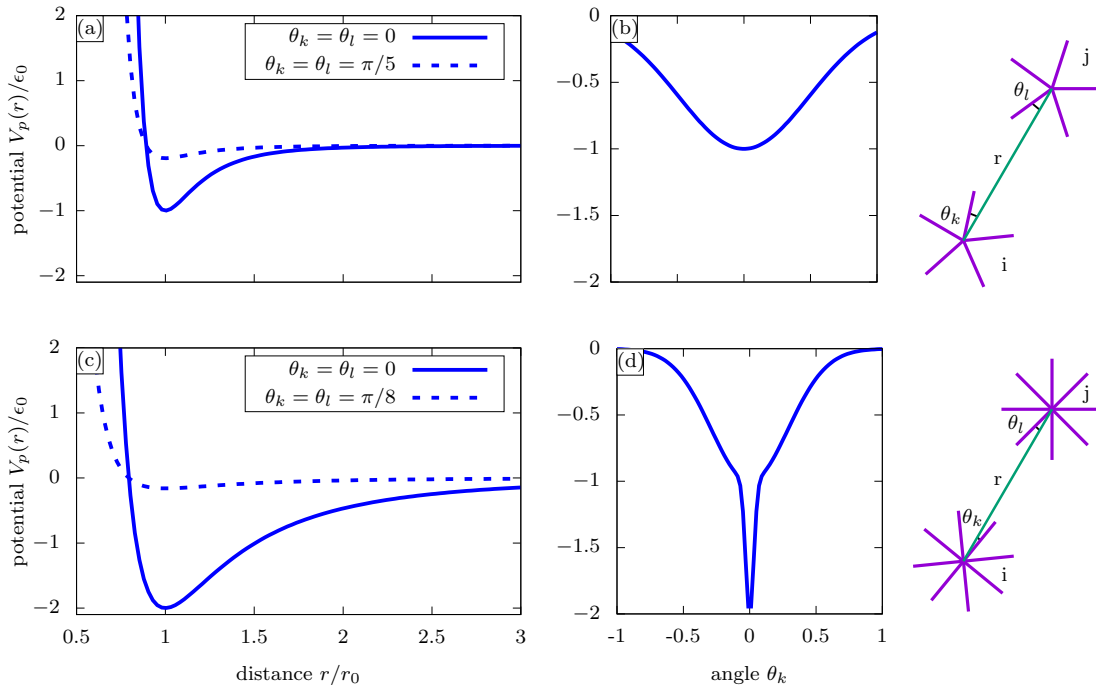


Figure 3.5: Pair potentials between patchy colloids with preferred bond angles. (a) and (b) show a potential with one patch width  $\sigma_{pw} = 0.49$  and Lennard-Jones exponent  $n = 6$ . The potential stabilizes dodecagonal quasicrystals in case of particles furnished with five patches. In (a) we depict the potential as a function of the pair distance  $r/r_0$ . The potential minimum is deepest for patches that are oriented towards each other (solid line) and lowest for opposite patches (dashed line). (b) illustrates the dependence of the potential on the binding angle  $\theta_k$  at fixed  $\theta_l = 0$  and  $r = r_0$ . (c) and (d) show a potential with two patch widths  $\sigma_1 = 0.02$  and  $\sigma_2 = 0.29$  and Lennard-Jones exponent  $n = 3$ . The potential stabilizes octagonal quasicrystals in case of particles decorated with eight patches. Similar to (a) and (b) we depict the dependence on (c) the distance and (d) the angle. On the right hand side we sketch particles with five and respectively eight symmetrically arranged patches illustrated by arms around the particles. We show a similar illustration in [121].

### 3.4.2 Simulation units and parameters

It is convenient to apply reduced or dimensionless units in simulations. This procedure has the advantage that the numerical values are in the order of unity instead of possibly very small values in the order of the atomic length scale.

Our potentials are given in Lennard-Jones units. With the length unit  $r_0$  the particle density  $\rho = N/(L_x L_y)$  with box lengths  $L_x$  and  $L_y$  is given in units of  $1/r_0^2$ . The energy is measured in units of  $\epsilon_0$  and, accordingly,  $\epsilon_0/k_B$  describes the temperature unit.  $k_B$  denotes the Boltzmann constant.

In case of Brownian dynamics simulations the time unit is the Brownian time  $\tau_B = \gamma r_0^2 / \epsilon_0$  with the friction coefficient  $\gamma$  of a particle. The time increment  $\Delta t$  of a single simulation step needs to be chosen deliberately. On the one hand,  $\Delta t$  has to be small enough such that the particles do not move too far in a single time step to prevent the loss of important information. On the other hand,  $\Delta t$  must not be too small since for small  $\Delta t$  the simulation time increases. We apply  $\Delta t = 1 \cdot 10^{-4}$ , which is just small enough to avoid too large forces.

### 3.4.3 Initial configurations

Simulations can be started with different initial configurations. In this thesis, we either start with particles placed on a perfect quasicrystalline lattice or with random initial positions. Concerning the former case we create perfect quasicrystalline lattices with octagonal, decagonal or dodecagonal symmetry by occupying the minima of an appropriate external laser potential with colloids (see Section 4.2). Further common construction methods are listed in Subsection 2.3.5. The lattices are scaled in a way that the desired particle densities are reached.

In case of initial random particle positions, the positions are determined numerically by a random number generator.

### 3.4.4 Boundary conditions and size of simulation box

We model particles in two-dimensional simulation boxes of finite size. The box lengths are termed  $L_x$  and  $L_y$ . In order to handle the boundaries one can model hard walls, i.e. the particles are repelled like in an elastic collision when touching a wall. However, such walls can have a great influence on the dynamics of the particles.

An alternative employed in this thesis is periodic boundary conditions which model a system of quasi infinite size (see Figure 3.6). Copies of the simulation box including copies of the particles are repeated periodically in all directions in space around the considered simulation box. Copies of the particles are called mirror particles. The motion of the particles in the simulation box and the motion of

their mirror particles in all neighboring boxes is parallel. Every time a particle leaves the simulation box at one side, it reappears at the opposite side. Thus, at any time there is a constant number of particles in the simulation box. In case of interacting particles, the interaction partners can be in the neighboring boxes, i.e. if the distance  $d$  in  $x$ - or  $y$ -direction between a particle  $a$  and a particle  $b$  is larger than  $L_x/2$  or  $L_y/2$ , then the considered particle  $a$  interacts with the closest mirror particle of  $b$ .

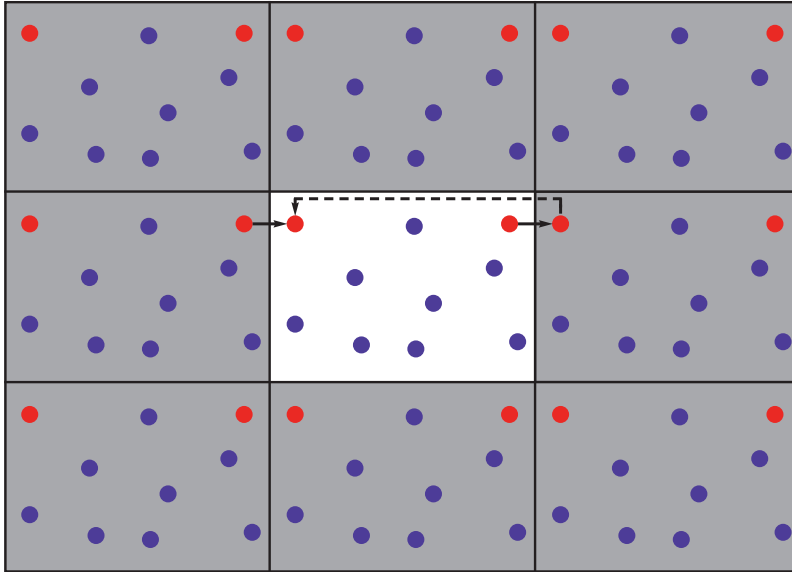


Figure 3.6: Illustration of a simulation box with periodic boundary conditions. The simulation box (white) is surrounded by copies of itself (gray) in each direction. A particle (red) that leaves the simulation box at one side reappears at the opposite side due to the parallel movement of mirror particles in the neighboring boxes.

Note that the finite box size can result in finite-size effects that modify the physical properties of the system. For instance, in systems with periodic boundaries the possible fluctuations are limited to the box size, i.e. the longest allowed wavelengths in  $x$ - and  $y$ -direction are  $\lambda_x = L_x$  and  $\lambda_y = L_y$ . In order to determine and study finite-size effects one needs to perform and compare simulations with different system sizes [307].

Since quasicrystals are quasi-periodic they cannot be modeled perfectly at the edges of a simulation box with periodic boundary conditions. To keep the discontinuities as low as possible, we search approximants for the considered quasicrystals. An approximant is a local quasicrystalline structure that is repeated periodically outside of the simulation box. The length  $L_x$  and the height  $L_y$  of the simulation

box are chosen in a way that particles crossing the boundaries are exposed to only small discontinuities.

We derive possible box sizes for continuous quasicrystalline potentials in two dimensions that can be created by means of  $n$  interfering laser beams. The potential reads [8, 125, 325]

$$V(\mathbf{r}) = -\frac{V_0}{n^2} \sum_{j=0}^{n-1} \sum_{k=0}^{n-1} \cos[(\mathbf{G}_j - \mathbf{G}_k) \cdot \mathbf{r}] \quad (3.56)$$

with wave vectors

$$\mathbf{G}_j = (2\pi/a_V \cos[2\pi j/n], 2\pi/a_V \sin[2\pi j/n]), \quad j = 0, \dots, (n-1) \quad (3.57)$$

where  $a_V = 2\pi/|\mathbf{G}_j|$ .  $-V_0$  denotes the minimal depth. A detailed deduction and description of such laser potentials is presented in Section 4.2.

The box dimensions are determined in a way that the potential is similar at the edges, i.e.  $V(x, y) \approx V(x + L_x, y)$  and  $V(x, y) \approx V(x, y + L_y)$ . Therefore, the side lengths  $L_x$  and  $L_y$  need to be integer multiples of the potential length scales that are given by  $2\pi/G_{j,x}$  and  $2\pi/G_{j,y}$ , i.e.

$$\begin{aligned} G_{j,x} L_x &\stackrel{!}{=} 2\pi k_j \quad \text{and} \\ G_{j,y} L_y &\stackrel{!}{=} 2\pi l_j \end{aligned} \quad (3.58)$$

with  $k_j, l_j \in \mathbb{Z}$ . We determine possible box lengths for decagonal and for dodecagonal quasicrystals which are modeled in this thesis.

A decagonal quasicrystal is constructed from five wave vectors out of which two are linearly independent. The length scales in  $x$ -direction read  $2\pi/G_{0,x} = a_V$ ,  $2\pi/G_{1,x} = 2\tau a_V$  and  $2\pi/G_{2,x} = -2/\tau a_V$  with the golden mean  $\tau$ . Since the ratios of the length scales are no rational numbers, it is not possible to find a box length that is a multiple of all length scales. In order to find a box length that fits as good as possible,  $L_x$  has approximately to fulfill

$$\begin{aligned} L_x &= k_1 a_V, \\ L_x &= k_2 2\tau a_V \quad \text{and} \\ L_x &= -k_3 2/\tau a_V, \quad k_1, k_2, k_3 \in \mathbb{Z}. \end{aligned} \quad (3.59)$$

Combining the first two equations the integers  $k_1$  and  $k_2$  have to fulfill  $k_1/k_2 = 2\tau$ . Since  $\tau$  can be approximated by the ratio of two consecutive Fibonacci numbers  $F_n$  and  $F_{n+1}$  (see Subsection 2.3.3) we may choose  $k_1 = 2F_{n+1}$  and  $k_2 = F_n$ . Then,  $L_x = 2F_n a_V$  is a proper box length. Since in decagonal quasicrystals there are only two incommensurate length scales, the third condition of equation (3.59) is

fulfilled trivially.

In  $y$ -direction the length scales are given by  $G_{1,y}/2\pi = \sin(2\pi/5) a_V$  and  $G_{2,y}/2\pi = \sin(4\pi/5) a_V$ . Again their ratio is  $\tau$  such that  $L_y = F_m a_V/\sin(\pi/5)$  with a Fibonacci number  $F_m$  is an appropriate box length.

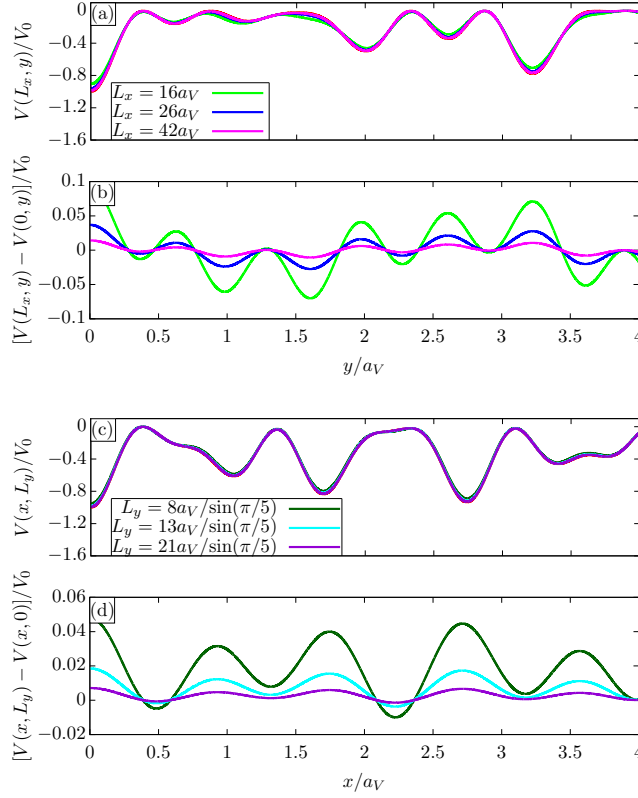


Figure 3.7: Laser potential  $V(\mathbf{r})$  with decagonal symmetry along the edges of the simulation box. (a) Potential along  $L_x = 2F_n a_V$  for  $F_n = 8, 13, 21$  (right border of the simulation box). The potential at  $x_0 = 0$  (left border) is additionally illustrated in red, but hardly visible due to the negligible small difference to the potentials at the mentioned lengths  $L_x$ . (b) Differences between the potentials at  $x_0$  and  $L_x$ . (c) Potential along  $L_y = F_m a_V/\sin(\pi/5)$  for  $F_m = 8, 13, 21$ . Again, the potential at  $y_0 = 0$  is hardly visible. (d) Differences between the potentials at  $y_0$  and  $L_y$ .

Figure 3.7 (a) depicts the considered decagonal laser potential  $V(\mathbf{r})$  as introduced in equation (3.56) at fixed  $x_0 = 0$  (left border of the simulation box) together with the potential at fixed  $L_x = 2F_n a_V$  for  $F_n = 8, 13, 21$  (right border of the simulation box). The differences between the potentials at the left and the right borders are very small as illustrated in Figure 3.7 (b). The greater the Fibonacci number  $F_n$  is, the smaller becomes the difference. Analogously, Figures 3.7 (c) and (d) show the potential at fixed  $y_0 = 0$  (lower border of the simulation box)

and  $L_y = F_m a_V / \sin(\pi/5)$  for  $F_m = 8, 13, 21$  (upper border of the simulation box) and the differences between the potentials at the upper and the lower border. In case of dodecagonal quasicrystals possible box dimensions are equal in  $x$ - and  $y$ -direction. The calculation is demonstrated for the box length  $L_x$ . The length scales are  $2\pi/G_{0,x} = a_V$ ,  $2\pi/G_{1,x} = 2a_V/\sqrt{3}$  and  $2\pi/G_{2,x} = 2a_V$ , which results in the conditions

$$\begin{aligned} L_x &= k_1 a_V \quad \text{and} \\ L_x &= 2/\sqrt{3}k_2 a_V, \quad k_1, k_2 \in \mathbb{Z}. \end{aligned} \quad (3.60)$$

Consequently, the ratio between  $k_1$  and  $k_2$  needs to fulfill  $k_1/k_2 = 2/\sqrt{3}$ . We approximate  $L_x = 2k a_V$  with the condition  $\exists l : l/k \approx \sqrt{3} (l, k \in \mathbb{Z})$ . Possible integer numbers are  $k = 4, 11, 15, 19, 22, 26, 30, 37, 41, 45, 52, \dots$ . For selected values of  $k$ , the dodecagonal laser potential at the edges of the simulation box and the potential differences are shown in Figure 3.8 (a) and (b). Since possible box dimensions are equal in  $x$ - and  $y$ -direction, we only illustrate the potential for constant  $L_x$  and varying  $y$ .

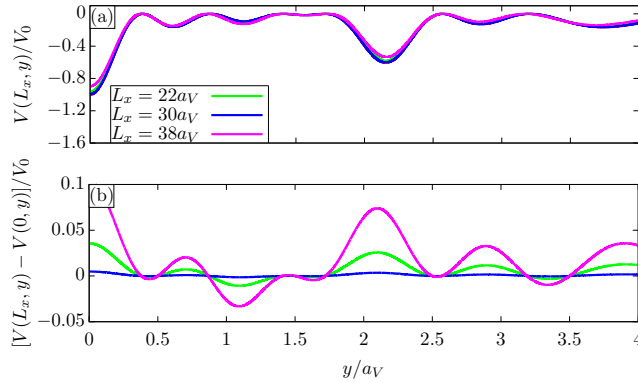


Figure 3.8: Laser potential  $V(\mathbf{r})$  with dodecagonal symmetry along the edges of the simulation box. (a) Potential along  $x_0 = 0$  and  $L_x = 2k a_V$  for  $k = 11, 15, 19$ . (b) Differences between the potentials at  $x_0$  and  $L_x$ .

Note that in order to get real approximants, i.e. structures with exactly the same potential at the edges, we have to adapt the wave vectors appropriately in a way that the box lengths become exact multiples of the length scales. Such real approximants are employed, e.g. to find phasonic flips with the help of the projection method (see Chapter 8).

## 3.5 Analyzing tools

In an arrangement of particles it is often not straightforward to identify the underlying order. In our systems we are interested in the positional and orientational order. Positional order means regular distances between the particles. Orientational order refers to the orientation of groups of particles, i.e. the directions between interparticle vectors.

In this Section we introduce mathematical tools that we will apply later in this thesis to determine the order of our structures. In addition, a method to identify and analyze defects in quasicrystals is presented.

### 3.5.1 Pair distribution and pair correlation function

The pair distribution function  $g(\mathbf{r})$  is a measure for the average packing of particles around a chosen particle dependent on the vector  $\mathbf{r}$ . Usually, the pair distribution function is averaged over all particles, i.e. each particle is once considered as central particle. One obtains

$$g(\mathbf{r}) = \frac{1}{(N-1)\rho} \left\langle \sum_{i=1}^N \sum_{\substack{j=1 \\ j \neq i}}^N \delta(\mathbf{r} - (\mathbf{r}_i - \mathbf{r}_j)) \right\rangle \quad (3.61)$$

where  $\mathbf{r}_i - \mathbf{r}_j$  denotes the vector between two particles at the positions  $\mathbf{r}_i$  and  $\mathbf{r}_j$ .  $N$  describes the number of particles and  $\rho$  the average density.

In case of the radial distribution or pair correlation function  $g(r)$  only the absolute distance  $|\mathbf{r}| = r$  between the particles is considered. For computation,  $g(r)$  is discretized according to [326]

$$g(r, dr) = \frac{\langle N(r+dr) - N(r) \rangle}{A_{\text{shell}}\rho}. \quad (3.62)$$

$\langle N(r+dr) - N(r) \rangle$  gives the average number of particles in a shell of inner radius  $r$  and outer radius  $r+dr$  (see Figure 3.9). The number is divided by the average global density  $\rho$  and the area  $A_{\text{shell}}$  of the considered shell in two dimensions. In case of a small thickness  $dr$  one obtains  $A_{\text{shell}} = 2\pi r dr$  in a good approximation.  $g(r)$  is stored in a histogram of bin size  $dr$ . Note that  $dr$  needs to be small compared to  $r$ , i.e. small enough to capture all important information, but large enough to obtain sufficient statistics in each bin.

In an ideal gas all distances between particles appear with the same probability such that  $g(r) = 1$ . In a system of hard particles with radius  $R$ , particles are not allowed to overlap such that  $g(r) = 0$  for small distances  $r < 2R$ . The behavior of  $g(r)$  for large distances depends on the configuration. For instance,

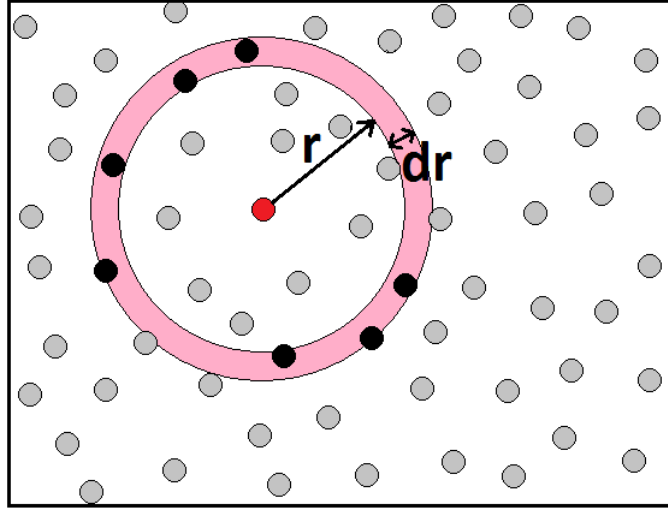


Figure 3.9: Determination of the radial distribution function  $g(r)$ . The black particles lie within a shell of inner radius  $r$  and width  $dr$  around a central particle (red).

in a fluid particles are uncorrelated and  $g(r) = 1$  for large distances  $r \gg 2R$ . Peaks in between reveal the local structure. In an ordered structure, e.g. a crystal or a quasicrystal,  $g(r)$  shows sharp peaks which give the distribution of distances between the particles.

In this thesis we apply  $g(r)$  to determine the positional order of the structures that assemble in our simulations.

### 3.5.2 Structure factor

In order to identify the orientational order or respectively the rotational symmetry of our structures we calculate the structure factor  $S(\mathbf{q})$  in reciprocal space, which is given as a function of the wave vector  $\mathbf{q}$ . The structure factor is defined by  $S(\mathbf{q}) = \frac{1}{N} \langle |\rho(\mathbf{q})|^2 \rangle$  with the Fourier density

$$\rho(\mathbf{q}) = \int_V \rho(\mathbf{r}) \exp(-i\mathbf{q} \cdot \mathbf{r}) d\mathbf{r} = \sum_{i=1}^N \exp(-i\mathbf{q} \cdot \mathbf{r}_i), \quad (3.63)$$

where we applied the local density  $\rho(\mathbf{r}) = \sum_{i=1}^N \delta(\mathbf{r} - \mathbf{r}_i)$  in a system with discrete particle positions  $\mathbf{r}_i$ . Brackets  $\langle \dots \rangle$  denote the ensemble average. Finally, one gets

$$\begin{aligned}
S(\mathbf{q}) &= \frac{1}{N} \langle |\rho(\mathbf{q})|^2 \rangle \\
&= \frac{1}{N} \sum_{i=1}^N \sum_{j=1}^N \langle \exp[-i \mathbf{q} \cdot (\mathbf{r}_i - \mathbf{r}_j)] \rangle \\
&= \frac{1}{N} \left( \sum_{i=1}^N \langle 1 \rangle + \sum_{i=1}^N \sum_{\substack{j=1 \\ j \neq i}}^N \langle \exp[-i \mathbf{q} \cdot (\mathbf{r}_i - \mathbf{r}_j)] \rangle \right) \\
&= 1 + \frac{1}{N} \left\langle \sum_{i=1}^N \sum_{\substack{j=1 \\ j \neq i}}^N \int_V d\mathbf{r} \exp(-i \mathbf{q} \cdot \mathbf{r}) \delta(\mathbf{r} - (\mathbf{r}_i - \mathbf{r}_j)) \right\rangle \\
&= 1 + \rho \int_V g(\mathbf{r}) \exp(-i \mathbf{q} \cdot \mathbf{r}) d\mathbf{r}. \tag{3.64}
\end{aligned}$$

The pair distribution function and the structure factor are, hence, Fourier transforms of each other: The structure factor describes density correlations in reciprocal space.

In the limit of long wavelengths  $\mathbf{q} \rightarrow 0$  long length scales are taken into account and fluctuations in the structure factor occur. It is

$$\lim_{\mathbf{q} \rightarrow 0} S(\mathbf{q}) = \rho k_B T \kappa_T \tag{3.65}$$

with the Boltzmann constant  $k_B$ , temperature  $T$  and isothermal compressibility  $\kappa_T = -\frac{1}{V} \left( \frac{\partial V}{\partial p} \right) |_T$  [327].

### 3.5.3 Angular distribution function

Another tool applied in this thesis to measure the orientational order is the angular distribution function  $g(\phi)$ . It counts how often bond angles between neighboring particles occur and thus shows which bond angles are preferred. It is defined as

$$g(\phi) = \sum_{i=1}^N \sum_{\substack{k \in NN_i \\ l \in NN_{i,k}}} \delta(\phi - \phi_{kl}). \tag{3.66}$$

$NN_i$  describes the nearest neighbors of particle  $i$  and  $NN_{i,k} = NN_i \cap NN_k$ .  $\phi_{kl} = \angle lik$  denotes the angle between the particles  $lik$  (see also [328]).

### 3.5.4 Order parameters and their correlation functions

Positional as well as orientational order of many-particle systems can also be characterized by order parameters and corresponding correlation functions. The latter show a characteristic decay in each phase and thus help to distinguish between phases. Correlation functions are especially useful to investigate phase transitions as done in Chapter 7 in this thesis.

#### Bond-orientational order

With the bond-orientational order parameter a system can be tested for a given symmetry. The complex local  $m$ -fold bond-orientational order parameter of a particle  $j$  at position  $\mathbf{r}_j$  reads [33, 249]

$$\psi_m(\mathbf{r}_j) = \frac{1}{N_k} \sum_{k=1}^{N_k} \exp(im\theta_{jk}). \quad (3.67)$$

The sum runs over all nearest neighbors  $k = 1, \dots, N_k$  of particle  $j$ .  $\theta_{jk}$  is the angle between the bond from particle  $j$  to particle  $k$  and an arbitrary but fixed reference direction, e.g. the  $x$ -axis (see Figure 3.10). A change of the reference axis would result in a rotation of the order parameter but the absolute value remains unchanged.  $m$  is an integer that indicates the symmetry that is tested for, for instance  $\psi_{10}$  and  $\psi_{12}$  detect the orientational order with respect to decagonal and dodecagonal symmetry. In a perfect lattice the bonds of nearest neighbors are restricted to the symmetry directions. Deviations from the symmetry directions lead to a decrease of the order parameter.

The order parameter highly depends on the definition of nearest neighbors [329]. One way is to consider all particles within a cutoff radius  $r_{\text{cut}}$  around particle  $j$  as nearest neighbors of  $j$ . A further method that does not introduce any parameter is based on a Voronoi construction [330], i.e. two particles are said to be nearest neighbors if their Voronoi cells share one side. We usually apply the first method with a cutoff radius that is larger than both length scales present in the quasicrystal in order to ensure that particles at both distances contribute to the order parameter.

The bond-orientational correlation function  $g_m(r)$  gives the correlation between the bond-orientational order parameter of pairs of particles as a function of the distance  $r$  between the particles.  $g_m(r)$  is defined as the average product of the order parameter  $\psi_m$  at position  $\mathbf{r}_i$  and its complex conjugate at position  $\mathbf{r}_j$  [249, 331]:

$$g_m(r) = \langle \psi_m(\mathbf{r}_i) \psi_m^*(\mathbf{r}_j) \rangle. \quad (3.68)$$

The average is taken over different pair positions with the same distance and over configurations. The imaginary part of the bond-orientational correlation function

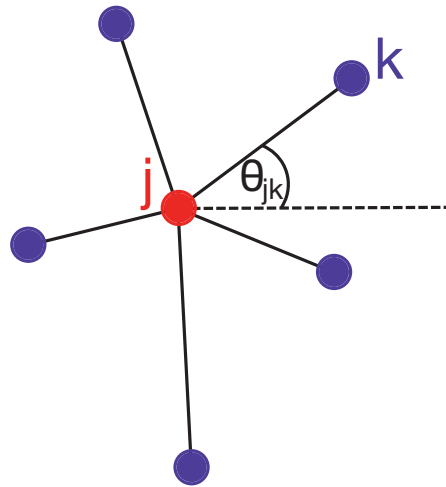


Figure 3.10: Definition of the angle  $\theta_{jk}$  between nearest neighbor particles. The outer particles (blue) are said to be nearest neighbors of the inner particle (red). The bond between two particles  $j$  and  $k$  and a reference axis (the  $x$ -axis in our illustration) defines the angle  $\theta_{jk}$  between the two particles. Note that the illustrated bonds do not represent chemical bonds.

cancels out within a pair of particles.

### Positional order

Similarly, the positional order can be measured by means of the positional order parameter

$$\rho_{\mathbf{G}}(\mathbf{r}) = \exp(i\mathbf{G} \cdot \mathbf{r}) \quad (3.69)$$

with a chosen wave vector  $\mathbf{G}_j$  of the reciprocal lattice.

The positional correlation function is defined as the average product

$$\begin{aligned} g_{\mathbf{G}}(r) &= \langle \rho_{\mathbf{G}}(\mathbf{r}_i) \rho_{\mathbf{G}}^*(\mathbf{r}_j) \rangle \\ &= \langle \exp[i\mathbf{G} \cdot (\mathbf{r}_i - \mathbf{r}_j)] \rangle. \end{aligned} \quad (3.70)$$

For symmetry reasons the imaginary part cancels out within a pair of particles at positions  $\mathbf{r}_i$  and  $\mathbf{r}_j$  and the resulting correlation function only consists of a real part.

### 3.5.5 Selective density wave analysis for dislocation detection

In periodic crystals it is often possible to recognize defects by regarding the arrangements of particles in real space. In quasicrystals it is usually difficult to observe defects in real space due to the lack of translational order.

We illustrate a method previously used by Korkidi *et al.* [332] to identify and analyze dislocations in quasiperiodic patterns (see Section 2.6 for a definition of dislocations). With the method dislocations can be made visible by illustrating individual density modes.

Due to the discrete diffraction pattern of crystals or quasicrystals one can express the density field  $\rho(\mathbf{r})$  as a sum of partial waves with the wave vectors  $\mathbf{G}_j$ , i.e. the complete density field  $\rho(\mathbf{r})$  is given by a superposition of single density modes [9, 61, 333]

$$\rho(\mathbf{r}) = \sum_{j=1}^n \rho_j \exp(-i\mathbf{G}_j \cdot \mathbf{r}). \quad (3.71)$$

The coefficients read  $\rho_j = |\rho_j| \exp(i\phi_j)$  with phases  $\phi_j$  (see also Subsection 2.5.1). We choose  $n$  symmetric wave vectors in order to describe a system with  $m$ -fold rotational symmetry. Here,  $m = n$  if  $n$  is even and  $m = 2n$  if  $n$  is odd. Note that only  $D$  wave vectors are linearly independent, where  $D$  is the rank of the system. Appropriate phases and wave vectors are specified in Section 4.2.

In order to obtain a single density mode,  $\rho(\mathbf{r})$  is transformed into Fourier space by

$$\tilde{\rho}(\mathbf{q}) = \sum_{\mathbf{r}} \rho(\mathbf{r}) \exp(i\mathbf{q} \cdot \mathbf{r}). \quad (3.72)$$

The process is illustrated in Figure 3.11 (a) using the example of a structure with decagonal order and a systematically incorporated dislocation pair (data obtained by Johannes Hielscher). The positions of the particles are shown in the main Figure, while the inset depicts the Fourier transform in reciprocal space. Bragg peaks appear where  $\mathbf{q}$  corresponds to a wave vector  $\mathbf{G}_j$  or a linear combination of several wave vectors. We filter out small regions around a Bragg peak  $\tilde{\rho}(\mathbf{G}_j)$  and its opposite  $\tilde{\rho}(-\mathbf{G}_j)$  (see insets of Figures 3.11 (b)-(f)).  $\tilde{\rho}(\mathbf{q})$  is set to zero in the remaining image. The inverse Fourier transform of the selected peaks provides the single density mode with wave vector  $\mathbf{G}_j$  in real-space (see Figures 3.11 (b)-(f)). The graphical illustration of a density mode is referred to as Bragg contrast image. In case of no dislocations, all density modes are composed of regular stripes. Dislocations are identified by discontinuities in the stripe pattern in the form of interrupted lines in certain Bragg contrast images, e.g. in Figures 3.11 (b)-(e) in our example.

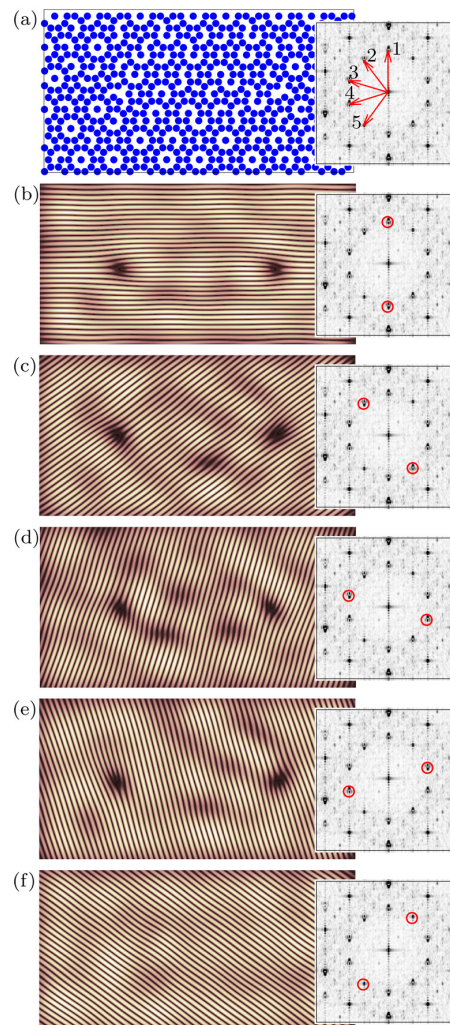


Figure 3.11: (a) Structure with decagonal order and a systematically incorporated pair of dislocations. The data for the positions of the particles are obtained by Johannes Hielscher who did the synthesis of the structure in hyperspace. The inset depicts the Fourier density  $\tilde{\rho}(\mathbf{q})$  in reciprocal space. The inner ring consists of ten symmetrically arranged Bragg peaks. The red arrows indicate the respective mode directions. (b)-(f) Single density modes obtained from inverse Fourier transforms of filtered regions around opposite Bragg peaks as depicted by red circles in the insets. Note that we plot the absolute value of the density modes such that in our illustrations the lines split up into three lines at the positions of a dislocation.

In order to analyze a dislocation quantitatively one can determine its Burgers vector  $\mathbf{b}$  on the basis of several Bragg contrast images with wave vectors in different directions. A detailed description is found in [247, 332].

Generally, the method cannot only be applied to athermal structures with sharp diffraction peaks, but also to structures with finite temperatures. In the latter case, the Bragg peaks are not well-defined but rather diffuse. The density modes depend on the size of the filtered areas which needs to be adopted appropriately to get the required information [332].

Note that isolated phasonic flips are hard to identify by Fourier mode analysis. Although they cause a local disorder compared to the perfect tiling the global order of the structure is not affected significantly [247].

# Chapter 4

## Colloids in two-dimensional quasicrystalline laser fields

Colloids as mesoscopic model systems are well-suited for predicting properties of atomic systems (see Section 2.7). Beside internal interactions between colloids that can influence the order and dynamics of the structures, also external fields can have an impact. For instance, in external light fields colloids are forced towards the highest light intensity [25, 26].

In this Chapter we investigate the arrangements and dynamics of colloidal particles in quasiperiodic interference patterns induced by laser beams. The setup was initially applied in experiments by Burns *et al.* [334] and picked up by Mikhael *et al.* [7, 129, 130]. Similar experimental and numerical studies followed [11, 12, 27, 126, 335]. Aside from colloidal suspensions, also liquid crystals [325], photosensitive materials [141, 142] or systems of cold atoms [135–137, 336–338] can arrange to quasicrystalline structures induced by interference patterns.

A great advantage of light-induced quasicrystals is the possibility of activating specific phasonic displacements by tuning the phases of the laser beams appropriately (see, e.g. [11, 12, 27]). In previous studies [11, 12] colloidal trajectories in two-dimensional quasicrystals with rank  $D = 4$  were predicted when a phasonic drift was applied. Therefore, the colloids were mapped inside characteristic areas of phononic and phasonic displacements which are similar to unit cells in periodic crystals. Here, we employ the method to determine the stability of colloids in quasicrystals with rank  $D = 4$  against phasonic perturbations. Furthermore, we predict colloidal trajectories in quasicrystals with rank  $D = 6$  in the presence of phasonic drifts.

The Chapter is organized as follows: In Section 4.1 we introduce optical tweezing – a method to confine particles by laser beams. In Section 4.2 interference patterns that induce quasiperiodic arrangements of colloids in the plane are described. In the following Sections 4.3 and 4.4 we present our studies concerning the stability

and trajectories of colloids exposed to phasonic displacements. The Chapter is finished with a conclusion in Section 4.5.

Parts of the investigations presented in this Chapter are reproduced with permission from our publication [A] or respectively our manuscript [F] which is accepted for publication. A detailed statement about the concerned Sections and the contributions of the authors is given in the *List of publications*.

## 4.1 Optical tweezing

Optical tweezing is a method to confine particles with the help of light [339]. For instance, colloids in charge stabilized colloidal suspensions feel a force towards the maximal light intensity when exposed to a laser beam. The effect was firstly investigated by Arthur Ashkin in 1970 [25]. Nowadays, optical tweezing is a tool that is widely used in physics, chemistry and biology to manipulate particles without mechanical influence. In 2018 the Nobel Prize in physics was granted “for groundbreaking inventions in the field of laser physics”. One half was awarded to Arthur Ashkin “for the optical tweezers and their application to biological systems” [340].

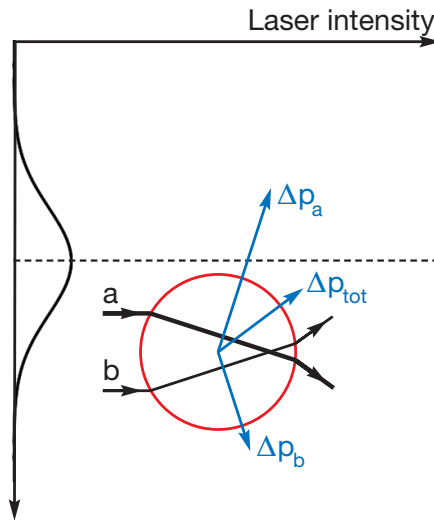


Figure 4.1: Momentum transfer from light rays to a colloid. A colloid (red circle) is located beside the center of a laser beam. The intensity profile is illustrated on the left. The light intensity increases towards the center of the beam, i.e. ray *a* carries more light than ray *b*. The transferred momenta (blue) and the resulting forces on the colloid increase near the beam focus. The total transferred momentum  $\Delta p_{tot}$  is the sum of the transferred momenta of all rays and is directed towards the beam focus.

For colloids that are larger than the wavelength of the incoming light, optical tweezing can be explained with ray optics. In Figure 4.1 we suppose a laser beam with a Gaussian intensity profile. The beam encounters a colloidal suspension in which the refraction index of the colloids  $n_1$  is larger than the one of the dispersion medium  $n_2$ . The light rays first penetrate and then leave a colloid. Reflections at the interfaces are neglected in our illustration. When passing the colloid, the light rays are refracted which causes a change of momenta in direction and magnitude. The momentum in the colloid and in the suspension – denoted by  $p_1$  and  $p_2$  – is given by  $p_i = \frac{E}{c}n_i$ , ( $i \in \{1, 2\}$ ), where  $E = h\nu$  is the energy of the beam.  $h$  denotes Planck's constant and  $\nu$  the frequency of the light beam.  $c$  gives the velocity of light. Due to momentum conservation the difference  $\Delta\mathbf{p} = \mathbf{p}_{\text{in}} - \mathbf{p}_{\text{out}}$  of the momentum of the incoming and outgoing rays is transferred to the colloid. In a Gaussian laser profile the laser intensity is largest in the center of the beam. Accordingly, the colloid is driven with a total force  $\mathbf{F} = \frac{d\mathbf{p}}{dt}$  in the direction of the maximal light intensity. These optical forces are in the range of Pico- to Nanonewton. The component in the direction of the light is called axial force and is also present in plane waves. The total perpendicular component gives the gradient force which makes the colloids move towards the center of the beam.

## 4.2 Quasicrystalline interference patterns

Interfering laser beams cause interference patterns in the plane. In the case of  $n = 5$  or  $n \geq 7$  symmetrically arranged laser beams quasicrystalline patterns form [7, 8, 11, 27, 125–127, 129, 130]. In Figure 4.2 we depict twelve laser beams that effect an interference pattern with dodecagonal rotational symmetry in the plane. In the following we derive the intensity distribution and the corresponding potential of an interference pattern created by  $n$  laser beams (see also [325, 341]): The electric field  $\mathbf{E}_j(\mathbf{r})$  of a single laser beam propagates with a polarization  $\mathbf{E}_{0j}$  and a phase  $\phi_j$  in the direction of the wave vector  $\mathbf{G}_j$ , i.e.

$$\begin{aligned}\mathbf{E}_j(\mathbf{r}) &= \mathbf{E}_{0j} \Re\{\exp[i(\mathbf{G}_j \cdot \mathbf{r} + \phi_j - \omega t)]\} \\ &= \mathbf{E}_{0j} \cos[\mathbf{G}_j \cdot \mathbf{r} + \phi_j - \omega t].\end{aligned}\tag{4.1}$$

$\mathbf{r} = (x, y)$  denotes the position. The temporal evolution is given by  $\omega t$  where  $\omega$  is the circular frequency of the light. The total electric field of  $n$  interfering laser beams is given by the sum of the electric fields of all laser beams:

$$\mathbf{E}(\mathbf{r}) = \sum_{j=0}^{n-1} \mathbf{E}_{0j} \cos[\mathbf{G}_j \cdot \mathbf{r} + \phi_j - \omega t].\tag{4.2}$$

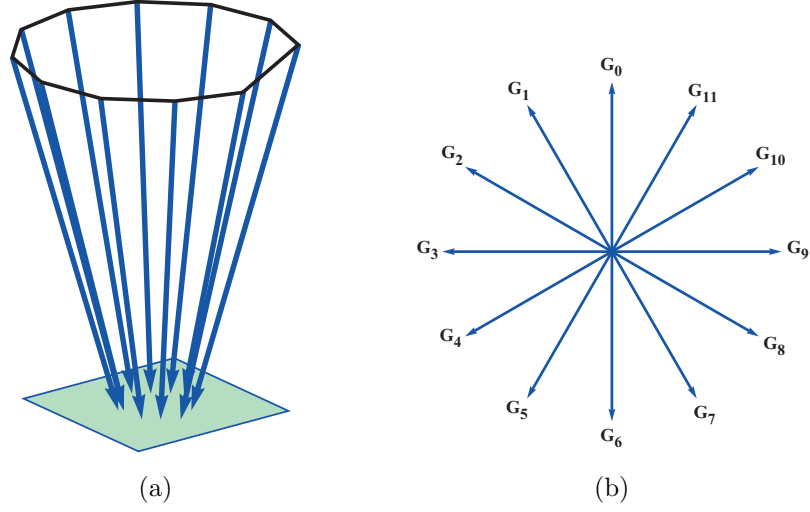


Figure 4.2: (a) Arrangement of twelve laser beams that create an interference pattern with dodecagonal symmetry. The beams are set symmetrically around the direction normal to the sample plane. The opening angle between a beam and the normal direction is small. The arrows depict the wave vectors of the laser beams. All beams have the same polarization. (b) The lattice vectors  $\mathbf{G}_j$  with  $j = 0, \dots, 11$  correspond to the wave vectors projected onto the sample plane. Similar settings are shown by Schmiedeberg *et al.* [8, 125] for five laser beams.

The intensity  $I(\mathbf{r})$  of the resulting interference pattern is proportional to the squared total electric field averaged over time. The average is taken over one oscillation period  $T = 2\pi/\omega$  of the oscillating pattern, i.e.

$$\begin{aligned}
 I(\mathbf{r}) &\propto \int_0^T dt \left\{ \sum_{j=0}^{n-1} \mathbf{E}_{0j} \cos[\mathbf{G}_j \cdot \mathbf{r} + \phi_j - \omega t] \right\}^2 \\
 &= \int_0^T dt \sum_{j=0}^{n-1} \sum_{k=0}^{n-1} \mathbf{E}_{0j} \cdot \mathbf{E}_{0k} \cos[\mathbf{G}_j \cdot \mathbf{r} + \phi_j - \omega t] \cos[\mathbf{G}_k \cdot \mathbf{r} + \phi_k - \omega t] \\
 &\propto \int_0^T dt \sum_{j=0}^{n-1} \sum_{k=0}^{n-1} \mathbf{E}_{0j} \cdot \mathbf{E}_{0k} \{ \cos[(\mathbf{G}_j + \mathbf{G}_k) \cdot \mathbf{r} + \phi_j + \phi_k - 2\omega t] \\
 &\quad + \cos[(\mathbf{G}_j - \mathbf{G}_k) \cdot \mathbf{r} + \phi_j - \phi_k] \} \\
 &\propto \sum_{j=0}^{n-1} \sum_{k=0}^{n-1} \mathbf{E}_{0j} \cdot \mathbf{E}_{0k} \cos[(\mathbf{G}_j - \mathbf{G}_k) \cdot \mathbf{r} + \phi_j - \phi_k] + const \tag{4.3}
 \end{aligned}$$

From the second to the third line we used the addition theorem  $\cos(x)\cos(y) = [\cos(x+y) + \cos(x-y)]/2$ . Within integration the first term cancels out.

In the following we assume identical polarizations of all beams, which can be realized most easily in experiments. In the limit of vanishing opening angles  $\theta$  between the beams and the normal direction, i.e.  $\theta \rightarrow 0$ , the intensity pattern possesses perfect rotational symmetry and the corresponding laser potential reads [8, 125, 325]

$$V(\mathbf{r}) = -\frac{V_0}{n^2} \sum_{j=0}^{n-1} \sum_{k=0}^{n-1} \cos[(\mathbf{G}_j - \mathbf{G}_k) \cdot \mathbf{r} + \phi_j - \phi_k]. \quad (4.4)$$

$V_0$  denotes the potential strength and it is  $V(\mathbf{r}) = -V_0$  at the place of the deepest minimum [8, 126].

To underline the symmetry we choose  $n$  symmetric wave vectors as shown in Figure 4.2. Their projections onto the sample plane read

$$\mathbf{G}_j = (2\pi/a_V \cos[2\pi j/n], 2\pi/a_V \sin[2\pi j/n]), \quad j = 0, \dots, (n-1) \quad (4.5)$$

with the length scale of the potential  $a_V = 2\pi/|\mathbf{G}_j|$ . Note that only  $D$  of the wave vectors are linear independent, where  $D$  denotes the rank of the structure (see Section 2.4).

The phases  $\phi_j$  of the laser beams are parameterized according to the phononic and phasonic variables. In case of quasicrystals with rank  $D = 4$  the parameterization of the phases reads [9, 12]

$$\phi_j = \mathbf{G}_j \cdot \mathbf{u} + \mathbf{G}_{kj \bmod N} \cdot \mathbf{w} + \gamma/n. \quad (4.6)$$

$\mathbf{G}_{kj \bmod N} = \mathbf{G}_j^\perp$  denote the wave vectors in perpendicular space and need to fulfill the relation  $\sum_j G_{jp} G_{jq}^\perp = 0$  [234] with  $p, q \in \{x, y\}$  describing the components of the respective vectors. A possible choice for the parameter  $k$  is  $k = 3$  for  $n = 5$  or  $n = 8$  laser beams and  $k = 5$  for  $n = 12$  beams. The vector  $\mathbf{u} = (u_x, u_y)$  describes the phononic displacement and  $\mathbf{w} = (w_x, w_y)$  the phasonic displacement. Quasicrystals with  $D > 4$  possess more phasonic variables. A possible parameterization of the phases of a quasicrystal with rank  $D = 6$  is given in [13] where we investigate quasicrystals with 14-fold rotational symmetry. Phases different from zero can lead to phasonic excitations. In contrast to  $\mathbf{u}$  and  $\mathbf{w}$  the global phase  $\gamma$  is no hydrodynamic variable and does not have an influence on the interference pattern. We choose  $\gamma = 0$ .

In Figure 4.3 we illustrate potential landscapes  $V(\mathbf{r})$  with various crystalline and quasicrystalline symmetries. Minima in the potential appear blue or yellow, larger values are depicted in red. Note that the symmetry of the interference pattern in two dimensions has to be even. I.e., when  $n$  laser beams are applied the resulting interference pattern possesses  $m$ -fold rotational symmetry, where  $m = 2n$  when  $n$  is odd and  $m = n$  when  $n$  is even [12, 234].

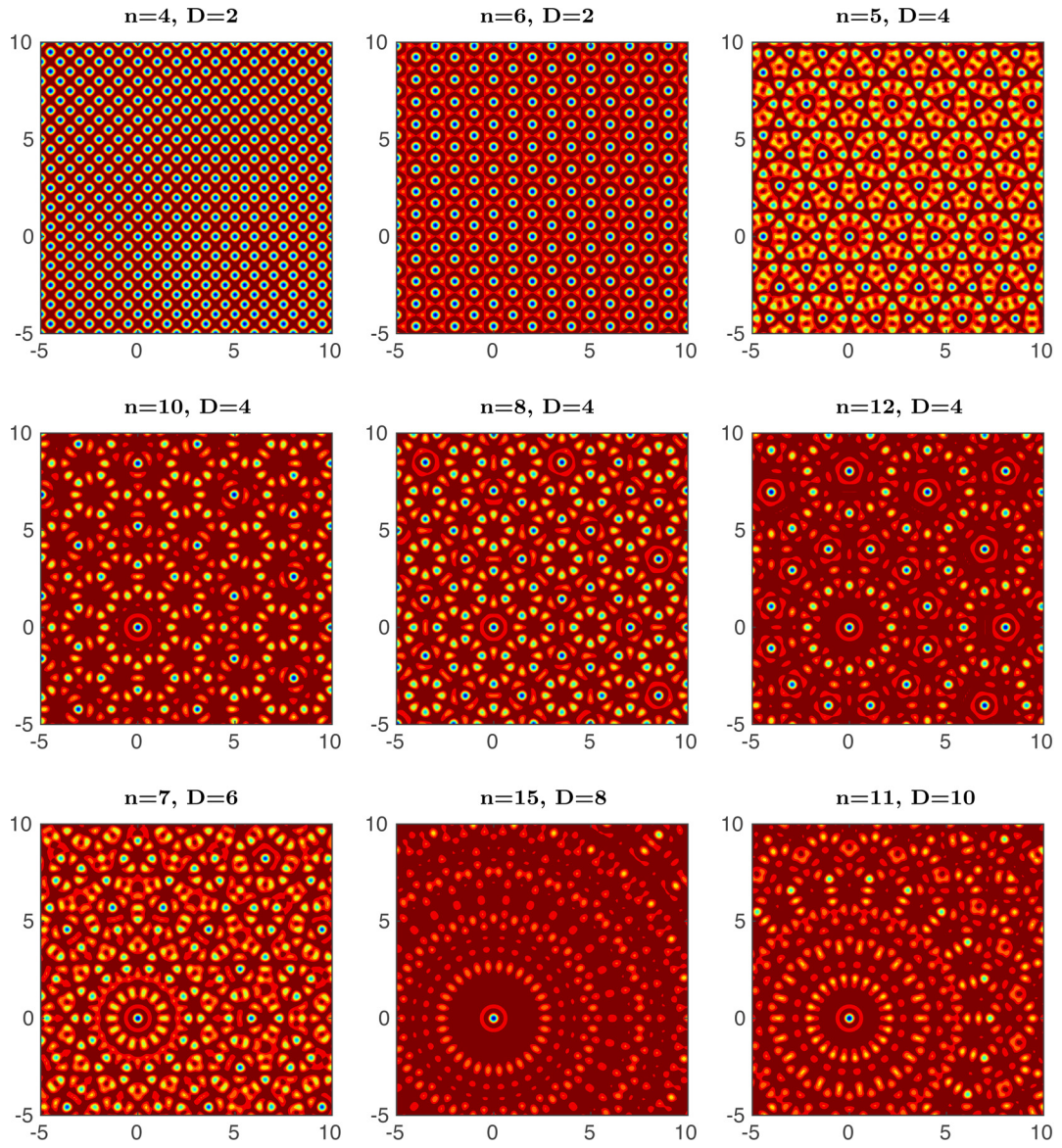


Figure 4.3: Potential landscapes  $V(\mathbf{r})$  created by various numbers  $n$  of laser beams. The phases are set to zero. In all pictures there is a global symmetry center at the origin where all laser beams are completely in phase. The Figures are sorted ascending in their rank  $D$ . The length scales in  $x$ - and  $y$ -direction correspond to  $a_V = 2\pi/G$ .

So far we have investigated continuous potential landscapes. In this work we additionally study quasicrystalline arrangements of colloids at discrete positions. For the synthesis we put colloids inside the continuous two-dimensional potential landscapes. In case of potential strengths that are much larger than the thermal energy of the particles, i.e.  $V_0 \gg k_B T$ , all colloids are located in the local potential minima [7, 12]. The arrangements of particles possess the symmetry prescribed by the light fields.

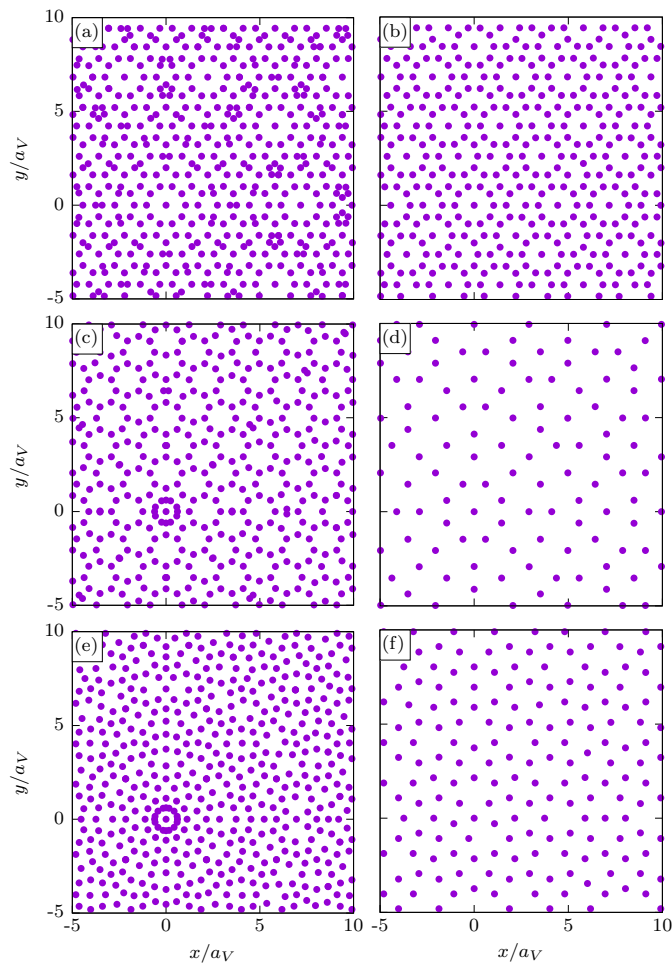


Figure 4.4: Arrangements of colloids in laser fields with  $\phi_j = 0$ . The fields provide (a) and (b) decagonal, (c) and (d) octagonal and (e) and (f) dodecagonal symmetry. Left column: All potential minima are filled with colloids. Right column: Only certain minima are occupied which results in (b) a Tuebingen tiling, (d) an Ammann-Beenker tiling and (f) a shield tiling. The criteria which minima are occupied are described in the following Section.

In Figure 4.4 we illustrate discrete colloidal positions in a decagonal, a dodecagonal and an octagonal potential landscape. In each case we show the positions when all potential minima are occupied in the left column, while in the right column we exclusively occupy the minima that lead to a typical tiling, i.e. a Tuebingen tiling, a shield tiling and an Ammann-Beenker tiling.

Note that the interference patterns of laser beams look similar to the density field  $\rho(\mathbf{r})$  (see equation 2.15 in Subsection 2.5.1). In laser fields the colloids occupy most likely the potential minima, while in a density field colloids are assigned to the maxima [12].

### 4.3 Stability of particles in two-dimensional quasicrystals against phasonic perturbations

In this Section we investigate colloids in two-dimensional quasicrystalline interference patterns created by interfering laser beams. By tuning the phases of the laser beams individually it is possible to change the phasonic displacement in a controlled way [11–13, 27, 126]. We study the stability of single colloids in two-dimensional quasicrystalline potentials under the influence of phasonic perturbations. We map all particles into characteristic areas, and find that particles close to the edges of these areas already flip for small perturbations, while particles close to the center are most stable.

We present our studies in the following way: First, we define and calculate characteristic displacements and characteristic areas. Second, a general method is explained how we obtain for each particle the phasonic displacement required for a flip. Third, we employ decagonal, dodecagonal and octagonal structures and illustrate the phasonic displacements in  $x$ -,  $y$ - and arbitrary directions that are needed to make the particles flip.

#### 4.3.1 Characteristic displacements and characteristic areas

In a periodic crystal, many properties can be deduced from a single unit cell [56, 342]. When the properties inside the unit cell are known one can draw conclusions to the properties of the whole crystal.

In quasicrystals, a unit cell does not exist due to the lack of translational symmetry. However, it is possible to define characteristic areas for phononic and phasonic displacements which are comparable to unit cells in periodic crystals. In recent works [11, 12] the authors present a method to determine characteristic areas in light-induced quasicrystals with rank  $D = 4$ . Characteristic phononic and phasonic displacements  $\Delta\mathbf{u}$  and  $\Delta\mathbf{w}$  that do not change the potential are introduced. By employing appropriate combinations of  $\Delta\mathbf{u}$  and  $\Delta\mathbf{w}$ , every particle within the

quasicrystal can be mapped inside the characteristic areas.

In the following we determine the characteristic displacements and characteristic areas of quasicrystals with decagonal, dodecagonal and octagonal rotational symmetry. The calculations are in accordance with recent works [11, 12].

### Determination of the characteristic displacements

Characteristic displacements are combinations of phononic and phasonic displacements  $\Delta\mathbf{u}$  and  $\Delta\mathbf{w}$  that do not change the laser potential  $V(\mathbf{r})$  given in equation (4.4), i.e.  $V_{\mathbf{w}+\Delta\mathbf{w}}(\mathbf{r} + \Delta\mathbf{u}) = V_{\mathbf{w}}(\mathbf{r})$ . Here,  $V_{\mathbf{w}}(\mathbf{r})$  denotes a potential at position  $\mathbf{r}$  with phasonic displacement  $\mathbf{w}$ . In  $V_{\mathbf{w}+\Delta\mathbf{w}}(\mathbf{r} + \Delta\mathbf{u})$  additional phononic and phasonic displacements are included.

We limit the directions of the characteristic displacements to the symmetry axes such that

$$\begin{aligned}\Delta\mathbf{u}_j &= (u_r \cos[2\pi j/m], u_r \sin[2\pi j/m]) \quad \text{and} \\ \Delta\mathbf{w}_j &= (w_r \cos[2\pi k j/m], w_r \sin[2\pi k j/m])\end{aligned}\tag{4.7}$$

with  $j = 1, \dots, m$ . Then,  $\Delta\mathbf{u} = \sum_j \Delta\mathbf{u}_j$  and  $\Delta\mathbf{w} = \sum_j \Delta\mathbf{w}_j$ . The value of  $k$  depends on the parameterization of the phases (see equation (4.6)). The step lengths  $u_r$  and  $w_r$  have to be chosen appropriately such that the displacements do not alter the potential. Possible values for  $u_r$  and  $w_r$  are given in table 4.1, where  $n_1$  and  $n_2$  denote integer numbers.

symmetry	decagonal	dodecagonal	octagonal
$u_r/a_V$	$\frac{2}{5}n_1 + \left(\frac{1}{5} + \frac{1}{\sqrt{5}}\right)n_2$	$n_1 + \frac{1}{\sqrt{3}}n_2$	$\frac{1}{2}n_1 + \frac{1}{\sqrt{2}}n_2$
$w_r/a_V$	$\frac{2}{5}n_1 + \left(\frac{1}{5} - \frac{1}{\sqrt{5}}\right)n_2$	$n_1 - \frac{1}{\sqrt{3}}n_2$	$\frac{1}{2}n_1 - \frac{1}{\sqrt{2}}n_2$

Table 4.1: Possible step lengths  $u_r$  and  $w_r$  of phononic and phasonic displacements in quasicrystals with decagonal, dodecagonal and octagonal symmetry.  $n_1$  and  $n_2$  denote integer numbers. A similar table is found in [12].

With the resulting characteristic displacements a colloid which is located at position  $\mathbf{r}$  in a potential  $V_{\mathbf{w}}(\mathbf{r})$  can be mapped onto a particle with reduced position  $\mathbf{r}^{(\text{red})} = \mathbf{r} - \Delta\mathbf{u}$  in a potential  $V_{\mathbf{w}^{(\text{red})}}(\mathbf{r}^{(\text{red})})$  with the reduced phasonic displacement  $\mathbf{w}^{(\text{red})} = \mathbf{w} + \Delta\mathbf{w}$ . The properties of a particle with reduced position and reduced phasonic displacement are the same as for the particle in real space. When mapping the particle as close to the origin in the  $u_x$ - $u_y$ - $w_x$ - $w_y$ -space as possible, the reduced values are located inside so-called characteristic areas. We illustrate

the mapping procedure in the next Subsection 4.3.2 and Figure 4.5.

### Determination of the characteristic areas

We consider a two-dimensional subspace that is spanned by a selected phononic direction  $\mathbf{e}_j = (\cos[2\pi j/m], \sin[2\pi j/m])$  and its phasonic counterpart  $\mathbf{e}_j = (\cos[2\pi k j/m], \sin[2\pi k j/m])$ . Rectangles of the side lengths  $\delta u$  and  $\delta w$  that fill the whole subspace when shifted about  $\Delta \mathbf{u}_j$  in phononic direction and  $\Delta \mathbf{w}_j$  in phasonic direction determine the sizes of the characteristic areas, because the potential remains unchanged after a simultaneous shift about  $\Delta \mathbf{u}_j$  and  $\Delta \mathbf{w}_j$ .  $\delta u$  and  $\delta w$  are termed characteristic intervals. For symmetry reasons we obtain the same values of  $\delta u$  and respectively  $\delta w$  for each subspace. The characteristic intervals are listed in table 4.2.

symmetry	decagonal	dodecagonal	octagonal
$\delta u/2a_V$	$\frac{1+\sqrt{5}}{10}$	$\frac{1}{2}$	$\frac{1}{2\sqrt{2}}$
$\delta w/2a_V$	$\frac{1+\sqrt{5}}{10}$	$\frac{1}{2} \left(1 + \frac{1}{\sqrt{3}}\right)$	$\frac{1}{2} \left(\frac{1}{2} + \frac{1}{\sqrt{2}}\right)$

Table 4.2: Characteristic intervals  $\delta u$  and  $\delta w$  in quasicrystals with decagonal, dodecagonal and octagonal symmetry. A similar table is found in [12].

Considering all symmetry directions we get the characteristic areas in the form of polygons. The reduced values  $\mathbf{r}^{(\text{red})}$  and  $\mathbf{w}^{(\text{red})}$  are located inside these polygons around the origin with

$$|\mathbf{r}^{(\text{red})} \cdot \mathbf{e}_j| \leq \frac{\delta u}{2a_V} \quad \text{and} \quad |\mathbf{w}^{(\text{red})} \cdot \mathbf{e}_j| \leq \frac{\delta w}{2a_V}. \quad (4.8)$$

Characteristic areas of a decagonal quasicrystal are exemplarily depicted in Figure 4.5.

### 4.3.2 Determination of phasonic displacements required for phasonic flips

Phasonic displacements in laser fields cause a redistribution of the potential minima and hence phasonic flips of the colloids. In the following we consider laser fields initially without phasonic displacements. We make use of a method also described in my master thesis [343] to determine the minimal amplitude of phasonic fluctuations that are required for phasonic flips of the colloids.

First we employ numerical simulations to calculate combinations of characteristic displacements that map the particles inside the characteristic areas. As the characteristic displacements proceed along the symmetry directions, colloids on a symmetry axis can usually be mapped inside the characteristic areas by displacements in only one direction. For particles that are not positioned on a symmetry axis we need displacements in different directions to reach the characteristic areas. I.e., we apply appropriate combinations of two characteristic displacements  $\Delta \mathbf{u}_i$  and  $\Delta \mathbf{w}_i$  and respectively  $\Delta \mathbf{u}_j$  and  $\Delta \mathbf{w}_j$  in different directions. In Figure 4.5 we illustrate the mapping on the example of a system with decagonal symmetry. Figure 4.5 (a) depicts colloids in real space, while Figures 4.5 (b) and (c) show the reduced positions and reduced phasonic displacements of the colloids within the characteristic areas. The characteristic areas are provided by blue decagons.

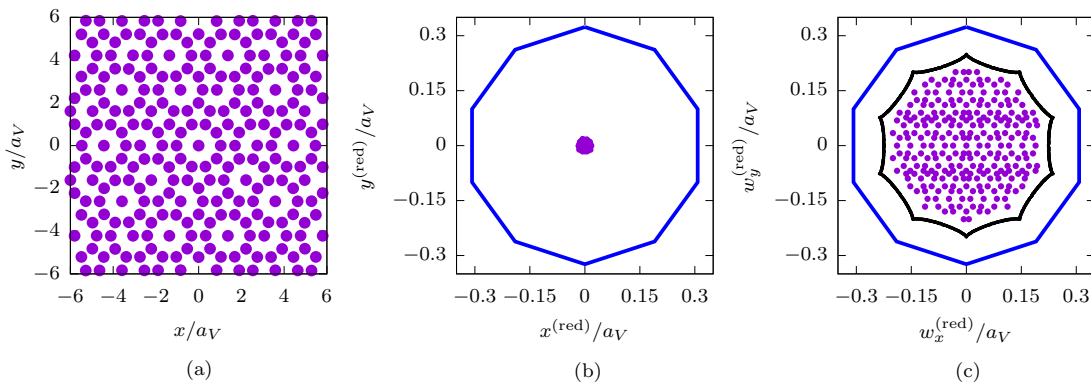


Figure 4.5: (a) Discrete positions of colloids inside a decagonal laser field in real space. (b) Reduced positions and (c) reduced phasonic displacements of the colloids shown in (a). The blue decagons depict the characteristic areas. The black borders in (c) mark the values of the reduced phasonic displacement at which the corresponding particle in real space flips.

In order to determine phasonic displacements that are required for phasonic flips we consider the diagram of reduced phasonic displacements  $\mathbf{w}^{(\text{red})}$  (see Figure 4.5 (c) in case of a decagonal quasicrystal). The reduced phasonic displacements are inside the characteristic area colored in blue. Furthermore, there is a black decagon inside the characteristic area. When  $\mathbf{w}^{(\text{red})}$  of a certain particle is increased so far that the black border is reached, then the particle in real space performs a phasonic flip. Since a change of  $\mathbf{w}^{(\text{red})}$  corresponds to a change of  $\mathbf{w}$  in real space, the distance of  $\mathbf{w}^{(\text{red})}$  to the black border corresponds to the phasonic displacement in real space at which the corresponding particle flips.

The black border is obtained as in [11, 12]: We consider a particle at the origin and increase the phasonic displacement. Recording the values at which the particle flips for phasonic displacements in all directions provides the black borders.

### 4.3.3 Distribution of flipping colloids dependent on the phasonic displacement

In the following we illustrate the distributions of flipping particles dependent on the phasonic displacement in quasicrystals with decagonal, dodecagonal and octagonal symmetry. We apply phasonic displacements in  $x$ -,  $y$ - and arbitrary directions, i.e. the minimal required displacement is given by the minimal distance of  $\mathbf{w}^{(\text{red})}$  to the black border in  $x$ -,  $y$ - and arbitrary direction. The minimal phasonic displacement can also be interpreted as the minimal amplitude of a phasonic fluctuation.

#### Decagonal quasicrystals

In Figure 4.6 we depict the distribution of flipping particles dependent on the phasonic displacement in a perfect Tuebingen tiling of  $N = 2728$  particles. The tiling is obtained by occupying exclusively minima with  $V(\mathbf{r}) < -0.4 V_0$  with colloids. In the left column of Figure 4.6 we illustrate the reduced phasonic displacements  $\mathbf{w}^{(\text{red})}$ . As in Figure 4.5 (c) the black lines indicate the values at which a particle flips. The color code gives the minimal distance to the borders in (a)  $x$ -direction, (c)  $y$ -direction and (e) arbitrary direction. In the right column of Figure 4.6 the positions of the particles in real space are shown with the same color code indicating the required amplitudes of fluctuations in (b)  $x$ -direction, (d)  $y$ -direction and (f) arbitrary direction.

All particles need a finite phasonic amplitude for a flip. Particles in symmetry centers, i.e. central particles surrounded by a ring of ten particles, need high amplitudes to flip because the potential minima in the symmetry centers are deepest. The deeper the minimum is, the higher must be the amplitude of the phasonic fluctuation to make the minimum disappear and the corresponding particle slide into a new minimum. We refer to these particles as stable. Dependent on the direction of the fluctuation there are further stable particles. For fluctuations in  $x$ -direction stable particles are arranged on angular lines in symmetry directions, while for fluctuations in  $y$ -direction stable particles are located on horizontal lines. In between we observe lines of particles that flip at small phasonic displacements. Those particles are unstable against phasonic perturbations. Since fluctuations in  $x$ -direction proceed along a symmetry direction and fluctuations in  $y$ -direction are between two symmetry directions, we obtain different distributions of required amplitudes in both cases. In the case of phasonic fluctuations in arbitrary directions most particles already flip at smaller amplitudes compared to fluctuations in  $x$ - and respectively  $y$ -direction because the distance to the border in any arbitrary direction is always smaller or equal to the distance in a fixed direction. Only the particles in the symmetry centers are stable.

We now quantitatively determine the fraction  $n_{\text{flip}} = N_{\text{flip}}/N$  of particles that

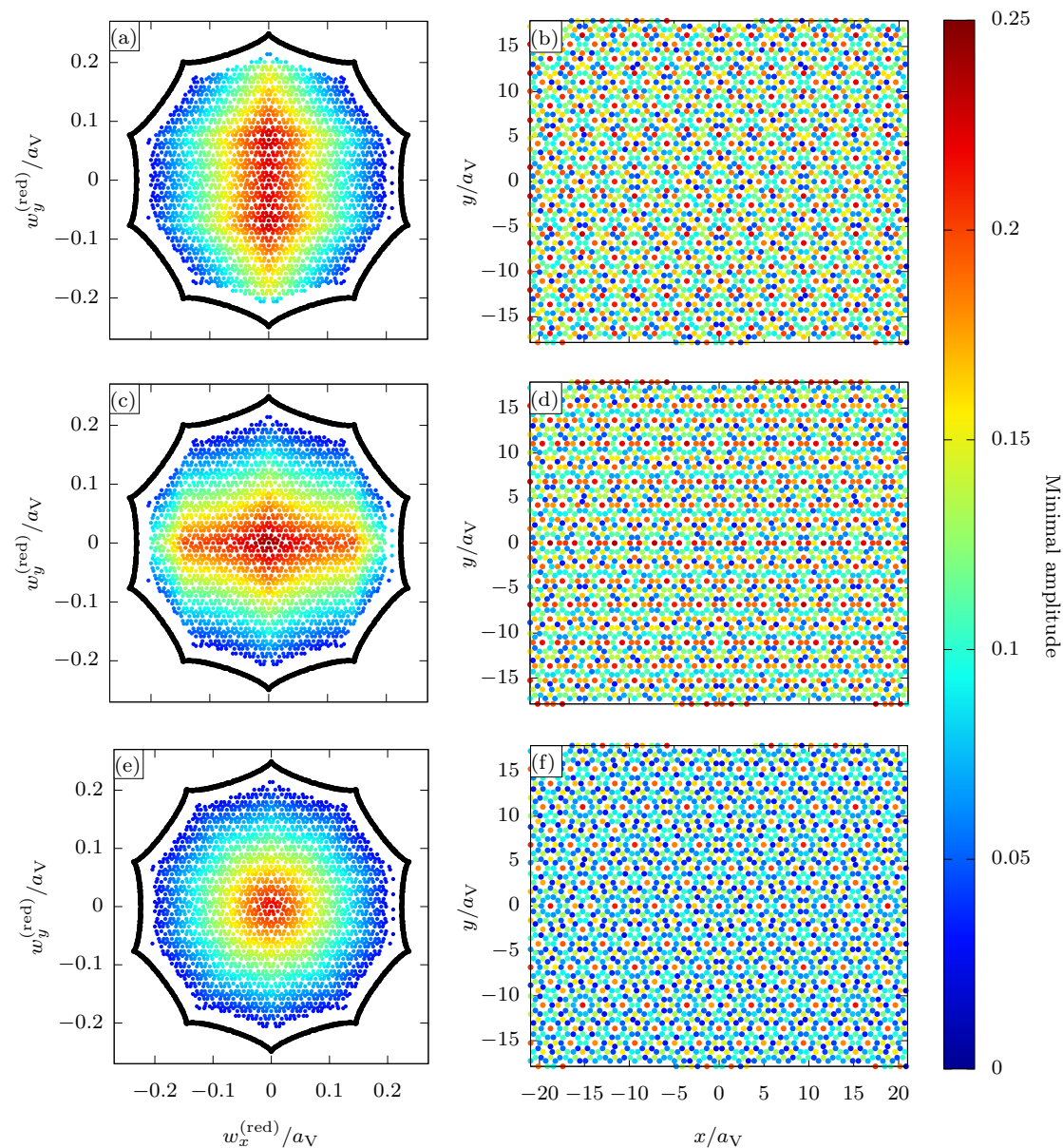


Figure 4.6: (a),(c) and (e) Reduced phasonic displacements of  $N = 2728$  particles in a decagonal Tübingen tiling. The black borders indicate the values of phasonic displacements at which particles flip. The colors reveal the minimal amplitude of the phasonic fluctuation in (a)  $x$ -direction, (c)  $y$ -direction and (e) arbitrary direction that is needed for a flip of the corresponding particle. (b),(d) and (f) Corresponding particles in real space with the same color code.

flip as a function of the applied amplitude.  $N_{\text{flip}}$  denotes the number of flipping particles in our test system of  $N$  particles. The results are presented in Figure 4.7.

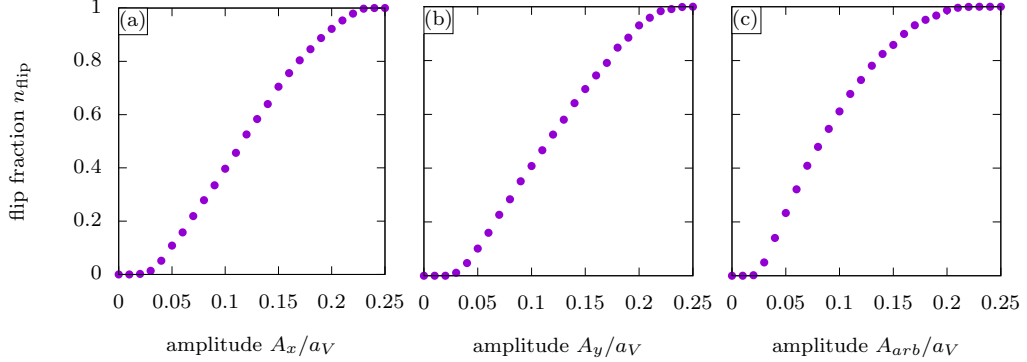


Figure 4.7: Fraction  $n_{\text{flip}}$  of flipping particles in a decagonal quasicrystal as a function of the amplitude. The phasonic fluctuations occur along (a) the  $x$ -direction, (b) the  $y$ -direction and (c) an arbitrary direction.

For all fluctuations particles begin to flip when the amplitudes exceed a value of 0.02. Rising amplitudes cause an increase of flipping particles which is similar for fluctuations in  $x$ - and  $y$ -direction (see Figures 4.7 (a) and (b)). While for low amplitudes the increase of flipping particles is approximately linear, for larger amplitudes the flip fraction increases more slowly. We obtain a saturation for amplitudes larger than 0.23 at which all particles rearrange. For fluctuations in arbitrary directions the fraction of flipping particles increases faster and a saturation is already reached at  $A_{\text{arb}} > 0.2$  (see Figure 4.7 (c)).

### Dodecagonal quasicrystals

In the following we map the particles of a quasicrystal with dodecagonal symmetry inside the characteristic areas. Curiously, in a system of particles that occupy all minima in the dodecagonal laser potential we are not able to map all particles inside the characteristic areas. By only considering the particles that can be mapped inside the characteristic areas we obtain a shield tiling. We consider a section of  $N = 2170$  particles of that shield tiling. The reduced phasonic displacements and the positions of the particles colored according to the minimal phasonic amplitude required for a flip are shown for fluctuations in  $x$ -direction (Figures 4.8 (a) and (b)), in  $y$ -direction (Figures 4.8 (c) and (d)) and in arbitrary directions (Figures 4.8 (e) and (f)). The reduced phasonic displacements lie inside a dodecagon.

Phasonic fluctuations in  $x$ - and in  $y$ -direction both proceed along symmetry directions. Hence, the distributions of flipping particles are the same but rotated about  $\pi/2$ . As for decagonal quasicrystals, the particles in symmetry centers, i.e.

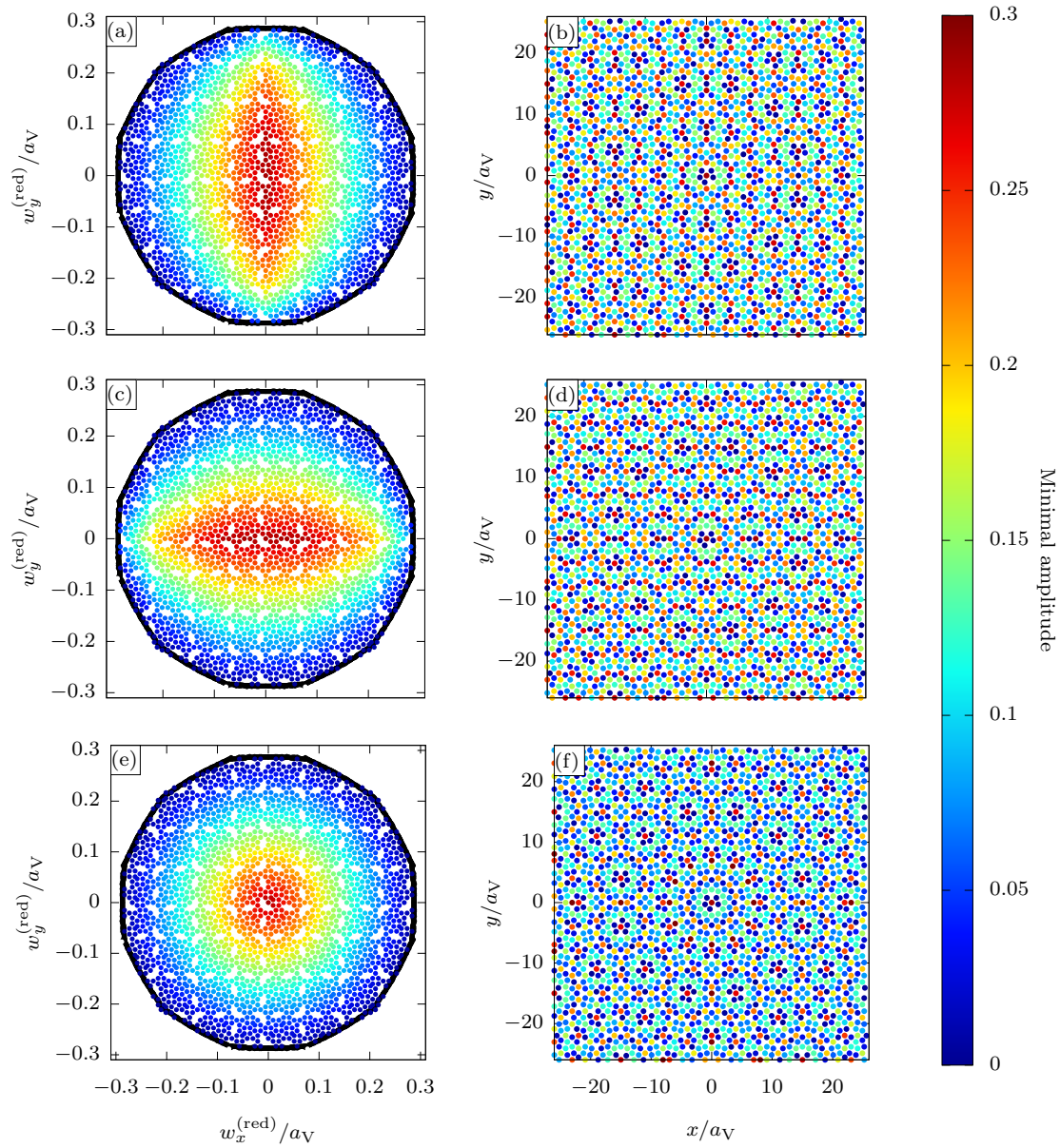


Figure 4.8: (a),(c) and (e) Reduced phasonic displacements of  $N = 2170$  particles in a dodecagonal shield tiling. The black borders indicate the values of phasonic displacements at which particles flip. The colors reveal the minimal amplitude of the phasonic fluctuation in (a)  $x$ -direction, (c)  $y$ -direction and (e) arbitrary direction that is needed for a flip of the corresponding particle. (b),(d) and (f) Corresponding particles in real space with the same color code.

the central particles inside a ring of twelve particles only flip at large phasonic amplitudes. Together with further stable particles they are arranged on zig-zag lines in the vertical direction in case of fluctuations in  $x$ -direction and in horizontal direction in case of fluctuations in  $y$ -direction. In case of fluctuations in arbitrary directions the number of stable particles is reduced.

As for the decagonal case we calculate the fraction of flipping particles dependent on the phasonic amplitude. For symmetry reasons the fraction of flipping particles for fluctuations in  $x$ - and  $y$ -direction is equal. Figure 4.9 illustrates the results for fluctuations in  $x$ - and arbitrary directions.

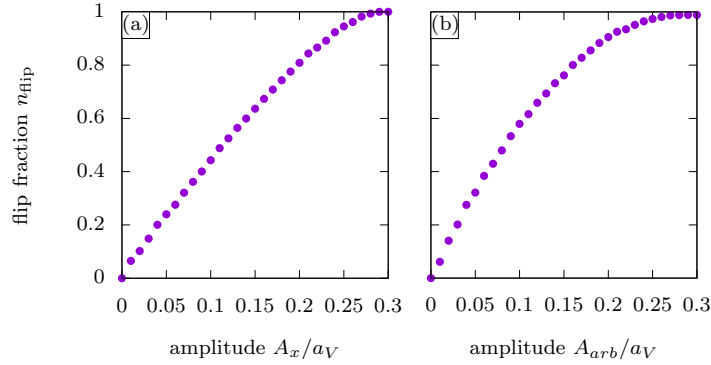


Figure 4.9: Fraction of flipping particles in a dodecagonal quasicrystal as a function of the amplitude. The phasonic fluctuations occur along (a) the  $x$ -direction and (b) an arbitrary direction.

In dodecagonal quasicrystals only small phasonic amplitudes are required to make the first particles flip. For fluctuations in arbitrary directions the fraction of flipping particles increases faster than for fluctuations in a limited direction. Saturation is reached for phasonic amplitudes larger than 0.27.

### Octagonal quasicrystals

We employ the described procedure for an Ammann-Beenker tiling of  $N = 2204$  particles. As for the dodecagonal case, the positions of the Ammann-Beenker tiling are given by the minima of the octagonal laser potential that we can map inside the characteristic areas. In Figure 4.10 the reduced phasonic displacements are inside an octagon and the positions of the particles are colored according to the minimal amplitude required for a phasonic flip. In Figures 4.10 (a) and (b) the phasonic fluctuation is limited to the  $x$ -direction, in Figures 4.10 (c) and (d) to the  $y$ -direction and in Figures 4.10 (e) and (f) the fluctuations occur in arbitrary directions.

As for dodecagonal quasicrystals fluctuations in  $x$ - and  $y$ -direction occur along

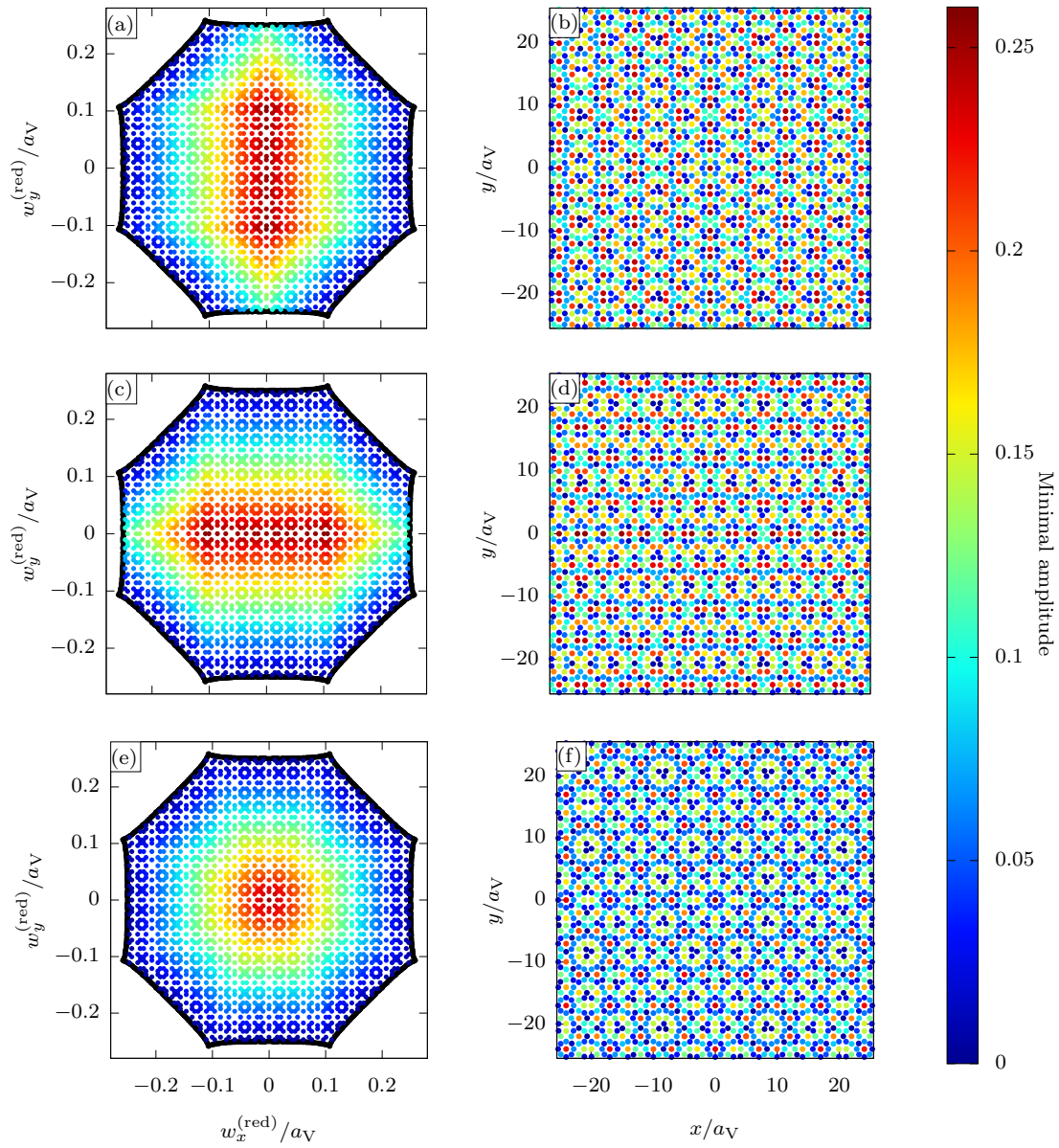


Figure 4.10: (a),(c) and (e) Reduced phasonic displacements of  $N = 2204$  particles in an octagonal Ammann-Beenker tiling. The black borders indicate the values of phasonic displacements at which particles flip. The colors reveal the minimal amplitude of the phasonic fluctuation in (a)  $x$ -direction, (c)  $y$ -direction and (e) arbitrary direction that is needed for a flip of the corresponding particle. (b),(d) and (f) Corresponding particles in real space with the same color code.

symmetry directions and the distributions of flipping particles are rotated about  $\pi/2$  against each other. We observe stable particles inside the symmetry centers, i.e. the particles that are surrounded by eight nearest neighbor particles. In case of fluctuations in  $x$ - or  $y$ -direction even more stable particles are located on vertical or horizontal lines. Between the lines of stable particles we observe lines of unstable particles.

The fraction of flipping particles  $n_{\text{flip}}$  dependent on the amplitude is presented in Figure 4.11. Since  $n_{\text{flip}}$  is the same for fluctuations in  $x$ - and in  $y$ -direction we only show the results for fluctuations in  $x$ -direction (Figure 4.11 (a)) together with the results for fluctuations in arbitrary directions (Figure 4.11 (b)).

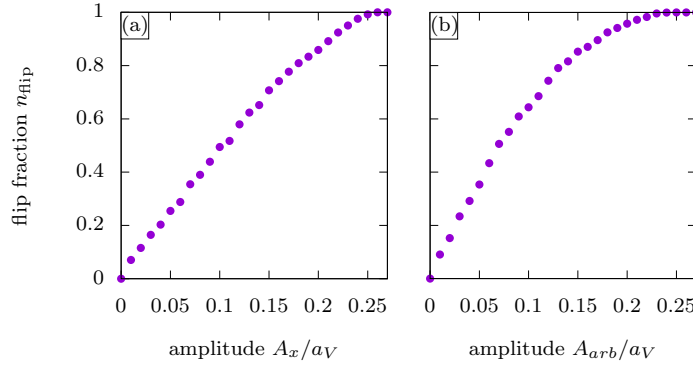


Figure 4.11: Fraction of flipping particles in an octagonal quasicrystal as a function of the amplitude. The phasonic fluctuations occur along (a) the  $x$ -direction and (b) an arbitrary direction.

The curves look similar to the ones of dodecagonal quasicrystals. The first particles already flip at small phasonic amplitudes. In case of fluctuations in  $x$ -direction a saturation is reached at  $A_x > 0.25$ , while for fluctuations in arbitrary directions all particles rearrange at  $A_{\text{arb}} > 0.23$ .

#### 4.4 Colloidal trajectories in two-dimensional light-induced quasicrystals with 14-fold symmetry due to phasonic drifts

In the previous Section we presented a method to map colloids inside characteristic areas. The method was previously used in [11, 12] in order to predict the trajectories of colloidal particles in quasicrystalline laser fields when a phasonic drift is applied, i.e. when the phasonic displacement changes with a constant rate in time. By mapping every colloid into the characteristic areas of reduced phasonic and

phasonic displacement one only has to study the paths inside these areas to derive the behavior inside the whole quasicrystal.

So far trajectories of colloids in quasicrystalline interference patterns with 8-, 10- and 12-fold rotational symmetry were determined [11, 12] which are all of rank  $D = 4$ . Here, we show on the basis of quasicrystals with 14-fold symmetry how the method can further be extended to laser fields with rank  $D = 6$ . Compared to the  $D = 4$  case, the additional phasonic modes lead to a more complex behavior and we identify several new types of colloidal trajectories.

Our investigations are organized as follows: First, we introduce the model system. Second, the corresponding characteristic areas of reduced phononic and phasonic displacement are determined. Third, we study the behavior inside these areas to predict the colloidal trajectories in general. Finally, selected trajectories are presented.

#### 4.4.1 Tetradecagonal laser field

We employ an interference pattern created by 7 laser beams that acts like an external potential with 14-fold symmetry on the colloids. The potential [8, 125, 325] is of the form

$$V(\mathbf{r}) = -\frac{V_0}{49} \sum_{j=0}^6 \sum_{k=0}^6 \cos[(\mathbf{G}_j - \mathbf{G}_k) \cdot \mathbf{r} + \phi_j - \phi_k] \quad (4.9)$$

with wave vectors  $\mathbf{G}_j$  as introduced in Section 4.2. Our parameterization of the phases is similar to [9, 10]

$$\phi_j = \mathbf{G}_j \cdot \mathbf{u} + \mathbf{G}_{3j \bmod 7} \cdot \mathbf{v} + \mathbf{G}_{5j \bmod 7} \cdot \mathbf{w} \quad (4.10)$$

where  $\mathbf{u} = (u_x, u_y)$  denotes the phononic,  $\mathbf{v} = (v_x, v_y)$  and  $\mathbf{w} = (w_x, w_y)$  the phasonic displacements. Let us note that compared to a  $D = 4$  quasicrystal an additional phasonic displacement vector is required.

In the following, we consider the limit of large potential strengths or low temperatures ( $V_0 \gg k_B T$ ), such that all colloids are located in the minima of the potential (cf. snapshot shown in Figure 4.12).

#### 4.4.2 Characteristic displacements and characteristic areas

In order to determine the characteristic areas, we first calculate phononic and phasonic displacements  $\Delta \mathbf{u}$ ,  $\Delta \mathbf{v}$  and  $\Delta \mathbf{w}$  that change the differences between the phases  $\phi_j - \phi_k$  in equation (4.9) only by integer multiples of  $2\pi$ . We solve

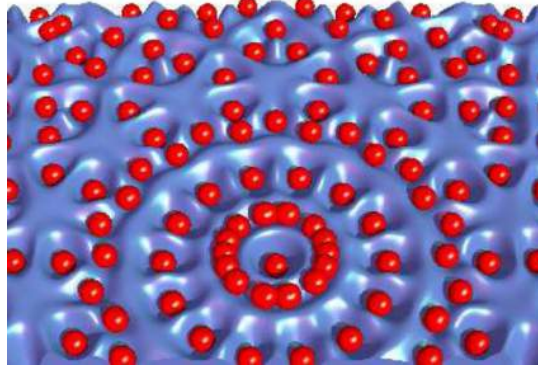


Figure 4.12: Colloids in the minima of a potential with 14-fold symmetry.

$V_{\mathbf{v}+\Delta\mathbf{v},\mathbf{w}+\Delta\mathbf{w}}(\mathbf{r} + \Delta\mathbf{u}) = V_{\mathbf{v},\mathbf{w}}(\mathbf{r})$  where  $V_{\mathbf{v},\mathbf{w}}(\mathbf{r})$  denotes a potential with the phasonic displacements  $\mathbf{v}$  and  $\mathbf{w}$ . For  $j = 0, \dots, 13$ , we obtain as suitable combinations

$$\begin{aligned}\Delta\mathbf{u}_j &= (u_r \cos[j\pi/7], u_r \sin[j\pi/7]), \\ \Delta\mathbf{v}_j &= (v_r \cos[3j\pi/7], v_r \sin[3j\pi/7]), \text{ and} \\ \Delta\mathbf{w}_j &= (w_r \cos[5j\pi/7], w_r \sin[5j\pi/7]).\end{aligned}\tag{4.11}$$

These displacements do not modify the potential when

$$\begin{aligned}u_r/a_V &= \frac{8}{49} (n_1 a + n_2 b + n_3 c), \\ v_r/a_V &= \frac{8}{49} (n_2 a + n_3 b + n_1 c), \\ w_r/a_V &= \frac{8}{49} (n_3 a + n_1 b + n_2 c),\end{aligned}\tag{4.12}$$

where  $n_1, n_2$  and  $n_3 \in \mathbb{Z}$  and  $a, b$  and  $c$  are the constant values

$$\begin{aligned}a &= (1 - \cos[10\pi/7])^2 - (1 - \cos[2\pi/7])(1 - \cos[6\pi/7]), \\ b &= (1 - \cos[6\pi/7])^2 - (1 - \cos[2\pi/7])(1 - \cos[10\pi/7]), \\ c &= (1 - \cos[2\pi/7])^2 - (1 - \cos[6\pi/7])(1 - \cos[10\pi/7]).\end{aligned}\tag{4.13}$$

Thus, a colloid at position  $\mathbf{r}$  in a potential with phasonic displacements  $\mathbf{v}$  and  $\mathbf{w}$  can be mapped to a reduced position  $\mathbf{r}^{(\text{red})} = \mathbf{r} - \Delta\mathbf{u}$  in a potential with reduced phasonic displacements  $\mathbf{v}^{(\text{red})} = \mathbf{v} + \Delta\mathbf{v}$  and  $\mathbf{w}^{(\text{red})} = \mathbf{w} + \Delta\mathbf{w}$  inside the particular characteristic area.

To determine the size of the characteristic areas we consider the subspaces spanned by a chosen phasonic direction  $\mathbf{e}_j = (\cos[\pi j/7], \sin[\pi j/7])$  and its phasonic counterparts. Thus, we get a three-dimensional subspace in every direction. We have

to find cuboids of the side lengths  $\delta u, \delta v$  and  $\delta w$  that fill out the whole volume when shifted about  $\Delta \mathbf{u}_j$  in phonic and  $\Delta \mathbf{v}_j$  and  $\Delta \mathbf{w}_j$  in phasonic directions. Then all reduced positions and reduced phasonic displacements are limited by

$$\begin{aligned} |\mathbf{r}^{(\text{red})} \cdot \mathbf{e}_j| &\leq \delta u / 2a_V, \\ |\mathbf{v}^{(\text{red})} \cdot \mathbf{e}_j| &\leq \delta v / 2a_V, \\ \text{and } |\mathbf{w}^{(\text{red})} \cdot \mathbf{e}_j| &\leq \delta w / 2a_V \end{aligned} \quad (4.14)$$

for all symmetry directions  $j = 0, \dots, 13$ . A possible choice is  $\delta u / 2a_V = \delta v / 2a_V = \delta w / 2a_V = 1/2(-a - b)$ .

### 4.4.3 Analyzing colloidal trajectories

In order to describe the colloidal trajectories in a quasicrystal with 14-fold symmetry, we have to consider a four-dimensional phasonic space spanned by  $v_x, v_y, w_x$  and  $w_y$ . Since it is too complex to sample the complete space, we restrict our analysis to drifts on selected planes in the phasonic space.

As a first attempt either  $\mathbf{w}$  is varied while  $\mathbf{v} = \mathbf{0}$  or  $\mathbf{v}$  is changed while  $\mathbf{w} = \mathbf{0}$ . We trace the paths of colloids started at the origin for all drift directions within the respective phasonic plane. Then the important points of the trajectories for reduced phasonic displacements  $\mathbf{w}^{(\text{red})}$  or  $\mathbf{v}^{(\text{red})}$  and the corresponding reduced positions  $\mathbf{r}^{(\text{red})}$  can be presented in the diagrams of Figure 4.13.

The diagrams correspond to those obtained for the  $D = 4$  quasicrystals in [11, 12]. The procedure to derive a trajectory for the case  $\mathbf{v} = \mathbf{0}$  (see Figures 4.13 (a) and (b)) is as follows: When the phasonic displacement  $\mathbf{w}^{(\text{red})}$  reaches a point marked by (1,2) the colloid jumps from its old position (1) to a new one (2) of the same color. Corresponding colors of selected lines are also denoted by (A), (B), and (C). Note that the positions (2') are only reached for a drift along a symmetry axis or slightly beside it. Since the colloidal position is now outside the characteristic area, one has to map it back inside by employing combinations of  $\Delta \mathbf{u}$ ,  $\Delta \mathbf{w}$  and also  $\Delta \mathbf{v}$ . Due to the latter, for the mapped quantity  $\mathbf{v}^{(\text{red})} \neq \mathbf{0}$ . Thus, one has to consider a new diagram for the reduced phasonic displacements  $\mathbf{w}^{(\text{red})}$  and the reduced positions  $\mathbf{r}^{(\text{red})}$  after every jump. The same difficulty arises for drifts in the  $\mathbf{w} = \mathbf{0}$  plane. Therefore, in contrast to quasicrystals with rank  $D = 4$ , the derivation of a colloidal trajectory for an arbitrary drift is for  $D = 6$  in most cases quite complex, as many diagrams would be required for a complete prediction.

### 4.4.4 Selected trajectories

There are drifts for which it is possible to deduce the trajectories with a single diagram for the reduced phasonic displacements. For certain drifts in the plane

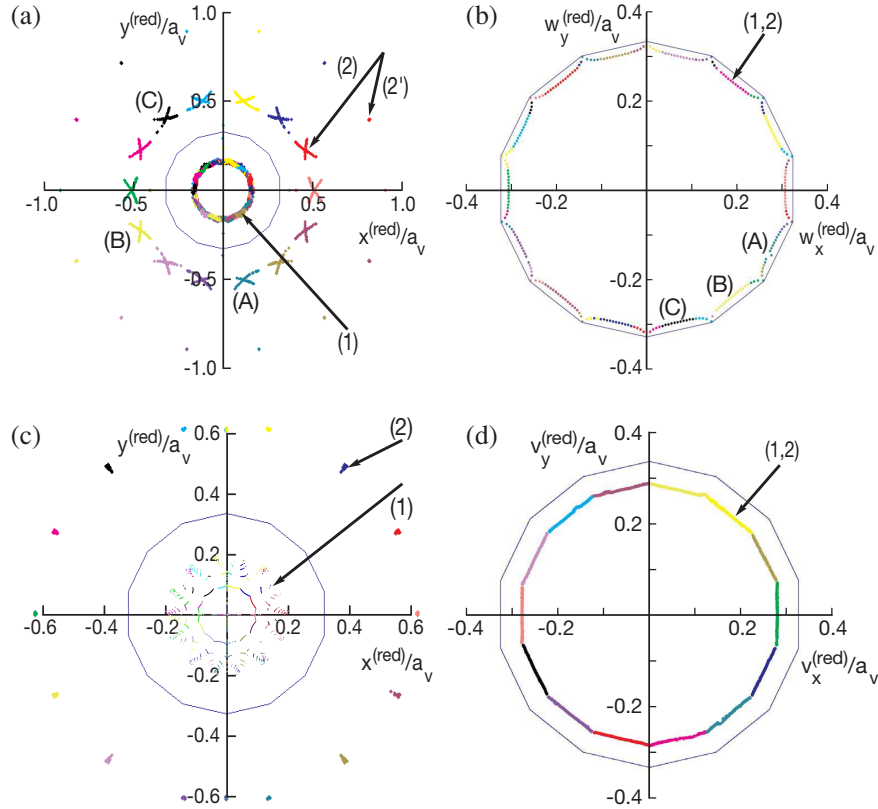


Figure 4.13: (a) and (b) Areas of reduced positions  $\mathbf{r}^{(\text{red})}$  and reduced phasonic displacements  $\mathbf{w}^{(\text{red})}$  for  $\mathbf{v} = \mathbf{0}$ . (c) and (d) Areas of reduced positions  $\mathbf{r}^{(\text{red})}$  and reduced phasonic displacements  $\mathbf{v}^{(\text{red})}$  for  $\mathbf{w} = \mathbf{0}$ . The characteristic areas are limited by blue polygons. The lines where particle start to slide or end up after sliding or remapping are marked by different colors. Selected lines are also labeled by letters (A), (B), or (C) in order to denote corresponding lines.

with  $v_y = w_y = 0$ , the colloid moves in  $x$  direction. In addition, the phasonic counterparts  $\Delta \mathbf{w}$  and  $\Delta \mathbf{v}$  to the required  $\Delta \mathbf{u}$  only affect the  $x$  components  $w_x$  and  $v_x$ . As a consequence, the phasonic plane with  $v_y^{(\text{red})} = w_y^{(\text{red})} = 0$  is never left during the mapping process. In the following, we discuss for selected drifts the colloidal trajectories that can be completely derived from the diagram in Figure 4.14 (a).

For a phasonic drift in the direction  $(v_x, v_y, w_x, w_y) = (\cos(3\pi/7), 0, \cos(5\pi/7), 0)$  we find a zig-zag path illustrated in Figure 4.14 (b). It is similar to the zig-zag paths in quasicrystals with rank  $D = 4$  which is why we refer for a detailed description to [11].

On the other hand, a new type of trajectory is depicted in Figure 4.14 (c). It

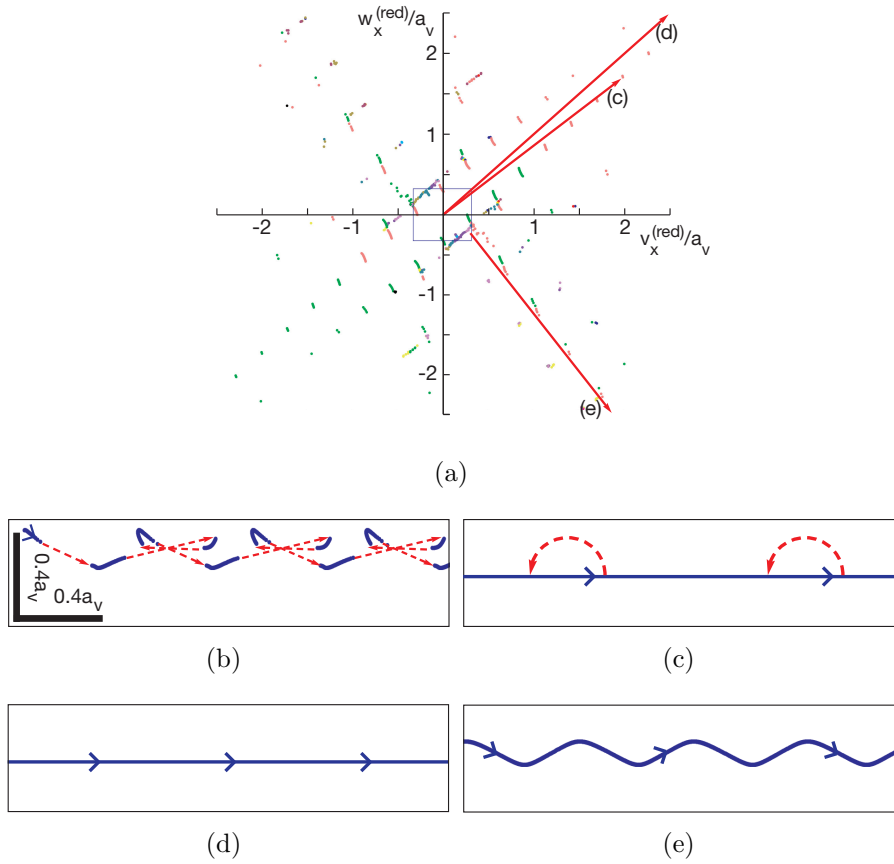


Figure 4.14: (a) Section of the characteristic diagram for the reduced phasonic displacements  $v_x^{(\text{red})}$  and  $w_x^{(\text{red})}$  with  $v_y = w_y = 0$ . (b)-(e) Selected typical colloidal trajectories arising for  $v_x - w_x$  drifts in certain directions. The directions of motion are indicated by arrows. The scale bar denotes the length scales in  $x$ - and  $y$ -direction.

consists of straight paths interrupted by jumps in the opposite direction and occurs when a drift in the direction  $(v_x, v_y, w_x, w_y) = (\cos(9\pi/70), 0, \cos(3\pi/14), 0)$  is applied. The particle moves on a straight line until the phasonic displacement reaches a point in the diagram in Figure 4.14 (a) such that the particle jumps. The phasonic displacements and the positions can be mapped back into the characteristic areas to predict the further path of the colloids when the displacement is further increased.

Figure 4.14 (d) illustrates an example of a straight path without any jumps. It arises for a phasonic drift in the direction  $(v_x, v_y, w_x, w_y) = (1, 0, 1, 0)$ . In this case, the phasonic displacement never reaches a point in the diagram in Figure 4.14 (a) and as a consequence the particle never leaves a minimum. Therefore,

the phasonic displacement is simply mapped back when it crosses the border of its characteristic area. This drift proceeds along a symmetry plane in the phasonic space such that the form of the trajectory is a straight line.

Another new type of trajectory has the shape of a winding line as shown in Figure 4.14 (e). It arises, e.g. when a drift in the direction  $(v_x, v_y, w_x, w_y) = (\cos(3\pi/7), 0, \cos(5\pi/7), 0)$  is applied for a colloid position whose initial reduced phasonic displacement is not in the origin but at  $v_x = 0.3a_V$  and  $w_x = -0.2a_V$ . Just as in the example before, the colloid never jumps. Compared to the previous case the drift does not move along a symmetry plane in the phasonic space which leads to the occurrence of curves in the path.

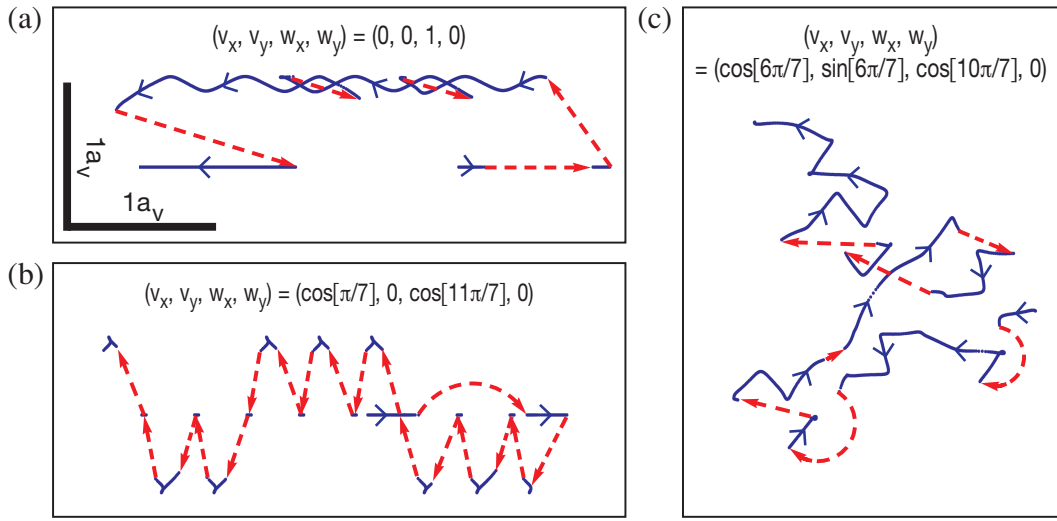


Figure 4.15: General colloidal trajectories representing the majority of the observed colloidal paths: (a) A combination of straight and winding lines separated by jumps. (b) Several jumps along an irregular zig-zag path. (c) Chaotic trajectory consisting of irregular slides and jumps in between.

Beside these presented typical paths, for most drifts we find much more complex trajectories. Further examples are shown in Figure 4.15. Note that all paths of the colloids are composed of the typical trajectories such that every section can be explained separately.

## 4.5 Conclusion

We have created potential landscapes with quasicrystalline symmetries by means of interfering laser beams. By locating colloids inside the minima of the potential

landscapes we have obtained two-dimensional quasicrystalline tilings with discrete colloidal positions. In principle, quasicrystalline tilings with any symmetry may be obtained with interfering laser beams.

We described a method how the stability of particles in quasicrystalline structures related to interference patterns can be predicted, i.e. we can determine which particles flip for a given phasonic displacement that might, e.g. be caused by thermal fluctuations. Therefore, we applied characteristic displacements introduced in previous studies [11, 12] to map each colloid inside characteristic areas of reduced phononic and phasonic displacements. We presented the results of our approach for the decagonal Tuebingen tiling, the dodecagonal shield tiling and the octagonal Ammann-Beenker tiling. We found that the particles in a Tuebingen tiling are all stable with respect to sufficiently small phasonic fluctuations, while in the other cases flips already occur for arbitrarily small phasonic displacements. Our method can also be applied to other quasicrystalline structures. This obviously includes all structures induced by laser fields [7, 8, 11–13, 27, 125, 126, 129, 135–137, 141, 142, 235, 325, 334–338, 344], but also quantum quasicrystals [345–348] have been shown to be similar [346]. Furthermore, even intrinsic quasicrystals and their thermally fluctuating phasonic displacements can be analyzed by comparing them to laser fields [14]. Note that phasonic flips due to thermal fluctuations are also important for the growth process of intrinsic quasicrystals as shown in [115, 116, 121, 247, 265]. Our results might be used to predict the particles that are unlikely to be flipped and those that are more likely to be displaced during the growth process.

Furthermore, on the basis of 14-fold rotational symmetry, we have extended the previous studies [11, 12] to quasicrystals with rank  $D = 6$ . We showed how one can still predict colloidal trajectories that are caused by phasonic drifts in spite of the increased complexity in the phasonic space. In addition, we were able to identify new types of trajectories in addition to the regular straight and zig-zag paths that are already known from quasicrystals with rank  $D = 4$ . In principle, we could apply the method to all quasicrystals including those with even higher ranks. Since quasicrystals with increased rank require a mapping in higher dimensions, we expect even more complex trajectories for those structures.



## Chapter 5

# Complex structures in systems of patchy colloids

In the previous Chapter two-dimensional quasiperiodic arrangements of colloids were obtained by means of external fields. In this Chapter we want to stabilize intrinsic colloidal quasicrystals in the presence of internal interactions. Various internal interaction potentials are known that give rise to quasicrystalline order (see Subsection 2.2.2). For instance, interactions in metals that lead to quasicrystalline structures can be modeled by double-well potentials with typical lengths [28, 29, 90, 91] or short-range repulsive potentials with additional maxima at distances typical of periodic structures [85, 86, 88, 89]. Soft quasicrystals are modeled, e.g. by hard core potentials combined with soft shells [100, 102]. Also interactions between polydisperse particles [104, 106, 107] can lead to quasicrystalline arrangements.

Another approach is interactions between patchy colloids, i.e. colloids with attractive regions at the surface [255, 256]. In previous studies [119–121] dodecagonal quasicrystals were stabilized with patchy colloids. Here, we employ Monte Carlo simulations to model quasicrystals with decagonal and octagonal symmetry. The internal interactions are easily tunable such that we can vary, e.g. the number of patches or the patch width. We explore the influence of the patch width on the assembling structures.

The structure of the Chapter is as follows: In Section 5.1 patchy colloids and their features are introduced in detail. In Section 5.2 we present our studies concerning decagonal and octagonal quasicrystals composed of patchy colloids. Section 5.3 contains a conclusion and discussion of our results.

Most parts of this Chapter are based on our publication [E]. The concerned Sections and the authors' contributions are given in the *List of publications*.

## 5.1 Patchy colloids

Patchy colloids [255, 256] are hard or soft spheres with a finite number of well-defined discrete attractive regions, called patches, at the surface. The number, arrangement and geometry of the patches is tunable. A spherical particle with five symmetrically arranged extended patches of equal size is exemplarily sketched in Figure 5.1 (a). Another simple example of patchy particles is Janus particles [349, 350], i.e. spherical particles with two hemispheres as depicted in Figure 5.1 (b). The hemispheres provide different features, for instance electrical, chemical or physical features.

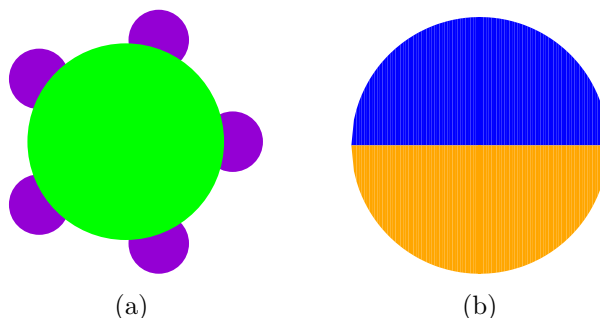


Figure 5.1: Patchy colloids. (a) Spherical particle (green) with five regularly arranged extended patches (purple) at the surface. (b) Janus particle consisting of two hemispheres with different properties.

A scientifically interesting research field contains the self-assembly processes of patchy particles. The self-assembly process is driven by the interactions between the particles. Compared to an isotropic pair potential between simple spherical particles, the patches cause an anisotropic, highly directional interaction. Since the properties of the patches are tunable, the directionality can be controlled to a certain degree and the self-assembly may be driven towards desired target structures [351]. Thus, patchy particles may be used in applications which require particular structures, e.g. in photonics [352] or electronics [353]. Further fields contain medical applications [354, 355], for instance targeted drug delivery, or applications as autonomous swimmers [351].

In order to systematically investigate self-assembly processes, patchy particles have been fabricated in experiments. Different fabrication methods are summarized in [351]. In first realizations clusters of colloids induced anisotropic interactions [356–358]. Further progress allowed the decoration of micro-spheres with metallic patches realized by gold nanodots [359–361]. However, the fabrication is still challenging and requires further research.

Aside from synthetic patchy particles there are as well natural examples of patchy

colloids. For instance, globular proteins are biological macromolecules which may be described as non- or weakly interacting particles with effectively attractive patches [362–367].

Moreover, patchy particles have been modeled in simulations with different methods summarized in [368]. For instance, preferred binding angles between the particles can be realized by an anisotropic term in the interaction potential (see Subsection 3.4.1). The ordering preferred by the isotropic part of the potential (with only one length scale) competes with structures that possess the binding angles preferred by the patches. Competitions between different symmetries are known to lead to interesting new phenomena, like the formation of Archimedean-tiling phases [126, 129, 262, 263], rhombic phases [264], or new types of growth behavior [344, 369]. In recent simulations [119–121] patchy colloids with 5 symmetrically arranged patches assembled into dodecagonal quasicrystals which have been the only quasicrystals observed in patchy colloidal systems.

## 5.2 Stabilizing quasicrystals composed of patchy colloids by narrowing the patch width

In this Section we model patchy colloids with ten and eight patches with a focus on the influence of different patch widths on the final arrangements. In case of narrow patch widths metastable decagonal and octagonal quasicrystals are received. With our studies we give a deeper insight into the building mechanism of quasicrystals. The Section is organized as follows: We first describe the setup of our simulations. Afterwards, colloids with ten and eight patches are modeled in order to stabilize decagonal and octagonal quasicrystals. Furthermore, we vary the length scales supported by the potential and test protocols to obtain quasicrystals from random initial configurations.

### 5.2.1 Simulation setup

We consider an interaction potential that is similar to the potentials previously used to investigate self-assembly or growth processes [30, 118–121, 257–261]. The interaction  $V_p(r, \theta_k, \theta_l)$  between two particles at a distance  $r$  is composed of an isotropic Lennard-Jones-like pair potential  $V_{LJ}(r)$  multiplied with an anisotropic angular term  $V_a(\theta_k, \theta_l)$ , i.e.  $V_p(r, \theta_k, \theta_l) = V_{LJ}(r) \cdot V_a(\theta_k, \theta_l)$  for  $r > r_0$  and  $V_p(r, \theta_k, \theta_l) = V_{LJ}(r)$  otherwise. The potential and its parameters are described in detail in Subsection 3.4.1. Note that the patches only act starting at the surface, i.e. for  $r > r_0$ . The Lennard-Jones-like part possesses one local minimum at  $r = r_0$  and the exponent  $n$  determines the width of the minimum. Note that we consider a radial Lennard-Jones-like part that is broader than the usual Lennard-Jones

potential with  $n = 6$ , because for  $n = 6$  the suppression of nearest neighbor distances that differ from the one favored length scale  $r_0$  seems to be too strong to allow the stabilization of quasicrystals different from dodecagonal structures, where all triangles and squares that occur have the side length  $r_0$ .

We apply an angular part  $V_a(\theta_k, \theta_l)$  which consists of two terms with two patch widths  $\sigma_1$  and  $\sigma_2$  (see equation (3.54) in Subsection 3.4.1). Thus, we can model a narrow patch width  $\sigma_1$ , while the superposed attraction with a broad patch width  $\sigma_2$  ensures that the patches still find each other within a reasonable time. Note that the broad patches do not influence the stability of the final structure, e.g. we have checked for the cases in Figure 5.2 that are started from the decagonal structure that the final structures are the same if only narrow patches are used. However, in case of other initial conditions, it might take too long for patches to find each other if only narrow patch potentials are employed. We will see in the next Section that narrow patches (i.e. small  $\sigma_1$ ) are required to stabilize octagonal and decagonal quasicrystals. The potentials are truncated and shifted appropriately at  $3r_0$ .

We model two-dimensional systems of  $N$  particles by employing Metropolis Monte Carlo simulations (see Section 3.2) with periodic boundary conditions in the  $NVT$ -ensemble. If not stated otherwise conventional displacement moves and rotation moves are proposed with the same probability. Simulations are started either with random positions of the particles or with particles placed on a perfect lattice. A perfect decagonal arrangement is obtained from the maxima of the interference pattern of five laser beams [8, 125, 325] (see also Section 4.2). A perfect octagonal lattice is received from substitution rules [221]. In case of random initial positions the orientations of the particles are also chosen randomly. In the perfect lattices the patches are oriented towards each other.

### 5.2.2 Systems of colloids with ten patches

We first model particles with ten symmetrically arranged patches with the aim to stabilize decagonal quasicrystals. Perfect decagonal structures possess two characteristic length scales  $d_0$  and  $d_1 = \tau d_0 \approx 1.618d_0$ , where  $\tau$  denotes the golden mean. In our simulations, however, we can only support one length by the potential minimum. From previous works [119–121] we know that dodecagonal quasicrystals can be stabilized with patchy colloids when the short length is supported. Therefore, here we also apply  $r_0 = d_0$ . We choose a small exponent  $n = 2$  which causes a broad potential minimum. Thus, the low gradient reduces the energy of the long length scale. For the attraction that is used to support the fast finding of bonds, we employ a broad width  $\sigma_2 = 0.23$ .  $\sigma_2$  is chosen in a way that the surface area covered by patches is similar like in previous works [119–121]. To model the actual patches we use a different width  $\sigma_1$  that is varied. The temperature reads  $T = 0.2\epsilon$  which is below the melting temperature but large enough to allow for sufficient

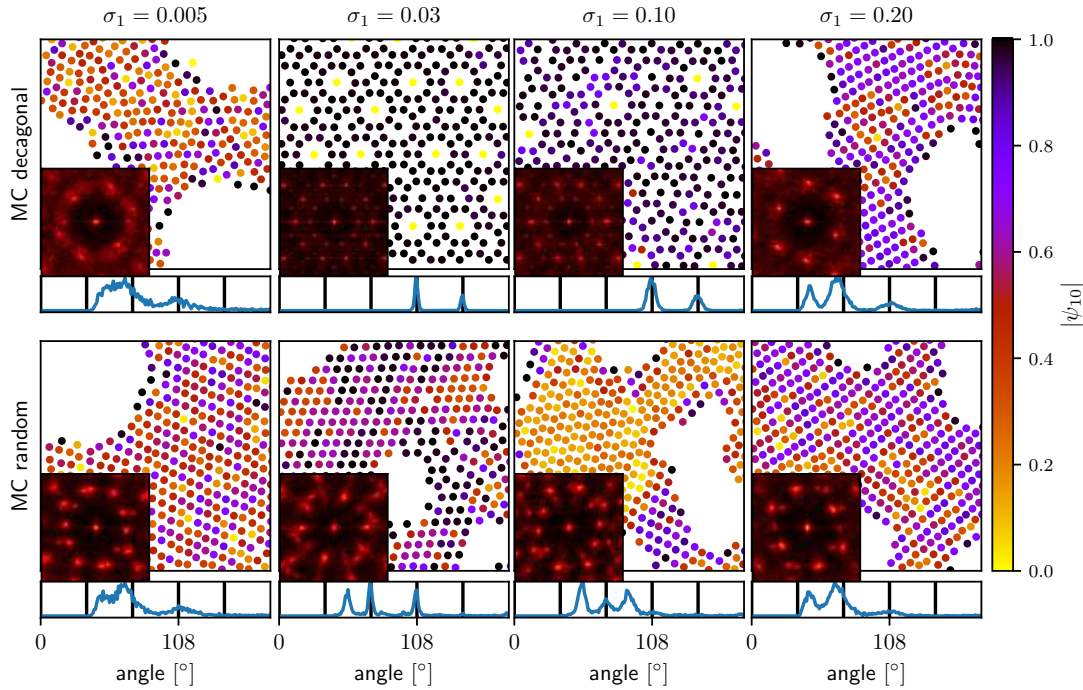


Figure 5.2: Configurations of  $N = 644$  particles obtained from simulations with an initial decagonal quasicrystal (upper row) and an initial random configuration (lower row). We vary the patch width  $\sigma_1 = 0.005$  (first column),  $\sigma_1 = 0.03$  (second column),  $\sigma_1 = 0.10$  (third column) and  $\sigma_1 = 0.20$  (fourth column). Further potential parameters read  $\sigma_2 = 0.23$ ,  $n = 2$ ,  $r_0 = d_0$  and we model colloids furnished with ten patches. The color code illustrates the bond-orientational order parameter  $|\psi_{10}|$ . The insets depict the corresponding structure factors. The graphs below the configurations show the corresponding angular distribution functions. The black lines serve as guide to the eye and indicate perfect decagonal bond angles, i.e.  $2\pi j/10$ ,  $j = 1, \dots, 10$ . All simulations were performed at  $T = 0.2\epsilon$ .

mobility of the particles. The density of a perfect decagonal tiling is chosen, i.e.  $\rho = N/A \approx 0.63/r_0^2$ , where  $A$  denotes the size of the simulation box.

As starting configurations we consider perfect decagonal, hexagonal, square, and random configurations. In our simulations the energy fluctuates around a constant energy value after no more than  $10^7$  Monte Carlo steps even if started with a structure that is different from the final structure. We performed simulations for at least  $2 \cdot 10^8$  Monte Carlo steps in order to check whether any further relaxation can be observed. Typical final structures obtained for initial decagonal and random configurations are illustrated in Figure 5.2 for various patch widths  $\sigma_1$ . Particles are colored according to their local bond-orientational order parameter  $|\psi_{10}|$ . Structure factors are depicted as insets and the angular distributions are shown below each configuration. The bond-orientational order parameter and the structure factor are defined in Subsections 3.5.4 and 3.5.2.

At very narrow patch widths  $\sigma_1 = 0.005$  it is difficult for the patches to find each other and the initial decagonal tiling is destroyed. At  $\sigma_1 = 0.03$  the decagonal tiling remains stable. The structure factor provides clear decagonal symmetry and the angular distribution shows sharp peaks. The bond-orientational order is maximal. Note that only particles close to contact are considered in the calculation of  $|\psi_{10}|$  such that central particles appear yellow. Particles with short distances to their neighbors are stabilized by the potential minimum in combination with the correct orientation. The long characteristic distance of a decagonal quasicrystal either occurs within a pentagon with the short distance as side length or as distance between a central particle in a decagon with the short length as side length. Pentagons and decagons are supported by the favored binding angles of  $\pi/5$  and  $2\pi/5$ . At increased patch widths bond angles deviate from the decagonal symmetry. The particles start to slightly rearrange at  $\sigma_1 = 0.1$ . Peaks of the angular distribution are broadened and order decreases. At  $\sigma_1 = 0.2$  a dense phase with predominant distances of  $r_0$  and angles of approximately  $45^\circ$  and  $66^\circ$  forms.

Applying the given protocol with initial random configurations, particles do not arrange to decagonal quasicrystals at any patch width. At  $\sigma_1 = 0.03$  most particles build a dense periodic structure. We observe angles with  $72^\circ$  and  $108^\circ$  that in principle could also appear in patterns with decagonal symmetry and an additional angle with  $54^\circ$ . Only a few elements of a decagonal tiling are found. At intermediate patch width  $\sigma_1 = 0.1$  this phase competes with an Archimedean ( $3^34^2$ ) tiling. For initial hexagonal and square phases we obtain similar final configurations.

In the following we test which structures are energetically favored by the employed potential. We apply a perfect decagonal, square and hexagonal tiling each with density  $\rho \approx 0.63/r_0^2$  and depict the average potential energy per particle  $\langle E/N \rangle$  as a function of the patch width  $\sigma_1$  in Figure 5.3. At low patch widths  $\sigma_1 \leq 0.2$  the perfect decagonal tiling is energetically favored. Increased patch widths allow for

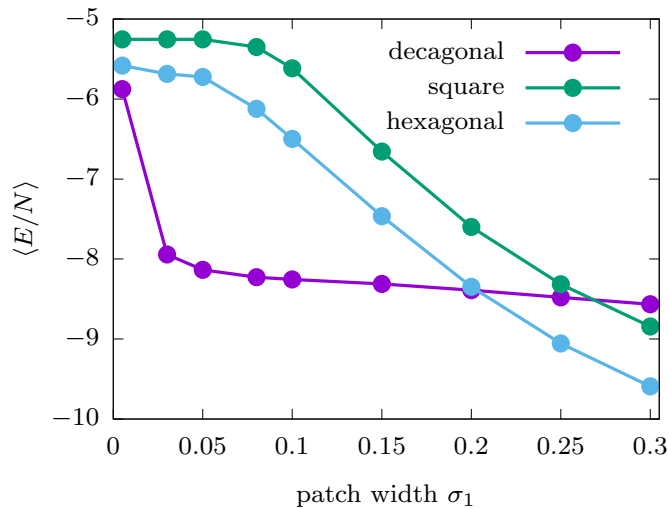


Figure 5.3: Average potential energy per particle of a perfect decagonal, square and hexagonal tiling as function of the patch width  $\sigma_1$ . Further potential parameters read  $\sigma_2 = 0.23$ ,  $n = 2$ ,  $r_0 = d_0$  and we model colloids with ten patches.

deviations from the decagonal angles and  $\langle E/N \rangle$  decreases for all structures. At  $\sigma_1 > 0.2$  the hexagonal tiling is energetically preferred.

### 5.2.3 Systems of colloids with eight patches

We now model particles with eight symmetrically arranged patches and try to stabilize quasicrystals with octagonal symmetry. Perfect octagonal structures possess the lengths  $l_0 = 2 \sin(\pi/8)l_1 \approx 0.77l_1$  and  $l_1$ . In our simulations we support  $l_1$ , i.e. we chose  $r_0 = l_1$ . In case of  $r_0 = l_0$  octagonal structures would be destroyed as will be shown in the next paragraph. Further potential parameters read  $n = 3$  and  $\sigma_2 = 0.29$ , while  $\sigma_1$  is varied. Note that  $\sigma_2$  is larger than for particles with ten patches in order to cover the same area with patches. We adjust a particle density  $\rho \approx 1.21/r_0^2$  of a perfect octagonal Ammann-Beenker tiling. Simulations are started with a perfect octagonal or a square tiling and last  $5 \cdot 10^8$  Monte Carlo steps. Figure 5.4 depicts final configurations at  $T = 0.3\epsilon$ . The temperature ensures mobile particles below melting.

As for particles with ten patches the structures show low positional and orientational order at narrow patch width  $\sigma_1 = 0.005$ . At  $\sigma_1 = 0.02$  the octagonal quasicrystal remains stable and the angular distribution function shows sharp peaks. As for the decagonal quasicrystal, the structure is stabilized by the supported length scale in combination with the orientational part. At  $\sigma_1 = 0.15$  the perfect tiling dissolves and the peaks broaden. Broad patch widths  $\sigma_1 > 0.2$  cause a co-

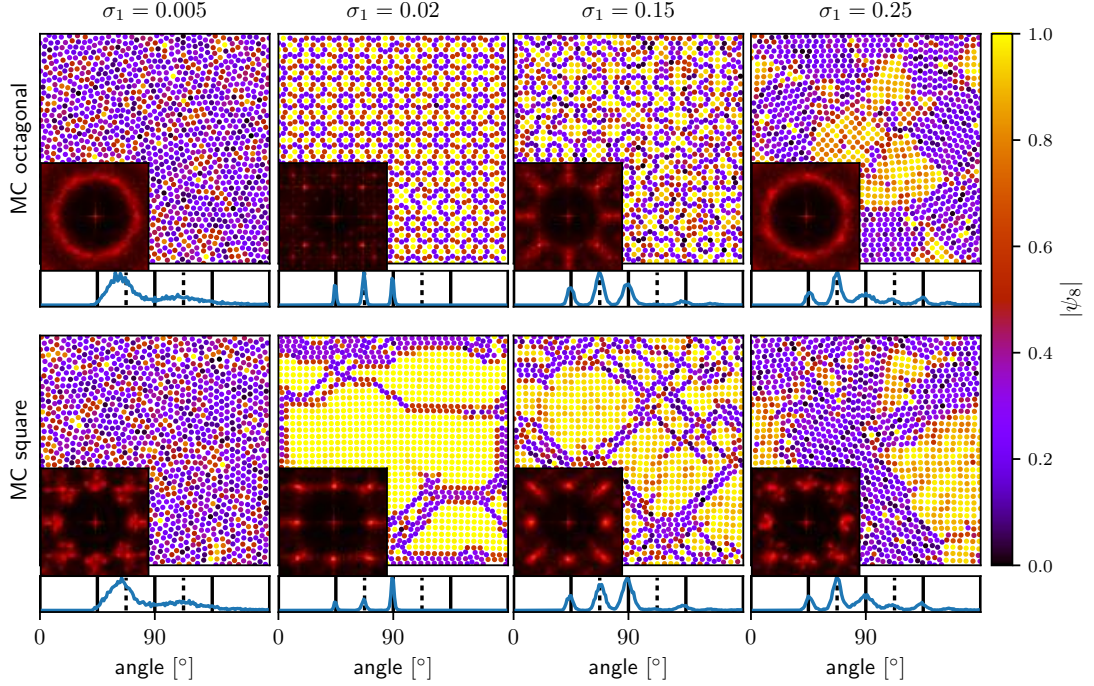


Figure 5.4: Configurations of  $N = 1393$  particles obtained from simulations with an initial octagonal Ammann-Beenker tiling (upper row) and an initial square configuration (lower row). We vary the patch width  $\sigma_1 = 0.005$  (first column),  $\sigma_1 = 0.02$  (second column),  $\sigma_1 = 0.15$  (third column) and  $\sigma_1 = 0.25$  (fourth column). Further potential parameters read  $\sigma_2 = 0.29$ ,  $n = 3$ ,  $r_0 = l_1$  and we model colloids furnished with eight patches. The color code illustrates the bond-orientational order parameter  $|\psi_8|$ . The insets depict the corresponding structure factors. The graphs below the configurations show the corresponding angular distribution functions. The black lines serve as guide to the eye and indicate perfect octagonal bond angles, i.e.  $2\pi j/8, j = 1, \dots, 8$ . The dashed black lines indicate angles in between, i.e.  $67.5^\circ$  and  $112.5^\circ$ . All simulations were performed at  $T = 0.3\epsilon$ .

existence of a square and zigzag phase with a predominant length  $r_0$ . The zigzag phase is a periodic lattice that consists of the same rhombs as in the Ammann-Beenker tiling. Zigzag and square phase both support angles of an octagonal tiling. The desired density is reached by a coexistence of both phases.

The initial square phase does not arrange to an octagonal tiling at any patch width. Instead, parts of the square lattice rearrange into the denser zigzag phase. The number of rearranging particles increases with the patch width. Only a few local octagonal elements are found. We also perform the simulations with initial zigzag and random phases. The final structures are similar like the ones obtained from initial square phases.

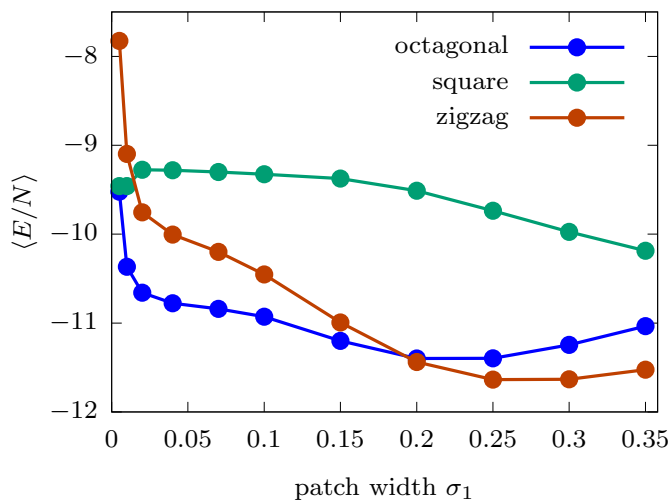


Figure 5.5: Average potential energy per particle of a perfect octagonal, square and zigzag tiling as function of the patch width  $\sigma_1$ . Further potential parameters read  $\sigma_2 = 0.29$ ,  $n = 3$ ,  $r_0 = l_1$  and we model colloids with eight patches.

Figure 5.5 illustrates the average potential energy per particle  $\langle E/N \rangle$  of a perfect octagonal, square and zigzag lattice as a function of the patch width  $\sigma_1$ . All structures have the density  $\rho \approx 1.21/r_0^2$  of a perfect octagonal tiling. At low patch widths  $\sigma_1 \leq 0.15$  the perfect octagonal quasicrystal is clearly energetically favored, while at larger patch widths the zigzag phase possesses the lowest energy.

### 5.2.4 Support of different length scales

We now study the arrangements of particles when the potential minimum is varied and another length scale is supported. To test structures with decagonal symmetry we support the long length with  $r_0 = d_1$ . Further simulation parameters remain unchanged. We choose  $\sigma_1 = 0.03$  for which the perfect decagonal tiling is stabilized

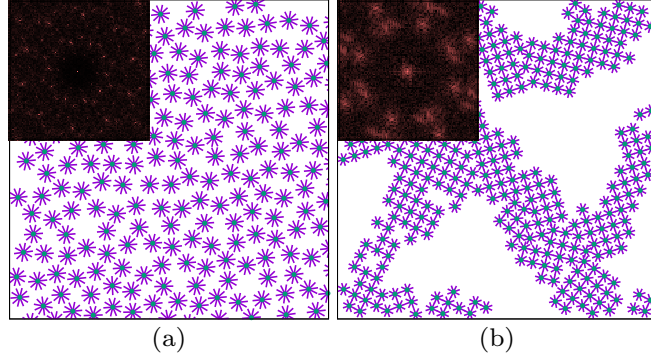


Figure 5.6: Variation of the potential length scale  $r_0$ . We depict configurations of particles with (a) ten patches and supported length  $r_0 = d_1$  and (b) eight patches and supported length  $r_0 = l_0$ . The illustrated configurations are obtained from simulations with random initial states. Patches are indicated by arms around the particles. Structure factors are shown as insets.

in case of  $r_0 = d_0$ . In our simulations, we do not obtain decagonal structures, i.e., neither a perfect quasicrystal remains stable, nor a random configuration self-assembles into a quasicrystal. However, in both cases the final configurations contain some decagonal motifs and pentagons. The structure factor indicates these motifs as illustrated in Figure 5.6 (a). Patches are illustrated by arms around the particles. Patches of particles that are separated by the long length are oriented towards each other. Patches of particles with shorter distance do not obey the correct orientation.

In the case of particles with eight patches we have so far supported the long length  $r_0 = l_1$  and now will test to support the short length, i.e.  $r_0 = l_0$ . Further parameters are kept as before, and we choose  $\sigma_1 = 0.02$ . Independent of the initial configuration the particles arrange to dense square tilings with distances  $r_0$  between nearest neighbor particles and with voids as shown in Figure 5.6 (b) for  $N = 392$  particles. Note that the 8-fold symmetry suggested by the structure factor results from domains of square tilings that are rotated against each other.

### 5.2.5 Formation of quasicrystals from random initial configurations

So far we have found metastable octagonal or decagonal quasicrystals. These structures can be observed if the simulations are started with the respective structures. In the following we check if we can obtain quasicrystals with octagonal or decagonal symmetry from a random initial state. We first model colloids furnished with ten patches. We choose the same potential parameters as in previous simulations

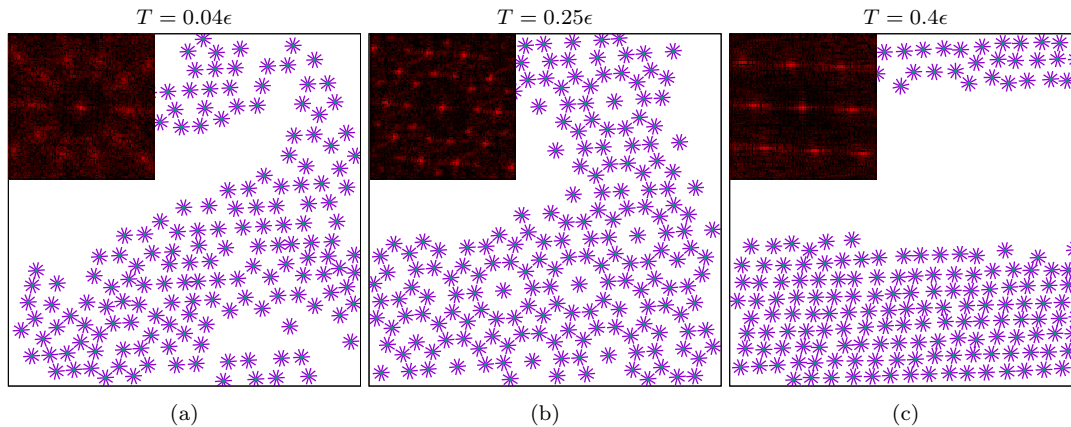


Figure 5.7: Configurations of  $N = 191$  particles with ten symmetrically arranged patches at the surface. Patches are illustrated by arms. Starting from the fluid we simulate the system at (a)  $T = 0.04\epsilon$  and increase the temperature to (b)  $T = 0.25\epsilon$  and (c)  $T = 0.4\epsilon$ . The potential parameters read  $\sigma_1 = 0.03$ ,  $\sigma_2 = 0.23$ ,  $n = 2$ ,  $r_0 = d_0$ . The insets show the structure factors of the corresponding configurations.

and stabilize the short length  $d_0$ . Simulations with a low temperature  $T = 0.04\epsilon$  result in elements of a decagonal tiling (see Figure 5.7 (a)) and indications of a decagonal symmetry provided by the structure factor (inset of Figure 5.7 (a)). We increase the temperature of this configuration to  $T = 0.25\epsilon$ . Beside conventional displacement and rotation moves we propose additional jumps that can lead to phasonic flips, i.e. rearrangements within quasicrystals that do not change or at least almost not change the total energy of the structure [11, 12, 14, 265]. Such flips are implemented by proposing displacements in a random direction with the distance  $d_{\text{flip}} = d_1 - d_0$  at which flips usually occur. We propose such possible phasonic flip steps with a probability of  $p = 0.2$ . We obtain a quasicrystalline arrangement of particles as illustrated in Figure 5.7 (b). The patches indicated by arms around the particles are nicely oriented towards each other. The long length scale is supported indirectly by the energy gain provided by the angular term. However, we observe an excess of the short length compared to the perfect tiling and voids arise. The structure is metastable and increased temperatures lead to a transition to a triangular phase as depicted for  $T = 0.4\epsilon$  in Figure 5.7 (c).

In case of colloids with eight patches we also apply the potential parameters as in previous investigations and stabilize the long length  $l_1$ . Even for low temperatures the particles arrange to a square tiling. Patches are oriented towards the patches of nearest and next nearest neighbors. Since square tilings are also supported by eight patches, it is hard to build an octagonal quasicrystal. For temperatures

$T < 10^{-4}$  we obtain random frozen arrangements that again turn into square tilings at increased temperatures.

### 5.3 Conclusion

We have studied how quasicrystals can be stabilized in patchy colloidal systems in two dimensions. Even though only one typical length can be supported by the potential minimum, the quasicrystalline order with two incommensurate lengths is induced by an additional anisotropic contribution. While it is known that dodecagonal orderings can be easily found even in systems in which the number of patches seems not to fit to the 12-fold symmetry [119–121], octagonal and decagonal quasicrystals seem to be harder to realize in soft-matter systems. Here we have shown that one needs narrow patches corresponding to sharply enforced preferred binding angles in order to stabilize quasicrystals with 8- or 10-fold symmetry. We have shown that these structures are energetically favored in case of narrow patches and that they can stay stable in Monte Carlo simulations that have been started with the respective patterns.

We have also shown that decagonal quasicrystals can be obtained from random initial conditions by cooling and subsequent reheating. Therefore, there are protocols that can be used to receive these quasicrystals as metastable structures. However, it remains an open question whether octagonal or decagonal structures might exist in thermal equilibrium in systems with patchy colloids (maybe with modified potentials).

Our results contribute to a better understanding of why metallic quasicrystals do not possess dodecagonal symmetry as often as soft-matter quasicrystals [22]. The reason might be due to preferred binding angles that are usually given in a very sharp way in case of metallic systems. Note that our findings are consistent with experimental results of quasicrystals in metallic alloys. Most stable metallic quasicrystals possess icosahedral symmetry. Also a few decagonal phases have been observed, while octagonal structures provide least examples and are usually metastable [16].

# Chapter 6

## Growth of two-dimensional colloidal quasicrystals

While in the previous Chapters we considered systems with fixed numbers of particles, we now model the growth of intrinsic colloidal quasicrystals.

The growth of quasicrystals is more complex than the growth of periodic crystals. In [115, 116] dynamical phase field crystal models [370, 371] with an additional second length scale (see also [372]) are applied to study the growth dynamics of two-dimensional decagonal or dodecagonal soft-matter quasicrystals from a seed. Dependent on the distance from the triple point, either stable defect-free quasicrystals or metastable random tilings with incorporated phasonic flips are observed [115]. In the case of the growth from two seeds phasonic strain fields emerge when the seeds converge and relax later on due to local phasonic flips [116]. The growth processes occur without dislocations which are probably suppressed because the excitation of phasons enables the relaxation of stresses. Approaches that are similar to the phase field crystal model have been used to study Faraday waves [112], cluster quasicrystals [114], or particles on quasicrystalline substrates [372, 373] in order to mimic colloidal particles in laser fields [7, 8, 27, 129]. Other variations of the free energy functional have also been considered, e.g. a mean field density functional theory has been employed to reveal the formation of complex structures [110, 374] and fundamental measure theory has been used in order to study the structure and the growth dynamics on incommensurate and/or quasicrystalline substrates [264, 344, 369].

Additionally, the growth behavior can be studied, e.g. with molecular dynamics simulations that have been employed to investigate atomic dodecagonal quasicrystals growing from clusters that form in the melt [375] or to determine the formation of quasicrystals [92, 102, 376–378].

In experimental studies on decagonal metallic Al-Ni-Co quasicrystals phasonic flips and their healing have been observed during a growth process that as a consequence

leads to almost defect- and excitation-free structures [379]. Further experiments investigate the interface-driven formation and growth of dodecagonal soft-matter oxide quasicrystals Ba-Ti-O<sub>3</sub> on periodic substrates [380, 381].

Finally, perfect quasicrystals may be grown by putting together at least two kinds of basic tiles according to local matching rules (see, e.g. [228, 382]).

In this Chapter we employ Brownian dynamics simulations to model the growth of two-dimensional colloidal quasicrystals out of vapor. We adjust different pair interactions that are known to stabilize decagonal and dodecagonal quasicrystals. The goal of this Chapter is to gain an understanding under which conditions quasicrystals can grow and what properties they possess.

We organize the Chapter in the following way: In Section 6.1 we study the growth of two-dimensional decagonal colloidal quasicrystals with an isotropic interaction between the colloids. In Section 6.2 the studies are extended to dodecagonal structures with either isotropic or anisotropic interactions. We conclude in Section 6.3. The Chapter is based on investigations that we published in [C] and [D]. The concerned Sections and a detailed contribution of the authors are given in the *List of publications*.

## 6.1 Growth of two-dimensional decagonal colloidal quasicrystals

In this Section we model the growth process of colloidal particles interacting by an isotropic pair potential of the Lennard-Jones–Gauss type [14, 28, 29]. We focus on structures with decagonal symmetry. Our goal is to study the growth that is obtained by sequential deposition of particles at a free surface. This corresponds to the growth at a solid-gas interface or the growth from a melt in the case that no significant homogeneous nucleation or cluster formation takes place. Note that we do not explore the growth for a case where clusters form in a supercooled liquid before they attach to the surface. We obtain nicely grown decagonal structures for appropriate simulation parameters. The phasonic degrees of freedom contribute to a nearly defect-free growth.

We organize the Section as follows: First, we explain the simulation setup. Afterwards, the results are presented. We study how the mobility of the particles at the surface depends on the temperature. Furthermore, we quantitatively identify and analyze the structures that result from the growth process by employing bond-orientational order parameters. The shapes and properties of the surfaces are studied and the occurrence of phasonic flips in the structures is examined. Finally, we vary the potential parameters and explore exemplary resulting grown structures.

### 6.1.1 Simulation setup and determination of layers

We apply two-dimensional Brownian dynamics simulations with particles interacting according to the Lennard-Jones–Gauss potential  $V_{LJG}(r)$  as described in Subsection 3.4.1. In accordance with [28] we choose the potential parameters  $r_G = 1.52\epsilon = 1.8$  and  $\sigma^2 = 0.02$  that cause a double-well potential with two incommensurate length scales. At zero pressure and within an appropriate temperature range the potential supports the formation of decagonal quasicrystals for the chosen parameters. The density and temperature values for which the quasicrystal is stable as well as the neighboring phases are shown in Figure 6.1.

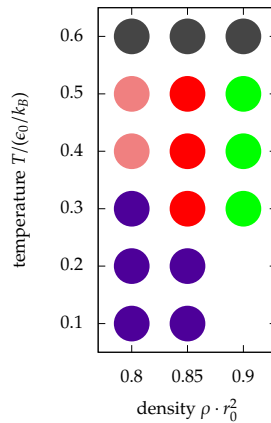


Figure 6.1: Rough overview of the arising equilibrium phases in bulk obtained by simulations started from the fluid. Dependent on the temperature  $T$  and the number density  $\rho = N/A$  with the number of particles  $N$  and the size of the simulation box  $A = L_x L_y$ , we obtain quasicrystalline structures with decagonal symmetry (red) at a density for which the pressure is roughly zero, complex periodic tilings (green) at larger densities, a liquid phase (grey) at large temperatures, a coexistence of quasicrystals and gas (lightred) at smaller densities, and a coexistence between the quasicrystalline and the triangular phase (darkpurple) at low temperatures. The triangles occur with an interparticle distance that corresponds to the long potential length scale.

In our study of the growth of a quasicrystalline structure we aim to prevent homogeneous nucleation that occurs, e.g. in an undercooled liquid (see [375]). Therefore, we model the growth at a solid-gas interface where the grown structure is at the bottom of the simulation box and particles are inserted at the top (see Figure 6.2). New particles are added with a certain rate  $R$  at the top of the simulation box. If not noted otherwise, the  $x$ -coordinates are random. An external force given by a gravitational-like force  $\mathbf{F}_g$  in negative  $y$ -direction causes the deposition of the injected particles on the surface.

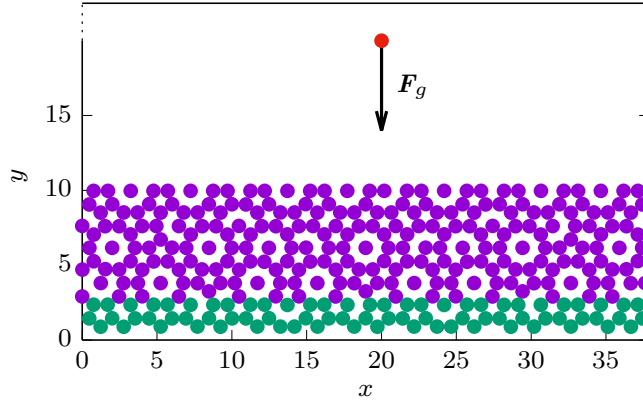


Figure 6.2: Initial setup of the simulation. The ground particles build a perfect decagonal quasicrystal. The lowest particles (green) are pinned. Injected particles (red) deposit due to a gravitational force. The exemplary box size results in a pressure-free state for a temperature  $T = 0.50$ .

As soon as the injected particle is trapped by the interaction with particles of the grown structure we turn off the force  $\mathbf{F}_g$  in order to avoid distortions of the structure. To be specific, a particle is considered to be trapped at the surface and therefore  $\mathbf{F}_g$  is not needed any more if its distance to the grown structure is  $d = 1.59$  or smaller, which is slightly larger than the second potential length scale. We study the growth process for various sedimentation rates which are given by the number of added particles per time. We simulate growth rates  $R \in [0.125/\tau_B; 20/\tau_B]$ . Note, the number of depositing particles per length is dependent on the box size  $L_x$  which we quantify in the next paragraph.

We start with 322 particles of a perfect decagonal quasicrystal on the bottom of the simulation box. In order to obtain the perfect quasicrystal, we decorate the brightest spots of the well-studied interference pattern of five laser beams [8, 125, 325]. To be specific, for the particle density that we are interested in colloids are placed in the minima of the laser potential that are deeper than 0.4 of the deepest potential minimum (see also Section 4.2). According to the described method the growing structures adjust themselves to a pressure  $p = 0$ . Thus, we choose the particle density of the initial quasicrystal such that it corresponds as well to a pressure-free state for the particular considered temperature.

In our setup the undermost 76 particles of the quasicrystal are pinned during the simulation while all other particles may move (see Figure 6.2). Thus, the simulation box is closed for small  $y$ -values and a free boundary can be used in  $+y$ -direction. In  $x$ -direction we employ periodic boundary conditions. We choose the box dimension  $L_x$  in  $x$ -direction in a way that a periodic approximant of the quasicrystal fits into the box. Therefore, the box length  $L_x$  should be a multiple

of the length scales given by the lattice vectors  $G_{j,x}$  (see Subsection 3.4.4). However, since the wave vectors are irrational, it is not possible to accommodate an undistorted quasicrystal in the box. We slightly distort the basis vectors in a way that the conditions are fulfilled.

Within the next Subsections we will grow structures according to the described method. For a quantitative characterization of their properties we divide the structures into layers. In the following, we explain the applied procedure.

We start with the identification of the surface particles, which we consider to be the outermost (first) layer. In periodic crystals, surface particles possess a reduced number of nearest neighbor particles compared to the bulk particles. However, in quasicrystals, even in a perfect bulk lattice the number of nearest neighbors might differ from particle to particle. Therefore, we determine the Voronoi volume  $v$  [330] of each particle. For surface particles  $v$  is either infinite or it corresponds to a finite value that is significantly larger than for bulk particles. In our analysis, we consider a particle to be on a surface if its two-dimensional Voronoi volume exceeds a value of  $v = 2.5$ . The next inner (second) layer is built by the nearest neighbors of the particles in the outermost (first) layer, i.e. the particles that are located within a certain distance  $r_{\max}$  around the surface particles. Here we choose  $r_{\max} = 1.58$  such that  $d_2 < r_{\max} < d_3$  with  $d_2$  and  $d_3$  being the positions of the second and respectively third peak of the pair distribution function. Furthermore, a subsequent layer consists of particles that have not been assigned to any layer and that are nearest neighbors of the previous layer. Note that we start the numeration of the layers at the surface, i.e. layers close to the surface are characterized by a low layer number. Two exemplary grown structures with differently colored layers are depicted in Figure 6.3.

Note that in our investigations we evaluate quantities as functions of their distance from the growth front which is measured by the layer number. Therefore, the enumeration of the layers starts at the surface and not at the substrate. For our analysis of the growth process we are interested in the steady state regime where the determined quantities do only depend on the layer number, i.e. the distance from the growth front but not on the absolute elapsed time or the distance from the substrate. In Figure 6.4 we show the temporal development of a structure grown with temperature  $T = 0.50$  and rate  $R = 1/\tau_B$ . In order to illustrate the steady state behavior, we determine the total number of nearest neighbor particles of the first, second, third, 12th and 30th layer at different times (see Figure 6.4(d)). The first (outermost) layer exhibits the lowest number of nearest neighbors while the number of nearest neighbors is larger in the other layers. However, in all cases the respective number of nearest neighbors reaches a constant value after some initial time. This indicates that the system is in a steady state at least concerning the layers that are no longer under the direct influence of the initial substrate.

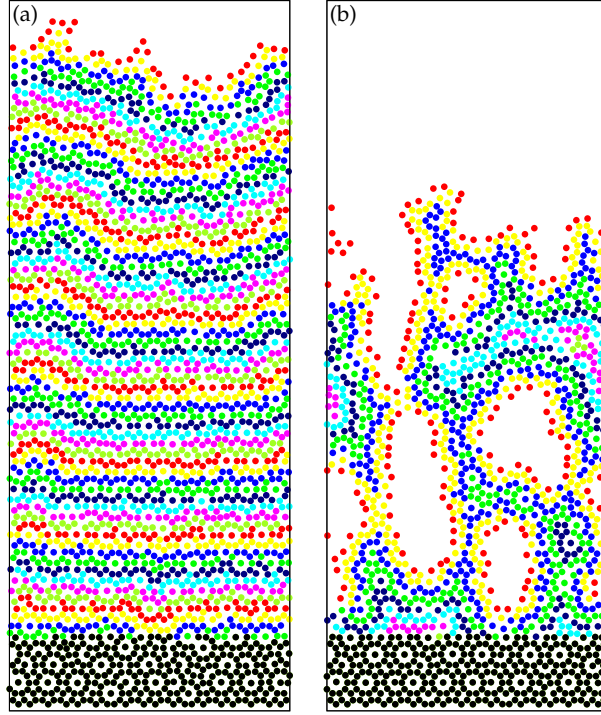


Figure 6.3: Examples of grown structures with particles colored with respect to their associated layers. Black particles on the ground correspond to the initially perfect quasicrystalline structure. (a)  $T = 0.50, R = 10/\tau_B$ . In a nicely grown quasicrystalline structure we identify 64 layers of particles. (b)  $T = 0.30, R = 1/\tau_B$ . In a quasicrystalline structure that is interrupted by voids we obtain 8 grown layers of particles. The determination of layers starts from all possible surfaces (particles shown in red), including the surfaces towards the voids.

### 6.1.2 Influence of surface diffusion

While usually particles are injected at random  $x$ -positions, in this Subsection we inject particles with fixed initial  $x$ -positions  $x_{\text{fix}} = L_x/2$ . The goal is to qualitatively investigate the diffusion on the surface. In Figure 6.5 we depict the grown structures arising for high and low temperatures, i.e.  $T = 0.50$  and  $T = 0.30$ , as well as high and low sedimentation rates  $R = 1/\tau_B$  and  $R = 0.125/\tau_B$ .

In systems grown with a large temperature  $T = 0.50$  and a low rate  $R = 0.125/\tau_B$  (Figure 6.5 (a)) the thermal energy of the particles is sufficiently large to let the particles widely diffuse on the surface during the time until the next particle is injected. Thus, the grown structure forms a cone with a large opening angle. A larger rate  $R = 1/\tau_B$  (Figure 6.5 (b)) results in less time for the injected particles to diffuse on the surface. Accordingly, the arising cone becomes steeper and the

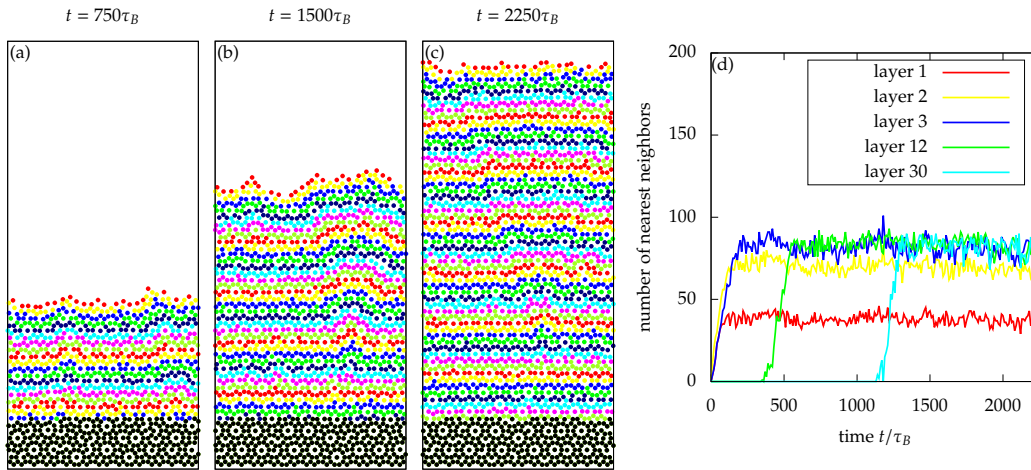


Figure 6.4: (a)-(c) Exemplary temporal evolution of a structure grown with temperature  $T = 0.50$  and sedimentation rate  $R = 1/\tau_B$ . The structure is shown after (a)  $t = 750\tau_B$ , (b)  $t = 1500\tau_B$  and (c)  $t = 2250\tau_B$ . (d) Total number of nearest neighbor particles of single layers as a function of time. All curves reach a steady state value after a sufficiently long waiting time that guarantees the independence of the respective layer from the initial substrate.

opening angle is smaller.

Regarding the growth with lower temperature  $T = 0.30$  (Figures 6.5 (c) and (d)) the thermal energy of the particles is reduced such that even for a low sedimentation rate  $R = 0.125/\tau_B$  the diffusion of the particles is limited. The structure grows in the shape of a zig-zag branch that hardly narrows with height. The zig-zag shape is caused by the limited possible directions of the surface which are characteristic of a grown quasicrystal as studied in more detail in Subsection 6.1.4. An increased sedimentation rate  $R = 1/\tau_B$  reduces the time for the particles to diffuse on the surface such that a branch grows that is thinner than the one for a smaller sedimentation rate.

Figure 6.5 (e) shows the diffusion on the surface quantitatively by means of the diffusion constant  $D$  as a function of temperature. We receive the diffusion constant by fitting a linear function through the mean square displacement of an injected particle along a free surface, i.e.  $\langle r^2(t) \rangle = 4Dt$ .  $D$  increases with rising temperature which explains the enhanced mobility in Figures 6.5 (a) and (b) in comparison to Figures 6.5 (c) and (d).

To grow a quasicrystal as perfect as possible, the illustrated examples indicate the necessity of large enough temperatures in combination with low enough sedimentation rates during the growth process to give the particles enough thermal energy and time to diffuse along the surface. Given these requirements, the particles may

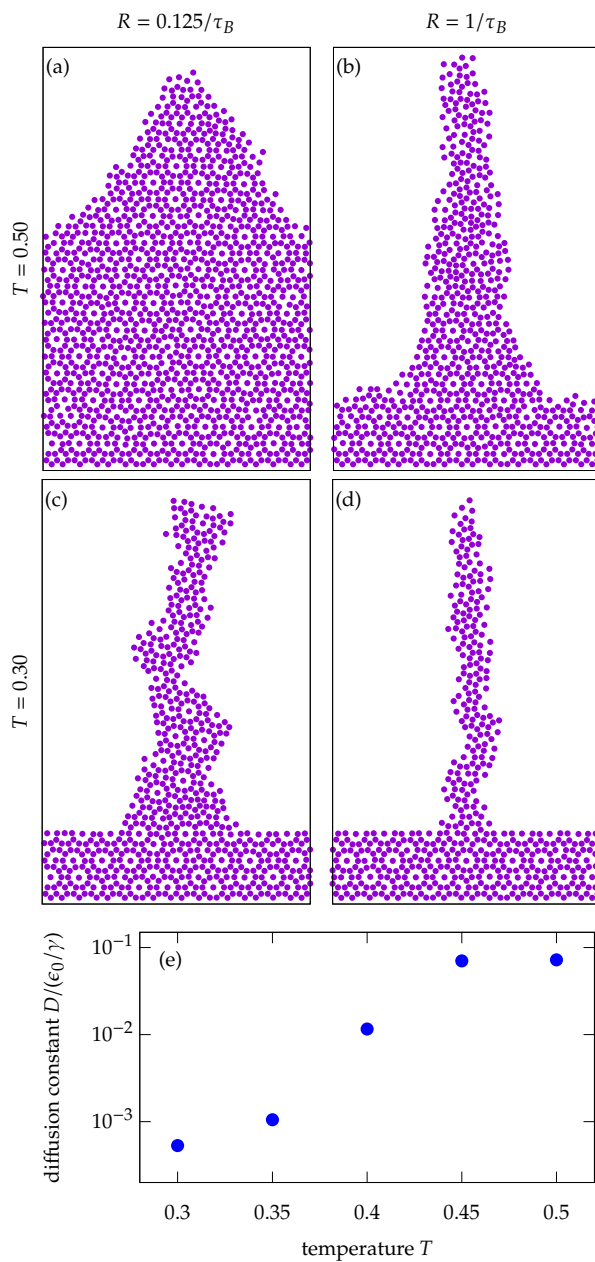


Figure 6.5: (a)-(d) Deposition of particles that are injected at a given position  $x_{\text{fix}} = L_x/2$  on the top of the simulation box. We study the temperatures  $T = 0.50$  (first row) and  $T = 0.30$  (second row) and the rates  $R = 0.125/\tau_B$  (left column) and  $R = 1/\tau_B$  (right column). (e) Diffusion constant  $D$  in units of  $\epsilon_0/\gamma$  of particles injected at a free surface as a function of temperature.

adopt the positions that are prescribed by the underlying ground particles.

### 6.1.3 Bond-orientational order

In the following, we expand our simulations to random initial  $x$ -positions of the injected particles and investigate how the growing structures at a free surface of a quasicrystal depend on the sedimentation rate  $R$  and the temperature  $T$ . The structures are usually composed of tiles known from quasicrystalline or triangular orderings. The triangular part is dominated by triangles with interparticle distances of the long potential length scale. Many grown structures are interrupted by large gaps.

For a quantitative classification of the grown structures we determine the local bond-orientational order parameter  $\psi_m$  (see Subsection 3.5.4) for  $m = 6$ - and for 10-fold rotational symmetry for each particle within the systems.

For particles with  $|\psi_{10}| > |\psi_6|$  the local quasicrystalline order dominates. Analogously, the particles with  $|\psi_6| > |\psi_{10}|$  are assigned to be part of a local triangular structure. We characterize the grown structures according to the fraction  $N_{10}/N$  with  $N_{10}$  denoting the number of particles within a local quasicrystalline arrangement and  $N$  gives the total number of particles in the system. Note, the fraction of particles with assigned local hexagonal surroundings reads  $N_6/N = 1 - N_{10}/N$ . Surface particles and the initial perfect quasicrystalline structure are not included in the calculation. In Figure 6.6 we distinguish the determined structures for various temperatures and sedimentation rates by a color code (see caption).

In addition, Figure 6.7 visualizes snapshots of structures grown with different temperatures and rates. We color each particle individually according to its absolute value of the local bond-orientational order parameter with respect to 10-fold rotational symmetry  $|\psi_{10}|$ .

For temperatures  $T \in [0.25; 0.55]$  and sufficiently low rates we usually observe a domination of the local quasicrystalline order which is indicated by the red color in Figure 6.6. For large temperatures  $T = 0.50$  and rates  $R < 10/\tau_B$  the grown quasicrystalline structure is almost perfect as visualized in the first row of Figure 6.7. The thermal energy is large enough for the particles to diffuse widely at the surface such that most particles reach the positions that are expected due to the quasicrystal that is initially placed at the bottom of the box. Only at the surface the quasicrystalline order decreases which is indicated by particles colored in intermediate colors within the color code bar. Since such surface particles may still diffuse we do not observe perfect decagonal structures at the surface. If the rates are increased we observe an increase of defects. For  $R \geq 10/\tau_B$  there are numerous particles with triangular order as well as some gaps in the structure (see Figure 6.7(d)). A similar behavior is observed for systems grown with  $T = 0.45$  (Figure 6.7, second row). However, here the surface particles arrange

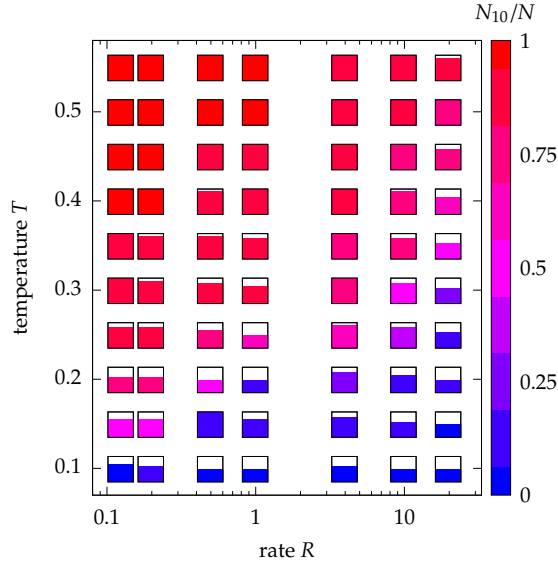


Figure 6.6: Classification of the grown structures dependent on the temperature  $T$  and the sedimentation rate  $R$  in a log-linear plot. The color code represents the number  $N_{10}$  of particles with local quasicrystalline order relatively to the total number of particles  $N$ . Red squares indicate structures that are dominated by local quasicrystalline order, blue squares denote triangular structures. Colors in between suggest a coexistence between both phases. The height of the color bars within the squares is proportional to the area fraction filled by particles, i.e. the lower the color bars, the more gaps occur within the grown structure. Completely filled squares indicate structures without gaps.

in a characteristic way as studied in detail in Subsection 6.1.4.

Structures grown with a lower temperature  $T = 0.35$  and a low rate  $R = 0.125/\tau_B$  (Figure 6.7 (i)) show only a few particles that deviate from the decagonal order. However, gaps and triangular regions start to arise and increase for larger rates (Figures 6.7 (j)-(l)) which reduces the decagonal order.

In general, if the temperature is decreased the dissipation rate decreases as well. For example, for  $T = 0.40$  gaps occur for  $R \geq 10/\tau_B$  and for  $T = 0.30$  gaps are already observed for  $R \geq 0.2/\tau_B$ . In structures built with an even lower temperature  $T = 0.25$  the decagonal order is already for low rates  $R = 0.125/\tau_B$  partly destroyed by triangular elements or gaps (Figure 6.7 (m)). Gaps arise because the thermal energy is too low or respectively the time is too short for the particles to widely diffuse on the surface. Consequently, the particles remain close to the position where they first touch the surface. For even larger rates the gaps are combined with a growing fraction of triangular regions (see Figures 6.7 (n)-(p)) since the time to adopt the correct ratio of short and long lengths

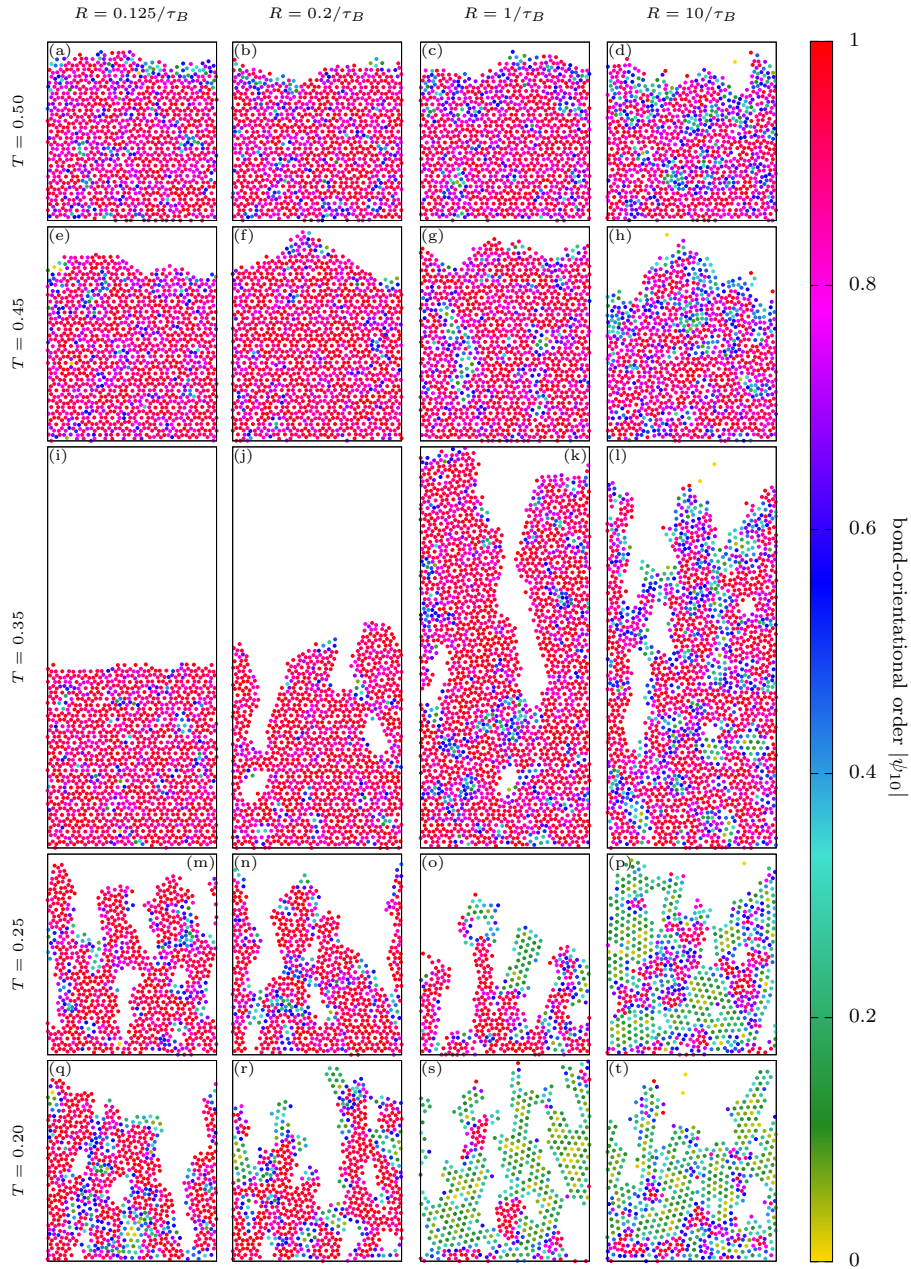


Figure 6.7: Phases resulting from the growth with a temperature  $T = 0.50$  (first row),  $T = 0.45$  (second row),  $T = 0.35$  (third row),  $T = 0.25$  (fourth row) and  $T = 0.20$  (fifth row) and a sedimentation rate  $R = 0.125/\tau_B$  (first column),  $R = 0.2/\tau_B$  (second column),  $R = 1/\tau_B$  (third column) and  $R = 10/\tau_B$  (fourth column). The particles are colored according to their absolute value of the local bond-orientational order parameter  $|\psi_{10}|$ . The lower borders of the grown structures are shown right above the initially perfectly arranged ground particles.

becomes smaller. Accordingly, an increased number of particles gets stuck in the deeper second potential minimum and contributes to triangular orderings of the long length.

For even lower temperatures the triangular regions increase (see Figures 6.7 (q)-(t) on the example of  $T = 0.20$ ). Systems grown with the lowest investigated temperature  $T = 0.10$  are nearly exclusively composed of triangular arrangements interrupted by gaps for all applied rates (see blue colored squares in Figure 6.6 for  $T = 0.10$ ).

In Figure 6.8 we quantitatively plot the average bond-orientational order parameters  $\langle |\psi_{10}| \rangle$  and  $\langle |\psi_6| \rangle$  as functions of the layers. The average is taken over the particles within the considered layer and over configurations. The numbers of averaged configurations are  $N_{\text{av}} = 800$  (for systems grown with  $R = 0.125/\tau_B$  and  $R = 0.2/\tau_B$ ),  $N_{\text{av}} = 450$  ( $R = 0.5/\tau_B$ ),  $N_{\text{av}} = 230$  ( $R = 1/\tau_B$ ),  $N_{\text{av}} = 400$  ( $R = 4/\tau_B$ ),  $N_{\text{av}} = 250$  ( $R = 10/\tau_B$ ) and  $N_{\text{av}} = 100$  ( $R = 20/\tau_B$ ).

The Figures 6.8 (a) and (b) display  $\langle |\psi_{10}| \rangle$  for systems grown with constant  $T = 0.50$  and various rates. For low rates  $R \leq 1/\tau_B$  we obtain  $\langle |\psi_{10}| \rangle \approx 0.7$  in the very first layer. Since the first layer consists of the outermost surface particles, the particles may still diffuse and are not arranged in a perfect quasicrystalline order. In the next layers, the order quickly increases until a constant value of about  $\langle |\psi_{10}| \rangle = 0.85$  is reached for layers larger than six. Since the orientational order is very similar in the displayed systems, the curves partly overlay with each other. The dotted line gives the reference value of  $\langle |\psi_{10}| \rangle \approx 0.87$  for an initially perfect system equilibrated at  $T = 0.50$ . The slightly lower value in our grown systems is probably due to a slightly larger number of defects built in during the growth process. For larger rates  $R > 1/\tau_B$  the orientational order increases more slowly: For  $R = 4/\tau_B$  a constant value is reached after about 17 layers, and in systems grown with  $R \geq 10/\tau_B$  a significantly increased number of defects prohibits the achievement of the maximal value of  $\langle |\psi_{10}| \rangle$  as obtained for lower rates.

The Figures 6.8 (b) and (c) emphasize  $\langle |\psi_{10}| \rangle$  within the uppermost surface layers. In (b) we show a magnification of the previously described systems with constant  $T = 0.50$  and various rates  $R$  and (c) depicts systems with a constant rate  $R = 0.125/\tau_B$  and various temperatures  $T$ . For reasons of clarity we only evaluate the temperatures  $T = 0.20, 0.30, 0.40$  and  $0.50$ . By trend, we obtain the best decagonal order in systems grown with low rates and low temperatures. However, systems grown with very low temperatures  $T \leq 0.20$  provide an exception: Here,  $\langle |\psi_{10}| \rangle$  decreases due to the formation of triangular elements.

Within the surface layers of the grown structures we observe an increased number of triangular elements. Thus, in Figure 6.8 (d) and (e) we present the development of the orientational order with respect to 6-fold rotational symmetry.  $\langle |\psi_6| \rangle$  has its largest value in the upper layers for all rates and temperatures. In contrast to  $\langle |\psi_{10}| \rangle$  we obtain the largest values for systems grown with large rates and large

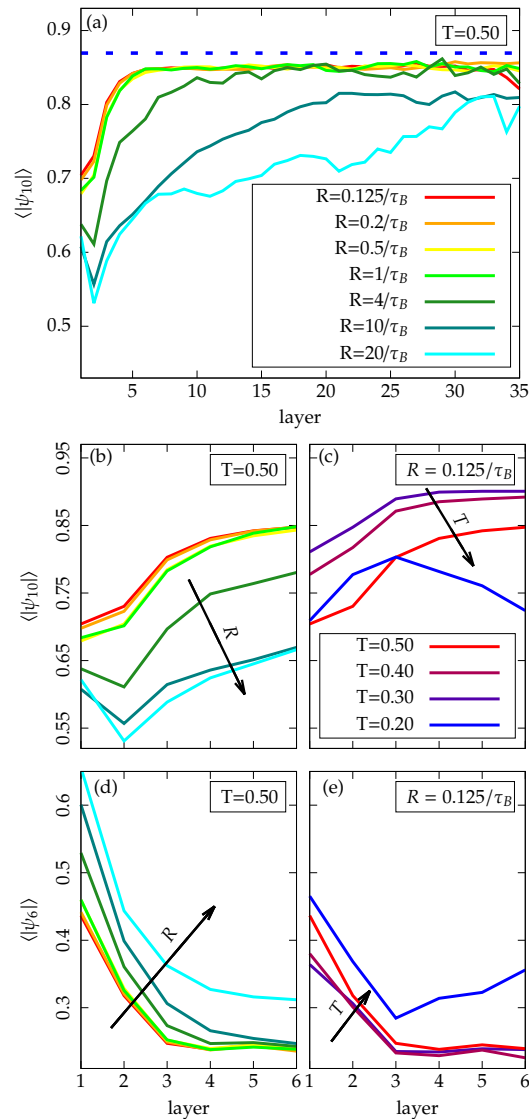


Figure 6.8: (a) Averaged absolute value of the bond-orientational order parameter  $\langle |\psi_{10}| \rangle$  as a function of the layer for systems grown with a constant temperature  $T = 0.50$  and various sedimentation rates  $R$ . The dotted line gives an average reference value of  $\langle |\psi_{10}| \rangle$  in a perfect structure equilibrated at  $T = 0.50$ . (b) and (c) Course of  $\langle |\psi_{10}| \rangle$  within the uppermost six layers for (b) a constant temperature  $T = 0.50$  and various rates  $R$  and for (c) a constant rate  $R = 0.125/\tau_B$  and various temperatures  $T$ . Note that (b) is a magnification of (a) and that the same color code is used. (d) and (e) Course of  $\langle |\psi_6| \rangle$  within the uppermost six layers. The same color code is used as in (a) and (c). The systems are grown with (d) a constant temperature  $T = 0.50$  and various rates  $R$  and (e) a constant rate  $R = 0.125/\tau_B$  and various temperatures  $T$ .

temperatures: The larger  $R$  and respectively  $T$ , the less time and respectively thermal energy remains for the deposited particles to free from the deeper second potential minimum. The consequence are hexagonal arrangements. Within the deeper layers  $\langle |\psi_6| \rangle$  quickly decreases and reaches constant values of about  $\langle |\psi_6| \rangle = 0.24$ . An exception are systems grown with the largest rate  $R = 20/\tau_B$  and respectively low temperatures  $T \leq 0.30$ . Here, local triangular order leads to an increase of  $\langle |\psi_6| \rangle$ .

### 6.1.4 Surfaces

The diffusion of particles along the surface as well as the order of the grown structures are mainly determined by the temperature and sedimentation rate with which the particles deposit (see Subsections 6.1.2 and 6.1.3). In addition, we observe characteristic shapes and arrangements of the surfaces. Typical surfaces of systems grown with various temperatures and rates may be observed in the snapshots in Figure 6.7 which we will now discuss in this respect.

For a high temperature  $T = 0.50$  as displayed in the first row of Figure 6.7 we receive quasicrystalline structures with rough surfaces. The large thermal energy causes large thermal fluctuations resulting in a rather disordered arrangement of the particles at the surface. Here, the applied rate does not have an influence on the degree of roughness.

In systems grown with lower temperatures (e.g.  $T = 0.45$  and  $T = 0.35$  as shown in Figure 6.7, second and third row) the particles form facets along the surfaces. We observe the tendency of the surface particles to build straight lines parallel to the five symmetry axes of the decagonal quasicrystal. For  $T = 0.35$ , increased sedimentation rates result in a rising number of gaps within the structure (see also Subsection 6.1.3) with extended surface lines. Note in particular the extremely nicely grown surface with wide straight facets in Figure 6.7 (k). Moreover, the local arrangement of the particles at the surface is mainly given by cuts through decagons around a central particle such that the long potential length scale dominates at the surface.

For even lower temperatures  $T = 0.25$  and respectively  $T = 0.20$  (Figure 6.7, fourth and fifth row) and in particular for high sedimentation rates the grown systems show areas of hexagonal order which on the surface also arrange along the symmetry lines of the hexagonal structure.

For a quantitative characterization of the surfaces we calculate the distribution of lengths of facets. Each surface particle  $i$  is connected with the next surface particle  $i + 1$  in front and together they build a bond vector  $\mathbf{r}_i$  (see Figure 6.9 (a)). Each bond vector is projected onto the nearest symmetry direction of the quasicrystal. A sequence of bonds with the same direction is referred to as a straight surface facet. For each bond  $\mathbf{r}_i$  we calculate the number  $N_b$  of following bonds that point

in the same direction. By averaging over all starting vectors  $\mathbf{r}_i$  we determine the cumulative probability  $P(N_b)$  that  $N_b$  bonds build a straight surface facet. Note, we here either apply bond vectors from a following particle  $j$  to its next neighbor  $j + 1$  or respectively to its second next neighbor  $j + 2$ . Thus, the surface is still considered to be straight if there are single particles that have not yet found a position fitting to the facet.

The Figures 6.9 (b) and (c) illustrate the probabilities  $P(N_b)$  of finding facets composed of  $N_b$  bonds for selected systems depicted in Figure 6.7. Note, our usual choice of parameters for the analysis ( $T = 0.50$  and various rates) is not meaningful for a study of facets because for  $T = 0.50$  we obtain a rough surface. Instead, we apply the calculation for convenient constant rates  $R = 0.2/\tau_B$  and  $R = 1/\tau_B$ .

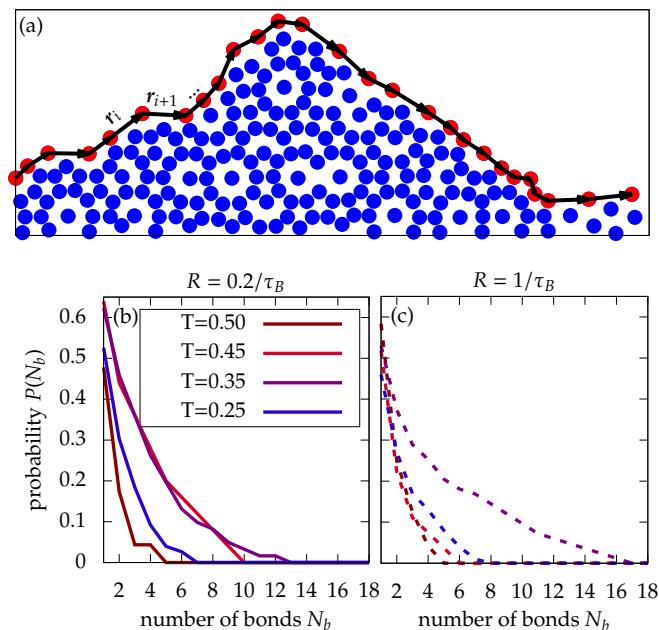


Figure 6.9: (a) Bond vectors  $\mathbf{r}_i$  between neighboring surface particles (red) of a grown structure. (b) and (c) Probability  $P(N_b)$  for a surface particle to be part of a straight facet that goes on for at least  $N_b$  bonds in one direction. We show an analysis of the systems illustrated in Figure 6.7 that are grown with  $R = 0.2/\tau_B$  (left column) and  $R = 1/\tau_B$  (right column) for various temperatures in each case.

$P(N_b)$  decreases most slowly for systems grown with temperature  $T \leq 0.45$  in which straight facets are observed. We obtain the longest facets for systems grown with  $R = 1/\tau_B$  and  $T = 0.35$ .  $P(N_b)$  reaches finite values up to  $N_b = 17$  (see Figure 6.9 (c)). For systems grown with the same rate  $R = 1/\tau_B$  and temperatures  $T = 0.45$  and respectively  $T = 0.25$  the facets are shorter. In a system grown with the largest applied temperature  $T = 0.50$  the facets are not longer than  $N_b = 5$

bonds which reflects the roughness of the surface. Note, since for  $T = 0.20$  the fraction of triangular elements dominates we do not study the surface for this temperature.

For systems grown with  $R = 0.2/\tau_B$  as illustrated in Figure 6.9 (b) we observe the longest facets for  $T = 0.45$  and  $T = 0.35$  which is also supported by the slowest decay of  $P(N_b)$ . Again, for  $T = 0.50$  the decay is fastest due to disordered surface particles.

Beside the characteristic shapes of the grown surfaces, we observe an increased appearance of neighbors with the long distance at the surface. Hence, we analyze the fraction of nearest neighbors with a distance of the long and respectively short length scale, denoted by  $N_l$  and respectively  $N_s$ . To be precise, we depict the fraction  $f_l = N_l/(N_l + N_s)$  of neighbors  $N_l$  with a long distance relative to the total number of nearest neighbors. Figure 6.10 illustrates  $f_l$  dependent on the layer for systems grown with various temperatures and sedimentation rates.

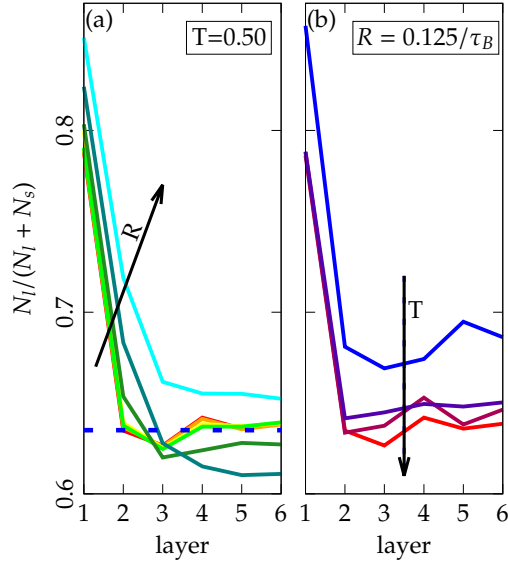


Figure 6.10: Fraction of nearest neighbors  $N_l$  with a distance of the long length scale relative to the number of all nearest neighbors  $N_l + N_s$  as a function of the layer. (a) The temperature is constant  $T = 0.50$  and the rates are varied. The dotted line marks the reference value of  $f_l$  in a perfect system equilibrated at  $T = 0.50$ . (b) The rate is constant  $R = 0.125/\tau_B$  and the temperatures are varied. The color codes correspond to the ones in Figure 6.8.

In all studied systems, the fraction  $f_l$  of neighbors with the long distance is largest within the outermost surface layers since deposited particles first fall in the second potential minimum.  $f_l$  decreases for an increasing layer index.

In Figure 6.10 (a) we first investigate systems grown with a constant temperature

$T = 0.50$  and various sedimentation rates.  $f_l$  is largest for large sedimentation rates since the particles have only little time to arrange properly at the surface and a large number of particles remains in the second potential minimum.  $f_l$  decreases up to layer five and remains approximately constant for deeper layers. For low rates  $R < 10/\tau_B$  we achieve values in the field of the reference value  $f_{\text{ref}} \approx 0.653$  that we obtain from a perfect quasicrystal equilibrated at  $T = 0.50$ . For the largest applied rate  $R = 20/\tau_B$  the fraction  $f_l$  lies above the reference value. Here, the particles do not have the time to arrange properly such that triangles of the long potential length scale arise. For the next lower rate  $R = 10/\tau_B$  the fraction  $f_l$  is below the reference value because of an increased number of defects in terms of triangles of the short length scale.

In Figure 6.10 (b) we depict the fraction  $f_l$  for systems grown with a constant rate  $R = 0.125/\tau_B$  and varying temperatures. The higher the temperature, the lower is the fraction of neighbors with the long distance since an increased thermal motion allows the particles to escape from the second potential minimum and to adopt the ideal fraction between long and short distances.

### 6.1.5 Phasonic flips

In quasicrystals with a finite temperature particles may flip to new places due to the phasonic degrees of freedom (see Section 2.5). The number of flipped particles  $N_{\text{flip}}$  divided by the total number of particles  $N$  depends on the temperature [14, 29].

Here, we analyze the fraction of flipped particles within the grown structures. We determine the flipped particles by comparing the positions of the particles to a perfect reference structure, which is a calculated continuation of the quasicrystalline structure that is initially placed at the bottom of the box. Particles are referred to as flipped particles if their positions deviate by more than  $d_{\text{flip}}/2$  from the nearest perfect reference position. Here,  $d_{\text{flip}}$  is the distance that a particle usually is displaced due to a flip. From geometrical considerations one finds  $d_{\text{flip}} = d_2 - d_1$  (see also Subsection 2.5.2) with  $d_1$  and  $d_2$  being the first and second peak of the radial distribution function of the considered system.

In Figure 6.11 we show structures grown with  $T = 0.50$  and various rates. The particles are colored dependent on performed flips, i.e. flipped particles are colored in red and particles that adopt an ideal position – aside from thermal fluctuations – are blue. The grown structures coincide well with the perfect quasicrystalline structure for sufficiently large temperatures in combination with low rates which prevent the formation of gaps or hexagonal regions. In our systems we observe the growth of perfect quasicrystals for  $T \geq 0.50$  and  $R \leq 1/\tau_B$  (see also Subsection 6.1.3 for a characterization of the phases).

For low rates  $R = 0.125/\tau_B$  (Figure 6.11 (a)) only a few particles have flipped with

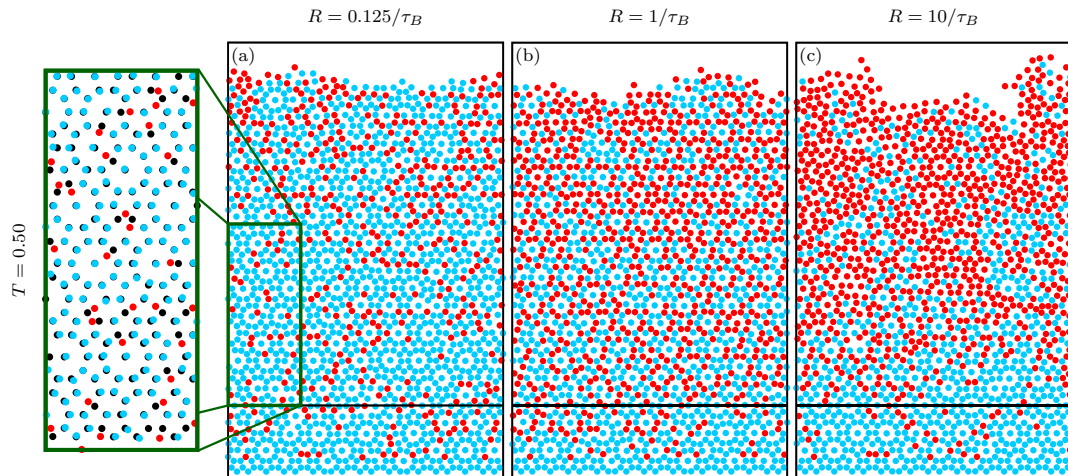


Figure 6.11: Phasonic flips in grown structures with  $T = 0.50$  and various sedimentation rates  $R$ . Particles whose positions significantly differ from the positions expected from the perfect reference structure are called flipped particles and colored in red; unflipped particles are shown in blue. The black horizontal lines mark the border between the initially perfect quasicrystalline pattern and the grown structure. In the magnification on the left the grown structure (blue and red) is shown together with the reference structure (black).

the largest fraction of flipped particles close to the surface. We find a preference for flips that occur along symmetry lines of the decagonal structure. The positions of unflipped particles are in excellent agreement with the positions that are expected for a perfect quasicrystal (see magnified structure in the green box on the left hand side of Figure 6.11).

An increased sedimentation rate (e.g.  $R = 1/\tau_B$  as shown in Figure 6.11 (b)) leads to more flipped particles. For even larger sedimentation rates ( $R = 10/\tau_B$ , Figure 6.11 (c)) the grown structure is blotched with defects and our method to detect flipped particles becomes unreliable.

In Figure 6.12 we show the fraction of flipped particles in each layer for systems with  $T = 0.50$  and low rates  $R \leq 1/\tau_B$ , i.e. for systems that are deep in the quasicrystalline phase according to the orientational order parameter (see also Figure 6.8). For all investigated rates the fraction of flipped particles decreases with the depth of the layer. This decrease of the number of flipped particles in deeper layers is in qualitative agreement with the observations from experiments reported in [379].

As can be expected, a lower sedimentation rate leads to a larger number of particles that find their perfect positions. For the lowest applied rate  $R = 0.125/\tau_B$  the flip fraction approaches the one of a thermally equilibrated structure with the

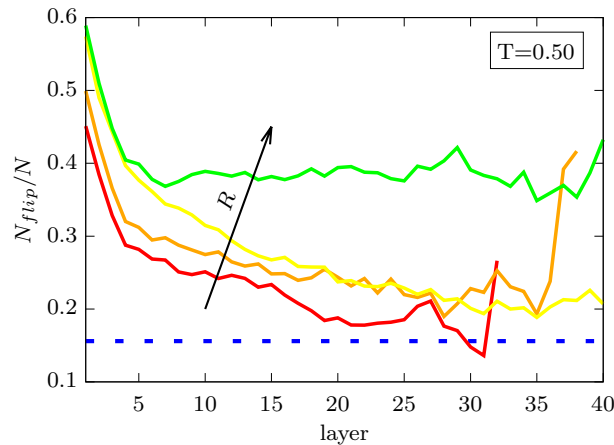


Figure 6.12: Fraction of flipped particles in systems with  $T = 0.50$  as a function of the layer. The color code is the same as in Figure 6.8. The dotted line indicates the average fraction of flips within a quasicrystal that is thermally equilibrated at  $T = 0.50$ . The increase of the flip fractions in the deepest layers results from the pure statistics within these layers that consist of only a few particles.

respective temperature as indicated by the dotted line ( $N_{\text{flip}}/N \approx 0.156$ ). The latter is determined by comparing the positions of the initially perfectly arranged ground particles to the positions after the system is in thermal equilibrium. As for the grown structures, particles that deviate by more than  $d_{\text{flip}}/2$  from their ideal positions are considered to be flipped. An average is taken over 800 configurations. For  $R = 1/\tau_B$  we observe a decrease of the flipped particles only within the first few layers. After about eight layers the flip fraction remains approximately constant with a larger value than for the lower rates or for the equilibrated structure. Therefore, at larger rates no equilibrium-like quasicrystals can be grown.

### 6.1.6 Changes of the parameters of the interaction potential

So far we have employed the Lennard-Jones–Gauss potential with fixed potential parameters  $r_G = 1.52, \epsilon = 1.8$  and  $\sigma^2 = 0.02$  as described in Subsection 6.1.1. Here, we shortly investigate the growth of structures with different interaction potential parameters. However, the modified parameters still support the formation of decagonal structures. For the possible choices of parameters we orient ourselves on [28]. Given a fixed width  $\sigma^2 = 0.02$  of the second potential minimum we first vary its depth  $\epsilon$  and later the position  $r_G$ .

First, we keep  $r_G = 1.52$  and vary the depth  $\epsilon$  in exemplary simulations with constant temperature  $T = 0.50$ . We find that the fraction of hexagonal elements

with interparticle distances of the second length scale increases with the depth of the second minimum. Due to the resulting reduced energy of the second minimum an increased number of particles gets stuck in that position. To be specific, with a depth  $\epsilon = 2.5$  we receive quasicrystalline structures interspersed with triangular elements for systems grown with rates  $R \geq 0.5/\tau_B$ . For lower rates  $R < 0.5/\tau_B$  the hexagonal elements vanish. For an essentially deeper minimum with  $\epsilon = 4$  the grown structures are completely composed of triangular patterns for all applied sedimentation rates. The structures are interrupted by gaps and the number of gaps decreases for decreasing rates.

Concerning the variation of the position  $r_G$  of the second minimum for a fixed depth  $\epsilon = 1.8$ , we may only slightly alter  $r_G$  without losing the decagonal order. For example,  $r_G = 1.54$  leads to a system close to the phase transition towards a triangular phase with the short length scale. For systems grown with  $T = 0.50$  and  $R \geq 1/\tau_B$  we indeed observe slightly more small triangles. However, the difference to the structures grown with  $r_G = 1.52$  is small.

## 6.2 Growth of two-dimensional dodecagonal colloidal quasicrystals: Particles with isotropic pair interactions with two length scales vs. patchy colloids with preferred binding angles

In the previous Section we modeled the growth of two-dimensional colloidal decagonal quasicrystals at a solid-gas interface. The particles interacted according to an isotropic pair potential. In this Section we employ a similar simulation setup in order to explore the growth of two-dimensional colloidal quasicrystals with dodecagonal symmetry. On the one hand, we study the growth behavior in case of an isotropic pair potential with two typical length scales. On the other hand, we consider patchy colloids (see Section 5.1) that possess only one typical interaction length scale but prefer given binding angles. In both cases we obtain dodecagonal quasicrystals for appropriate simulation parameters. Phasonic flips contribute to a nearly defect-free growth.

The study is ordered as follows: First, we describe the setup of our simulations. Afterwards, the results are discussed. We first introduce diffusion-limited aggregation that occurs at low temperatures. Afterwards, we present the structures grown with different control parameters and characterize them according to the occurrence of the long length scale. The bond-orientational and positional order are determined for the grown quasicrystalline structures. Afterwards, we describe the dynamics of the particles with a special emphasis on phasonic flips and parti-

cles at the surface. Finally, we explore the consequences of the observed lines or regions with phasonic flips in order to find out how perfect the grown quasicrystals are.

### 6.2.1 Simulation setup and determination of layers

In case of particles interacting according to an isotropic interaction a Lennard-Jones–Gauss potential  $V_{LJG}(r)$  given in equation (3.50) in Subsection 3.4.1 of the same type as in the previous Section is employed. In accordance with [91] we apply the potential parameters  $r_G = 1.95$ ,  $\epsilon = 2.0$  and  $\sigma^2 = 0.02$  for which the resulting pair potential supports the formation of dodecagonal quasicrystals for appropriate pressure and temperature.

The directional pair potential employed in our simulations is given by a Lennard-Jones potential multiplied with an additional term that depends on the binding angles (see equation (3.51) in Subsection 3.4.1). We employ particles with five patches and one patch with  $\sigma_{pw} = 0.49$ . The Lennard-Jones exponent reads  $n = 6$ . Such systems are known to form dodecagonal quasicrystals [119, 120]. In our simulations the angular term given in equation (3.53) is present for all distances  $r$ .

We again employ Brownian dynamics simulations. For particles that interact according to the isotropic potential we only need displacement moves, while for the directional interaction additional orientational moves are required (see Subsection 3.1.3).

As in previous simulations we want to study the growth of structures out of vapor by sequential deposition of new particles on the surface. Our setup is chosen similar to the one used for the growth of decagonal structures (see Subsection 6.1.1). Now the initial configuration of ground particles is given by a section of a perfect square-triangle tiling which is obtained by substitution rules [383]. In case of the isotropic Lennard-Jones–Gauss interaction the gravitational-like force of injected particles is switched off once a distance  $d_{\text{off}} < 1.97$  to a neighboring particle is reached. Since  $d_{\text{off}}$  is a little larger than the second potential length  $l_2$  both length scales may be adopted during the growth process. In case of the patchy particles that only support the short length scale, the gravitational-like force is turned off at distances  $d_{\text{off}} < 1.25$ .

We vary the temperature  $T$  of the system and the sedimentation rate  $R$  as our control parameters. In order to obtain comparable sedimentation rates  $R$  for different box sizes we scale the rate appropriately with a reference length  $L_0$  such that  $R = N_{\text{inj}}/\tau_B \cdot L_0/L_x$ . Here,  $N_{\text{inj}}$  is the number of particles that are injected during the Brownian time  $\tau_B$ . We choose  $L_0 = 38.532$  which corresponds to the box dimension for systems grown with isotropic interactions and  $T = 0.50$ .

For a quantitative analysis of our grown structures we divide the structures into layers similar as described in Subsection 6.1.1: The outermost particles whose

Voronoi volume  $v$  [330] exceeds  $v = 1.9$  are identified as surface particles. Particles with a distance  $d < 1.2$  to the surface particles build the second layer. Any subsequent layers are determined analogously.  $d$  is chosen in a way that  $1 < d < \sqrt{2}$ , i.e. larger than the short distance and smaller than the diagonal within a square tile. Note that the numeration begins at the surface, and particles deeper in the bulk are assigned larger layer numbers.

## 6.2.2 Diffusion-limited aggregation

First, we consider extreme examples of very low temperatures, for which the diffusion of particles along the surface of a grown structure is very small. Figures 6.13 (a) and (b) show two typical snapshots of systems grown with  $R = 2/\tau_B$  and (a)  $T = 0.001$  for particles interacting according to the isotropic potential and (b)  $T = 0.00001$  in the case of the potential with preferred bond angles. In both cases we find network-like structures as expected for diffusion-limited aggregation (see [384]), i.e. the diffusion time for a particle to find its ideal position is smaller than the time between two injected particles.

In the case of the isotropic system, we observe thin branches composed of particles for which the nearest neighbor distance corresponds to the long length scale of the interaction potential. The preference of the long length scale is due to the fact that newly injected particles first get stuck at the surface with this long distance to their neighbors and the temperature is too low for the particles to escape from the corresponding minimum of the interaction potential. At a few places the particles build local triangular arrangements.

In the case of the system with preferred binding angles, we also observe the formation of network-like structures. Naturally, we only observe the short length scale between neighboring particles in these systems, as this is the only length supported by the potential. Unlike the isotropic system, the patchy particles form thicker branches with triangular and square tiles corresponding to local dodecagonal arrangements.

Figures 6.13 (c) and (d) quantify the grown structures by illustrating the fraction of particles in the surface layer over the total number of particles as a function of the temperature for (c) isotropic and (d) patchy particles. Note, due to the different types (and energies) of the interaction, it is hard to compare the temperature of a quasicrystalline structure observed for isotropic interactions to the temperature for which a quasicrystal with patchy colloids is found. However, we choose a reference temperature for each of the systems where the resulting quasicrystals are comparable. To be precise, for  $T = 0.70$  in case of isotropic interactions and  $T = 0.15$  in case of directed interactions we obtain nicely grown quasicrystals that for similar rates are comparable concerning the orientational order (see Subsection 6.2.4) and the averaged number of flips (see Subsection 6.2.5) within the systems.

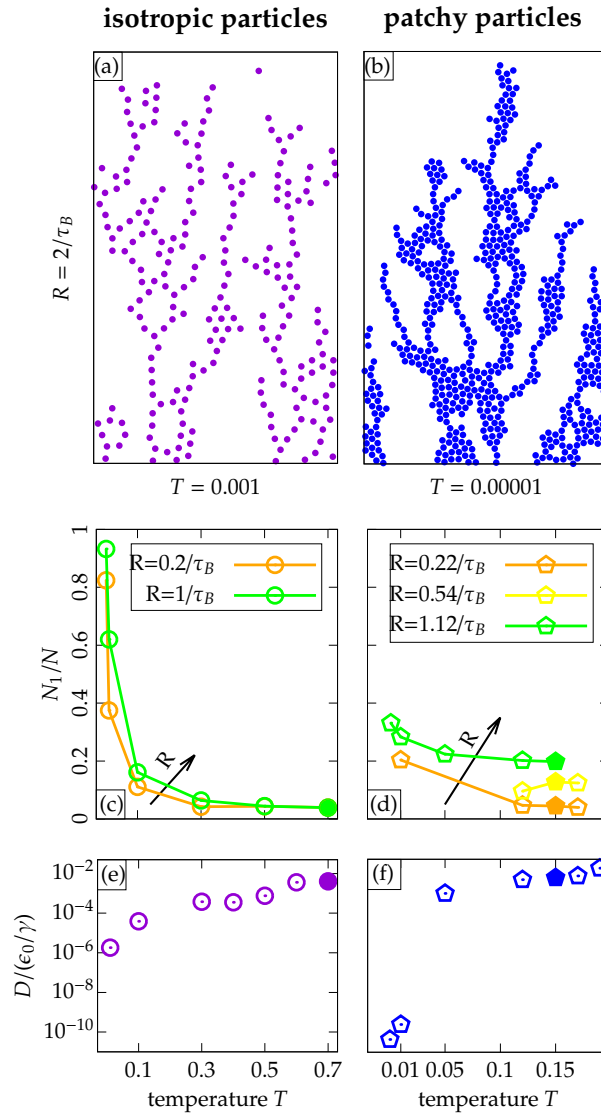


Figure 6.13: Network-like structures grown at very low temperatures, i.e. diffusion-limited aggregation with isotropic and patchy particles on the left and right hand side, respectively. The initially perfectly ordered substrate particles are not shown. (a) Isotropic particles arrange to thin branches with the distance between neighboring particles given by the long length scale of the interaction potential. (b) Patchy particles form thicker branches with local dodecagonal order. (c) and (d) illustrate the fraction of surface particles as a function of the temperature. Different rates are depicted in different colors. (e) and (f) show the diffusion constants of a particle on a free surface dependent on the temperature. Systems grown with our standard temperatures  $T = 0.70$  or  $T = 0.15$  for isotropic or patchy particles, respectively, are marked by filled symbols.

I.e. in isotropic systems with  $T = 0.70$  the averaged bond-orientational order parameter in layers deeper than six reads  $\langle |\psi_{12}| \rangle = 0.724\dots$  and the averaged number of flips is  $N_{\text{flip}}/N = 0.048\dots$ , which is similar to systems with directed interactions and  $T = 0.15$  in which  $\langle |\psi_{12}| \rangle = 0.728\dots$  and  $N_{\text{flip}}/N = 0.061\dots$ . Accordingly, in the following we refer to the temperatures mentioned above as standard temperatures and data for systems grown with these temperatures are shown with solid points or thicker lines in all Figures of this Section. Furthermore, snapshots of the systems grown with our standard temperatures are usually emphasized by a frame colored in magenta.

The results of Figures 6.13 (c) and (d) show that with increasing temperature the number of surface particles decreases indicating that for larger temperatures no network-like structures occur. Different colors of the data points represent systems grown with different rates.

In the case of the isotropic particles, we observe quasicrystalline bulk structures in the temperature regime  $T \in [0.5; 0.7]$ . Here, the fraction of surface particles does not significantly depend on the rate. For lower temperatures the fraction of surface particles is larger for systems grown with higher rates since a reduced time between injected particles causes gaps and respectively increasingly thinner branches. In the case of the patchy particles, the fraction of surface particles also rises at low temperatures due to the formation of network-like structures. However, the branches of the structures built in these systems are thicker, such that the fraction of surface particles is lower than for the corresponding cases in the isotropic systems. Furthermore, the network-like structures are still observable for larger temperatures, especially in case of large rates. Even at larger temperatures the fraction of surface particles depends on the rate in case of patchy colloids. At high temperatures  $T \geq 0.15$ , this is due to increased cluster formation, which will be discussed in Subsection 6.2.5. In conclusion, while for isotropic interactions the dependence of the surface particles on the rate is small in case of large temperatures, in case of patchy colloids, the rate even matters at larger temperatures and in order to avoid diffusion-limited aggregation a low injection rate is required.

Additionally, in order to give a quantitative estimate of the diffusion of the particles on the surface dependent on the temperature, we extract the diffusion constant  $D$  from the mean square displacement of single particles on a free surface (see Figures 6.13 (e) and (f)). For both, isotropic and patchy particles,  $D$  increases with temperature and covers several orders of magnitude within the investigated temperature ranges. Low diffusion constants explain the formation of networks, while increased  $D$  allow wide diffusion and the growth of quasicrystals. Note that the diffusion constants of patchy colloids on average are larger than for particles with isotropic interactions at comparable temperatures, because they usually do not bind with a patch to the surface during the diffusion along the surface. As

soon as a patchy colloid connects to the surface by a patch it stays at that position much longer than an isotropic particle.

### 6.2.3 Overview of observed structures and occurrence of the long length scale

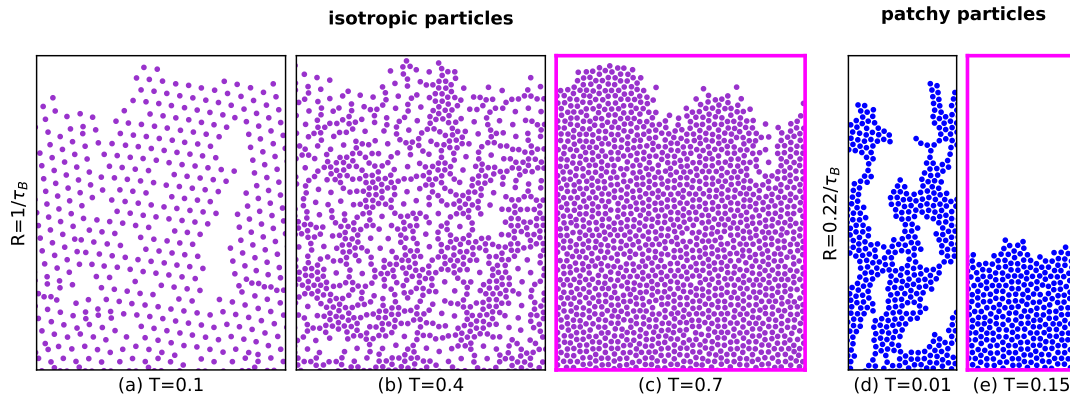


Figure 6.14: Exemplary snapshots of systems with isotropic and directed interactions for different temperatures. (a)-(c) show isotropic systems grown with  $R = 1/\tau_B$  and (a)  $T = 0.1$ , (b)  $T = 0.4$  and (c)  $T = 0.7$ . (d) and (e) illustrate systems of patchy particles grown with  $R = 0.22/\tau_B$  and (d)  $T = 0.01$  and (e)  $T = 0.15$ .

In the next step, we want to explore at which temperatures quasicrystals can be grown. Figure 6.14 qualitatively depicts typical snapshots of systems obtained from both studied potentials for different temperatures. In Figures 6.14 (a)-(c) we illustrate systems with isotropic interactions grown with a constant rate  $R = 1/\tau_B$ . We observe two structures where the long length scale dominates and an almost perfect quasicrystal. By almost perfect quasicrystal we mean that most of the particles sit at the positions that are expected from the perfect square-triangle tiling that we employ as a substrate. A quantitative characterization of possible deviations from a perfect square-triangle tiling will be given starting in Subsection 6.2.4. While we usually compare the positions of the particles of the grown structure to that of the square-triangle tiling in real space, one can also check the long-range order by calculating the structure factor as we will show in Subsection 6.2.4.

In our systems grown with  $T = 0.10$  (see Figure 6.14 (a)) the particles arrange to local triangular structures with nearly exclusively particle distances of the long

length scale. Only a few particles reach the first potential minimum of the short length. The structure is interrupted by gaps due to a reduced diffusion at low temperatures. Increased temperatures result in an increased local dodecagonal ordering, which is illustrated on the example of a system grown with  $T = 0.40$  in Figure 6.14 (b). A striking feature here is the formation of rings or parts thereof, which are composed of a central particle that is surrounded by twelve colloids. The distance of the central particle to the outer particles corresponds to the long potential length while the distances between the surrounding particles is the short length. For even larger temperatures the number of rings decreases and finally the denser, almost perfect quasicrystalline structures grow (e.g. Figure 6.14 (c) for  $T = 0.70$ ).

In Figures 6.14 (d) and (e) structures grown with patchy particles are shown. The snapshots illustrate systems grown with  $R = 0.22/\tau_B$ . Even for very low temperatures (e.g.  $T = 0.01$ , Figure 6.14 (d)) we do not observe a domination of the long length scale. Instead, the discussed network-like structure is present over a wide temperature range. With rising temperature the networks become thicker until quasicrystalline structures grow for sufficiently large temperatures as depicted for  $T = 0.15$  in Figure 6.14 (e).

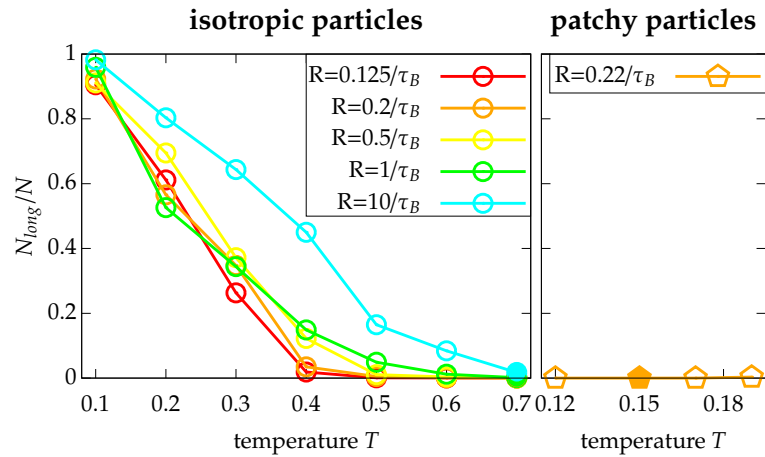


Figure 6.15: Fraction of particles for which all distances to neighboring particles except at most one correspond to the long length scale as a function of the temperature. Different rates are shown with different colors and the standard temperatures are marked by filled symbols. Systems grown with isotropic interactions are shown on the left hand side, patchy particle systems on the right hand side.

In Figure 6.15 we characterize the occurrence of the long length scale quantitatively. As a function of the temperature, we show the fraction of particles that possess - except for at most one neighbor - only neighbors at a distance corresponding to the long length scale. Such particles are either part of a local triangular

arrangement with the long length or they are the central particle of a ring-like formation. The initial particles of the substrate and the surface particles are not included in the evaluation. Particles with a distance  $d < 1.6$  are defined as nearest neighbors with the short distance, while particles with  $1.6 < d < 2.2$  are counted as nearest neighbors with the long distance. For each temperature we consider systems grown with various rates as given by the color code.

For isotropic particles the long length scale dominates for low temperatures. Furthermore, increasing the rates seems to support the long length scale. For  $T = 0.10$  and  $R = 10/\tau_B$  nearly all particles exclusively have distances of the long length to their neighbors. For sufficiently large temperatures we observe the formation of quasicrystalline structures, e.g. for  $T = 0.70$  we observe hardly any particles with only neighbors of the long length for any rate. In systems grown with patchy particles we do not observe any particles that possess only neighbors with the long length distance which is shown on the example of one representative rate.

#### 6.2.4 Order of the grown quasicrystalline structures

In the following, we concentrate on the almost perfectly grown quasicrystalline structures, i.e. the structures grown with or close to our standard temperatures which are sufficiently large. Furthermore, we consider sedimentation rates that are sufficiently low.

We characterize the structures according to their bond-orientational as well as positional order (see Figure 6.16). Therefore, we calculate the bond-orientational order parameter  $\psi_m(\mathbf{r}_j)$  for each particle  $j$  at position  $\mathbf{r}_j$ . The bond-orientational order parameter is defined in Subsection 3.5.4. In Figures 6.16 (a) and (b) we depict exemplary snapshots of systems grown with our standard temperature and give the absolute value of the local bond orientational order parameter by the colors. Most particles show a good local dodecagonal order indicated by the black color. Slight deviations are caused by thermal fluctuations. In addition, in Figures 6.16 (c) and (d) we depict the corresponding structure factors  $S(\mathbf{q})$  (see Subsection 3.5.2 for a definition of  $S(\mathbf{q})$ ). Discrete Bragg peaks indicate long-range order of the structures. Positional order is also indicated by sharp peaks in the radial distribution functions  $g(r)$  shown in Figures 6.16 (e) and (f) (see Subsection 3.5.1 for a definition of  $g(r)$ ). The positions of the peaks correspond to the ones of a perfect square-triangle tiling. Note that the peak at the short length scale is larger and thinner in the case of interactions with preferred angles. All in all, at the respective standard temperatures the structures grown with isotropic interactions and the structures for interactions with preferred bond angles are almost the same and they correspond to nearly perfect square-triangle tilings as can be revealed by comparing the positions of the particles in real space (see also quantitative analysis in the next Subsection).

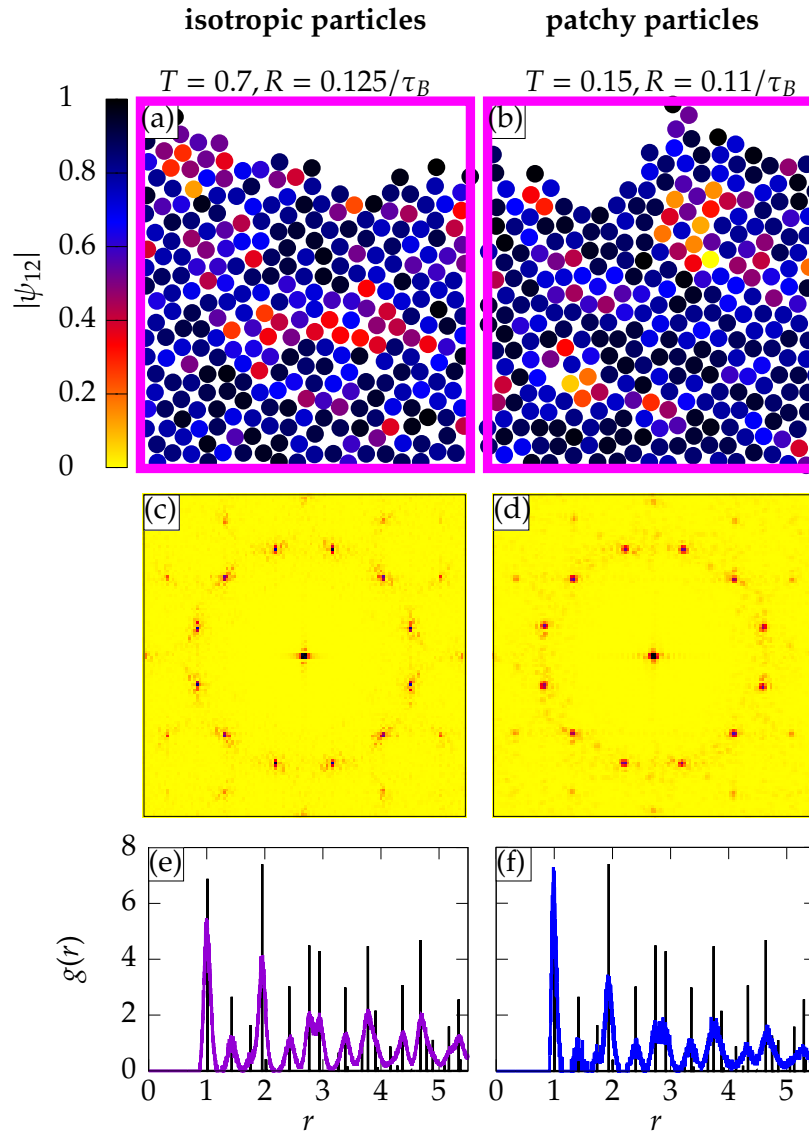


Figure 6.16: Characterization of structures grown with our standard temperatures. The interactions between the particles are isotropic (left column) and with preferred bond angles (right column). (a) and (b) Snapshots of grown structures with the particles colored according to their absolute value of the bond-orientational order parameter  $|\psi_{12}|$ . (c) and (d) Structure factors  $S(\mathbf{q})$  and (e) and (f) radial distribution functions  $g(r)$  depicted in purple or blue of the illustrated snapshots. The radial distribution function of a perfect square-triangle tiling is shown in black for comparison. Note that  $g(r)$  of the perfect tiling is compressed by a factor of 70 in  $y$ -direction.

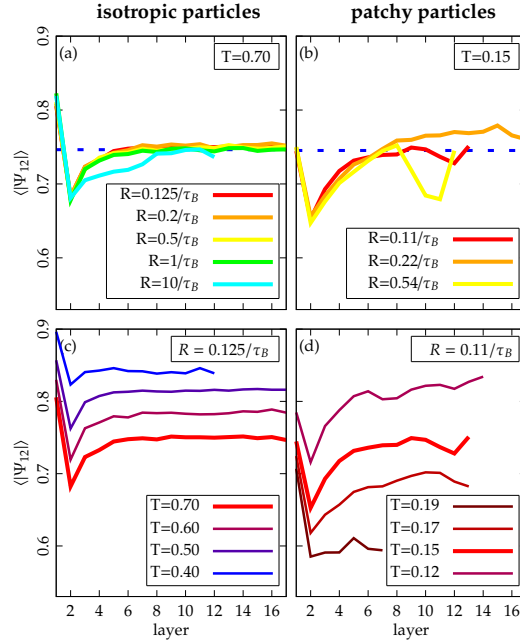


Figure 6.17: Averaged bond-orientational order parameters  $\langle |\psi_{12}| \rangle$  as functions of the layer in systems with isotropic particles (left column) and for patchy particles (right column). The bond-orientational order for our standard temperatures ( $T = 0.70$  for isotropic interactions,  $T = 0.15$  for patchy colloids) is indicated by thick curves. In (a) and (b) the rates are varied for constant temperatures ( $T = 0.7$  for isotropic interactions,  $T = 0.15$  for patchy colloids). In (c) and (d) the temperatures are varied for constant rates ( $R = 0.125/\tau_B$  for isotropic interactions,  $R = 0.11/\tau_B$  for patchy colloids). The dotted lines indicate the reference values of  $\langle |\psi_{12}| \rangle$  obtained when the respective system is equilibrated in bulk with the respective standard temperature. The layers are counted starting at the surface, which corresponds to layer one.

In Figure 6.17 we quantitatively show the orientational order as a function of the layers for systems grown with different control parameters that support quasicrystalline structures. The left column illustrates isotropic particles; in the right column we depict patchy particles. Figures 6.17 (a) and (b) show the orientational order for systems grown with our standard temperature  $T = 0.70$  for isotropic particles and  $T = 0.15$  for patchy particles. These temperatures are comparable regarding the averaged value of  $|\psi_{12}|$  (shown by the blue dotted lines) in a system equilibrated at the corresponding temperature.

For all rates the orientational order possesses a large value in the first layer, which is due to several surface particles with only one nearest neighbor. Starting from the second layer, the system first is less ordered but the order increases with increasing

distance from the surface. Finally, the orientational order parameter approaches the bulk reference value after about six layers. The orientational order usually is independent of the rate. However, for very high rates, as shown on the example of  $R = 10/\tau_B$  for isotropic particles, the increase of the order is slower and it takes more layers to approach the bulk value because the injected particles have less time to find their ideal positions. The behavior of the bond orientational order at the standard temperatures is similar for isotropic interactions and patchy colloids. In Figures 6.17 (c) and (d) we display the course of the order in systems grown with a constant rate, i.e.  $R = 0.125/\tau_B$  for isotropic particles and  $R = 0.11/\tau_B$  for patchy particles. The temperatures are varied. In all systems the orientational order is largest for low temperatures since thermal fluctuations are reduced.

### 6.2.5 Dynamics of phasonic excitations

Within our grown systems there might still occur rearrangements of the particles: Beside thermal phononic fluctuations, phasonic flips play an important role in the discussion of the dynamics. In the well-studied decagonal tiling local phasonic flips of single particles have been observed at many positions in the tiling [14, 28, 29, 91, 265]. We will now discuss the case of dodecagonal quasicrystals in which we observe two kinds of flips which occur for both, systems with isotropic interactions as well as interactions with preferred binding angles.

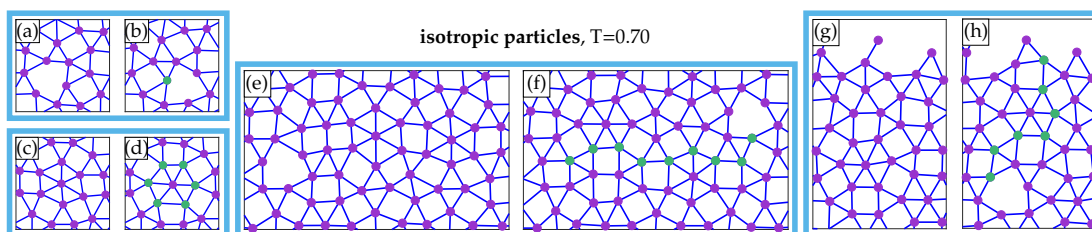


Figure 6.18: Local rearrangements during the dynamical evolution of a system with isotropic interactions and standard temperature. In each blue box a part of the system is shown at two different times. Particles that have changed their position about  $d_{\text{flip}}$  are colored in green. A tiling is drawn by connecting the particles with a distance of the short length. (a) and (b) Single flip enabled by a shield tile. (c) and (d) Correlated flips of a ring of six particles rotating around a central particle. (e) and (f) Successive flips starting from a shield tile in the bulk and leading to a displacement of the shield tile. (g) and (h) Successive flips starting at the surface and leading to a shield tile that moves into the bulk. Similar dynamics are also observed in systems of patchy particles.

First, even though in a local arrangement composed of only squares and triangles the particles are so dense that they do not have the possibility of flipping independently from each other, we observe correlated flips of six particles that rotate about  $2\pi/12$  around a central particle as shown in Figures 6.18 (c) and (d). The covered distance of each particle corresponds to the flip distance  $d_{\text{flip}}$ . The ideal flip distance reads  $d_{\text{flip}} = 1/(2\cos(\pi/12))$ , calculated from geometrical considerations.

Second, beside the triangles and squares known from the square-triangle tiling, our grown structures exhibit shield tiles which are additional tiles composed of six particles as illustrated, e.g. in Figures 6.18 (a) and (b). Such shield tiles serve as starting points of phasonic flips (see [385, 386]), since particles on the sides of a shield may flip inside the shield (see Figures 6.18 (a) and (b)). The covered distance after a flip is also  $d_{\text{flip}}$ . After such a flip the shield tile is conserved and only changes its position within the sample. As a consequence, we observe chains of flipping particles (see, e.g. Figures 6.18 (e) and (f)) corresponding to the motion that is known as zipper motion [385, 386]. Once one particle has flipped the subsequent flip of the zipper motion may occur very fast, e.g. the time between the two illustrated snapshots is only  $\Delta t = 1\tau_B$ .

In addition, during the growth process new shield tiles may build at the free surface of the quasicrystal and move into the structure by subsequent flips as illustrated in Figures 6.18 (g) and (h). Conversely, shield tiles within the bulk may also move to the surface and disappear. Note that the examples in Figure 6.18 are drawn for isotropic interactions but similar flipping dynamics also occur in systems of patchy particles.

In the following we show grown systems of isotropic and patchy particles and compare them with regard to phasonic flips. In Figure 6.19 we illustrate snapshots of systems grown with our standard temperatures. The isotropic systems are shown in the first column, patchy systems in the second column. An additional system of patchy particles grown with the slightly larger temperature of  $T = 0.17$  is depicted in the third column. The particles are colored according to performed flips after  $\Delta t = 10\tau_B$  and  $\Delta t = 100\tau_B$  in the first and second line, respectively. We consider a particle to be flipped if it has moved by more than  $d_{\text{flip}}/2$  after the considered time  $\Delta t$ . Flipped particles are colored in green or red. Dark-green and dark-red particles possess at least four flipped neighbors. Those particles typically belong to a region where all particles have moved, which we also refer to as rearranged regions. However, note that there might be some particles detected as rearranged regions, although there is only a crossing of flipped lines. Nonetheless, we chose four neighbors or more as threshold, in order to detect all regions.

In all snapshots we observe the flips discussed in Figure 6.18. As expected, by trend the number of flips is larger in case of a longer time between the snapshots

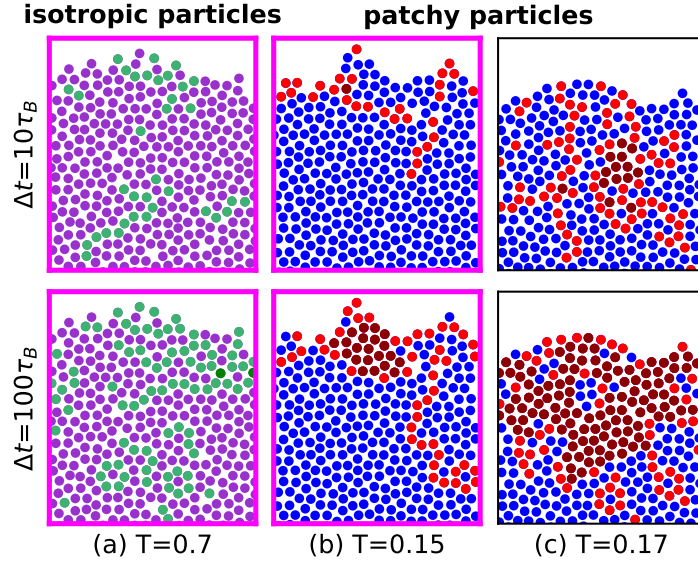


Figure 6.19: Phasonic flips in systems grown with our standard temperatures (a)  $R = 0.2/\tau_B$  for isotropic particles and (b)  $R = 0.22/\tau_B$  for patchy particles. (c) depicts an additional system of patchy particles grown with a larger temperature  $T = 0.17$ . Particles that will flip after  $\Delta t = 10\tau_B$  (first row) or  $\Delta t = 100\tau_B$  (second row) are colored in green or red. Particles that belong to a region that collectively rearranges are colored in dark-green or dark-red.

since there is more time for the flips to occur. Furthermore, there are more flipped particles close to the surface than in the bulk. In systems with isotropic interactions we hardly observe any regions of collectively rearranged particles. In systems of patchy particles, we observe regions that have rearranged. A quantitative analysis will be given in the next paragraph and Figure 6.21. Such regions even become larger if the temperature is slightly increased and usually occur close to the surface. A possible reason might be that patchy particles need a longer time to orient correctly.

In order to discuss the phasonic flips quantitatively, we show the average fraction of flipped particles in a growing system after a simulation time  $\Delta t = 10\tau_B$  as a function of the layer in Figure 6.20. The shown systems are the same as in Figure 6.17. In all systems the fraction of flipped particles is largest close to the surface where particles still need to find their ideal positions. Moreover, in the upper layers we observe slightly more flips in systems of patchy particles compared to isotropic particles. The flip fraction decreases with an increasing distance from the surface. Figures 6.20 (a) and (b) depict the functions for various rates and our standard temperatures. For systems grown with low sedimentation rates the flip fraction

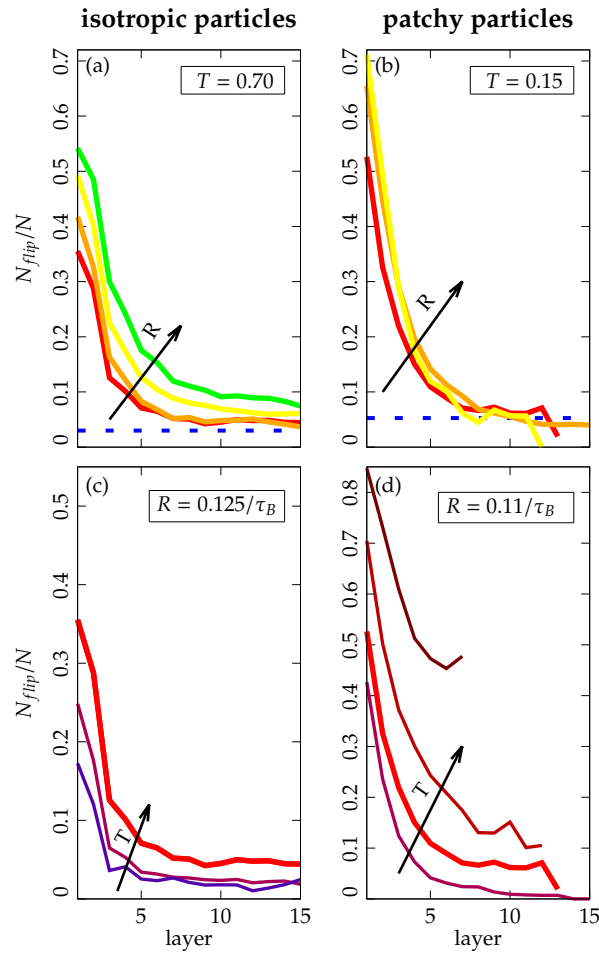


Figure 6.20: Averaged flip fraction after  $\Delta t = 10\tau_B$  as functions of the layer. The same systems as in Figure 6.17 are employed. The dotted lines in (a) and (b) give the reference values of  $N_{\text{flip}}/N$  obtained from a structure equilibrated in bulk.

decreases fastest since the particles have the most time to find their ideal positions. Far away from the surface, the fraction of flipped particles approaches the bulk value (dotted blue lines) that is determined by counting the flips in structures equilibrated at the corresponding standard temperatures in bulk. Figures 6.20 (c) and (d) show the fraction of flipped particles for systems with a constant rate for various temperatures. We observe a pronounced temperature dependence, i.e. for large temperatures there are more phasonic flips even at large distances from the surface.

In the following we investigate the rearranged regions quantitatively. Figure 6.21 depicts the fraction of particles belonging to a rearranged region as a function of the rate. The data confirms that the isotropic particles form less rearranged regions,

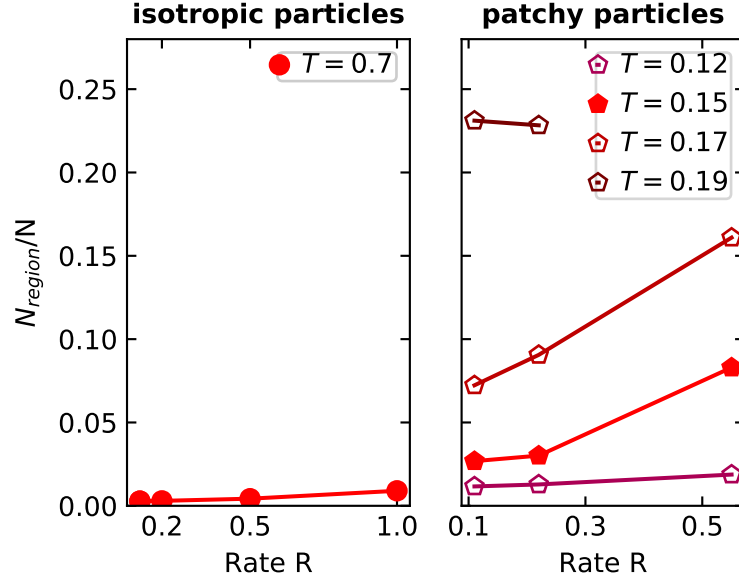


Figure 6.21: Number of particles belonging to a rearranged region after  $\Delta t = 10\tau_B$  over the total number of particles within the considered system as a function of the sedimentation rate  $R$ . Different temperatures are shown in different colors. The results for isotropic particles are shown on the left, patchy particles on the right.

i.e. there are hardly any rearranged regions except for a few particles on the surface, which is shown using the example of the largest investigated temperature  $T = 0.70$ , e.g.  $N_{\text{region}}/N = 0.0028\dots$  for  $R = 0.125/\tau_B$ . In case of the patchy systems, the fraction of rearranged regions is much larger and increases with increasing rate for all considered temperatures. Additionally, the fraction of rearranged regions is dependent on the temperature as we have already conjectured due to the snapshots shown in Figure 6.19. For example,  $N_{\text{region}}/N = 0.0253\dots$  for  $T = 0.15$  and  $R = 0.11/\tau_B$ .

Another kind of dynamics observed during the growth is the dissociation of particles from the surface. Especially within the systems of patchy colloids there are sometimes single particles or chains of particles that detach from the surface. The detached particles subsequently trigger the formation of larger clusters of particles. In Figure 6.22 we show the two different possibilities of how such clusters are formed with time. First, we illustrate the dissociation of a single particle in a system that grows with  $T = 0.17$  and  $R = 0.54/\tau_B$  (see Figures 6.22 (a)-(c)). Second, we depict the detachment of a chain of particles that typically occurs at large rates (e.g.  $R = 1.12/\tau_B$ ) and not too large temperatures (e.g.  $T = 0.15$ )

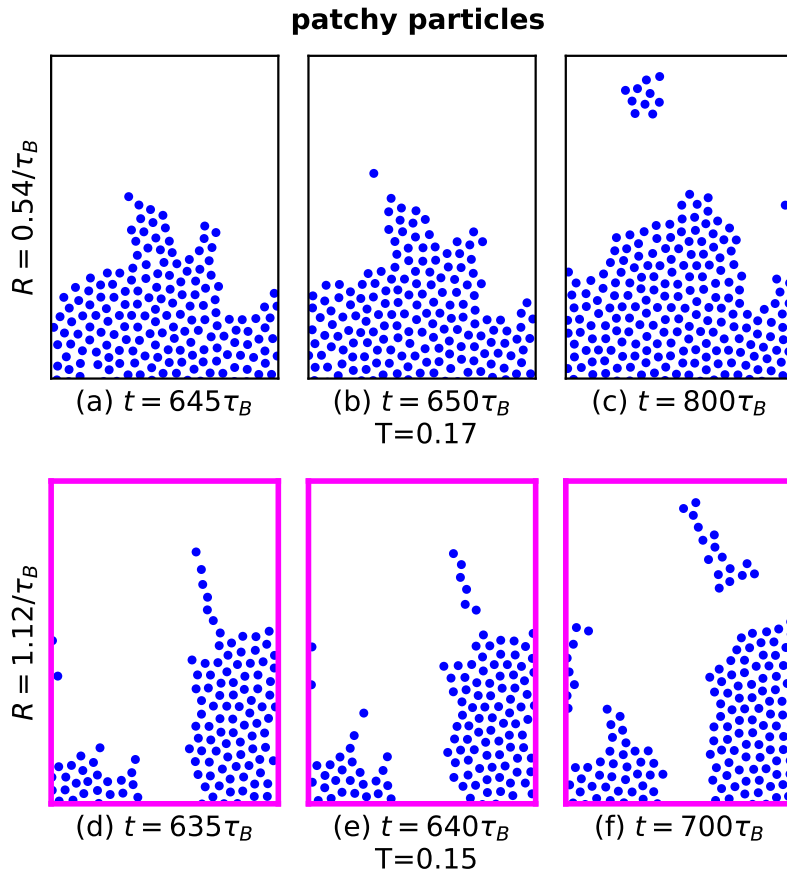


Figure 6.22: Two examples of cluster formation with time. (a)-(c) depict a single particle that diffuses from the surface. Particles, that are added to the system attach to it and form a small cluster. (d)-(f) shows a complete chain of particles that detach from the surface.

as shown in Figures 6.22 (d)-(f). Naturally, the first way of forming clusters is observed more often, as it does not require diffusive motion along the surface.

### 6.2.6 Lines and regions of flipped particles in almost perfect structures

In the following we investigate how the dynamics of phasonic flips influences the structures that are grown. Specifically, we are interested in deviations from perfect quasicrystals as given by the square-triangle tiling that we have also used for the initial substrate particles. In Figure 6.23 we depict systems that have grown with different sufficiently low sedimentation rates  $R \leq 1/\tau_B$  and appropriate tem-

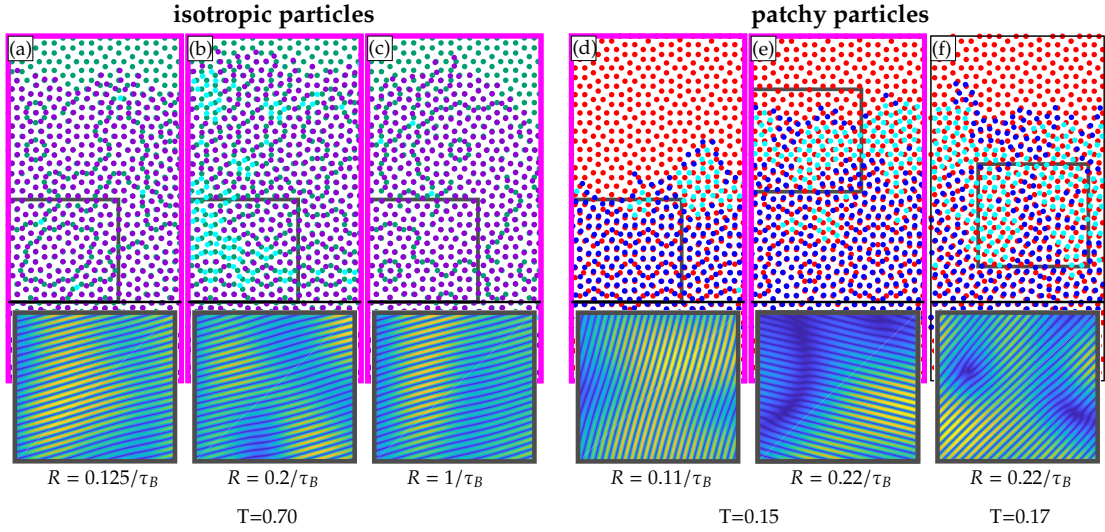


Figure 6.23: Comparison of grown structures (purple or blue points) to quasicrystals according to perfect square-triangle tilings (green or red points). (a)-(c) depict systems grown with isotropic interactions, (d)-(f) show particles with preferred binding angles. The rates and temperatures are given in the Figure. The border to the initial substrate particles is indicated by black lines. In order to indicate regions with phasonic or phasonic offset, particles that are neighbored by particles that all are displaced from the perfect structure are colored in light-blue. The insets show the Fourier back transformations of symmetrically chosen peaks of the structure factor in order to detect dislocations. Within the snapshots of the grown structures we highlight the regions which are illustrated in the insets by gray borders. Note that dislocations only have been found for patchy particles (see insets of (e) and (f)).

peratures in order to form quasicrystalline structures. The grown structures are illustrated in purple (isotropic particles) or blue (patchy particles) while in the background the perfect square-triangle tiling with particles colored in green or red are shown.

In case of the isotropic interactions (see Figures 6.23 (a)-(c)) most particles of the grown structures coincide very well with the positions expected from the perfect square-triangle tiling. However, we observe lines of particles that are located between two ideal lattice positions. The deviation from the next ideal position corresponds to the distance of a phasonic flip  $d_{\text{flip}}$ . Note, we do not observe single particles whose positions deviate from the prescribed ideal positions. To be specific, we observe the rotation by  $2\pi/12$  of rings of six particles around a central particle similar to Figures 6.18 (c) and (d). Furthermore, there arise even longer chains of displaced particles. Such chains are either closed or open. The endpoints

of open chains are either at the surface of the structure or in the bulk. In the latter case they begin with a shield tile. Note that on a first glance the patterns of closed and open lines in Figures 6.23 (a)-(c) seem to be quite different. However, the patterns of circles and lines can change very fast. In total, we do not find any dependence of the phasonic flip lines on the sedimentation rate for the isotropic interactions. Note that we do not show the complete width  $L_x$  such that the patterns are not continued periodically in the snapshots.

In case of the systems grown with preferred binding angles as depicted in Figures 6.23 (d)-(f), similar circles and lines of flipped particles are observed. However, close to the surface the patchy particles generally do not coincide well with the perfect structure. Even regions of mismatched particles occur probably as a direct consequence of the dynamically rearranging regions that we have observed in Subsection 6.2.5. Particles belonging to a rearranged region are colored in light-blue. Hence, we calculated the displacement fraction, i.e. the fraction  $f_{\text{disp}} = N_{\text{disp}}/N$  of particles  $N_{\text{disp}}$  belonging to a displaced region averaged over 1000 snapshots. In case of the patchy systems, we find a displaced particle fraction of  $f_{\text{disp}} = 20.8\%$  for the system grown with  $T = 0.15$  and  $R = 0.11/\tau_B$  and  $f_{\text{disp}} = 36.7\%$  for  $R = 0.22/\tau_B$ . In contrast, the displaced particle fraction in case of the isotropic particles is only  $f_{\text{disp}} = 0.9\%$  for  $T = 0.70$  and  $R = 0.125/\tau_B$  and  $f_{\text{disp}} = 13.9\%$  for  $R = 0.2/\tau_B$ . Thus, the displaced particle fraction depends on the rate and is much higher for the patchy systems. However, note that in case of lines that lay closely side by side the particles may misleadingly be counted to a rearranged region (see, e.g. Figure 6.23 (b)).

Finally, we checked whether dislocations occur in the grown structures. By using the method described in [332] (see also Subsection 3.5.5), we find that for isotropic interactions no dislocations can be found while in case of patchy colloids dislocations might build, especially in case of large rates or large temperatures (see insets in Figure 6.23). The dislocations seem to form at the border between the almost perfect part of the grown quasicrystal and a region that is collectively displaced with respect to the perfect structure.

## 6.3 Conclusion

By using Brownian dynamics simulations we have examined the growth of two-dimensional colloidal quasicrystals. While in [115, 116] the growth of quasicrystals was studied by employing phase field crystal models, we here investigated the growth on the particle-resolved level by depositing particles at a free surface. The method corresponds to the growth out of vapor.

In first investigations the particles interacted according to an isotropic Lennard-Jones–Gauss pair potential with two incommensurate length scales that are char-

acteristic of decagonal structures. Analyzes of the grown structures based on their orientational order revealed different fractions of decagonal and hexagonal elements dependent on the temperature and sedimentation rate.

The surfaces of the grown quasicrystals provide characteristic shapes given by straight lines along the symmetry lines. Additionally, distances corresponding to the long potential length scale dominate at the surface. In further studies we have identified phasonic flips in quasicrystalline systems that have grown without gaps or local triangular order. Phasonic flips and their healing have recently been investigated experimentally during the growth of metallic quasicrystals [379]. They are also essential in the quasicrystalline systems described by phase field crystal models [115, 116]. We depict similar processes in our simulated colloidal quasicrystals in which the flip fraction decreases in deep layers.

The depth and position of the second potential minimum play an important role in the formation of quasicrystals. A deep minimum increases the number of particles with a distance of the long length scale and causes an increased formation of large triangles. Varying positions result in an excess of triangles with the length scale being dependent on the direction of variation.

Our model can be applied to all quasicrystalline systems that are stabilized by an isotropic interaction potential with multiple length scales. We expect to find similarities in quasicrystals with even other rotational symmetries as well.

In further simulations we have studied the growth of dodecagonal quasicrystals consisting of particles that either interact according to the Lennard-Jones–Gauss potential or of structures formed by patchy colloids that interact with a Lennard-Jones potential and additionally possess preferred bond angles.

We have analyzed structures grown with different sedimentation rates and temperatures according to their orientational order. While for low temperatures we observe the phenomenon of diffusion-limited aggregation that leads to network-like structures, the best quasicrystals are obtained for large temperatures as long as we stay below the melting transition. With larger temperatures, phasonic flips occur more frequently in the structures. Since the flips close to the surface dominate, these flips support the growth of almost perfect quasicrystals as similarly observed for decagonal quasicrystals.

At intermediate temperatures differences between the structures grown with isotropic particles and those obtained with patchy colloids can be observed. In case of the isotropic particles the long potential length scale dominates for low temperatures. Note that we have made similar observations for the decagonal quasicrystals studied in [265]. In case of the dodecagonal square-triangle quasicrystals considered here, the long length scale leads to triangular arrangements or ring-like defect tiles. In addition, phasonic flips corresponding to zipper motions with additional shield tiles are observed (cf. the theoretical work in [385]).

The growth of quasicrystals that consist of patchy particles is not based on the competition of two given length scales. Therefore, patchy particles have the advantage that the second length scale of the quasicrystal is not supported directly by the pair potential but only indirectly via the preferred binding angles. As a consequence, we do not find defects based on an undesired dominance of the long length scale, e.g. the ring structures with long nearest neighbor distances that can be found for isotropic interactions do not occur for patchy colloids. On the downside, for patchy colloids we observe the occurrence of regions with different phasonic or phasonic displacements. These regions sometimes are connected to dislocations that have not been observed in case of isotropic particles. The regions with different phasonic displacement and the dislocations are probably due to the smaller mobility at the surface in combination with the requirement to not only adjust the positions to the perfect structure but also the orientation.

In conclusion, patchy particles provide an interesting alternative way to obtain almost perfect soft-matter quasicrystals. They also might present an interesting approach concerning the struggle to obtain well-controlled colloidal quasicrystals in experiments. However, some questions remain open for future studies, e.g. concerning the mechanism how the second length scale of the quasicrystal is supported by the binding angles and why colloidal particles with five or seven patches form dodecagonal quasicrystals [119, 120] instead of structures with rotational symmetries that are related to the number of patches as one might naively expect.

Generally, since we have investigated two-dimensional systems, an extension of our studies could include the influence of a substrate as is present in experiments (e.g. [380, 381]), in theoretical studies [344, 369], or in simulations [247]. Concerning the growth of quasicrystals in three dimensions we expect that some features are similar to the growth behavior in two dimensions that we have studied in this Chapter. For example, the development of the orientational order, facets in forms of surface particles that arrange along the symmetry planes of the growing structure, or local phasonic flips probably occur in a similar way in three dimensions. However, there might be some differences between the growth in two and three dimensions. The diffusion of deposited particles on the surface of a three-dimensional structure is smaller due to a stronger binding by an augmented number of neighbor particles. Furthermore, the formation of defects is different because dislocation lines can occur in three dimensions as shown in simulations [247]. Note that while perfect long-range quasiperiodic positional order can exist in three dimensions, in two dimensions the positional order decays algebraically at non-zero temperatures (see, e.g. [387, 388]).

Finally, while we only study the growth obtained by depositing one particle after the other on the surface, it might be interesting to have a closer look at the growth that occurs if small clusters can form in the melt and such clusters are deposited

on the surface of the quasicrystal (see [375]).

# Chapter 7

## Phase transitions in two-dimensional colloidal quasicrystals

While in the previous Chapter we discussed the growth of two-dimensional colloidal quasicrystals, in this Chapter we study their melting. As in the previous Chapter the particles interact with an isotropic pair potential supporting the two length scales present in decagonal quasicrystals. With our investigations we want to find out the similarities and differences of the melting process in periodic and quasiperiodic systems.

We order the Chapter as follows: In Section 7.1 we introduce common theories on the melting process in two-dimensional periodic and quasiperiodic systems. In Section 7.2 our numerical studies of the melting of decagonal quasicrystals are presented. A conclusion is given in Section 7.3.

The major part of this Chapter is based on the manuscript of our publication [G]. A statement about the concerned Sections and a detailed contribution of the authors is provided in the *List of publications*.

### 7.1 Melting in two dimensions

Melting in two dimensions is an interesting and intriguing process. While in three dimensions the phase transition between a solid crystal and a liquid is of first order [389], in two dimensions there exist different competing melting theories. Solids in two dimensions possess long-range orientational order and quasi-long-range positional order [387, 390]. The KTHNY theory [32–35] which was developed by Kosterlitz and Thouless [32] (and independently by Berezinskii [31]) and completed by Halperin, Nelson and Young [33–35] predicts the melting to occur in two

steps via an intermediate hexatic phase between solid and liquid. According to the KTHNY theory the transition from the solid to the hexatic phase is induced by the decomposition of pairs of dislocations into single dislocations when the temperature is increased (see Section 2.6 for a definition of dislocations). The process of decomposition is illustrated in Figure 7.1.

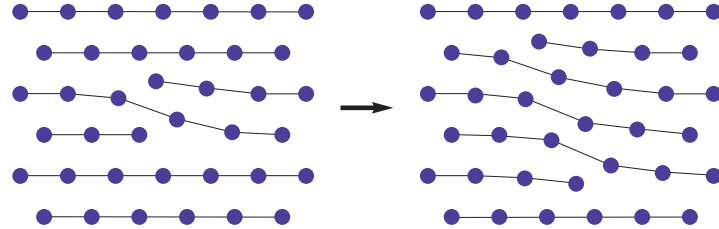


Figure 7.1: Dissociation of a pair of dislocations into two single dislocations. Blue dots represent particles. Left: Pair of dislocations as present in a solid. Right: Decomposed pair of dislocations as present in the hexatic phase. Lattice lines are drawn by connecting particles on horizontal lines or slight deviations from horizontal lines.

Note that in contrast to the melting process in three dimensions that usually starts at the surface of the structure, in two dimensions defects can arise in the bulk and the surface is rather irrelevant. In the hexatic phase free dislocations cause short-range positional and quasi-long-range orientational order, expressed by exponentially and algebraically decaying correlation functions, respectively. When the temperature reaches a second threshold value, the single dislocations dissociate into two separate disclinations as illustrated in Figure 7.2 (see Section 2.6 for a definition of disclinations). In the resulting fluid orientational order is broken as well.

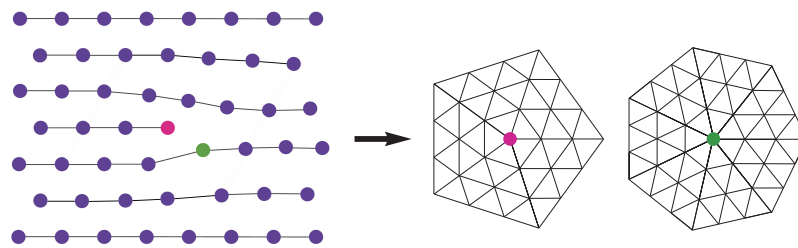


Figure 7.2: Dissociation of a dislocation into two disclinations. Left: Single dislocation as present in the hexatic phase. Right: Decomposed dislocation, i.e. two single disclinations as present in the liquid. The pink and the green particle are surrounded by five and seven nearest neighbor particles, respectively.

The solid-hexatic and the hexatic-liquid transition are both predicted to be continuous. The two-step melting is confirmed in numerous simulations and experiments [331, 391–397]. However, systems of hard disks suggest a hexatic-liquid transition of first order [310, 398–400]. In case of soft disks the hexatic-liquid transition depends on the parameters of the system. Increasing softness in purely repulsive potentials leads to a change from first-order to continuous transitions [315]. Similar observations are made for further model systems with rising densities [401]. Alternative theories (see, e.g. [402, 403]) predict a first-order solid-liquid transition which is either induced by grain boundaries [404–406] or due to the simultaneous dissociation of dislocations and disclinations as studied in mean-field theories [407]. Another theory suggests a melting induced by vacancies [408].

The melting of quasicrystals has hardly been studied yet. A melting theory for two-dimensional pentagonal quasicrystals was developed by Piali De and Robert A. Pelcovits [388, 409–411] who predicted the melting to occur in two steps with an intermediate phase called pentahedric phase in analogy to the hexatic phase in crystals [388]. The process is supposed to be similar to the melting of periodic crystals as predicted by the KTHNY theory. Note that the correlation of phasonic displacements  $\varphi$  that arise due to additional degrees of freedom in quasicrystals (see Section 2.5) is expected to diverge as  $\langle(\varphi(0) - \varphi(R))^2\rangle \propto \ln(R)$  with distance  $R$  in two-dimensional quasicrystals [156, 412], i.e. perfect long-range phasonic order is not possible.

## 7.2 Event-chain Monte Carlo simulations of the liquid to solid transition of two-dimensional decagonal colloidal quasicrystals

In this Section we investigate phase transitions in two-dimensional systems of decagonal colloidal quasicrystals. We apply the event-chain Monte Carlo algorithm to a pair potential of the Lennard-Jones–Gauss type [28, 29] with two typical length scales. We find a rich phase diagram for various densities and temperatures and a first-order solid-liquid transition.

We order the Section in the following way: First, we describe our system as well as the simulation method. Second, we give an overview of phases that form at various densities and temperatures. Third, the phase transition between quasicrystal and liquid is studied at a fixed temperature in detail. Afterwards, we investigate the orientational and positional order of the structures by employing appropriate correlation functions. Finally, we discuss the impact of phason relaxation by means of correlation functions.

### 7.2.1 System and method

We simulate two-dimensional systems of identical particles that interact according to an isotropic Lennard-Jones–Gauss pair potential  $V_{LJG}(r)$  as given in equation (3.50) in Subsection 3.4.1. Like in our studies presented in Section 6.1 we choose the potential parameters  $r_G = 1.52$ ,  $\epsilon = 1.8$  and  $\sigma^2 = 0.02$  such that two incommensurate length scales that are typical of decagonal quasicrystals are supported [28]. We consider interactions that are typical in colloidal systems. However, in principle our approach can also be seen as model for quasicrystals on other length scales.

In order to model large systems we apply event-chain Monte Carlo simulations based on chains of displacements as previously described in [309] (see Section 3.3 for a detailed description of event-chain Monte Carlo simulations). We further extend the algorithm to our Lennard-Jones–Gauss potential with two minima, i.e. we model two repulsive and two attractive regions. We only search for short-range events with possible event partners within the cutoff radius.

The event-chain Monte Carlo algorithm is usually applied in the  $NVT$ -ensemble. In order to obtain a phase diagram and to find out whether an intermediate pentahedric phase occurs within the melting process, we model systems with various densities  $\rho$  and temperatures  $T$ . Note that the  $NVT$ -ensemble is well-suited for our concerns. The simulation box is chosen with periodic boundary conditions and with a size that makes a periodic approximant structure that is similar to the perfect decagonal quasicrystal fit into the box. In our examples we either simulate  $N = 645$  particles in a box with  $L_x/L_y \approx 1.91030$  or  $N = 18698$  particles with  $L_x/L_y \approx 1.17557$ . Our simulations are either started from a liquid or a decagonal approximant. The positions of the perfect decagonal approximant are obtained from the most pronounced maxima of the interference pattern of five laser beams [7, 8, 125, 129, 325] (see also Section 4.2).

### 7.2.2 Phase behavior – overview

First, we investigate the phases that emerge in two-dimensional systems of  $N = 645$  particles interacting according to the Lennard-Jones–Gauss potential. The simulations are started from a liquid. The energies of the simulated systems fluctuate around constant energy values after about  $3 \cdot 10^6$  or less sweeps. In order to check for any further relaxation we run the simulations for at least  $5 \cdot 10^6$  sweeps. In the region where quasicrystals build we perform up to  $8 \cdot 10^7$  sweeps. Dependent on the temperature and density we observe a rich variety of different structures which are summarized in a phase diagram (see Figure 7.3 (a)). We identify the phases by means of the structure factor in reciprocal space (see Subsection 3.5.2 for a definition of the structure factor). Furthermore, we consult the real-space

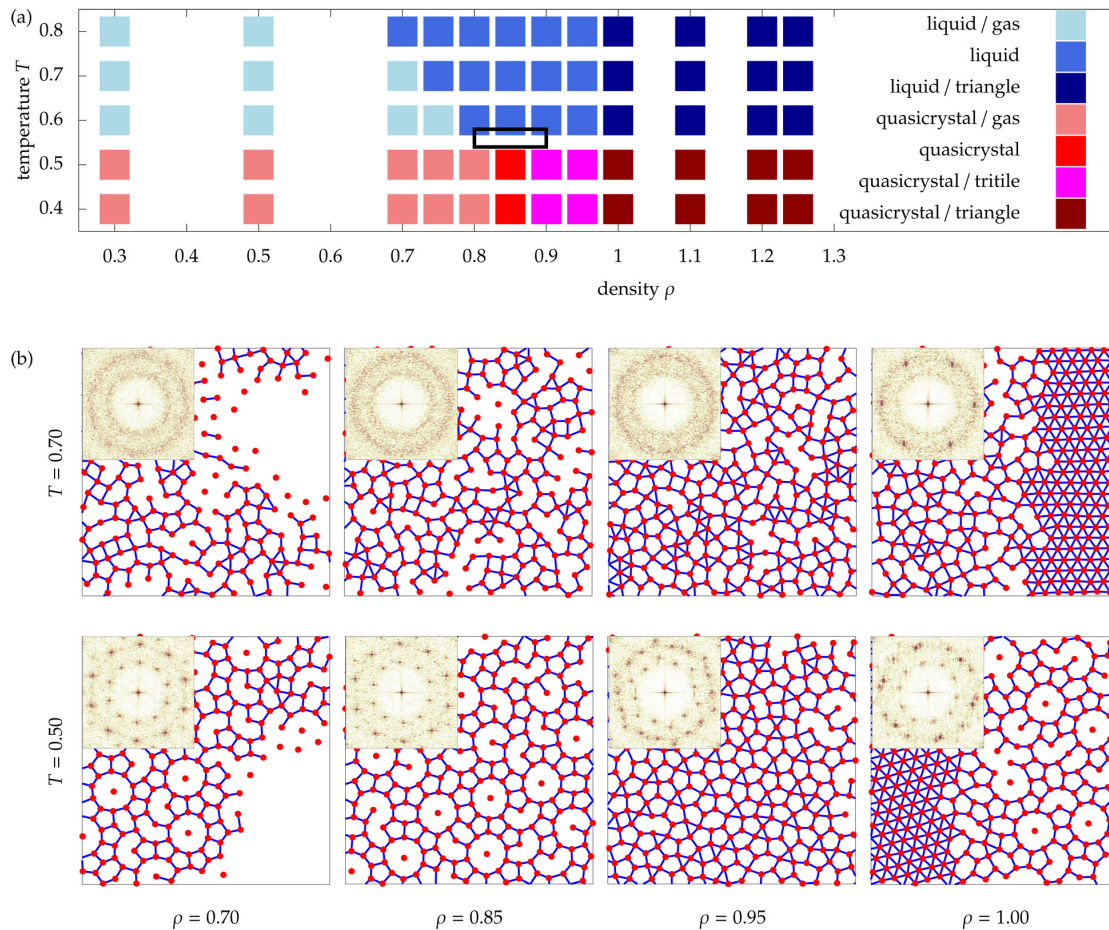


Figure 7.3: (a) Phase diagram dependent on the density  $\rho$  and temperature  $T$  in systems of  $N = 645$  particles. Simulations are started from the liquid. The color code on the right denotes the phases, which are either pure or a mixture of two coexisting phases marked by “/”. The region within the black rectangle contains phase transitions from quasicrystal to liquid and will be investigated in detail in the next Subsection. (b) Arrangements of particles at  $T = 0.70$  (upper row) and  $T = 0.50$  (lower row) and various densities  $\rho = 0.70$  (first column),  $\rho = 0.85$  (second column),  $\rho = 0.95$  (third column) and  $\rho = 1.00$  (fourth column). Nearest neighbor particles are connected. The insets depict the according structure factors.

tilings which are drawn by connecting nearest neighbor particles with a distance  $d < (d_1 + d_2)/2$ , where  $d_1$  and  $d_2$  denote the first and second peak of the radial distribution function.

For temperatures  $T \geq 0.6$  the thermal energy of the particles is too large for the formation of quasicrystalline structures. Exemplary snapshots of systems with  $T = 0.7$  and various densities are visualized in Figure 7.3 (b) (upper row). We observe a coexistence between liquid and gas at low densities. The gas phase is dilute. With rising density the gas phase vanishes and the fraction of triangles with side lengths of the short potential length grows. At  $\rho \geq 1.00$  the triangles arrange to an ordered lattice in coexistence with the liquid. Six peaks in the structure factor indicate hexagonal symmetry.

For low temperatures  $T < 0.6$  the particles arrange to quasicrystalline structures at appropriate densities. Later in this Section, we will have a closer look at the region where a phase transition from quasicrystal to liquid can be observed. The region is marked by a black rectangle in Figure 7.3 (a). In Figure 7.3 (b) (lower row) we illustrate snapshots with  $T = 0.5$  and various densities. At low densities a quasicrystal coexists with a gas. At  $\rho \approx 0.85$  we get a nearly perfect quasicrystal with a structure factor with sharp peaks underlining the decagonal symmetry with globally constant orientation. Remarkably, at rising densities  $\rho > 0.85$  the quasicrystal partially turns into a crystalline structure built from pentagons and triangles (see also [91]), which coexist with the quasicrystal. Note that pentagons belong to the five basic tiles of a decagonal quasicrystal and possess the highest particle densities among these. Triangles are supported by the short potential length. We refer to the arrangement as tritile phase. Its structure factor possesses a 6-fold symmetry. Surprisingly, at densities that exceed the density of the tritile phase, the particles again rearrange to a quasicrystalline structure that now coexists with a hexagonal lattice with a lattice parameter of the short potential length. The structure factor shows a superposition of peaks that are arranged with decagonal and hexagonal symmetry, respectively. The hexagonal region grows with rising density.

In our systems of  $N = 645$  particles the assembled structures can be clearly identified. Therefore, these systems are used in order to obtain a rough overview. Note that for the detailed study of the melting transition and especially for all correlation functions we always employ the large systems with  $N = 18698$  particles.

### 7.2.3 Phase transitions

In the following the region of the phase diagram in which we find quasicrystals is investigated in detail, i.e. we present studies of phases with  $\rho \in [0.8; 0.9]$  and  $T \in [0.54; 0.58]$  that are received from simulations started with a liquid (see box in Figure 7.3 (a)). In particular, we are interested in the transition from quasicrystal

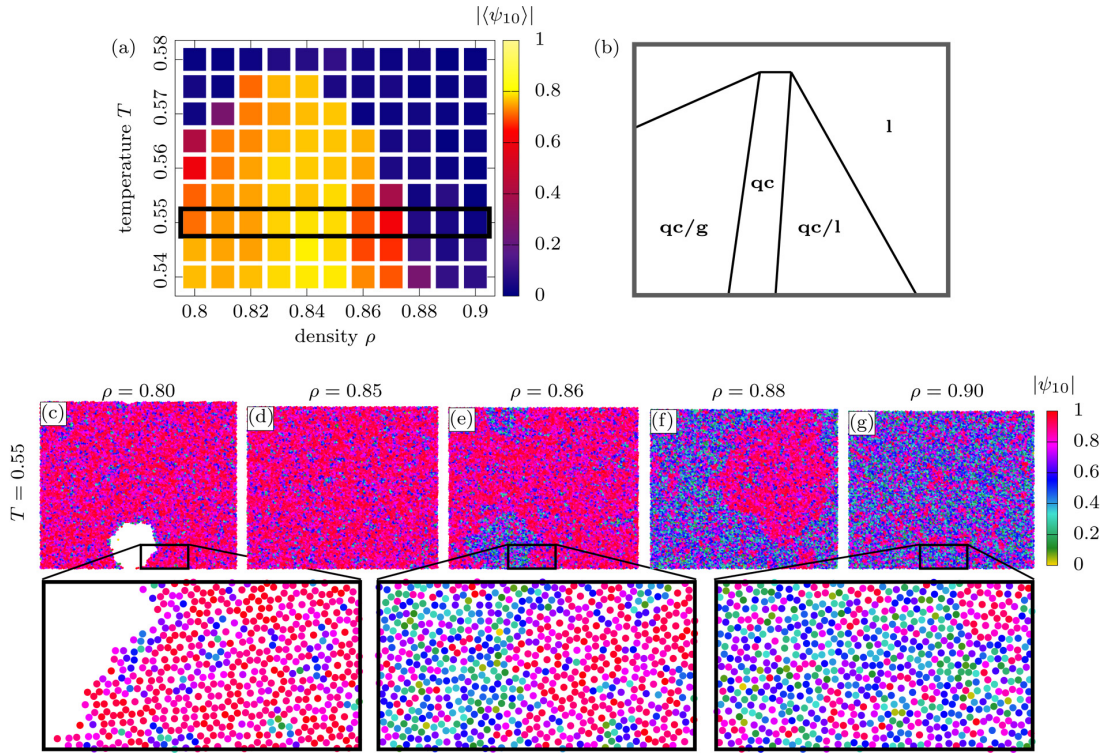


Figure 7.4: Detailed view at the solid-liquid phase transition. (a) Absolute value of the average bond-orientational order parameter  $|\langle\psi_{10}\rangle|$  in systems of  $N = 645$  particles with various densities and temperatures. A color code bar is on the right. The black rectangle indicates systems at a fixed temperature  $T = 0.55$  which are investigated in detail. (b) Rough schematic characterization of the corresponding phases consisting of quasicrystals (qc), gas (g) and liquid (l) or coexistences between two phases. (c)-(g) Arrangements of  $N = 18698$  particles at  $T = 0.55$  and various densities. The particles are colored according to their absolute value of the local bond-orientational order parameter  $|\psi_{10}|$ . The color code is shown on the right. (c) Coexistence between quasicrystal and gas at low density  $\rho = 0.80$ . (d) Quasicrystal at  $\rho = 0.85$ . (e) and (f) Coexistences between quasicrystal and liquid at  $\rho = 0.86$  and  $0.88$ . (g) Liquid at  $\rho = 0.90$ . Bottom: Amplified particle-resolved sections of the systems. All depicted systems were simulated from the liquid.

to liquid. In Figure 7.4 (a) we plot  $|\langle\psi_{10}\rangle|$  obtained from systems of  $N = 645$  particles as a function of the temperature and density.  $\psi_{10}$  describes the local bond-orientational order parameter with respect to 10-fold rotational symmetry (see Subsection 3.5.4 for a definition of  $\psi_{10}$ ). We consider particles with a distance  $d < (d_2 + d_3)/2$  as neighboring particles.  $d_2$  and  $d_3$  denote the second and third peak of the radial distribution function. In the quasicrystalline phase  $|\langle\psi_{10}\rangle|$  obtained from single configurations deviates up to  $\pm 4\%$  from the illustrated average over 50 configurations. In Figure 7.4 (b) a corresponding phase diagram is shown schematically. For sufficiently small temperatures the region with clearly largest  $|\langle\psi_{10}\rangle|$  provides quasicrystalline order. The quasicrystal is surrounded by coexistences between quasicrystal and gas or respectively liquid at lower or higher densities.

We now choose a fixed temperature  $T = 0.55$  at which a solid-liquid phase transition is observed (see black rectangle in Figure 7.4 (a)). We perform extensive simulations of large systems with  $N = 18698$  particles and various densities. In these large systems we perform at least  $6 \cdot 10^6$  sweeps. In the region where quasicrystals build we even perform up to  $2 \cdot 10^7$  sweeps. Snapshots of different phases obtained from simulations started with a liquid are visualized in Figures 7.4 (c)-(g). The particles are colored according to  $|\psi_{10}|$ .

The coexistence between quasicrystal and gas at low densities is accompanied with a sharp surface between both phases (see Figure 7.4 (c)). At  $\rho = 0.85$  we observe a quasicrystalline phase with decagonal symmetry as illustrated in Figure 7.4 (d). Small deviations from the decagonal symmetry in terms of phononic displacements are caused by thermal fluctuations. At  $\rho \geq 0.86$  a liquid coexists with a phase with at least local quasicrystalline order (see Figures 7.4 (e) and (f)). The phase coexistence suggests a first-order transition to the liquid. In principle, a similar behavior was observed for the phase transitions of periodic crystals [310, 315], where the coexistence is between a hexatic phase with local crystalline order and unbound dislocations and a liquid. However, in the next Subsection we show that in our case the phase is not a pentahedric phase (corresponding to the hexatic phase in periodic systems) as predicted in [388], but a quasicrystal. At  $\rho \geq 0.90$  the orientational order is lost, resulting in a liquid (see Figure 7.4 (g)).

In Figure 7.5 we illustrate the potential energy per particle  $E_{\text{pot}}/N$  of the investigated systems with  $T = 0.55$  and  $N = 18698$  as a function of the density  $\rho$ . Results are shown from simulations started with a liquid or a perfect decagonal approximant. The suggested first-order transition from the ordered phase to the liquid is supported. In case of simulations started from the solid, the energy increases at slightly larger density  $\rho \approx 0.86$  where coexistence with the liquid begins. Note that at low densities  $\rho < 0.85$  the energy increases due to the coexistence with gas.

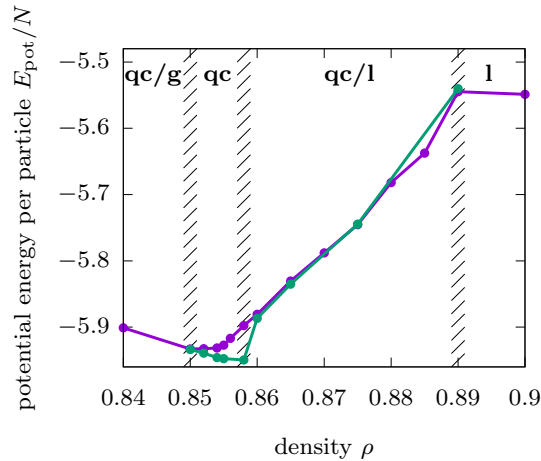


Figure 7.5: Potential energy per particle  $E_{\text{pot}}/N$  as a function of the density. The systems are simulated with  $T = 0.55$  and  $N = 18698$ . The initial configurations are either a perfect decagonal approximant (green) or a liquid (purple). The corresponding phases are indicated on the top using the same abbreviations as in Figure 7.4 (b). Lines roughly separate the phases.

## 7.2.4 Correlation functions

In order to decide whether the phase that coexists with the liquid is a solid quasicrystalline phase or a pentahedric phase, we analyze the orientational and positional correlation functions of our systems with  $N = 18698$  and  $T = 0.55$  for various densities (see Figure 7.6).

We start with the orientational correlation function with respect to decagonal symmetry  $g_{10}(r)$  (see Subsection 3.5.4). For densities  $\rho = 0.85$  and  $\rho = 0.855$  below the beginning of the coexistence region,  $g_{10}(r)$  is nearly constant which indicates long-range orientational order. This behavior is found in both, simulations started from an initially perfect quasicrystal (see Figure 7.6 (a)) and from a liquid (see Figure 7.6 (b)). Even at the beginning of the coexistence interval with densities  $\rho = 0.86$  and  $\rho = 0.865$  the correlations decay slower than the algebraic decay  $g_{10}(r) \propto r^{-0.25}$  that is predicted to arise at a possible transition from a pentahedric phase to the liquid [388]. Accordingly, the orientational order suggests that there is no pentahedric phase neither for low densities before the coexistence nor in coexistence with a liquid. In the liquid, the correlation functions decay exponentially and orientational order is lost.

In periodic solids, the positional order can well be measured by means of the two-dimensional pair correlation  $g(\mathbf{r})$ . Here, we apply the method to our quasicrystals. In Figures 7.6 (c) and (d) we depict the cut of  $g(\mathbf{r}) - 1$  along the  $x$ -axis, i.e.  $\mathbf{r} = (x, 0)$  (see also [310, 315] for the so-called coherent pair correlation

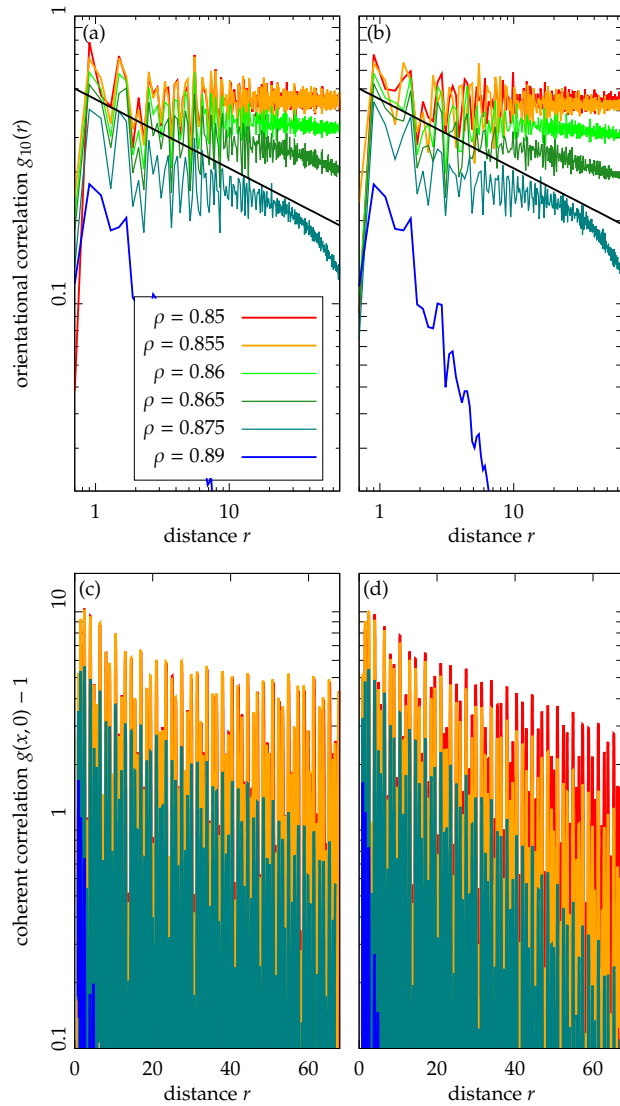


Figure 7.6: (a)-(d) Correlation functions of systems with  $T = 0.55$  and various densities obtained from simulations started with a perfect decagonal structure (left column) or with a liquid (right column). (a) and (b) Bond-orientational correlation functions  $g_{10}(r)$ . The black lines illustrate the decay as predicted within the KTHNY theory for quasicrystals [388] at the transition from pentahedric to liquid, i.e.  $g_{10}(r) \propto r^{-0.25}$ . Note that the correlation functions depicted in green are obtained from systems in the coexistence region. (c) and (d) Coherent correlation functions  $g(x, 0)$  along the symmetry directions.

function). Simulations started from a perfect decagonal structure (see Figure 7.6 (c)) show an algebraic decay of the peak height envelope for systems with low densities  $\rho = 0.85$  and  $\rho = 0.855$ . Such an algebraic decay is expected from a two-dimensional solid [387] and is in accordance with the results of the orientational order. In case of simulations started from a liquid (see Figure 7.6 (d)) the positional correlation decays exponentially already for low densities  $\rho = 0.85$  and  $\rho = 0.855$ , which indicates short-range positional order. Note that in periodic crystals, short-range positional order is not compatible with long-range orientational order. In a solid, the positional order should only decay algebraically as predicted by the Mermin-Wagner theorem [387, 390].

### 7.2.5 Dislocations and phason relaxation

In order to approach the origin of the short-range positional order, we analyze the considered structures regarding dislocations by filtering single density modes as previously described by Korkidi *et al.* [332] (see also Subsection 3.5.5). In the quasicrystalline phase, both in the pure case and in coexistence with a liquid, we find a few pairs of bound dislocations as expected in a solid, no matter whether the system has been equilibrated from a perfect decagonal structure or from a liquid. However, we do not observe unbound dislocations, which are the characteristic features of the pentahedric phase. This supports the absence of an intermediate pentahedric phase during the phase transition, and the observed fast decay of the positional correlation function cannot be explained by dislocations.

In a further approach we investigate how phasonic excitations impact the positional correlation function. Phasonic flips are local rearrangements that retain local decagonal symmetry, hence are energetically cheap. In a perfect decagonal structure, the positions of the particles are on well-positioned lines that are arranged according to a Fibonacci sequence (see Figure 7.7 (a)). Single flips cause only local deviations from the Fibonacci sequence and always retain quasicrystalline order. Furthermore, the flips can occur in a correlated way, and in the limit of excitations with infinite wave length, they do not cost any free energy at all. If phasonic excitations occur at a finite wavelength, incomplete lattice lines occur that destroy the global order according to the Fibonacci chain. We systematically insert correlated phasonic flips into the perfect decagonal structure by shifting half lattice lines (see Figure 7.7 (b)). The resulting structure is again a quasicrystal with neither local tiling defects nor dislocations. In Monte Carlo simulations we heat both systems at  $T = 0.5$  (see Figures 7.7 (c) and (d)). During heating, local flips occur, but the interrupted lines in the prepared system usually remain. Note that the systems are not meant to fully equilibrate, but serve as test systems for the decay of  $g(\mathbf{r})$  in the presence of phasonic flips. The positional correlation functions along the  $x$ -direction of both heated systems are illustrated in Figure 7.7 (e).

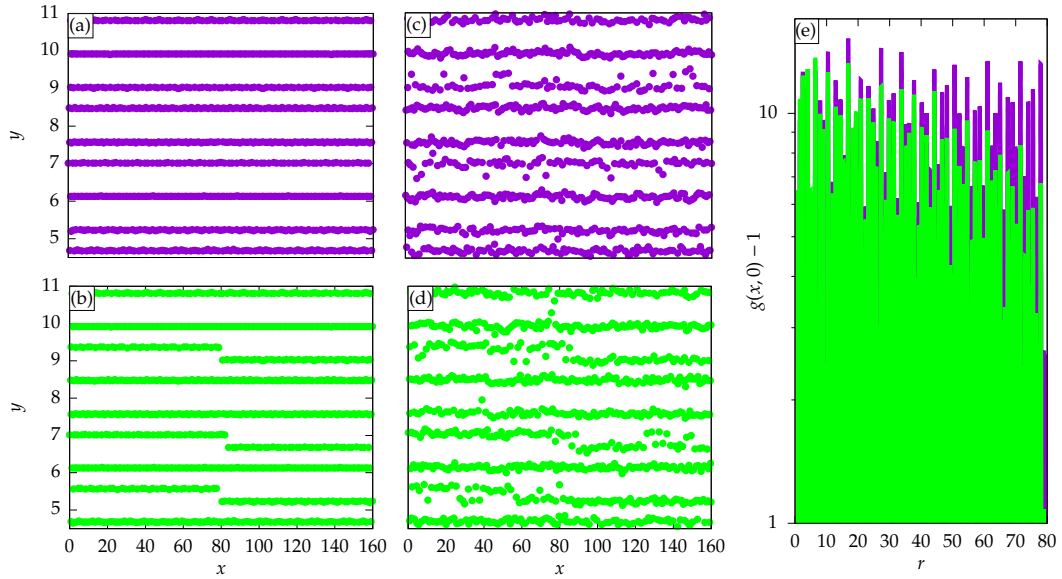


Figure 7.7: Oblique views on systems with decagonal order (particle positions in physical  $(x, y)$  space). (a) Perfect decagonal approximant. (b) Structure from (a) with inserted correlated phasonic flips in the form of shifted lattice lines. (c) and (d) Structures from (a) and (b) heated at  $T = 0.5$ . (e) Coherent correlation functions along the  $x$ -direction of the structures shown in (c) and (d).

In case of the system with inserted phasonic flips the correlation function decays faster. Since no defects – in particular no unbound dislocations – are present, the fast decay can be attributed to the correlated flips. Consequently,  $g(\mathbf{r})$  is not a clear criterion in order to determine the positional order in quasicrystals.

In the systems investigated in the previous Subsection that are obtained from a liquid, we observe similar interrupted lines of particles which do not find together, at least not within the simulation time. Thus, the fast decay of  $g(\mathbf{r})$  seems to be due to phasons which are not completely relaxed compared to the perfect quasicrystal.

We were not able to determine beyond doubt whether the equilibrium structure of the quasicrystal should contain the phasonic excitations as observed for the systems started from the liquid or not as seen for systems started from a perfect decagonal order. The excitation or the relaxation of correlated phasonic flips occurs on timescales that are far too long to be studied with Monte Carlo simulations. While we can study the dynamics of local phasonic flips over long times in much smaller systems, we cannot explore the phasonic excitations that matter for the long-distance behavior of the correlation functions and that correspond to rearrangements correlated over long distances which are only accessible with large

simulation boxes. Simulations where exclusively phasonic flips can occur indicate that phasonic flips are part of thermal equilibrium [413] and the structure can still be dislocation free or at least usually no isolated dislocations occur.

Furthermore, the logarithmic decay of the correlations of phasonic displacements [156, 412] prohibits a perfect long-range phasonic order. As a consequence it seems possible that the fast decay of the positional order is an equilibrium feature of two-dimensional quasicrystals that can only be avoided if the quasicrystal is stuck in a metastable state and the equilibrium phasonic excitations take too long to occur.

## 7.3 Conclusion

By using event-chain Monte Carlo simulations we have examined the phase diagram of two-dimensional systems of particles that interact according to a Lennard-Jones–Gauss potential. While in previous works, the event-chain Monte Carlo algorithm was applied to particles with purely repulsive interactions [315], our potential possesses two minima providing two incommensurate length scales as present in decagonal quasicrystals. The analysis of the observed configurations based on their orientational order revealed gas, liquid and quasicrystalline phases as well as coexistence regions.

We observed a first-order transition between quasicrystal and liquid. We did not find any pentahedric phase like suggested within the KTHNY theory for quasicrystals [388]. While the orientational order of the solid is long-range, the positional order (suggested by the coherent correlation function) is either quasi long-range as predicted by the Mermin-Wagner theorem [387, 390] when started from a perfect decagonal structure or short-range when the initial structure is a liquid. We found that excited phasonic degrees of freedom can be responsible for the faster decay of the correlation functions. I.e., since  $g(\mathbf{r})$  is affected by phasons, it is not fundamental for the determination of order in quasiperiodic structures.

Our results demonstrate that intrinsic quasicrystals obtained by special pair interactions [102, 113–115, 374, 414] can possess phasonic excitations that lead to a fast decay of the positional correlation function. Note that the growth of quasicrystals [115, 116, 121, 265] is usually accompanied by single or correlated phasonic flips. Only close to the triple point, perfect quasicrystals without phasonic flips may grow [115]. Similarly, tilings obtained from construction rules can be excitation-free [36] or dominated by phasonic flips [156]. It might also be interesting to study the positional order in substrate-induced quasicrystals as obtained in experiments [380, 381], simulations [247] or theoretical studies [344, 369].

Even though our simulations did not reveal a pentahedric phase, we cannot rule out the possibility to find a melting transition according to the KTHNY theory with an intermediate phase in systems with other quasicrystalline symmetries or

structures induced by different pair potentials [102, 113–115, 374, 414]. Furthermore, one might determine the phase transition with different methods like density functional theory or phase field crystal models for quasicrystals [110, 111, 113, 117], or for anisotropic particles that support quasicrystalline order [119–121, 415].

# Chapter 8

## Mode analysis in hyperspace

In the previous Chapters we presented methods to generate colloidal quasicrystalline structures by means of external light fields or internal interactions. As already introduced in Subsection 2.3.5 further methods exist to construct quasicrystalline tilings, e.g. matching rules, substitution rules or the projection method. In this Chapter we make use of the latter method, i.e. we construct quasicrystals as projections or sections of structures that are periodic in a higher-dimensional space (hyperspace) [36]. In hyperspace, phasons correspond to displacements perpendicular to the physical space. Local inversions, equivalent to an embedding into the hyperspace have been applied before to quasicrystals forming in metal alloys. This permits distinguishing random tilings from low-defect quasicrystals [416], and identification of domains with uniform phasonic offsets [417, 418]. Reconstructions of phason strain distributions are used to observe phasonic relaxation processes in the bulk [419] and at the growth front [379] of metallic quasicrystals.

In the following we present our studies of two-dimensional colloidal decagonal quasicrystals obtained from hyperspace, and analyze phononic and phasonic modes in intrinsic colloidal quasicrystals by reconstructing their structure in hyperspace (Section 8.1). A conclusion is given in Section 8.2.

The Chapter contains an accepted manuscript version of our article [B]. Reproduced with permission. Authors' contributions are given in the *List of publications*.

### 8.1 Detection of phonon and phason modes in intrinsic colloidal quasicrystals by reconstructing their structure in hyperspace

In this Section we present a detailed discussion of the embedding procedure in the context of intrinsic colloidal quasicrystals. Both the phononic and phasonic

static displacements are investigated in Brownian dynamics simulations. In particular, we synthesize ideal quasicrystals and quasicrystals with defined non-uniform phasonic strains and study their dynamics during annealing at finite temperature. Particles interact by an isotropic double-well pair potential of Lennard-Jones–Gauss type [28, 29]. Since the detection of dislocations, e.g. by analyzing the first order peaks of the structure factor [142, 247, 332] has been studied before, we here focus on systems at low temperatures, where the formation of dislocations is suppressed. However, local rearrangements of particles also known as phasonic flips do occur, and we show that they correlate with phononic displacement fields. We find that finite phononic strain is pinned by phasonic excitations, even after cooling down to zero temperature.

We first present the methods, i.e. we describe the synthesis of quasicrystals by the section method, we specify phonons and phasons in hyperspace and discuss their analysis, and we describe our Brownian dynamics simulations. Afterwards, the results are presented. We determine the number of phasonic flips that result from a synthetic phason, analyze a synthetic phason in order to test our method, and explore how thermally excited phasonic flips and phononic modes can be extracted from an intrinsic colloidal quasicrystal. Finally, the dynamics of synthetically excited phasons is studied.

### 8.1.1 Quasicrystal synthesis by section method

Quasicrystals may be constructed as projections or sections of higher-dimensional crystals [36]. Conversely, embedding the physical space into hyperspace naturally restores the symmetry between phonons and phasons as hyperspace excitations on an equal footing. In the following we consider for concreteness a two-dimensional decagonal quasicrystal that is derived from the five-dimensional integer lattice. Our technique naturally adapts to quasicrystals of other symmetry and dimensionality.

In order to construct the decagonal quasicrystal, we employ the Penrose basis vectors  $\mathbf{p}_i$  that are also known from the Penrose tiling [420]. Two of these vectors,  $(\mathbf{p}_1)_j = \cos(2j\pi/5)$  and  $(\mathbf{p}_2)_j = \sin(2j\pi/5)$  for  $j = 0 \cdots 4$ , are chosen to span the physical space. Orthogonal to  $\mathbf{p}_1$  and  $\mathbf{p}_2$ , the two-dimensional complementary space is spanned by  $(\mathbf{p}_3)_j = \cos(4j\pi/5)$  and  $(\mathbf{p}_4)_j = \sin(4j\pi/5)$ . Note that the Penrose basis vectors are similar to the wave vectors  $\mathbf{G}_j$  (see equation (4.5) in Section 4.2). The fifth basis vector,  $(\mathbf{p}_5)_j = 1$ , corresponds to the body diagonal of the hypercubic lattice. Projections along  $\mathbf{p}_5$  do not lead to new degrees of freedom because  $\mathbf{p}_5$  is commensurate with the hyperlattice. Hence,  $\mathbf{p}_5$  will not play an important role in our analysis. The length of the physical-space projection of a primitive hypercubic lattice vector is  $a_{\parallel} := (5/2)^{-1/2}$ , and corresponds to the long length scale in the quasicrystal. The short length scale is given by  $a_{\parallel}/\tau$  where

$\tau = (\sqrt{5} + 1)/2$  is the golden ratio (see Subsection 2.3.3).

In order to construct the two-dimensional quasicrystal, only particles are considered that are within a so-called acceptance domain. For the decagonal case, we choose an acceptance domain of decagonal shape in the  $\mathbf{p}_{3,4}$ -plane with a circumradius of  $a_{\parallel}/3$ , and infinite extent in  $\mathbf{p}_5$ -direction. The acceptance domain is attached to each lattice point of the five-dimensional integer lattice such that the whole structure is periodic. The resulting decagonal quasicrystal is similar to laser-induced quasicrystals [7, 126, 129, 334], because the decagonal acceptance domain does closely resemble the equipotential surfaces of the laser field potential energy (circles in the  $\mathbf{p}_{3,4}$ -plane). The polygonal truncation of the acceptance domain corresponds to enforcing a minimal-distance criterion between two neighbouring particles in physical space. This relationship between projected and laser-induced quasicrystals was discussed by Jagannathan and Duneau for the case of octagonal structures [136].

In simulations, we employ finite periodic approximants to the aperiodic quasicrystal: The irrational Penrose vectors are approximated such that the physical-space box is spanned by multiples of lattice vectors of the hyperlattice, i.e. the modified Penrose vectors satisfy  $(L_x \mathbf{p}_1)_j = m_j$  and  $(L_y \mathbf{p}_2)_j = n_j$ , where  $m_j$  and  $n_j$  are integers for all  $j$  (see also Subsection 3.4.4). Unless otherwise noted, in our examples we will use a system with  $m_1 = 13$  and  $n_1 = 21$  ( $L_x/L_y \approx 1.90251$ ). The excitation-free approximant in this simulation box consists of  $N = 1686$  particles. A larger system, with  $m_1 = 8$  and  $n_1 = 55$  ( $N = 2728$ ,  $L_x/L_y \approx 0.44867$ ), is used in Subsection 8.1.7.

### 8.1.2 Phonons and phasons

The hyperlattice can be subject to spatially non-uniform displacements. If the displacements associated with an excitation occur in the direction of physical space, such modes are called phonons, and phasons otherwise (see also Subsection 2.3.5.2). In periodic approximants, all modes can be decomposed into discrete modes that are the harmonics of the simulation box, such as displayed in Figure 8.1. In the following, we also refer to modes by their Miller index  $(h_x, h_y)$ , by their wave vector  $\mathbf{k} = (2\pi h_x/L_x, 2\pi h_y/L_y)$  or by the corresponding wavelength  $\lambda = 2\pi/|\mathbf{k}|$ .

Each mode carries a polarization consisting of two phononic ( $u_{1,2}$  along  $\mathbf{p}_{1,2}$ ) and two phasonic ( $w_{1,2}$  along  $\mathbf{p}_{3,4}$ ) components. The modes are subsumed into a four-dimensional displacement field  $(u_1, u_2, w_1, w_2)$ . For each hyperlattice point, the acceptance domain is shifted by the local value of this field, figuratively stretching (phononic) and buckling (phasonic components) the physical plane. While phonon modes displace particles in the physical space directions, phason modes shift the cut plane in a complementary-space direction. A phasonic excitation (see bold dashed line in Figure 8.2) alters the pattern of hits and misses between the cut

plane and the acceptance domain. The physical expression is the insertion or deletion of particles. In the case of small phasonic gradients, a deletion is typically associated with an insertion at another nearby position (colored squares in Figure 8.2). In the physical-space view, this gives the impression of a particle jumping. Such phasonic flips occur along well-defined displacement vectors which can be derived from the hyperspace geometry. The orientational discreteness of those physical-space motion vectors reflects in the small number of ten possible jump directions (i.e. colors) in Figure 8.1. In this rather extreme example, about one in four particles undergoes a flip as a result of the phasonic excitation.

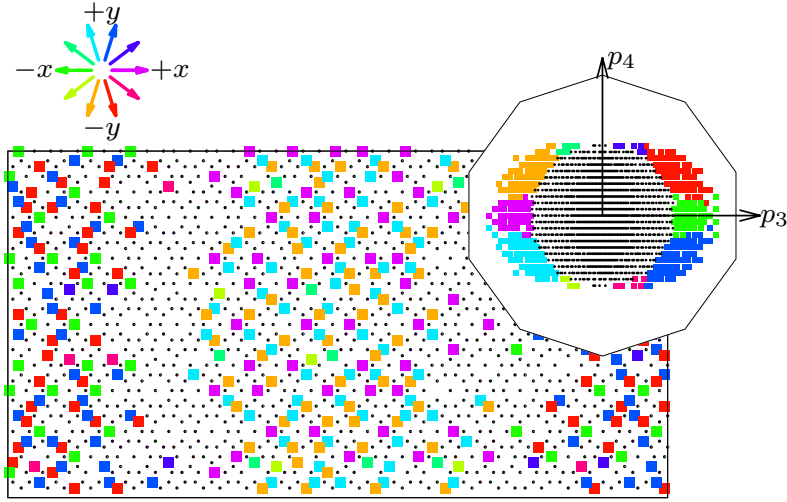


Figure 8.1: A synthetic plane-wave phason in real space (main figure). The displayed phason is a  $(1,0)$  mode, i.e. its wave vector is  $\mathbf{k} = (2\pi/L_x, 0)$ . Its polarization lies in  $w_1$  direction, and the amplitude is  $0.19a_{\parallel}$ . The main figure presents particles in the physical space, with the colored dots representing flipped particles. The colors indicate the jump direction as given in the key at top left, which is also used in the other Figures in this Section. At the crests of the harmonic wave, flip rates are highest. The inset on the top right shows the original acceptance domain (inner decagon) within the complementary space; particles that underwent a phasonic flip are colored identical to the physical-space picture and are identified by lying outside the original decagon.

### 8.1.3 Reconstruction of hyperspace embedding

In this Section we discuss the analysis of phonons and phasons in a quasicrystal by reconstructing its embedding into hyperspace. In addition to the analysis of phonons, which can be straightforwardly carried out in physical space, this will

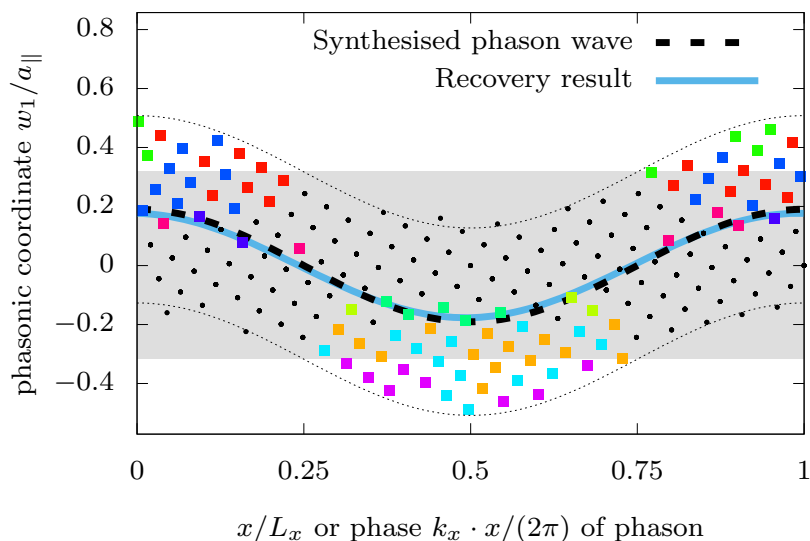


Figure 8.2: Illustration of the synthetic phason wave of Figure 8.1 in an image with one direction of the physical space and one direction of the complementary space. The horizontal direction corresponds to the  $x$ -direction of the physical space (in which the phason wave vector  $\mathbf{k}$  lies), and the vertical direction denotes the  $w_1$ -direction in complementary space of the phason polarization. Colored squares again mark flipped particles, with the same color code as in Figure 8.1. The shaded area gives the projection of the envelope of the acceptance domain of the quasicrystal without phasonic distortion, the thin dotted curves describe the domain as modulated by the phasonic wave (overlaid as a bold dashed curve). The bold blue curve is the result of the phason reconstruction algorithm described in Subsection 8.1.3.

give indications about the phasonic distortions underlying the observed flip patterns.

Basically, the reconstruction is achieved by reversing the projection procedure described in the previous Section. For any two-dimensional particle configuration derived from a decagonal quasicrystal with known origin, one can construct an embedding into hyperspace as explained in the following. First, each particle  $i$  of the test pattern is embedded into five-dimensional space at the location  $\mathbf{R}_i = x_i \mathbf{p}_1 + y_i \mathbf{p}_2$  parameterized by its physical-space coordinates  $(x_i, y_i)$ .

The particle  $i$  is then assigned to the hyperlattice site  $\mathbf{L}_i$  closest to its position. In order to eliminate the trivial  $\mathbf{p}_5$  component from the embedding, we project the five-dimensional integer lattice onto a subspace orthogonal to  $\mathbf{p}_5$ . The hyperspace points that are assigned to a lattice point  $\mathbf{L}_i$  correspond to a four-dimensional Voronoi cell around that point. The residual parts of coordinates  $\mathbf{R}_i - \mathbf{L}_i$  carry, separated into the physical and complementary directions, the information about

phononic ( $\mathbf{u}$ ) and phasonic ( $\mathbf{w}$ ) displacements, respectively. In this way, we are able to reconstruct four-dimensional occupations from two-dimensional information, as long as deviations from an ideal embedded crystal are small compared to the extent of the acceptance domain, or rather the extension of the four-dimensional Voronoi cell.

In effect, we assign each physical particle to a point in hyperspace. The phononic offset is fully recovered, and all the residuals  $\mathbf{u}_i$  indeed collapse to the origin if no phonons are present. The phasonic residuals  $\mathbf{w}$  fall into the acceptance domain in complementary space, and fill it densely in the infinite-system limit. Displays of the residual phasonic coordinates along  $\mathbf{p}_3$  and  $\mathbf{p}_4$  are given as insets of Figure 8.1 and the systems in Subsections 8.1.5, 8.1.6, 8.1.7 and 8.1.8 with the central decagonal domain containing all particles which have not been flipped (black dots). In the hyperspace picture, a phasonic flip corresponds to an assignment of a particle to an adjacent lattice site, so that its complementary-space coordinates lie outside the acceptance domain of the original lattice site (colored squares in inset of Figure 8.1). Conversely, the physical directions of the embedding contain the phononic part of particle motions between an idealized template and the analyzed structure. This decoupling between phononic and phasonic movements effectively separates the two modes of hyperspace displacement. We exploit this to identify phasonic flips.

We now proceed to describe our analysis method for the system as a whole, to extract amplitudes of collective phononic and phasonic excitations. We apply the downhill simplex optimization algorithm [421] to determine the amplitudes of a set of modes which have been chosen in advance. Our choice are plane waves with amplitudes and polarizations given by  $\mathbf{u}$  and  $\mathbf{w}$  for the phononic and phasonic part of the distortion space, respectively. In order to avoid mixing amplitude-type and phase-type variables, we use as orthogonal basis the harmonic functions  $\cos(\mathbf{k} \cdot \mathbf{r})$ ,  $\sin(\mathbf{k} \cdot \mathbf{r})$ .

The reconstruction of a phononic displacement field by embedding it into the hyperspace is lossless. Therefore, we may extract the field directly by applying the downhill simplex optimization to an energy functional that is proportional to the sum of phononic misfits (excluding jumped particles).

In contrast, the reconstruction of phason modes uses a more sophisticated energy functional: Given the current parameter set, a trial system is constructed by the method described in Subsection 8.1.2. Its particle placements are evaluated with penalties for false predictions. With the goal of an approximative recovery of thermal systems in mind, we design the energy functional to be a continuous function of the distortion amplitudes. Rather than a hard binary hit-or-miss criterion, we choose the error function, as a function of distance from the edge of the acceptance domain, to penalize badly-placed particles. The downhill simplex algorithm now

minimizes the difference in distribution of particles between the probed system and trial configurations. During the optimization run, the sigmoid width of the error function is reduced, starting from a value of  $0.03a_{\parallel}$ , reduced step-wise by an overall factor of two.

The result of these two schemes is a quantitative interpretation of how the real-space distortions and phasonic jumps can be understood by deformations of the physical plane within its embedding into hyperspace.

### 8.1.4 Brownian dynamics simulations

We study thermally activated phononic and phasonic excitations in colloidal quasicrystals by employing Brownian dynamics simulations as described in Section 3.1. The particles in our system interact through the Lennard-Jones–Gauss potential  $V_{LJG}(r)$  [28, 29] with the parameters  $r_G = 1.52$ ,  $\epsilon_G = 1.8$  and  $\sigma^2 = 0.02$  favoring local decagonal symmetry and supporting quasicrystalline structures [29] (see Subsection 3.4.1).

We determine the unit distance  $r_{LJ} = 0.6554a_{\parallel}$  as the length scale of the pair potential such that – in accordance with the barostat used in references [29, 91] – a pressure-free system at  $T = 0$  is achieved. Note there is a substantial detuning of the Lennard-Jones minimum relative to the pair distances of the actual system, in contrast to the near-perfect match of the Gauss minimum.

We obtain initial positions of the particles from the projection method using a periodic approximant. The systems are heated up and held at a constant temperature for  $t = 10\tau_B$ , so that thermal equilibrium is reached. We remain well below the melting temperature  $T_M = 0.56 \pm 0.02$  from [29]. Prior to analysis, systems are instantaneously quenched: We continue the Brownian dynamics simulation at  $T = 0$  for a duration of  $t = 5\tau_B$  to allow the particles to find the equilibrium positions in their local environment, i.e. to freeze out phononic thermal noise.

### 8.1.5 Phason amplitudes and numbers of phasonic flips

We first determine the number of phasonic flips which are introduced by a phasonic excitation with respect to the reference state. The phasonic excitation is constructed by choosing a set of mutually orthogonal harmonics with respect to the box size. To each individual mode  $\mathbf{k}$ , a random amplitude vector  $\mathbf{w}(\mathbf{k})$  and a random phase are assigned. We quantify the total magnitude of the excitation  $W$  by the sum of the absolute values of the amplitudes of the individual modes, i.e.  $W = \sum_{\mathbf{k}} |\mathbf{w}(\mathbf{k})|$ .

Figure 8.3 (left) displays the phasonic flip fraction, i.e. the number of flipped particles divided by the total number of particles, as a function of the total amplitude  $W$  of the phasonic excitation.

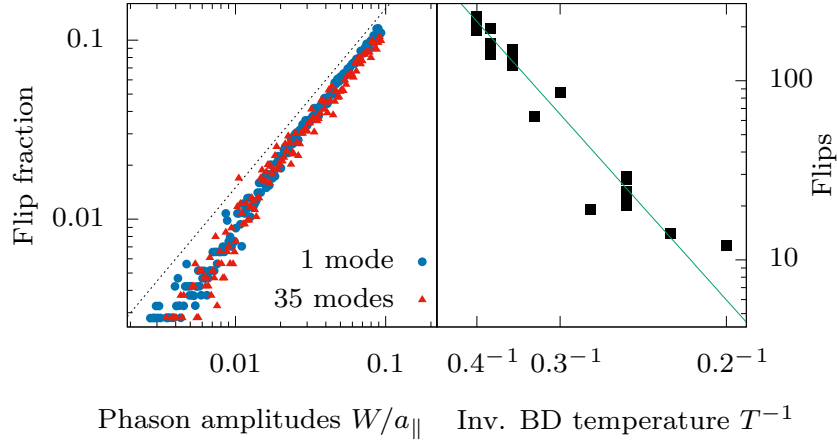


Figure 8.3: Left: Fraction of flipped particles in systems with a single or multiple synthetic phasons dependent on the total amplitude  $W$ . The dotted line shows the slope of a linear relation. Right: Flip fractions after a Brownian dynamics annealing as a function of inverse temperature. The data scatter around an Arrhenius fit (green line).

We find that the flip fraction increases linearly with the total amplitude and therefore with the amplitude of phasonic strain. Under the premise that all particle jumps in a given configuration are caused by phasonic excitations, this relationship could be used to estimate the total phasonic amplitude from the number of flips. Surprisingly, the number of wave vectors in the mode set seems to be insignificant, i.e. it is irrelevant if the total amplitude is contained in a single harmonic or in arbitrarily many modes.

Figure 8.3 (right) displays the flip fraction found after annealing by using Brownian dynamics simulations of duration  $t = 10 \tau_B$  as a function of the inverse temperature. The flip fraction exhibits Arrhenius behavior  $\propto \exp(-\Delta E/k_B T)$  with  $\Delta E \approx 1.43\epsilon_0$  and is compatible with a thermal activation of phasonic waves.

### 8.1.6 Recovery of known phasons from flip pattern

In this Section we test the reliability of recovering a single, known phasonic excitation from a flip pattern that was constructed using the method described in Subsection 8.1.2. An example of such a system is given in Figure 8.1. We now apply the optimization algorithm of Subsection 8.1.3, restricted to the known phasonic wave vector. As can be seen in Figure 8.2, the recovery result (blue bold line) agrees well with the original phason wave (black dashed line). The top panel of Figure 8.4 displays where particles were flipped (black squares) due to the synthesized phason. In addition, we show where the best-fit reconstructed phason

wave predicts the deletion (blue circle) and insertion (red) of particles. In 94.0% of the created and 94.7% of the deleted particle positions, the fit agrees with the synthetic test system, hence the majority of flips has been correctly interpreted. False predictions usually occur if particles in hyperspace are close to the border of the acceptance domain (indicated by a lighter color in the top pane of Figure 8.4). Part of these discrepancies are due to the deliberate smoothening of the energy functional that we use for optimization.

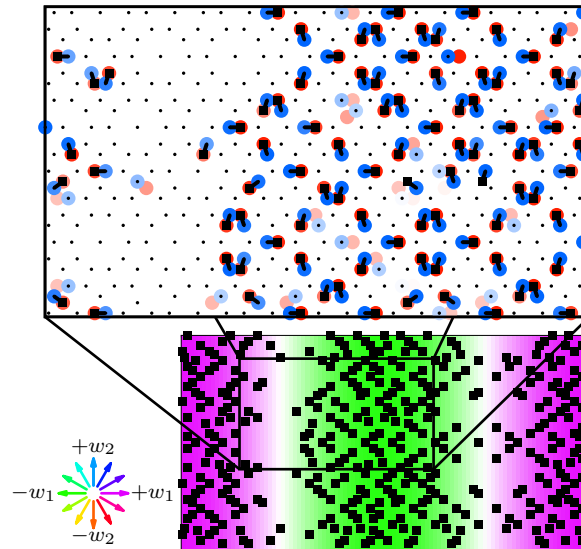


Figure 8.4: Applying the phason fit method to recover the flip configuration from the synthetic phason shown in Figures 8.1 and 8.2. Bottom: Recovered phason wave where the  $w_1$ -displacement is given by the color code. Black squares are flipped particles. Top: Magnification of the marked rectangle. Phasonic flips in the test pattern are denoted by black squares, with the jump vector attached to it. Particles disappearing or appearing due to the recovered phasonic field are indicated by blue and red circles, respectively. Point colors are lightened if embedded phasonic coordinates lie close to the border of the acceptance domain.

The quality of recovery of synthetic phasons depends on the wavelength of the phason. As Figure 8.5 demonstrates, the recovery improves with the wavelength of the phasonic wave. The spatial resolution of a phason mode is limited by the typical distance between particles, making short-wavelength phasons less well-defined. Phasons with wavelengths  $\lambda > 10 a_{\parallel}$  are discovered with good accuracy.

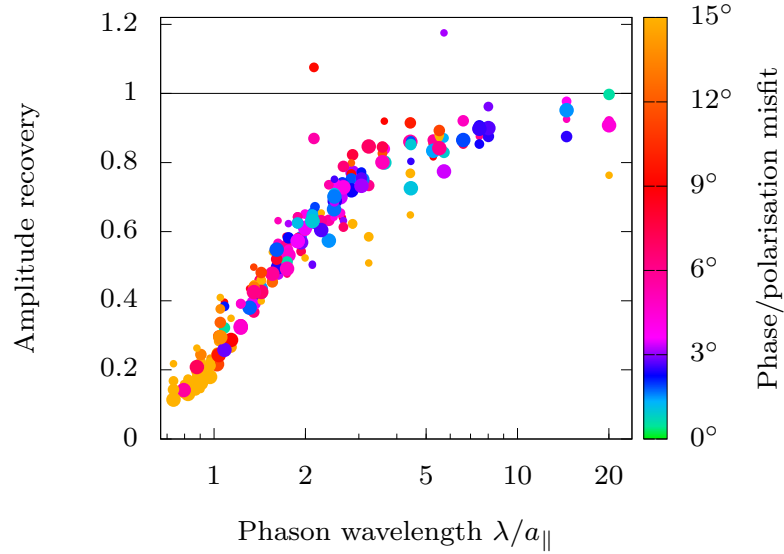


Figure 8.5: Recovery of a single-mode synthetic phason via our fit procedure depending on its wavelength  $\lambda$ . The recovered fraction of phason amplitude (ordinate) and mismatch in phase and polarization (color scale) are reasonable for long-wavelength modes, and decline when the wavelength gets closer to the inter-particle length scale  $a_{\parallel}$ . The absolute value  $|\mathbf{w}|$  of the phason amplitude that we try to recover is encoded into point size, ranging  $0.03 < |\mathbf{w}|/a_{\parallel} < 0.11$ . Its influence is minor, only accounting for a slightly increased variance in amplitude and polarization recovery for low amplitudes.

### 8.1.7 Creation of excitations by annealing

We now explore what kind of excitations occur due to thermal fluctuations and how we can analyze them. We use excitation-free quasicrystals as starting configurations of Brownian dynamics simulations at constant temperature  $T$ . Noticeable numbers of phasonic flips start to occur above  $T = 0.2$  (compare with right-hand panel of Figure 8.3). The vast majority of these flips persist when the system is quenched to  $T = 0$  for analysis. These phasonic flips support, even at  $T = 0$ , a static phononic displacement field. Below  $T = 0.35$ , we find that the phonon field is typically dominated by a transversal (1,0) mode aligned with the long dimension of the simulation box. Figure 8.6 illustrates this effect: After annealing for  $t = 10\tau_B$  at  $T = 0.3$  the final configuration differs by 82 phasonic flips from the initial configuration. The flips enable a phononic strain field that does not level out at  $T = 0$ .

We now use our optimization procedure to extract the amplitudes of the six longest-wavelength modes ( $\lambda > 13a_{\parallel}$ ). For the system shown in Figure 8.6,

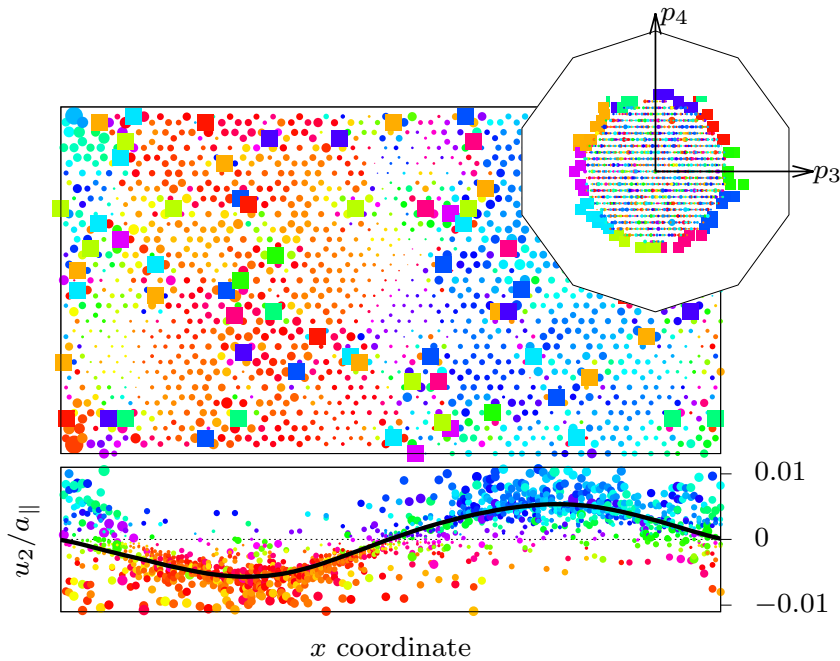


Figure 8.6: Top: Quasicrystal in physical space, annealed by Brownian dynamics simulations at temperature  $T = 0.3$ . Phononic displacements are encoded into point sizes with the point area proportional to the displacement distance; flipped particles are represented by squares. Besides local strain fields around flips, an almost sinusoidal displacement profile has formed, corresponding to a transversal ( $u_2$ -polarized) phonon. The inset denotes the positions in complementary space. Bottom:  $u_2$  displacement and the reconstructed phononic field obtained by optimizing six modes.

we find that the majority of strain lies within the transversal  $(1, 0)$  mode with amplitude  $u_2(1, 0) = 0.053a_{||}$ , while the other modes vanish within fit accuracy ( $|u(\mathbf{k})| < 10^{-2} \times u_2(1, 0)$ ). The best-fit results are consistent between successive runs of the optimization with different random initial parameters. A system with a larger number of particles is shown in Figure 8.7. In this case, a different approximant is used (see Subsection 8.1.1), and the quasicrystal is rotated by 90 degrees with respect to the long dimension of the box. Again, a transversal phonon mode dominates the displacement field, but in this larger system, it is accompanied by additional long-wavelength harmonics.

Next, we want to interpret flips as manifestation of a continuous phasonic displacement field. Again, we consider the system of Figure 8.6. In the optimization procedure, we use the same modes as for the phonon fit, but with phasonic polarizations. In the bottom pane of Figure 8.8, we display the best-fit phasonic

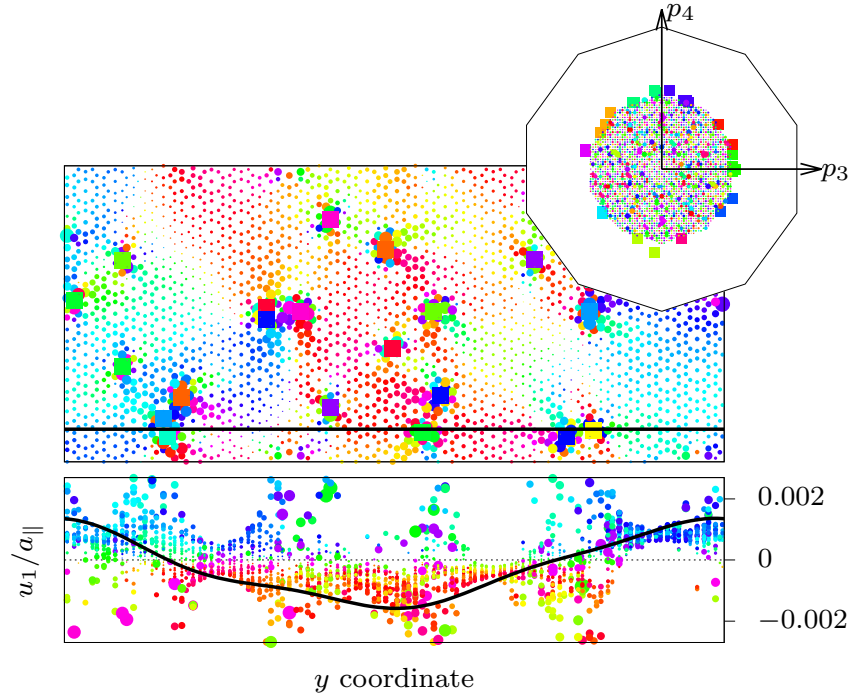


Figure 8.7: Top: Quasicrystal annealed by Brownian dynamics,  $T = 0.3$ , larger system than in Figure 8.6 and with a different approximant, which rotates the orientation by  $\pi/2$  ( $x$ - and  $y$ -directions swapped for depiction purposes; color code stays identical to Figure 8.1 with respect to the visible box orientation). A fit to the phononic displacements with the six longest-wavelength harmonic waves has been conducted. Bottom: The transversal phononic displacement  $u_1$ . It is overlaid with the  $u_1$  component of the fit phonon field (bold line), evaluated along the line in the top image.

displacement field within these modes. No mode clearly dominates the phason field. The total amplitude amounts to  $W = 0.059(14) a_{\parallel}$ , with the largest contribution coming from a  $(2, 0)$  mode with  $|\mathbf{w}(2, 0)| = 0.019(5) a_{\parallel}$  and elliptical polarization. When we interpret the density of flips in the annealed system in the context of Subsection 8.1.5, we expect the summed phason amplitude at about  $0.045 a_{\parallel}$ , which is in reasonable agreement with the value of  $W$  determined in this section by the optimization method.

The phason fit is less reliable than the phonon fit. For different initial parameters, the phason fit yields parameter sets which vary within a standard deviation of about 30%. Furthermore, the top pane of Figure 8.8 demonstrates that the optimization performs worse when predicting the phasonic flips in the Brownian dynamics simulations than for synthetic phasons. Overall, 32% of the created and

34% of the deleted particles agree between the annealed configuration and the recovered phasonic field. Note that wrong predictions are concentrated on particles close to the boundary of the acceptance domain (light colored circles) while flips of particles well within the acceptance domain are usually described correctly (intense colored circles).

The fraction of correctly characterized flips in principle could be increased by including phason modes with shorter wavelength into the optimization process. On the other hand, with an increasing number of parameters, the deviations of the final parameters for different initializations would further increase. Inherently, long-wavelength harmonics can only account for flip events that occur coherently through the whole system. Hence the optimization systematically ignores strongly localized flip patterns, e.g. driven by thermal fluctuations. Nevertheless, with our choice of mode selection, we are able to extract the smooth part of the phasonic field, at the cost of ignoring localized effects.

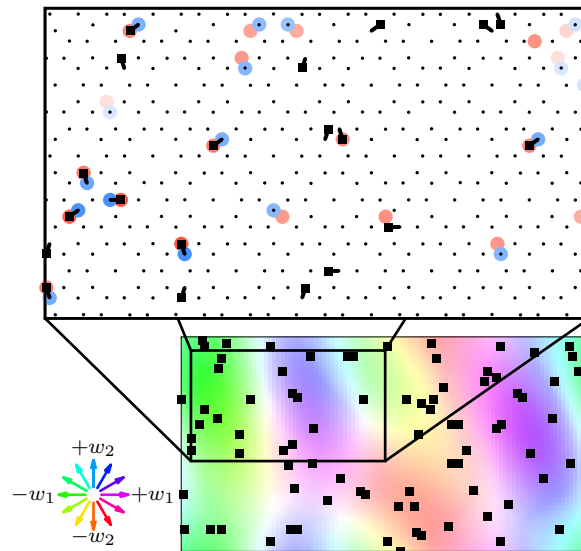


Figure 8.8: Phason recovery for a system annealed at  $T = 0.3$ , presentation identical to Figure 8.4. Bottom: phasonic displacement field (intensity proportional to magnitude of displacement) as the result of the multi-mode fit process, flipped particles as black squares. Top: observations of Brownian dynamics flips (black) and those in the fit (red, blue).

In a continuum picture, phononic and phasonic strain fields are expected to be coupled [9]. In principle, one could conclude from this that a continuous phasonic strain field (evidenced by frozen-in phasonic flips) might give rise to the observed static phononic distortions. Our analysis does not reveal any strong correlation between the observed phonon modes and the dominant phasonic modes. However,

as shown above, a large fraction of observed phasonic flips cannot be accounted for without shorter wavelength phasons. In this limit, a continuum description of the quasicrystal might not be appropriate, such that the phonon/phason coupling is not observed on the atomic scale.

### 8.1.8 Dynamics of synthetic phasons during annealing

Phasonic strain usually is not relaxed at zero temperature: in order to flip a particle one has to cross an energy barrier. However, thermal fluctuations can in principle enable the system to overcome energy barriers and level out phasonic strain. Therefore, we study the relaxation of synthetic phasonic strain fields during Brownian dynamics annealing.

We start with a synthetic single-mode phason and track the relaxation of its amplitude over Brownian dynamics simulation time. Its amplitude may relax, and its phase and polarization may drift with respect to the original phason. One test system exhibits a  $(1, 0)$  mode corresponding to a wavelength of  $40.0 a_{\parallel}$  and a phasonic amplitude of  $0.19 a_{\parallel}$ . A second system has a  $(2, 3)$  mode, i.e. a shorter wavelength of  $6.6 a_{\parallel}$  and an amplitude of  $0.105 a_{\parallel}$ . The relaxation of both systems is studied at two temperatures,  $T = 0.2$  and  $T = 0.3$ . We take periodic snapshots and fit a phasonic wave to each. The amplitude of the recovered phasons is shown in Figure 8.9 as a function of time. As shown by the color code, drifts of the phase and changes of the polarization stay small during our simulation.

For the temperatures considered, the magnitude of the  $(1, 0)$  mode shows no indications of relaxation in the presence of thermal noise. Some phase or polarization misfit is determined from the beginning of the simulation, but it stays constant during the simulation. With its shorter wavelength, the  $(2, 3)$  mode behaves differently: Initially, a fast, relaxation-like process reduces the amplitude. Then, the amplitude stabilizes at a saturation level which is lower for higher temperatures. Our results may be rationalized considering the fact that, at the same amplitudes, the phasonic strain becomes more localized for shorter wavelengths, which might be conducive to relaxation. The saturation indicates that depending on the temperature there is a certain amount of phasonic stress that can prevail in the system. In other words, the phasonic stress associated with the saturation amplitudes is not large enough to initiate correlated phasonic flips that would be necessary to further relax the system.

## 8.2 Conclusion

We have examined phononic and phasonic excitations of two-dimensional decagonal quasicrystals. Our approach combines the synthesis of quasicrystalline pat-

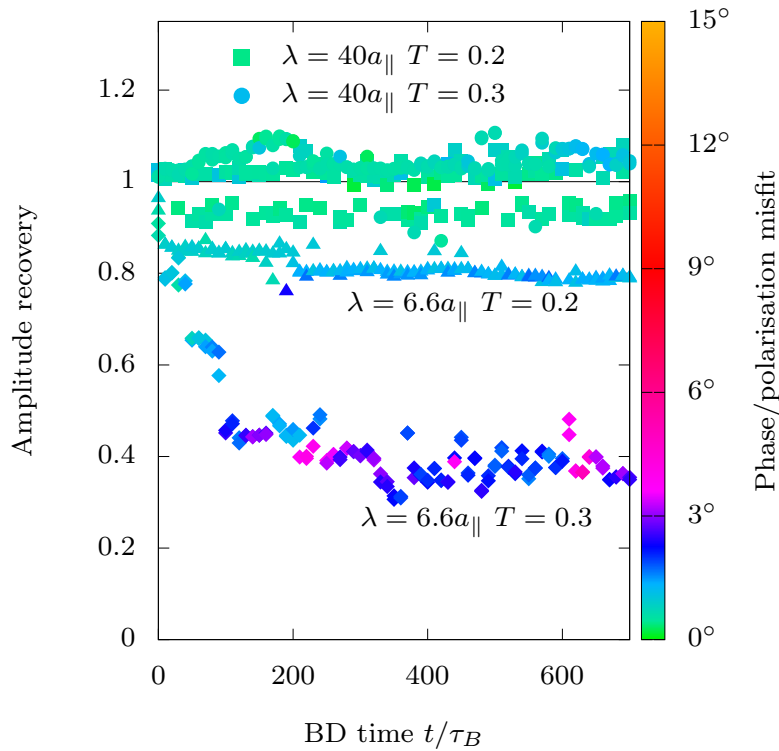


Figure 8.9: Systems with given synthetic phasonic waves are exposed to annealing by Brownian dynamics simulations. As a function of time, the particle configurations at different times are fitted to recover phason amplitude. The sum of a possible phase shift or change of polarization with respect to the original phason is given by the color code (identical to Figure 8.5). Phasonic waves with very long wavelengths stay stable within the simulation time, whereas shorter-wavelength phasons tend to balance out. The higher the temperature, the faster the amplitude decays.

terns, analysis of physical-space location information, and interpretation of excitations in terms of harmonic modes. This can be applied to all quasicrystalline systems of which the ideal structure can be obtained by a projection or section from higher-dimensional space. We quantify spatially non-uniform deviations of the hyperspace embedding in terms of their phononic (stretching) and phasonic (buckling) fields.

The problem of reconstructing the distortion fields from the physical-space coordinates is underdetermined. Nevertheless, our method succeeds in recovering phononic and phasonic distortion fields, especially in the long-wavelength limit. Moreover, we apply this method to probe the excitations which develop in quasicrystals through annealing with Brownian dynamics simulations. Phononic fits,

based on a low-harmonic Fourier ansatz, describe residual strains in thermal systems well. As for phasonic strains, however, the same modes are insufficient to explain all phasonic flips. Hence, for the colloidal system considered, high-frequency phasonic strains corresponding to localized thermal excitations must be assumed as well.

For synthetic phasonic waves, subject to prolonged thermalization, amplitude recovery reveals either stability or decay as a function of time, depending on the gradient of phasonic strain and temperature. Relaxation of phasonic gradients has previously been observed in phason field reconstructions of metallic alloys [419]. We demonstrate that similar processes occur in intrinsic colloidal quasicrystals. In addition, we find a significant degree of temperature-dependent phasonic noise, which is not captured by long-wavelength harmonics.

We are confident that our method, in combination with the known tools for the detection of dislocations [142, 247, 332], is useful to analyze quasicrystals. Quasicrystals, even when free of dislocations, may contain residual deviations from the ideal structure. For example, a dislocation-free quasicrystal grown from a seed might be far from perfect due to built-in local phasonic rearrangements [115]. For another example, namely intrinsic colloidal quasicrystals obtained by Brownian dynamics simulations with perfect initial structures, we have shown in this Chapter that phasonic excitations and as a consequence finite phononic displacement fields even occur at zero temperature. Using our method, we are able to detect and quantify this type of imperfections.

# Chapter 9

## Conclusions

The aim of this thesis was to gain a deeper understanding of quasicrystals and their properties, in particular the dynamics that result from the phasonic degrees of freedom. For that purpose we employed different numerical techniques to model colloidal quasicrystals in two dimensions. Colloidal systems allowed to get access to important and interesting features of quasicrystals that usually cannot be studied in corresponding atomic systems.

One presented approach was generating quasicrystalline order by means of interfering laser beams (Chapter 4). We found a method to obtain discrete typical tilings from continuous interference patterns. By locating colloids inside specific minima in the corresponding potential landscapes of decagonal, octagonal and dodecagonal light fields we received a Tuebingen tiling, an Ammann-Beenker tiling and a shield tiling. The setup resembles atoms on quasicrystalline substrates. Based on the discrete tilings important dynamical properties of quasicrystals were examined. For that purpose specific phasonic displacements were included by manipulating the phases of the laser beams accordingly. With the help of characteristic areas we found particles that easily flip and particles that are hardly affected by phasonic perturbations. In principle, one could even analyze the thermally fluctuating phasonic displacements in intrinsic quasicrystals by comparing them to laser fields. Furthermore, the colloidal dynamics in light-induced quasicrystals were investigated in the presence of phasonic drifts. Using the example of tetradecagonal quasicrystals with rank  $D = 6$  we demonstrated that the method to predict colloidal trajectories in quasicrystals with rank  $D = 4$  as presented in previous publications [11, 12] can further be extended to structures with higher rank. We predicted new and interesting trajectories of the colloids. The complexity of the paths was shown to rise in quasicrystals with rank  $D = 6$  and is expected to increase even more in structures with more phasonic degrees of freedom.

Aside from the generation of quasicrystals by means of external fields, it was illus-

trated that appropriate internal interactions between colloids can lead to fascinating self-assembly processes of quasicrystals (Chapters 5, 6, 7). For that purpose we applied different simulation techniques and interaction potentials and investigated the arising structures and their properties.

In Monte Carlo simulations with an anisotropic pair potential we modeled patchy colloids with attractive regions at the surfaces (Chapter 5). While in previous studies [119, 120] dodecagonal quasicrystals were stabilized in systems of colloids with five patches, we here modeled eight and ten symmetrically arranged patches and found various interesting phases dependent on the patch widths. In case of narrow patch widths metastable octagonal and decagonal quasicrystals built for the first time in systems of patchy colloids. Phasonic flips contributed to the formation. The results are remarkable since even though only one length scale was supported by the potential minimum, the second length was induced by the anisotropic term. Our findings especially contribute to the understanding of the formation of quasicrystals in metallic alloys since narrow patch widths model the sharp binding angles between atoms.

Furthermore, by using Brownian dynamics simulations with an isotropic Lennard-Jones–Gauss potential supporting typical length scales as present in decagonal quasicrystals we employed a novel method to model the growth out of vapor by sequentially depositing particles at a free surface (Chapter 6). It was shown that different fractions of quasicrystalline and hexagonal elements grow dependent on the temperature and sedimentation rate. For appropriate parameters unexpectedly nicely grown quasicrystals were identified. We examined phasonic flips that contributed to a nearly defect-free growth which has already been observed in metallic quasicrystals [379]. Our studies of the growth process were extended to isotropic and anisotropic interactions that support dodecagonal order. A comparison revealed that for both interactions structures with clear dodecagonal symmetry grow for appropriate parameters. Similar results are expected for the growth process of quasicrystals with different symmetries. However, the simulation of structures with more than two length scales is still challenging.

Finally, phase transitions in quasicrystals were investigated on the example of structures with decagonal order (Chapter 7). For that purpose we implemented the Lennard-Jones–Gauss potential in event-chain Monte Carlo simulations for the first time. The event-chain Monte Carlo method allowed to sample equilibrium configurations of large systems efficiently. It was illustrated that the potential induces a surprisingly rich phase diagram for various densities and temperatures. The phase behavior with coexistences between quasicrystal and gas at low densities and respectively quasicrystal and triangular phase at increased densities is completely different from what is known from the phase behavior of periodic crystals. Remarkably, even in the solid the positional order was found to be short-

---

ranged due to excited phasonic degrees of freedom. In an appropriate temperature regime a first-order solid-liquid phase transition was found which did not comply with theoretical predictions of a two-step melting via an intermediate phase [388]. However, we do not rule out the possibility of finding a two-step melting, e.g. at another point in the phase diagram or in other quasicrystalline systems with different interactions or different symmetries.

At last, in a rather technical approach the projection of an ordered structure in hyperspace onto a two-dimensional physical space provided decagonal quasicrystals (Chapter 8). The great advantage of this method is the possibility of systematically inserting and conversely detecting phason modes in quasicrystals. In Brownian dynamics simulations we annealed the quasicrystals in physical space. By embedding the structures in hyperspace phasonic excitations and finite phononic displacements were found that remarkably remained even at zero temperature. Generally, the method can be applied to all structures of which the perfect structure can be obtained in hyperspace.

All in all, many properties of quasicrystals were found to be significantly different from the properties of periodic crystals. Studying the dynamical features disclosed particles that were stable and other ones that were unstable against phasonic perturbations. In the presence of phasonic drifts new complex trajectories of particles were demonstrated. Investigations of colloids with internal interactions revealed further important novel insights. Fascinating self-assembly processes of quasicrystals were observed, e.g. in systems of patchy colloids that built metastable octagonal and decagonal quasicrystals. The positional order of decagonal quasicrystals was unexpectedly found to be short-ranged even in the solid and a first-order transition to liquid was identified. The growth turned out to be essentially dependent on thermodynamic parameters as well as phasonic flips. Finally, remarkable phasonic and phononic excitations were discovered in hyperspace.

On the one hand, our results contribute to a better understanding of the order and dynamics of soft-matter quasicrystals. On the other hand, our approach can also serve as model for quasicrystals on other length scales. Thus, our findings are important not only for the colloidal physics community, but also for other fields in physics, chemistry or material science.

In principle, at least some of the colloidal quasicrystals that we synthesized in our simulations can be realized experimentally. In particular, the presented light-induced quasicrystals have already successfully been implemented in experiments [7, 129, 130, 334]. We expect that our results advance further experimental research, e.g. the realization of specific phasonic rearrangements. Furthermore, regarding patchy particles there are different experimental fabrication methods [351]. We are confident that our work contributes to the progress of the creation of patchy colloids that lead to targeted structures. In future research our results could even

help to realize patchy particles that stabilize quasicrystals. Due to the principal experimental feasibility of our model systems this work provides a basis for novel applications, e.g. in the field of photonics or electronics.

# List of publications

[A] **Colloidal trajectories in two-dimensional light-induced quasicrystals with 14-fold symmetry due to phasonic drifts**

Miriam Martinsons, Matthias Sandbrink and Michael Schmiedeberg  
*Acta Physica Polonica A* **126**, 568 (2014)

DOI: <https://doi.org/10.12693/APhysPolA.126.568>

Copyright 2014 by the Institute of Physics, Polish Academy of Science

## **Abstract**

Quasicrystals are structures that are not periodic but possess a long-range positional order. They can have any rotational symmetry including those that are forbidden in periodic crystals. The symmetry is classified by the point group and the rank  $D$ . In quasicrystals, phasons as additional hydrodynamic modes cause correlated rearrangements of the particles. The number of phasonic degrees of freedom depends on the rank. For colloidal quasicrystals that are induced by laser fields, specific phasonic displacements can be realized by changing the phases of the laser beams in a well-determined way. The arising trajectories of colloids in two-dimensional light-induced colloidal quasicrystals with rank  $D = 4$  have already been analyzed in detail. Here, we analyze the colloidal trajectories in two-dimensional quasicrystals with 14-fold symmetry having rank  $D = 6$ . We observe complex paths of the colloids consisting of straight and winding lines as well as jumps.

## **Author's contribution and appearance in this thesis**

Article [A] is based on results of my master thesis [343]. I performed most of the analytic calculations and the numerical analysis and did the presentation of the data. M. Sandbrink and M. Schmiedeberg supervised the project. All authors were involved in the preparation of the manuscript and have read and approved the final manuscript.

In Section 4.4 of this thesis, the article is reproduced with permission. Slight changes to the formatting are carried out in order to fit the style of the thesis. The conclusion of article [A] is adopted in Section 4.5.

[B] **Detection of phonon and phason modes in intrinsic colloidal quasicrystals by reconstructing their structure in hyperspace**

Johannes Hielscher, Miriam Martinsons, Michael Schmiedeberg and Sebastian C. Kapfer

Journal of Physics: Condensed Matter **29**, 094002 (2017)

DOI: <https://doi.org/10.1088/1361-648X/aa55a5>

Copyright 2017 by IOP Publishing Ltd

**Abstract**

Phasons are additional degrees of freedom which occur in quasicrystals alongside the phonons known from conventional periodic crystals. The rearrangements of particles that are associated with a phason mode are hard to interpret in physical space. We reconstruct the quasicrystal structure by an embedding into extended higher-dimensional space, where phasons correspond to displacements perpendicular to the physical space. In dislocation-free decagonal colloidal quasicrystals annealed with Brownian dynamics simulations, we identify thermal phonon and phason modes. Finite phononic strain is pinned by phasonic excitations even after cooling down to zero temperature. For the phasonic displacements underlying the flip pattern, the reconstruction method gives an approximation within the limits of a multi-mode harmonic ansatz, and points to fundamental limitations of a harmonic picture for phasonic excitations in intrinsic colloidal quasicrystals.

**Author's contribution and appearance in this thesis**

Article [B] results from a cooperation between J. Hielscher, me, M. Schmiedeberg and S. C. Kapfer. J. Hielscher did the synthesis of quasicrystals, the analysis and the graphical presentation of the data, while I did the Brownian dynamics simulations. All authors wrote the manuscript together.

In this thesis, article [B] provides the basis of Chapter 8. The article is reproduced with permission with slight changes in order to fit the style of the thesis.

---

**[C] Growth of two-dimensional decagonal colloidal quasicrystals**

Miriam Martinsons and Michael Schmiedeberg

Journal of Physics: Condensed Matter **30**, 255403 (2018)

DOI: <https://doi.org/10.1088/1361-648X/aac503>

Copyright 2018 by IOP Publishing Ltd

**Abstract**

The growth of quasicrystals, i.e. structures with long-range positional order but no periodic translational symmetry, is more complex than the growth of periodic crystals. By employing Brownian dynamics simulations in two dimensions for colloidal particles that interact according to an isotropic pair potential with two incommensurate lengths, we study the growth of quasicrystalline structures by sequentially depositing particles at their surface. We quantify the occurrence of quasicrystalline order as a function of the temperature and the rate of added particles. In addition, we explore the defects like local triangular order or gaps within the quasicrystalline structure. Furthermore, we analyze the shapes of the surfaces in grown structures which tend to build straight lines along the symmetry axes of the quasicrystal. Finally, we identify phasonic flips which are rearrangements of the particles due to additional degrees of freedom. The number of phasonic flips decreases with the distance to the surface.

**Author's contribution and appearance in this thesis**

Article [C] results from a project by me and M. Schmiedeberg. The numerical simulations and the graphical presentations of the data provided in this article have been done by me. Both authors were involved in the analysis of the data and preparation of the manuscript. Both authors have read and approved the final manuscript.

Section 6.1 in this thesis is based on an accepted manuscript version of article [C]. The article is reproduced with permission with slight changes in order to fit the style of the thesis. The introduction of Chapter 6 as well as the conclusion in Section 6.3 are combined from the introductions and conclusions of articles [C] and [D].

[D] **Growth of two-dimensional dodecagonal colloidal quasicrystals: Particles with isotropic pair interactions with two length scales vs. patchy colloids with preferred binding angles**

Anja Gemeinhardt, Miriam Martinsons and Michael Schmiedeberg  
European Physical Journal E **41**, 126 (2018)

DOI: <https://doi.org/10.1140/epje/i2018-11737-1>

Copyright 2018 by EDP Sciences, SIF, Springer-Verlag Germany

**Abstract**

We explore the growth of colloidal quasicrystals with dodecagonal symmetry in two dimensions by employing Brownian dynamics simulations. On the one hand, we study the growth behavior of structures obtained in a system of particles that interact according to an isotropic pair potential with two typical length scales. On the other hand, we consider patchy colloids that possess only one typical interaction length scale but prefer given binding angles. In case of the isotropic particles, we show that an imbalance in the competition between the two distances might lead to defects with wrong nearest neighbor distances in the resulting structure. In contrast, during the growth of quasicrystals with patchy colloids such defects do not occur due to the lack of a second interaction length scale. However, as a downside, the diffusion of patchy particles along a surface typically is slower such that domains occur where the particles possess different phononic and phasonic offsets. Our results are important to understand how soft-matter quasicrystals can be grown as perfectly as possible and to obtain a deeper insight into the mechanisms of the growth of quasicrystals in general.

**Author's contribution and appearance in this thesis**

Article [D] results from a cooperation between A. Gemeinhardt, me and M. Schmiedeberg. A. Gemeinhardt and me contributed equally to the manuscript. In the scope of her master thesis [328] A. Gemeinhardt carried out all simulations on the patchy colloids, while I did all simulations with isotropic interactions. Both of us were involved in the graphical presentation of the data. All authors were involved in the evaluation and analysis of the data, in the preparation of the manuscript, and have read and approved the final manuscript.

Article [D] gives the fundament of Section 6.2. The article is adopted with kind permission with slight changes in order to fit the style of the thesis. The introduction of Chapter 6 as well as the conclusion in Section 6.3 are combined from the introductions and conclusions of articles [C] and [D].

---

[E] **Stabilizing quasicrystals composed of patchy colloids by narrowing the patch width**

Anja Gemeinhardt, Miriam Martinsons and Michael Schmiedeberg  
Europhysics Letters **126**, 38001 (2019)

DOI: <https://doi.org/10.1209/0295-5075/126/38001>

Copyright 2019 by EPLA

**Abstract**

We explore the behavior of two-dimensional patchy colloidal particles with 8 or 10 symmetrically arranged patches by employing Monte Carlo simulations. The particles interact according to an isotropic pair potential that possesses only one typical length. The patches lead to additional attractions that are anisotropic and depend on the relative orientation of two neighboring particles. We investigate the assembled structures with a special interest in quasicrystals. We found that the patch width is of great importance: Only in case of narrow patch widths we are able to observe metastable octagonal and decagonal quasicrystals, while dodecagonal quasicrystals can also occur for broad patches. These results are important to understand the role of interactions with preferred binding angles in order to obtain quasicrystals. Our findings suggest that in case of sharp binding angles, as they occur in metallic alloys, octagonal and decagonal symmetries might be observed more often than in systems with less sharp binding angles as it is the case in soft-matter systems where dodecagonal quasicrystals dominate.

**Author's contribution and appearance in this thesis**

Article [E] is the result of a cooperation between A. Gemeinhardt, me and M. Schmiedeberg. In the framework of her master thesis [328], A. Gemeinhardt performed the simulations to obtain the diagrams dependent on the patch width and calculated the average energies. I obtained the protocol to receive decagonal quasicrystals from random initial configurations as well as structures with different supported lengths. Both of us were involved in the graphical presentation of the data. Partly based on the master thesis of A. Gemeinhardt [328], the manuscript was written by me and M. Schmiedeberg. All authors approved the final version of the manuscript.

Article [E] gives the basis of Sections 5.2 and 5.3, as well as the last paragraph of Section 5.1. The article is adopted with permission with slight changes in order to fit the style of the thesis.

[F] **Stability of particles in two-dimensional quasicrystals against phasonic perturbations**

Miriam Martinsons and Michael Schmiedeberg

*accepted for publication in:* Journal of Physics: Conference Series (2019)

arXiv: <https://arxiv.org/abs/1905.10152>

**Abstract**

We investigate particles in two-dimensional quasicrystalline interference patterns and present a method to determine for each particle at which phasonic displacement a phasonic flip occurs. By mapping all particles into characteristic areas of reduced phasonic and phasonic displacements, we identify the particles that are close to edges of these areas and can easily flip. In contrast, the particles in the center are hardly affected by phasonic fluctuations. Our results are important e.g. for light-induced colloidal structures or cold atomic gases in laser traps. In addition, our approach can help to predict how thermal fluctuations induce phasonic flips in intrinsic quasicrystals with structures close to interference patterns.

**Author's contribution and appearance in this thesis**

Article [F] is a manuscript by me and M. Schmiedeberg which is accepted for publication. The numerical calculations and data analysis presented in the article were performed by me. The results for decagonal structures are based on findings of my master thesis [343]. The results for octagonal and dodecagonal structures are new. Both authors were involved in the preparation of the manuscript and have read and approved the final manuscript.

Manuscript [F] is based on findings presented in Section 4.3. The conclusion of the article is adopted in Section 4.5. The graphics as present in this thesis were designed by me and slightly changed by M. Schmiedeberg in order to fit the requirements of the journal.

---

[G] **Event-chain Monte Carlo simulations of the liquid to solid transition of two-dimensional decagonal colloidal quasicrystals**

Miriam Martinsons, Johannes Hielscher, Sebastian C. Kapfer and Michael Schmiedeberg

Journal of Physics: Condensed Matter **31**, 475103 (2019)

DOI: <https://doi.org/10.1088/1361-648X/ab3519>

Copyright 2019 by IOP Publishing Ltd

**Abstract**

In event-chain Monte Carlo simulations we model colloidal particles in two dimensions that interact according to an isotropic short-ranged pair potential which supports the two typical length scales present in decagonal quasicrystals. We investigate the assembled structures as we vary the density and temperature. Our special interest is related to the transition from quasicrystal to liquid. In contrast to the KTHNY melting theory for quasicrystals which predicts an intermediate pentahedratic phase, we find a one-step first-order melting transition. However, we discover that the slow relaxation of phasonic flips, i.e. rearrangements of the particles due to additional degrees of freedom in quasicrystals, changes the positional correlation functions such that structures with long-range orientational correlations but exponentially decaying positional correlations are observed.

**Author's contribution and appearance in this thesis**

Article [G] results from a cooperation between me, J. Hielscher, S. C. Kapfer and M. Schmiedeberg. The event-chain Monte Carlo simulation was provided by S. C. Kapfer. I performed the numerical simulations and did the graphical presentations. All authors were involved in the analysis of the data. Most parts of the manuscript were written by me. All authors approved the final version of the manuscript.

Article [G] provides the fundament of Chapter 7. The manuscript is reproduced with permission with little additions and slight changes in order to fit the style of the thesis.

[H] **Phasonic Diffusion and Self-confinement of Decagonal Quasicrystals in Hyperspace**

Johannes Hielscher, Miriam Martinsons, Michael Schmiedeberg and Sebastian C. Kapfer

*accepted for publication in:* Journal of Physics: Conference Series (2019)

arXiv: <https://arxiv.org/abs/1906.07045>

**Abstract**

We introduce a novel simulation method that is designed to explore fluctuations of the phasonic degrees of freedom in decagonal colloidal quasicrystals. Specifically, we attain and characterize thermal equilibrium of the phason ensemble via Monte Carlo simulations with particle motions restricted to elementary phasonic flips. We find that, at any temperature, the random tiling ensemble is strongly preferred over the minimum phason-strain quasicrystal. Phasonic flips are the dominant carriers of diffusive mass transport in physical space. Subdiffusive transients suggest cooperative flip behavior on short time scales. In complementary space, particle mobility is geometrically restricted to a thin ring around the acceptance domain, resulting in self-confinement and persistent phasonic order.

**Author's contribution and appearance in this thesis**

Article [H] is the result of a cooperation between J. Hielscher, me, M. Schmiedeberg and S. C. Kapfer. J. Hielscher performed the numerical simulations in hyperspace and did the presentation of the graphics. I performed the Brownian dynamics simulations. All authors were involved in the analysis of the data. Most parts of the manuscript were written by J. Hielscher. All authors approved the final manuscript.

Article [H] is not part of this thesis.

# Bibliography

- [1] D. Shechtman, I. Blech, D. Gratias, and J. W. Cahn. Metallic Phase with Long-Range Orientational Order and No Translational Symmetry. *Phys. Rev. Lett.*, 53:1951, 1984.
- [2] D. Levine and P. J. Steinhardt. Quasicrystals: A New Class of Ordered Structures. *Phys. Rev. Lett.*, 53:2477, 1984.
- [3] D. Monroe. Focus: Nobel Prize-Discovery of Quasicrystals. *Phys. Rev. Focus*, 28:14, 2011.
- [4] International Union of Crystallography. Report of the Executive Committee for 1991. *Acta Cryst. A*, 48:922, 1992.
- [5] The Nobel Prize in Chemistry 2011, . URL [https://www.nobelprize.org/nobel\\_prizes/chemistry/laureates/2011/](https://www.nobelprize.org/nobel_prizes/chemistry/laureates/2011/). Accessed: 2017-09-11.
- [6] J. E. S. Socolar, P. J. Steinhardt, and D. Levine. Quasicrystals with arbitrary orientational symmetry. *Phys. Rev. B*, 32:5547, 1985.
- [7] J. Mikhael, M. Schmiedeberg, S. Rausch, J. Roth, H. Stark, and C. Bechinger. Proliferation of anomalous symmetries in colloidal monolayers subjected to quasiperiodic light fields. *Proc. Natl. Acad. Sci. USA*, 107:7214, 2010.
- [8] M. Schmiedeberg and H. Stark. Comparing light-induced colloidal quasicrystals with different rotational symmetries. *J. Phys. Condens. Matter*, 24:284101, 2012.
- [9] D. Levine, T. C. Lubensky, S. Ostlund, S. Ramaswamy, P. J. Steinhardt, and J. Toner. Elasticity and Dislocations in Pentagonal and Icosahedral Quasicrystals. *Phys. Rev. Lett.*, 54:1520, 1985.
- [10] J. E. S. Socolar, T. C. Lubensky, and P. J. Steinhardt. Phonons, phasons, and dislocations in quasicrystals. *Phys. Rev. B*, 34:3345, 1986.

- 
- [11] J. A. Kromer, M. Schmiedeberg, J. Roth, and H. Stark. What Phasons Look Like: Particle Trajectories in a Quasicrystalline Potential. *Phys. Rev. Lett.*, 108:218301, 2012.
- [12] M. Sandbrink and M. Schmiedeberg. Trajectories of colloidal particles in laser fields with eight-, ten-, or twelve-fold symmetry and phasonic drift. In S. Schmid, R. L. Withers, and R. Lifshitz, editors, *Aperiodic Crystals*. Springer, 2013.
- [13] M. Martinsons, M. Sandbrink, and M. Schmiedeberg. Colloidal trajectories in two-dimensional light-induced quasicrystals with 14-fold symmetry due to phasonic drifts. *Acta Phys. Pol. A*, 126:568, 2014.
- [14] J. Hielscher, M. Martinsons, M. Schmiedeberg, and S. C. Kapfer. Detection of phonon and phason modes in intrinsic colloidal quasicrystals by reconstructing their structure in hyperspace. *J. Phys. Condens. Matter*, 29:094002, 2017.
- [15] E. Maciá. The role of aperiodic order in science and technology. *Rep. Prog. Phys.*, 69:397, 2006.
- [16] W. Steurer. Why are quasicrystals quasiperiodic? *Chem. Soc. Rev.*, 41:6719, 2012.
- [17] X. B. Zeng, G. Ungar, Y. Liu, A. E. Dulcey, and J. K. Hobbs. Supramolecular dendritic liquid quasicrystals. *Nature*, 428:157, 2004.
- [18] X. B. Zeng. Liquid quasicrystals. *Curr. Opin. Colloid Interface Sci.*, 9:384, 2005.
- [19] A. Takano, W. Kawashima, A. Noro, Y. Isono, N. Tanaka, T. Dotera, and Y. Matsushita. A mesoscopic Archimedean tiling having a new complexity in an ABC star polymer. *J. Polym. Sci. Pol. Phys.*, 43:2427, 2005.
- [20] K. Hayashida, T. Dotera, A. Takano, and Y. Matsushita. Polymeric quasicrystal: Mesoscopic quasicrystalline tiling in ABC star polymers. *Phys. Rev. Lett.*, 98:195502–1, 2007.
- [21] S. Fischer, A. Exner, K. Zielske, J. Perlich, S. Deloudi, W. Steurer, P. Lindner, and S. Förster. Colloidal quasicrystals with 12-fold and 18-fold diffraction symmetry. *Proc. Natl. Acad. Sci. USA*, 108:1810, 2011.
- [22] T. Dotera. Quasicrystals in Soft Matter. *Isr. J. Chem.*, 51:1197, 2011.

- [23] L. Bindi, P. J. Steinhardt, N. Yao, and P. J. Lu. Natural Quasicrystals. *Science*, 324:1306, 2009.
- [24] D. H. Everett. *Basic Principles of Colloidal Science*. Royal Society of Chemistry, 1988.
- [25] A. Ashkin. Acceleration and Trapping of Particles by Radiation Pressure. *Phys. Rev. Lett.*, 24:156, 1970.
- [26] A. Ashkin. Applications of Laser Radiation Pressure. *Science*, 210:1081, 1980.
- [27] M. Schmiedeberg and H. Stark. Colloidal Ordering on a 2D Quasicrystalline Substrate. *Phys. Rev. Lett.*, 101:218302, 2008.
- [28] M. Engel and H.-R. Trebin. Self-Assembly of Monatomic Complex Crystals and Quasicrystals with a Double-Well Interaction Potential. *Phys. Rev. Lett.*, 98:225505, 2007.
- [29] M. Engel, M. Umezaki, H.-R. Trebin, and T. Odagaki. Dynamics of particle flips in two-dimensional quasicrystals. *Phys. Rev. B*, 82:134206, 2010.
- [30] J. P. K. Doye, Lin Louis A. A., Allen I.-C., L. R., E. G. Noya, A. W. Wilber, H. C. Kok, and R. Lyus. Controlling crystallization and its absence: proteins, colloids and patchy models. *Phys. Chem. Chem. Phys.*, 9:2197, 2007.
- [31] V. Berendsen. Destruction of Long-range Order in One-dimensional and Two-dimensional Systems having a Continuous Symmetry Group I. Classical Systems. *Sov. Phys. JETP*, 32:493, 1971.
- [32] J. M. Kosterlitz and D. J. Thouless. Ordering, metastability and phase transitions in two-dimensional systems. *J. Phys. C*, 6:1181, 1973.
- [33] B. I. Halperin and D. R. Nelson. Theory of Two-Dimensional Melting. *Phys. Rev. Lett.*, 41:121, 1978.
- [34] A. P. Young. Melting and the vector Coulomb gas in two dimensions. *Phys. Rev. B*, 19:1855, 1979.
- [35] D. R. Nelson and B. I. Halperin. Dislocation-mediated melting in two dimensions. *Phys. Rev. B*, 19:2457, 1979.
- [36] V. Elser. The diffraction pattern of projected structures. *Acta Cryst. A*, 42:36, 1986.

- [37] R.-J. Haüy. *Essai d'une Théorie sur la Structure des Crystaux*. Gogué & Née, 1784.
- [38] N. W. Ashcroft and N. D. Mermin. *Festkörperphysik*. Oldenbourg, 2007.
- [39] C. Kittel. *Einführung in die Festkörperphysik*. Oldenbourg, 2002.
- [40] M. A. Bravais. Mémoire sur les systèmes formés par des points distribués régulièrement sur un plan ou dans l'espace. *J. Éc. Polytech.*, 33:1, 1850.
- [41] J. Kepler. *Harmonices Mundi*, 1619. (English translation by E. J. Aiton, A. M. Duncan, and J. V. Field, American Philosophical Society, 1997).
- [42] D. Shechtman. Quasi-Periodic Crystals - The Long Road from Discovery to Acceptance. *Rambam Maimonides Med. J.*, 4:1, 2013.
- [43] D. Shechtman and I. A. Blech. The Microstructure of Rapidly Solidified Al<sub>6</sub>Mn. *Metall. Trans. A*, 16:1005, 1985.
- [44] P. Lannin and Veronica Ek. Ridiculed crystal work wins Nobel for Israeli, 2011. <http://www.reuters.com/article/us-nobel-chemistry/ridiculed-crystal-work-wins-nobel-for-israeli-idUSTRE7941EP201111005> Accessed: 2017-09-09.
- [45] L. Pauling. Apparent icosahedral symmetry is due to directed multiple twinning of cubic crystals. *Nature*, 317:512, 1985.
- [46] L. Pauling. The nonsense about quasicrystals. *Science News*, 129:3, 1986.
- [47] L. Pauling. So-called icosahedral and decagonal quasicrystals are twins of an 820-atom cubic crystal. *Phys. Rev. Lett.*, 58:365, 1987.
- [48] L. Pauling. Icosahedral quasicrystals of intermetallic compounds are icosahedral twins of cubic crystals of three kinds, consisting of large (about 5000 atoms) icosahedral complexes in either a cubic body-centered or a cubic face-centered arrangement or smaller (about 1350 atoms) icosahedral complexes in the  $\beta$ -tungsten arrangement. *Proc. Natl. Acad. Sci. USA*, 22:8595, 1989.
- [49] J. W. Christian and S. Mahajan. Deformation twinning. *Prog. Mater. Sci.*, 39:1, 1995.
- [50] R. W. K. Honeycombe. *Plastic Deformation of Metals*. Cambridge University Press, 1969.
- [51] R. E. Reed-Hill, J. P. Hirth, and H. C. Rogers. *Deformation Twinning*. Gordon and Breach, 1964.

- [52] P. A. Bancel, P. A. Heiney, P. M. Horn, and P. J. Steinhardt. Comment on a Paper by Linus Pauling. *Proc. Natl. Acad. Sci. USA*, 86:8600, 1989.
- [53] T. S. Kuhn. *The Structure of Scientific Revolutions*. University of Chicago Press, Chicago, 1962.
- [54] R. Lifshitz. Quasicrystals: A matter of definition. *Found. Phys.*, 33:1703, 2003.
- [55] M. Senechal. Thoughts on “crystal”. *Z. Kristallogr.*, 222:311, 2007.
- [56] R. Lifshitz. What is a crystal? *Z. Kristallogr.*, 222:313, 2007.
- [57] S. I. Ben-Abraham. What is a crystal? *Z. Kristallogr.*, 222:310, 2007.
- [58] J.-P. Allouche and J. Shallit. *Automatic Sequences: Theory, Applications, Generalizations*. Cambridge University Press, 2003.
- [59] M. Baake and U. Grimm. Kinematic diffraction is insufficient to distinguish order from disorder. *Phys. Rev. B*, 79:020203–1, 2009.
- [60] M. Baake and U. Grimm. Mathematical diffraction of aperiodic structures. *Chem. Soc. Rev.*, 41:6821, 2012.
- [61] D. A. Rabson, N. D. Mermin, D. S. Rokhsar, and D. C. Wright. The space groups of axial crystals and quasicrystals. *Rev. Mod. Phys.*, 63:699, 1991.
- [62] N. D. Mermin. The space groups of icosahedral quasicrystals and cubic, orthorhombic, monoclinic, and triclinic crystals. *Rev. Mod. Phys.*, 64:3, 1992.
- [63] N. D. Mermin, D. A. Rabson, D. S. Rokhsar, and D. C. Wright. Stacking quasicrystallographic lattices. *Phys. Rev. B*, 41:10498, 1990.
- [64] Platon. *Timaios*. Reclam, 2003.
- [65] J. Donohue. *The structure of the elements*. Krieger Publishing Company, 1982.
- [66] E. J. Lavernia and T. S. Srivatsan. The rapid solidification of materials: science, principles, technology, advances, and applications. *J. Mater. Sci.*, 45:287, 2010.
- [67] A. P. Tsai. Icosahedral clusters, icosahedral order and stability of quasicrystals - a view of metallurgy. *Sci. Technol. Adv. Mater.*, 9:013008, 2008.

- [68] A. P. Tsai. Discovery of stable icosahedral quasicrystals: progress in understanding structure and properties. *Chem. Soc. Rev.*, 42:5352, 2013.
- [69] D. T. Hawkins. *Chemical Vapour Deposition*. Plenum, 1981.
- [70] A. P. Tsai, A. Inoue, and T. Masumoto. A Stable Quasicrystal in Al-Cu-Fe System. *Jpn. J. Appl. Phys.*, 26:L1505, 1987.
- [71] A. P. Tsai. “Back to the Future” – An Account Discovery of Stable Quasicrystals. *Acc. Chem. Res.*, 36:31, 2003.
- [72] A. P. Tsai. Metallurgy of quasicrystals. In Z. M. Stadnik, editor, *Physical Properties of Quasicrystals*. Springer, 1999. pp. 5-50.
- [73] M. D. Ball and D. J. Lloyd. Particles apparently exhibiting five-fold symmetry in Al-Li-Cu-Mg alloys. *Scr. Metall.*, 19:1065, 1985.
- [74] A. P. Tsai, J. Q. Guo, E. Abe, H. Takakura, and T. J. Sato. A stable binary quasicrystal. *Nature*, 408:537, 2000.
- [75] M. Schmiedeberg. Quasikristalle. *Welt der Physik*, 2012.
- [76] L. X. He, Z. Zhang, Y. K. Wu, and K. H. Kuo. Stable decagonal quasicrystals with different periodicities along the tenfold axis in  $\text{Al}_{65}\text{Cu}_{20}\text{Co}_{15}$ . *Inst. Phys. Conf. Ser. No. 93*, 2:501, 1988.
- [77] A. P. Tsai, A. Inoue, and T. Masumoto. A Stable Decagonal Quasicrystal in the Al-Cu-Co System. *Mater. Trans. JIM*, 30:300, 1989.
- [78] A. P. Tsai, A. Inoue, and T. Masumoto. Stable decagonal Al-Co-Ni and Al-Co-Cu quasicrystals. *Mater. Trans. JIM*, 30:463, 1989.
- [79] T. Ishimasa, H. U. Nissen, and Y. Fukano. New ordered state between crystalline and amorphous in Ni-Cr particles. *Phys. Rev. Lett.*, 55:511, 1985.
- [80] M. Conrad, F. Krumeich, and B. A. Harbrecht. A dodecagonal quasicrystalline chalcogenide. *Angew. Chem. Int. Ed.*, 37:1384, 1998.
- [81] N. Wang, H. Chen, and K. H. Kuo. Two-dimensional quasicrystal with eightfold rotational symmetry. *Phys. Rev. Lett.*, 59:1010, 1987.
- [82] W. Steurer. Twenty years of structure research on quasicrystals. Part I. Pentagonal, octagonal, decagonal and dodecagonal quasicrystals. *Z. Kristallogr.*, 219:391, 2004.

- [83] J. Hafner. *From Hamiltonians to Phase Diagrams: the electronic and statistical-mechanical theory of sp-bonded metals and alloys*. Springer-Verlag, 1987.
- [84] D. G. Pettifor. *Bonding and Structure of Molecules and Solids*. Oxford University Press, 1995.
- [85] M. Dzugutov. Glass formation in a simple monatomic liquid with icosahedral inherent local order. *Phys. Rev. A*, 46:R2984, 1992.
- [86] M. Dzugutov. Formation of a dodecagonal quasicrystalline phase in a simple monatomic liquid. *Phys. Rev. Lett.*, 70:2924, 1993.
- [87] J. Roth and A. R. Denton. Solid-phase structures of the Dzugutov pair potential. *Phys. Rev. E*, 61:6845, 2000.
- [88] A. Quandt and M. P. Teter. Formation of quasiperiodic patterns within a two-dimensional model system. *Phys. Rev. B*, 59:8586, 1999.
- [89] M. Elenius, F. H. M. Zetterling, M. Dzugutov, D. C. Fredrickson, and S. Lidin. Structural model for octagonal quasicrystals derived from octagonal symmetry elements arising in  $\beta$ -Mn crystallization of a simple monatomic liquid. *Phys. Rev. B*, 79:144201, 2009.
- [90] M. Engel and H.-R. Trebin. Structural complexity in monodisperse systems of isotropic particles. *Z. Kristallogr.*, 223:721, 2008.
- [91] M. Engel. *Dynamics and Defects of Complex Crystals and Quasicrystals: Perspectives from Simple Model Systems*. PhD thesis, Universität Stuttgart, 2008.
- [92] M. Engel, P. F. Damasceno, C. L. Phillips, and S. C. Glotzer. Computational self-assembly of a one-component icosahedral quasicrystal. *Nat. Mater.*, 14:109, 2015.
- [93] C. R. Iacovella, A. S. Keys, and S. C. Glotzer. Self-assembly of soft-matter quasicrystals and their approximants. *Proc. Natl. Acad. Sci. USA*, 108:20935, 2011.
- [94] R. Lifshitz and H. Diamant. Soft quasicrystals - Why are they stable? *Philos. Mag.*, 87:3021, 2007.
- [95] C. Xiao, N. Fujita, K. Miyasaka, Y. Sakamoto, and O. Terasaki. Dodecagonal tiling in mesoporous silica. *Nature*, 487:349, 2012.

- [96] D. V. Talapin, E. V. Shevchenko, M. I. Bodnarchuk, X. Ye, J. Chen, and C. B. Murray. Quasicrystalline order in self-assembled binary nanoparticle superlattices. *Nature*, 461:964, 2009.
- [97] G. Ungar, V. Percec, X. Zeng, and P. Leowanawat. Liquid Quasicrystals. *Isr. J. Chem.*, 51:1206, 2011.
- [98] J. Zhang and F. S. Bates. Dodecagonal Quasicrystalline Morphology in a Poly(styrene-*b*-isoprene-*b*-styrene-*b*-ethylene oxide) Tetrablock Terpolymer. *J. Am. Chem. Soc.*, 134:7636, 2012.
- [99] M. I. Bodnarchuk, R. Erni, F. Krumeich, and M. V. Kovalenko. Binary Superlattices from Colloidal Nanocrystals and Giant Polyoxometalate Clusters. *Nano Lett.*, 13:1699, 2013.
- [100] E. A. Jagla. Phase behavior of a system of particles with core collapse. *Phys. Rev. E*, 58:1478, 1998.
- [101] A. Skibinsky, S. V. Buldyrev, A. Scala, S. Havlin, and H. E. Stanley. Quasicrystals in a Monodisperse System. *Phys. Rev. E*, 60:2664, 1999.
- [102] T. Dotera, T. Oshiro, and P. Ziherl. Mosaic two-lengthscale quasicrystals. *Nature*, 506:208, 2014.
- [103] M. Sandbrink. *Tailored Colloidal Quasicrystals*. PhD thesis, Universität Düsseldorf, 2014.
- [104] M. Widom, K. J. Strandburg, and R. H. Swendsen. Quasicrystal equilibrium state. *Phys. Rev. Lett.*, 58:706, 1987.
- [105] F. Lançon and L. J. Billard. Two-dimensional system with a quasi-crystalline ground state. *J. Phys. (France)*, 49:249, 1988.
- [106] F. Scheffler, P. Maass, J. Roth, and H. Stark. Quasicrystalline Order in Binary Dipolar Systems. *Eur. Phys. J. B*, 42:85, 2004.
- [107] J. W. Roth, R. Schilling, and H.-R. Trebin. Nucleation of quasicrystals by rapid cooling of a binary melt: A molecular-dynamics study. *Phys. Rev. B*, 51:15833, 1995.
- [108] G. Ungar, Y. Liu, X. Zeng, V. Percec, and W. D. Cho. Giant supramolecular liquid crystal lattice. *Science*, 299:1208, 2003.
- [109] S. Lee, M. J. Bluemle, and F. S. Bates. Discovery of a Frank-Kasper  $\sigma$  Phase in Sphere-Forming Block Copolymer Melts. *Science*, 330:349, 2010.

- 
- [110] A. J. Archer, A. M. Rucklidge, and E. Knobloch. Quasicrystalline Order and a Crystal-Liquid State in a Soft-Core Fluid. *Phys. Rev. Lett.*, 111:165501, 2013.
- [111] A. J. Archer, A. M. Rucklidge, and E. Knobloch. Soft-core particles freezing to form a quasicrystal and a crystal-liquid phase. *Phys. Rev. E*, 92:012324, 2015.
- [112] R. Lifshitz and D. M. Petrich. Theoretical Model for Faraday Waves with Multiple-Frequency Forcing. *Phys. Rev. Lett.*, 79:1261, 1997.
- [113] K. Barkan, H. Diamant, and R. Lifshitz. Stability of Quasicrystals Composed of Soft Isotropic Particles. *Phys. Rev. B*, 83:172201, 2011.
- [114] K. Barkan, M. Engel, and R. Lifshitz. Controlled Self-Assembly of Periodic and Aperiodic Cluster Crystals. *Phys. Rev. Lett.*, 113:098304, 2014.
- [115] C. V. Achim, M. Schmiedeberg, and H. Löwen. Growth Modes of Quasicrystals. *Phys. Rev. Lett.*, 112:255501, 2014.
- [116] M. Schmiedeberg, C. V. Achim, J. Hielscher, S. C. Kapfer, and H. Löwen. Dislocation-free growth of quasicrystals from two seeds due to additional phasonic degrees of freedom. *Phys. Rev. E*, 96:012602, 2017.
- [117] P. Subramanian, A. J. Archer, E. Knobloch, and A. M. Rucklidge. Three-dimensional Icosahedral Phase Field Quasicrystals. *Phys. Rev. Lett.*, 117:075501, 2016.
- [118] G. Doppelbauer, E. Bianchi, and G. Kahl. Self-assembly scenarios of patchy colloidal particles in two dimensions. *J. Phys. Condens. Matter*, 22:104105, 2010.
- [119] M. N. van der Linden, J. P. K. Doye, and A. A. Louis. Formation of dodecagonal quasicrystals in two-dimensional systems of patchy particles. *J. Chem. Phys.*, 136:054904, 2012.
- [120] A. Reinhardt, F. Romano, and J. P. K. Doye. Computing Phase Diagrams for a Quasicrystal-Forming Patchy-Particle System. *Phys. Rev. Lett.*, 110:255503, 2013.
- [121] A. Gemeinhardt, M. Martinsons, and M. Schmiedeberg. Growth of two-dimensional dodecagonal colloidal quasicrystals: Particles with isotropic pair interactions with two length scales vs. patchy colloids with preferred binding angles. *Eur. Phys. J. E*, 41:126, 2018.

- [122] A. Haji-Akbari, M. Engel, A. S. Keys, X. Zheng, R. G. Petschek, P. Palffy-Muhoray, and S. C. Glotzer. Disordered, quasicrystalline and crystalline phases of densely packed tetrahedra. *Nature*, 462:773, 2009.
- [123] A. Haji-Akbari, M. Engel, and S. C. Glotzer. Degenerate Quasicrystal of Hard Triangular Bipyramids. *Phys. Rev. Lett.*, 107:215702, 2011.
- [124] P. F. Damasceno, M. Engel, and S. C. Glotzer. Predictive Self-Assembly of Polyhedra into Complex Structures. *Science*, 337:453, 2012.
- [125] M. Schmiedeberg, J. Roth, and H. Stark. Brownian particles in random and quasicrystalline potentials: How they approach the equilibrium. *Eur. Phys. J. E*, 24:367, 2007.
- [126] M. Schmiedeberg, J. Mikhael, S. Rausch, J. Roth, L. Helden, C. Bechinger, and H. Stark. Archimedean-like colloidal tilings on substrates with decagonal and tetradecagonal symmetry. *Eur. Phys. J. E*, 32:25, 2010.
- [127] P. Kählitz, M. Schoen, and H. Stark. Clustering and mobility of hard rods in a quasicrystalline substrate potential. *J. Chem. Phys.*, 137:224705, 2012.
- [128] P. Kählitz and H. Stark. Phase ordering of hard needles on a quasicrystalline substrate. *J. Chem. Phys.*, 136:174705, 2012.
- [129] J. Mikhael, J. Roth, L. Helden, and C. Bechinger. Archimedean-like tiling on decagonal quasicrystalline surfaces. *Nature*, 454:501, 2008.
- [130] J. Mikhael, G. Gera, T. Bohlein, and C. Bechinger. Phase behavior of colloidal monolayers in quasiperiodic light fields. *Soft Matter*, 7:1352, 2011.
- [131] T. Bohlein and C. Bechinger. Experimental Observation of Directional Locking and Dynamical Ordering of Colloidal Monolayers Driven across Quasiperiodic Substrates. *Phys. Rev. Lett.*, 109:058301, 2012.
- [132] J. E. Lye, L. Fallani, C. Fort, V. Guarrera, M. Modugno, D. S. Wiersma, and M. Inguscio. Effect of interactions on the localization of a Bose-Einstein condensate in a quasiperiodic lattice. *Phys. Rev. A*, 75:061603(R), 2007.
- [133] G. Roati, C. D'Errico, L. Fallani, M. Fattori, C. Fort, M. Zaccanti, G. Modugno, M. Modugno, and M. Inguscio. Anderson localization of a non-interacting Bose-Einstein condensate. *Nature*, 453:895, 2008.
- [134] C. D'Errico, E. Lucioni, L. Tanzi, L. Gori, G. Roux, I. P. McCulloch, T. Giamarchi, M. Inguscio, and G. Modugno. Observation of a disordered bosonic insulator from weak to strong interactions. *Phys. Rev. Lett.*, 113:095301, 2014.

- [135] K. Viebahn, M. Sbroscia, E. Carter, C. Yu, and U. Schneider. Matter-Wave Diffraction from a Quasicrystalline Optical Lattice. *Phys. Rev. Lett.*, 122:110404, 2019.
- [136] A. Jagannathan and M. Duneau. An eightfold optical quasicrystal with cold atoms. *Europhys. Lett.*, 104:66003, 2013.
- [137] L. Sanchez-Palencia and L. Santos. Bose-Einstein condensates in optical quasicrystal lattices. *Phys. Rev. A*, 72:053607, 2005.
- [138] P. Bordia, H. Lüschen, S. Scherg, S. Gopalakrishnan, M. Knap, U. Schneider, and I. Bloch. Probing Slow Relaxation and Many-Body Localization in Two-Dimensional Quasiperiodic Systems. *Phys. Rev. X*, 7:041047, 2017.
- [139] Z. V. Vardeny, A. Nahata, and A. Agrawal. Optics of photonic quasicrystals. *Nat. Photonics*, 7:177, 2013.
- [140] M. Zoorob and G. Flinn. Photonic quasicrystals boost LED emission characteristics. *LEDs Mag.*, Aug.:21, 2006.
- [141] B. Freedman, G. Bartal, M. Segev, R. Lifshitz, D. N. Christodoulides, and J. W. Fleischer. Wave and defect dynamics in nonlinear photonic quasicrystals. *Nature*, 440:1166, 2006.
- [142] B. Freedman, R. Lifshitz, J. W. Fleischer, and M. Segev. Phason dynamics in nonlinear photonic quasicrystals. *Nat. Mater.*, 6:776, 2007.
- [143] G. J. MacPherson, C. L. Andronicos, L. Bindi, V. V. Distler, M. P. Eddy, J. M. Eiler, Y. Guan, L. S. Hollister, A. Kostin, V. Kryachko, W. M. Steinhardt, M. Yudovskaya, and P. J. Steinhardt. Khatyrka, a new CV3 find from the Koryak Mountains, Eastern Russia. *Meteorit. Planet. Sci.*, 48:1499, 2013.
- [144] L. Bindi, P. J. Steinhardt, N. Yao, and P. J. Lu. Icosahedrite,  $\text{Al}_{63}\text{Cu}_{24}\text{Fe}_{13}$ , the first natural quasicrystal. *Am. Mineral.*, 96:928, 2011.
- [145] L. Bindi and P. J. Steinhardt. The Discovery of the first natural Quasicrystal - A New Era for Mineralogy? *Elements*, 8:13, 2012.
- [146] L. Bindi, J. M. Eiler, Y. Guan, L. S. Hollister, G. MacPherson, P. J. Steinhardt, and N. Yao. Evidence for the extra-terrestrial origin of a natural quasicrystal. *Proc. Natl. Acad. Sci. USA*, 109:1396, 2012.

- [147] L. Bindi, N. Yao, C. Lin, L. S. Hollister, C. L. Andronicos, V. V. Distler, M. P. Eddy, A. Kostin, V. Kryachko, G. J. MacPherson, W. M. Steinhardt, M. Yudovskaya, and P.J. Steinhardt. Natural quasicrystal with decagonal symmetry. *Sci. Rep.*, 5:9111, 2015.
- [148] A. P. Tsai, A. Inoue, and T. Masumoto. New decagonal Al-Ni-Fe and Al-Ni-Co alloys prepared by liquid quenching. *Mater. Trans. JIM*, 30:150, 1989.
- [149] U. Lemmerz, B. Grushko, C. Freiburg, and M. Jansen. Study of decagonal quasicrystalline phase formation in the Al-Ni-Fe alloy system. *Philos. Mag. Lett.*, 69:141, 1994.
- [150] M. Baake and D. Joseph. Ideal and defective vertex configurations in the planar octagonal quasilattice. *Phys. Rev. B*, 42:8091, 1990.
- [151] C. L. Henley. Random Tiling Models. In D. P. DiVincenzo and P. J. Steinhardt, editors, *Quasicrystals: The State of the Art*. World Scientific, 1991. pp. 429-524.
- [152] F. Gaehler and H. C. Jeong. Quasicrystalline Ground States Without Matching Rules. *J. Phys. A*, 28:1807, 1995.
- [153] D. Levine and P. J. Steinhardt. Quasicrystals. I. Definition and structure. *Phys. Rev. B*, 34:596, 1986.
- [154] J. E. S. Socolar and P. J. Steinhardt. Quasicrystals. II. Unit-cell configurations. *Phys. Rev. B*, 34:617, 1986.
- [155] V. Elser. Comment on “Quasicrystals: A New Class of Ordered Structure”. *Phys. Rev. Lett.*, 54:1730, 1985.
- [156] C. L. Henley. Random tilings with quasicrystal order: transfer-matrix approach. *J. Phys. A*, 21:1649, 1988.
- [157] P. Lançon, L. J. Billard, and P. Chaudhari. Thermodynamical Properties of a Two-Dimensional Quasi-Crystal from Molecular Dynamics Calculations. *Europhys. Lett.*, 2:625, 1986.
- [158] M. Widom, D. P. Deng, and C. L. Henley. Transfer-Matrix Analysis of a Two-Dimensional Quasicrystal. *Phys. Rev. Lett.*, 63:310, 1989.
- [159] K. J. Strandburg, L.-H. Tang, and M. V. Jarić. Phason Elasticity in Entropic Quasicrystals. *Phys. Rev. Lett.*, 63:314, 1989.

- [160] L.-H. Tang and M. V. Jarić. Equilibrium quasicrystal phase of a Penrose tiling model. *Phys. Rev. B*, 41:4524, 1990.
- [161] C. L. Henley, M. de Boissieu, and W. Steurer. Discussion on clusters, phasons and quasicrystal stabilisation. *Philos. Mag.*, 86:1131, 2006.
- [162] W. Steurer. Structural phase transitions from and to the quasicrystalline state. *Acta Cryst. A*, 61:28, 2005.
- [163] A. Kiselev, M. Engel, and H.-R. Trebin. Confirmation of the Random Tiling Hypothesis for a Decagonal Quasicrystal. *Phys. Rev. Lett.*, 109:225502, 2012.
- [164] J.-M. Dubois. Quasicrystals. *J. Phys. Condens. Matter*, 13:7753, 2011.
- [165] F. Samavat, M. H. Tavakoli, S. Habibi, B. Jaleh, and P. T. Ahmad. Quasicrystals. *Open J. Phys. Chem.*, 2:7, 2012.
- [166] P. Archambault and C. Janot. Thermal Conductivity of Quasicrystals and Associated Processes. *MRS Bull.*, 22:48, 1997.
- [167] Y. Yokoyama, A. P. Tsai, A. Inoue, and T. Masumoto. Production of Quasicrystalline Al-Pd-Mn Alloys with Large Single Domain Size. *Mater. Trans. JIM*, 32:1089, 1991.
- [168] Y. Yokoyama, T. Miura, A. P. Tsai, A. Inoue, and T. Masumoto. Preparing of a Large  $Al_{70}Pd_{20}Mn_{10}$  Single-Quasicrystal by the Czochralski Method and Its Electrical Resistivity. *Mater. Trans. JIM*, 33:97, 1992.
- [169] J.-M. Dubois. Properties and applications of quasicrystals and complex metallic alloys. *Chem. Soc. Rev.*, 41:6760, 2012.
- [170] J. M. Dubois. A survey of the potential applications of quasicrystals. In A. I. Goldman, D. J. Sordelet, P. A. Thiel, and J. M. Dubois, editors, *New Horizons in Quasicrystals: Research and Applications*. World Scientific, Singapore, 1997.
- [171] J. M. Dubois. In F. Gaehler, P. Kramer, H.-R. Trebin, and K. Urban, editors, *Proceedings of the 7th International Conference on Quasicrystals*. World Scientific, Singapore, 1999.
- [172] U. Köster, W. Liu, H. Liebertz, and M. Michel. Mechanical properties of quasicrystalline and crystalline phases in Al-Cu-Fe alloys. *J. Non-Cryst. Solids*, 153-154:446, 1993.

- [173] J.-M. Dubois and P. Weinland. Coating Materials for Metal Alloys and Metals. *U.S. Patent No. 5*, 204:191, 1993.
- [174] S. Takeuchi, H. Iwanaga, and T. Shibuya. Hardness of Quasicrystals. *Jpn. J. Appl. Phys.*, 30:561, 1991.
- [175] R. Mikulla, J. Stadler, F. Krul, H.-R. Trebin, and P. Gumbsch. Crack propagation in quasicrystals. *Phys. Rev. Lett.*, 81:3163, 1998.
- [176] S. S. Kang and J. M. Dubois. Compression testing of quasicrystalline materials. *Philos. Mag. A*, 66:151, 1992.
- [177] Y. Yokoyama, A. Inoue, and T. Masumoto. Mechanical Properties, Fracture Mode and Deformation Behavior of Al<sub>70</sub>Pd<sub>20</sub>Mn<sub>10</sub> Single-Quasicrystal. *Mater. Trans. JIM*, 34:135, 1993.
- [178] P. A. Thiel and J.-M. Dubois. Quasicrystals. Reaching maturity for technological applications. *Mater. Today*, 2:3, 1999.
- [179] A. Perrot, J. M. Dubois, M. Cassart, and J. P. Issi. In C. Janot and R. Mosseri, editors, *Proceedings of the 5th International Conference on Quasicrystals*. World Scientific, Singapore, 1995.
- [180] J.-M. Dubois, S. S. Kang, P. Archambault, and B. Colleret. Thermal diffusivity of quasicrystalline and related crystalline alloys. *J. Mater. Res.*, 8:38, 1993.
- [181] D. Mayou, C. Berger, F. Cyrot-Lackmann, T. Klein, and P. Lanco. Evidence of unconventional electronic transport in quasicrystals. *Phys. Rev. Lett.*, 70:3915, 1993.
- [182] A. P. Tsai, H. Suenaga, M. Ohmori, Y. Yokoyama, A. Inoue, and T. Masumoto. Temperature Dependence of Hardness and Expansion in an Icosahedral Al-Pd-Mn Alloy. *Jpn. J. Appl. Phys.*, 31:2530, 1992.
- [183] S. Roche, G. Trambly de Laissardière, and D. Mayou. Electronic transport properties of quasicrystals. *J. Math. Phys.*, 38:1794, 1997.
- [184] J. Y. Park and P. A. Thiel. Atomic scale friction and adhesion properties of quasicrystal surfaces. *J. Phys. Condens. Matter*, 20:314012, 2008.
- [185] N. Rivier. Non-stick quasicrystalline coatings. *J. Non-Cryst. Solids*, 153:458, 1993.

- [186] J. M. Dubois, P. Plaindoux, E. Belin-Ferre, N. Tamura, and D. J. Sordelet. In S. Takeuchi and T. Fujiwara, editors, *Proceedings of the 6th International Conference on Quasicrystals*. World Scientific, 1998.
- [187] S. L. Chang, W. B. Chin, C. M. Zhang, C. J. Jenks, and P. A. Thiel. Oxygen Adsorption on a Single-Grain, Quasicrystal Surface. *Surf. Sci.*, 337:135, 1995.
- [188] S. L. Chang, C. M. Zhang, C. J. Jenks, J. W. Anderegy, and P. A. Thiel. In C. Janot and R. Mosseri, editors, *Proceedings of the 5th International Conference on Quasicrystals*. World Scientific, Singapore, 1995.
- [189] C. J. Jenks, P. J. Pinhero, S. L. Chang, J. W. Anderegy, M. F. Besser, D. J. Sordelet, and P. A. Thiel. In A. I. Goldman, D. J. Sordelet, P. A. Thiel, and J. M. Dubois, editors, *Proceedings of the Conference New Horizons in Quasicrystals*. World Scientific, 1997.
- [190] Cybernox. URL [www.dvorsons.com/Sitram/Cybernox/Cybernox.html](http://www.dvorsons.com/Sitram/Cybernox/Cybernox.html). Accessed: 2018-02-09.
- [191] M. Kalman. The Quasicrystal Laureate, 2011. URL <https://www.technologyreview.com/s/425729/the-quasicrystal-laureate/>.
- [192] J.-M. Dubois. *Useful Quasicrystals*. World Scientific, 2005.
- [193] J.-M. Dubois and E. Belin-Ferré. *Complex Metallic Alloys, Fundamentals and Applications*. Wiley-VCH, Weinheim, 2011.
- [194] Z. Zhenwei, T. Xinying, Z. Guorong, L. Jinfeng, and G Jiwei. Effect of Mg-Zn-Nd Quasicrystal Addition on Corrosion Resistance of AZ91 Alloys. *Rare Metal Mat. Eng.*, 43:791, 2014.
- [195] J.-M. Dubois, S. S. Kang, and J. von Stebut. Quasicrystalline low-friction coatings. *J. Mater. Sci. Lett.*, 10:537, 1991.
- [196] B. Phung Ngoc, C. Geantet, M. Aouine, G. Bergeret, S. Raffy, and S. Marlin. Quasicrystal derived catalyst for steam reforming of methanol. *Int. J. Hydrog. Energy*, 33:1000, 2008.
- [197] A. P. Tsai and M. Yoshimura. Highly active quasicrystalline Al-Cu-Fe catalyst for steam reforming of methanol. *Appl. Catal. A*, 214:237, 2001.
- [198] M. E. Zoorob, M. D. B. Charlton, G. J. Parker, J. J. Baumberg, and M. C. Netti. Complete photonic bandgaps in 12-fold symmetric quasicrystals. *Nature*, 404:740, 2000.

- [199] Y. S. Chan, C. T. Chan, and Z. Y. Liu. Photonic band gaps in two dimensional photonic quasicrystals. *Phys. Rev. Lett.*, 80:956, 1998.
- [200] W. Man, M. Megens, P. J. Steinhardt, and P. M. Chaikin. Experimental measurement of the photonic properties of icosahedral quasicrystals. *Nature*, 436:993, 2005.
- [201] M. Gardner. *Penrose Tiles to Trapdoor Ciphers*. Cambridge University Press, 1997.
- [202] R. Berger. *The Undecidability of the Domino Problem*. American Mathematical Society, 1966.
- [203] J. Bohannon. Quasi-crystal conundrum opens a tiling can of worms. *Science*, 315:1066, 2007.
- [204] P. J. Lu and P. J. Steinhardt. Decagonal and quasi-crystalline tilings in medieval Islamic architecture. *Science*, 315:1106, 2007.
- [205] R. A. Al Ajlouni. The global long-range order of quasi-periodic patterns in Islamic architecture. *Acta Cryst. A*, 68:235, 2012.
- [206] E. Makovicky. 800-year old pentagonal tiling from Maraghan, Iran, and the new varieties of aperiodic tiling it inspired. In I. Hargittai, editor, *Fivefold symmetry*. World Scientific, 1992. pp. 67.
- [207] A. Duerer. *Underweysung der Messung, mit dem Zirckel und Richtscheyt, in Linien, Ebenen unnd gantzen corporen*. Hieronymus Andreae, Nüremberg, 1525. URL [digital.slib-dresden.de/werkansicht/dlf/17139/66/](http://digital.slib-dresden.de/werkansicht/dlf/17139/66/).
- [208] D. W. Crowe. Albrecht Dürer and the regular pentagon. In I. Hargittai, editor, *Fivefold symmetry*. World Scientific, 1992. pp. 465.
- [209] H. Wang. Proving Theorems by Pattern Recognition - II. *Bell Syst. Tech. J.*, 40:1, 1961.
- [210] H. Wang. Games, Logic and Computers. *Sci. Am.*, 213:98, 1965.
- [211] K. Culik II. An aperiodic set of 13 Wang tiles. *Discrete Math.*, 160:245, 1996.
- [212] R. M. Robinson. Undecidability and Nonperiodicity for Tilings of the Plane. *Invent. Math.*, 12:177, 1971.
- [213] R. Penrose. The role of aesthetics in pure and applied mathematical research. *Bull. Inst. Math. Appl.*, 10:266, 1974.

- [214] A. L. Mackay. Crystallography and the penrose pattern. *Physica*, 114:609, 1982.
- [215] A. Beutelspacher and B. Petri. *Der Goldene Schnitt*. Spektrum, 1988.
- [216] T. Ida. “Vitruvian Man” by Leonardo da Vinci and the Golden Ratio. URL [www.crl.nitech.ac.jp/~ida/education/VitruvianMan/](http://www.crl.nitech.ac.jp/~ida/education/VitruvianMan/). Accessed: 2018-12-04.
- [217] R. Penrose. Pentaplexity - A class of non-periodic tilings of the plane. *Eureka*, 39:16, 1978.
- [218] M. Duneau and A. Katz. Quasiperiodic Patterns. *Phys. Rev. Lett.*, 54:2688, 1985.
- [219] J. H. Conway and K. M. Knowles. Quasiperiodic tiling in two and three dimensions. *J. Phys. A*, 19:3645, 1986.
- [220] M. Baake, P. Kramer, M. Schlottmann, and D. Zeidler. Planar patterns with fivefold symmetry as sections of periodic structures in 4-space. *Int. J. Mod. Phys. B*, 4:2217, 1990.
- [221] B. Grünbaum and G. C. Shepard. *Tilings and Patterns*. Freeman and Company, 1987.
- [222] F. Gaehler. Crystallography of dodecagonal quasicrystals. In C. Janot and J. M. Dubois, editors, *Quasicrystalline Materials*. World Scientific, 1988.
- [223] P. Stampfli. A dodecagonal quasi-periodic lattice in 2 dimensions. *Helv. Phys. Acta*, 59:1260, 1986.
- [224] Tilings encyclopedia. URL <https://tilings.math.uni-bielefeld.de>. Accessed: 2018-03-27.
- [225] N. G. de Bruijn. Algebraic theory of Penrose’s nonperiodic tilings of the plane I. *Nederl. Akad. Wetensch. Indag. Math.*, 43:39, 1981.
- [226] N. G. de Bruijn. Algebraic theory of Penrose’s nonperiodic tilings of the plane II. *Nederl. Akad. Wetensch. Indag. Math.*, 43:53, 1981.
- [227] C. L. Henley. Quasicrystal order, its origins and its consequences: A survey of current models. *Comments Condens. Matt. Phys.*, 13:59, 1987.
- [228] G. Y. Onoda, P. J. Steinhardt, D. P. DiVincenzo, and J. E. S. Socolar. Growing Perfect Quasicrystals. *Phys. Rev. Lett.*, 60:2653, 1988.

- [229] P. J. Steinhardt and S. Ostlund. *The Physics of Quasicrystals*. World Scientific, 1987.
- [230] C. Goodman-Strauss. Matching rules and substitution tilings. *Ann. Math.*, 147:181, 1998.
- [231] R. Klitzing, M. Schlottmann, and M. Baake. Perfect matching rules for undecorated triangular tilings with 10-, 12- and 8-fold symmetry. *Int. J. Mod. Phys. B*, 7:1455, 1993.
- [232] S. E. Burkov. Enforcement of matching rules by chemical ordering in the decagonal AlCuCo quasicrystal. *Phys. Rev. B*, 47:12326, 1993.
- [233] W. Steurer and D. Sutter-Widmer. Photonic and phononic quasicrystals. *J. Phys. D*, 40:R229, 2007.
- [234] T. C. Lubensky. Symmetry, Elasticity, and Hydrodynamics in Quasiperiodic Structures. In M. V. Jaric, editor, *Introduction to Quasicrystals*. Academic Press, 1988.
- [235] J. A. Kromer, M. Schmiedeberg, J. Roth, and H. Stark. Phason-induced dynamics of colloidal particles on quasicrystalline substrates. *Eur. Phys. J. E*, 36:25, 2013.
- [236] M. Engel and H.-R. Trebin. Stability of the decagonal quasicrystal in the Lennard-Jones-Gauss system. *Philos. Mag.*, 88:1959, 2008.
- [237] E. Abe, S. J. Pennycook, and A. P. Tsai. Direct observation of a local thermal vibration anomaly in a quasicrystal. *Nature*, 421:347, 2003.
- [238] K. Edagawa and K. Kajiyama. High temperature specific heat of Al-Pd-Mn and Al-Cu-Co quasicrystals. *Mater. Sci. Eng. A*, 646:294, 2000.
- [239] F. Gähler, S. Hocker, U. Koschella, J. Roth, and H.-R. Trebin. Phason elasticity and atomic dynamics of quasicrystals. In H.-R. Trebin, editor, *Quasicrystals: Structure and Physical Properties*. Wiley-VCH, 2003.
- [240] M. Feuerbacher and D. Caillard. Dynamics of phason diffusion in icosahedral Al-Pd-Mn quasicrystals. *Acta Mater.*, 108:1810, 2011.
- [241] U. Koschella, F. Gähler, J. Roth, and H.-R. Trebin. Phason Elastic Constants of a Binary Tiling Quasicrystal. *J. Alloys Compd.*, 342:287, 2002.
- [242] M. Widom. Bethe ansatz solution of the square-triangle random tiling model. *Phys. Rev. Lett.*, 70:2094, 1993.

- [243] K. J. Strandburg. Random-tiling quasicrystal. *Phys. Rev. B*, 40:6071, 1989.
- [244] K. J. Strandburg. Entropy of a three-dimensional random-tiling quasicrystal. *Phys. Rev. B*, 44:4644, 1991.
- [245] K. Edagawa, K. Suzuki, and S. Takeuchi. High Resolution Transmission Electron Microscopy Observation of Thermally Fluctuating Phasons in Decagonal Al-Cu-Co. *Phys. Rev. Lett.*, 85:1674, 2000.
- [246] M. de Boissieu. Phonons, phasons and atomic dynamics in quasicrystals. *Chem. Soc. Rev.*, 41:6778, 2012.
- [247] M. Sandbrink and M. Schmiedeberg. Course of dislocation lines in templated three-dimensional colloidal quasicrystals. *Phys. Rev. B*, 90:064108, 2014.
- [248] F. R. N. Nabarro. *Theory of Dislocations*. Clarendon, 1967.
- [249] D. R. Nelson. *Defects and Geometry in Condensed Matter Physics*. Cambridge University Press, 2002.
- [250] B. V. Derjaguin and L. Landau. Theory of stability of highly charged lyophobic sols and adhesion of highly charged particles in solutions of electrolytes. *Acta Physicochim. U.R.S.S.*, 14:633, 1941.
- [251] E. J. Verwey and J. T. G. Overbeek. *Theory of the Stability of Lyophobic Colloids*. Elsevier, 1948.
- [252] W. Poon. Colloids as big atoms. *Science*, 304:830, 2004.
- [253] H. Löwen. Colloidal soft matter under external control. *J. Phys. Condens. Matter*, 13:R415, 2001.
- [254] H. Löwen. Kolloide - auch für Physiker interessant? *Phys. Bl.*, 51:165, 1995.
- [255] Z. Zhang and S. C. Glotzer. Self-Assembly of Patchy Particles. *Nano Lett.*, 4:1407, 2004.
- [256] S. C. Glotzer and M. J. Solomon. Anisotropy of building blocks and their assembly into complex structures. *Nat. Mater.*, 6:557, 2007.
- [257] E. G. Noya, C. Vega, J. P. K. Doye, and Louis A. A. Phase diagram of model anisotropic particles with octahedral symmetry. *J. Chem. Phys.*, 127:054501, 2007.

- [258] A. W. Wilber, J. P. K. Doye, A. A. Louis, E. G. Noya, M. A. Miller, and P. Wong. Reversible self-assembly of patchy particles into monodisperse icosahedral clusters. *J. Chem. Phys.*, 127:085106, 2007.
- [259] E. G. Noya, C. Vega, J. P. K. Doye, and Louis A. A. The stability of a crystal with diamond structure for patchy particles with tetrahedral symmetry. *J. Chem. Phys.*, 132:234511, 2010.
- [260] A. J. Williamson, A. W. Wilber, J. P. K. Doye, and A. A. Louis. Templated self-assembly of patchy particles. *Soft Matter*, 7:3423, 2011.
- [261] G. Doppelbauer, E. G. Noya, E. Bianchi, and G. Kahl. Competing ordered structures formed by particles with a regular tetrahedral patch decoration. *J. Phys. Condens. Matter*, 24:284124, 2012.
- [262] A. Patrykiewicz and S. Sokołowski. Two-Dimensional Quasicrystals of Decagonal Order in One-Component Monolayer Films. *Phys. Rev. Lett.*, 99:156101, 2007.
- [263] M. Schmiedeberg and H. Stark. Comment on “Two-Dimensional Quasicrystals of Decagonal Order in One-Component Monolayer Films”. *Phys. Rev. Lett.*, 100:019601, 2008.
- [264] T. Neuhaus, M. Marechal, M. Schmiedeberg, and H. Löwen. Rhombic Pre-ordering on a Square Substrate. *Phys. Rev. Lett.*, 110:118301, 2013.
- [265] M. Martinsons and M. Schmiedeberg. Growth of two-dimensional decagonal colloidal quasicrystals. *J. Phys. Condens. Matter*, 30:255403, 2018.
- [266] A. Chowdhury, B. J. Ackerson, and N. A. Clark. Laser-Induced Freezing. *Phys. Rev. Lett.*, 55:833, 1985.
- [267] C. Bechinger, M. Brunner, and P. Leiderer. Phase Behavior of Two-Dimensional Colloidal Systems in the Presence of Periodic Light Fields. *Phys. Rev. Lett.*, 86:930, 2001.
- [268] C. Bechinger and E. Frey. Phase behaviour of colloids in confining geometry. *J. Phys. Condens. Matter*, 13:R321, 2001.
- [269] D. Chen, E. Lomba, and S. Torquato. Binary mixtures of charged colloids: a potential route to synthesize disordered hyperuniform materials. *Phys. Chem. Chem. Phys.*, 20:17557, 2018.

- [270] N. Hoffmann, F. Ebert, C. N. Likos, H. Löwen, and G. Maret. Partial Clustering in Binary Two-Dimensional Colloidal Suspensions. *Phys. Rev. Lett.*, 97:078301, 2006.
- [271] J. Baumgartl, R. P. A. Dullens, M. Dijkstra, R. Roth, and C. Bechinger. Experimental observation of structural crossover in binary mixtures of colloidal hard spheres. *Phys. Rev. Lett.*, 98:198303, 2007.
- [272] K. Okada and A. Satoh. Regime of aggregate structures and magnetorheological characteristics of a magnetic rod-like particle suspension: Monte Carlo and Brownian dynamics simulations. *J. Magn. Magn. Mater.*, 437:29, 2017.
- [273] A. E. González. Stratification of colloidal aggregation coupled with sedimentation. *Phys. Rev. E*, 74:061403, 2006.
- [274] W. R. Heinson, C. M. Sorensen, and A. Chakrabarti. Shear History Independence in Colloidal Aggregation. *Langmuir*, 28:11337, 2012.
- [275] S. Markutsya, R. O. Fox, and S. Subramaniam. Characterization of sheared colloidal aggregation using Langevin dynamics simulations. *Phys. Rev. E*, 89:062312, 2014.
- [276] D. J. W. Aastuen, N. A. Clark, L. K. Cotter, and B. J. Ackerson. Nucleation and growth of colloidal crystals. *Phys. Rev. Lett.*, 57:1733, 1986.
- [277] S. Auer and D. Frenkel. Prediction of absolute crystal-nucleation rate in hard-sphere colloids. *Nature*, 409:1020, 2001.
- [278] U. Gasser. Crystallization in three- and two-dimensional colloidal suspensions. *J. Phys. Condens. Matter*, 21:203101, 2009.
- [279] U. Gasser, E. R. Weeks, A. Schofield, P. N. Pusey, and D. A. Weitz. Real-space imaging of nucleation and growth in colloidal crystallization. *Science*, 292:258, 2001.
- [280] S. van Teeffelen, C. N. Likos, and H. Löwen. Colloidal crystal growth at externally imposed nucleation clusters. *Phys. Rev. Lett.*, 100:108302, 2008.
- [281] P. N. Pusey and W. Van Megen. Phase behaviour of concentrated suspensions of nearly hard colloidal spheres. *Nature*, 320:340, 1986.
- [282] P. N. Pusey and W. Van Megen. Observation of a glass transition in suspensions of spherical colloidal particles. *Phys. Rev. Lett.*, 59:2083, 1987.

- [283] I. S. Aranson. Active colloids. *Physics - Uspekhi*, 56:79, 2013.
- [284] S. J. Ebbens. Active Colloids: Progress and challenges towards realising autonomous applications. *Curr. Opin. Colloid Interface Sci.*, 21:14, 2016.
- [285] J. Ingen-Housz. Bemerkungen über den Gebrauch des Vergrößerungsglases. In N. C. Molitor, editor, *Vermischte Schriften physisch-medicinischen Inhalts*. Christian Friedrich Wappler, 1784.
- [286] R. Brown. A brief account of microscopical observations. *Edinb. N. Ph. J.*, 5:358, 1828.
- [287] A. Einstein. Zur Theorie der Brownschen Bewegung. *Ann. Phys.*, 19:371, 1906.
- [288] M. Smoluchowski. Zur kinetischen Theorie der Brownschen Molekularbewegung und der Suspensionen. *Ann. Phys.*, 21:757, 1906.
- [289] J. Perrin. Mouvement Brownien et réalité moléculaire. *Ann. Chim. Phys.*, 18:5, 1909.
- [290] D. Kleppner and R. J. Kolenkow. *An Introduction to Mechanics*. Cambridge University Press, 2010.
- [291] P. Langevin. Sur la théorie du mouvement brownien. *C. R. Acad. Sci.*, 146:530, 1908.
- [292] W. Paul and J. Baschnagel. *Stochastic processes - from physics to finance*. Springer Verlag, 1999.
- [293] A. Einstein. Über die von der molekularkinetischen Theorie der Wärme geforderte Bewegung von in ruhenden Flüssigkeiten suspendierten Teilchen. *Ann. Phys. (N.Y.)*, 17:549, 1905.
- [294] A. W. C. Lau and T. C. Lubensky. State-dependent diffusion: Thermodynamic consistency and its path integral formulation. *Phys. Rev. E*, 76:011123, 2007.
- [295] M. Matsumoto and T. Nishimura. Mersenne Twister: A 623-dimensionally equidistributed uniform pseudorandom number generator. *ACM Trans. Model. Comp. Simul.*, 8:3, 1998.
- [296] M. H. Kalos and P. A. Whitlock. *Monte Carlo Methods*. Wiley, 1986.

- 
- [297] W. H. Press, B. P. Flannery, S. A. Teukolsky, and W. T. Vetterling. *Numerical Recipes: The Art of Scientific Computing*. Cambridge University Press, 1986.
- [298] K. Binder and D. W. Heermann. *Monte Carlo Simulation in Statistical Physics*. Springer, 1988.
- [299] M. E. J. Newman and G. T. Barkema. *Monte Carlo Methods in Statistical Physics*. Oxford University Press, 1999.
- [300] D. P. Landau and K. Binder. *A Guide to Monte Carlo Simulations in Statistical Physics*. Cambridge University Press, 2000.
- [301] H. L. Anderson. Metropolis, Monte Carlo, and the MANIAC. *Los Alamos Science*, 14:96, 1986.
- [302] N. Metropolis. The beginning of the Monte Carlo method. *Los Alamos Sci.*, 12:125, 1987.
- [303] N. Metropolis, A. W. Rosenbluth, M. N. Rosenbluth, A. H. Teller, and E. Teller. Equation of State Calculations by Fast Computing Machines. *J. Chem. Phys.*, 21:1087, 1953.
- [304] W. W. Wood. Monte Carlo calculations for hard disks in the isothermal-isobaric ensemble. *J. Chem. Phys.*, 48:415, 1968.
- [305] I. R. McDonald. NpT-ensemble Monte Carlo calculations for binary liquid mixtures. *Mol. Phys.*, 23:41, 1972.
- [306] R. Eppinga and D. Frenkel. Monte Carlo study of the isotropic and nematic phases of infinitely thin hard platelets. *Mol. Phys.*, 52:1303, 1984.
- [307] D. Frenkel and B. Smit. *Understanding Molecular Simulation: From Algorithms to Applications*. Academic Press, 2002.
- [308] M. P. Allen and D. J. Tildesley. *Computer Simulation of Liquids*. Oxford University Press, 1989.
- [309] E. P. Bernard, W. Krauth, and D. B. Wilson. Event-chain Monte Carlo algorithms for hard-sphere systems. *Phys. Rev. E*, 80:056704, 2009.
- [310] E. P. Bernard and W. Krauth. Two-Step Melting in Two Dimensions: First-Order Liquid-Hexatic Transition. *Phys. Rev. Lett.*, 107:155704, 2011.

- 
- [311] T. A. Kampmann, H.-H. Boltz, and Kierfeld J. Parallelized event chain algorithm for dense hard sphere and polymer systems. *J. Comput. Phys.*, 281:864, 2014.
- [312] T. A. Kampmann, H.-H. Boltz, and Kierfeld J. Monte Carlo simulation of dense polymer melts using event chain algorithms. *J. Chem. Phys.*, 143:044105, 2015.
- [313] Isobe M. and Krauth W. Hard-sphere melting and crystallization with event-chain Monte Carlo. *J. Chem. Phys.*, 143:084509, 2015.
- [314] M. Michel, S. C. Kapfer, and W. Krauth. Generalized event-chain Monte Carlo: Constructing rejection-free global-balance algorithms from infinitesimal steps. *J. Chem. Phys.*, 140:054116, 2014.
- [315] S. C. Kapfer and W. Krauth. Two-Dimensional Melting: From Liquid-Hexatic Coexistence to Continuous Transitions. *Phys. Rev. Lett.*, 114:035702, 2015.
- [316] S. C. Kapfer and W. Krauth. Cell-veto Monte Carlo algorithm for long-range systems. *Phys. Rev. E*, 94:031302–1, 2016.
- [317] M. Michel, J. Mayer, and W. Krauth. Event-chain Monte Carlo for classical continuous spin models. *Europhys. Lett.*, 112:20003–p1, 2015.
- [318] G. M. Whitesides and B. Grzybowski. Self-Assembly at All Scales. *Science*, 295:2418, 2002.
- [319] M. Rechtsman, F. Stillinger, and S. Torquato. Designed interaction potentials via inverse methods for self-assembly. *Phys. Rev. E*, 73:011406, 2006.
- [320] M. C. Rechtsman, F. H. Stillinger, and S. Torquato. Optimized Interactions for Targeted Self-Assembly: Application to a Honeycomb Lattice. *Phys. Rev. Lett.*, 95:228301, 2005.
- [321] M. C. Rechtsman, F. H. Stillinger, and S. Torquato. Self-assembly of the simple cubic lattice with an isotropic potential. *Phys. Rev. E*, 74:021404, 2006.
- [322] M. C. Rechtsman, F. H. Stillinger, and S. Torquato. Synthetic diamond and wurtzite structures self-assemble with isotropic pair interactions. *Phys. Rev. E*, 75:031403, 2007.

- [323] J. A. Moriarty and M. Widom. First-principles interatomic potentials for transition-metal aluminides: Theory and trends across the 3d series. *Phys. Rev. B*, 56:7905, 1997.
- [324] V. E. Dmitrienko and Astaf'ev S. B. Oscillating interatomic potentials and growth of icosahedral quasicrystals. *Phys. Rev. Lett.*, 75:1538, 1995.
- [325] S. Gorkhali, J. Qi, and G. Crawford. Switchable quasi-crystal structures with five-, seven-, and ninefold symmetries. *J. Opt. Soc. Am. B*, 23:149, 2006.
- [326] D. C. Rapaport. *The Art of Molecular Dynamics Simulation*. Cambridge University Press, 2004.
- [327] J. P. Hansen and I. R. McDonald. *Theory of Simple Liquids*. Academic Press, 1986.
- [328] A. Gemeinhardt. 2D simulations of quasicrystals with patchy colloids. Master's thesis, Universität Erlangen-Nürnberg, 2018.
- [329] W. Mickel, S. C. Kapfer, G. E. Schröder-Turk, and K. Mecke. Shortcomings of the Bond Orientational Order Parameters for the Analysis of Disordered Particulate Matter. *J. Chem. Phys.*, 138:044501, 2013.
- [330] G. Voronoi. Recherches sur les paralléloèdres primitifs. *J. Reine Angew. Math.*, 134:198, 1908.
- [331] K. Zahn, R. Lenke, and G. Maret. Two-Stage Melting of Paramagnetic Colloidal Crystals in Two Dimensions. *Phys. Rev. Lett.*, 82:2721, 1999.
- [332] L. Korkidi, K. Barkan, and R. Lifshitz. Analysis of Dislocations in Quasicrystals Composed of Self-assembled Nanoparticles. In S. Schmid, R. L. Withers, and R. Lifshitz, editors, *Aperiodic Crystals*. Springer, 2013.
- [333] D. Rokhsar, D. C. Wright, and N. D. Mermin. The Two-Dimensional Quasicrystallographic Space Groups with Rotational Symmetries less than 23-Fold. *Acta Cryst. A*, 44:197, 1988.
- [334] M. M. Burns, J.-M. Fournier, and J. A. Golovchenko. Optical Matter: Crystallization and Binding in Intense Optical Fields. *Science*, 249:749, 1990.
- [335] F. Rühle, M. Sandbrink, H. Stark, and M. Schmiedeberg. Effective substrate potentials with quasicrystalline symmetry depend on the size of the adsorbed particles. *Eur. Phys. J. E*, 38:54, 2015.

- [336] L. Guidoni, C. Triché, P. Verkerk, and G. Grynberg. Quasiperiodic Optical Lattices. *Phys. Rev. Lett.*, 79:3363, 1997.
- [337] L. Guidoni, B. Dépret, A. di Stefano, and P. Verkerk. Atomic diffusion in an optical quasicrystal with five-fold symmetry. *Phys. Rev. A*, 60:R4233(R), 1999.
- [338] M. J. Ablowitz, B. Ilan, E. Schonbrun, and R. Piestun. Solitons in two-dimensional lattices possessing defects, dislocations, and quasicrystal structures. *Phys. Rev. E*, 74:035601, 2006.
- [339] A. Ashkin, J. Dziedzic, J. Bjorkholm, and S. Chu. Observations of a single-beam gradient force optical trap for dielectric particles. *Opt. Lett.*, 11:288, 1986.
- [340] The Nobel Prize in Physics 2018, . URL <https://www.nobelprize.org/prizes/physics/2018/summary/>. Accessed: 2019-04-11.
- [341] M. Born and E. Wolf. *Principles of Optics*. Cambridge University Press, 1999.
- [342] R. Lifshitz. Symmetry Breaking and Order in the Age of Quasicrystals. *Isr. J. Chem.*, 51:1156, 2011.
- [343] M. Martinsons. Phasonische Drift und Fluktuationen in Quasikristallen. Master's thesis, Universität Düsseldorf, 2013.
- [344] T. Neuhaus, M. Schmiedeberg, and H. Löwen. Compatibility waves drive crystal growth on patterned substrates. *New J. Phys.*, 15:073013, 2013.
- [345] S. Gopalakrishnan, I. Martin, and E. A. Demler. Quantum Quasicrystals of Spin-Orbit-Coupled Dipolar Bosons. *Phys. Rev. Lett.*, 111:185304, 2013.
- [346] M. Sandbrink, J. Roth, and M. Schmiedeberg. Comment on “Quantum Quasicrystals of Spin-Orbit-Coupled Dipolar Bosons”. *Phys. Rev. Lett.*, 113:079601, 2014.
- [347] R. Lifshitz. Comment on “Quantum Quasicrystals of Spin-Orbit-Coupled Dipolar Bosons”. *Phys. Rev. Lett.*, 113:079602, 2014.
- [348] W. Han, X.-F. Zhang, D.-S. Wang, H.-F. Jiang, W. Zhang, and S.-G. Zhang. Chiral Supersolid in Spin-Orbit-Coupled Bose Gases with Soft-Core Long-Range Interactions. *Phys. Rev. Lett.*, 121:030404, 2018.

- [349] C. Casagrande, P. Fabre, E. Raphaël, and M. Veyssié. “Janus Beads”: Realization and Behaviour at Water/Oil Interfaces. *Europhys. Lett.*, 9:251, 1989.
- [350] P. G. de Gennes. Soft Matter. *Rev. Mod. Phys.*, 64:645, 1992.
- [351] A. B. Pawar and I. Kretzschmar. Fabrication, Assembly, and Applications of Patchy Particles. *Macromol. Rapid Commun.*, 31:150, 2010.
- [352] C. M. Liddell, C. J. Summers, and A. M. Gokhale. Stereological estimation of the morphology distribution of ZnS clusters for photonic crystal applications. *Mater. Charact.*, 50:69, 2003.
- [353] M. Grätzel. Photoelectrochemical cells. *Nature*, 414:338, 2001.
- [354] R. Langer and D. A. Tirrell. Designing materials for biology and medicine. *Nature*, 428:487, 2004.
- [355] J. A. Champion, Y. K. Katare, and S. Mitragotri. Particle shape: a new design parameter for micro- and nanoscale drug delivery carriers. *J. Control. Release*, 121:3, 2007.
- [356] van Blaaderen. Colloids get complex. *Nature*, 439:545, 2006.
- [357] V. N. Manoharan, M. T. Elsesser, and D. J. Pine. Dense Packing and Symmetry in Small Clusters of Microspheres. *Science*, 301:483, 2003.
- [358] Y.-S. Cho, G.-R. Yi, S.-H. Kim, D. J. Pine, and S.-M. Yang. Colloidal Clusters of Microspheres from Water-in-Oil Emulsions. *Chem. Mat.*, 17:5006, 2005.
- [359] Z. Zhang, D. Wang, and H. Möhwald. Patterning Microsphere Surfaces by Templating Colloidal Crystals. *Nano Lett.*, 5:143, 2005.
- [360] Z. Zhang, D. Wang, and H. Möhwald. Decoration of Microspheres with Gold Nanodots – Giving Colloidal Spheres Valences. *Angew. Chem. Int. Ed.*, 44:7767, 2005.
- [361] Z. Zhang, D. Wang, and H. Möhwald. Nanoembossment of Au Patterns on Microspheres. *Chem. Mat.*, 18:3985, 2006.
- [362] N. M. Dixit and C. F. Zukoski. Crystal nucleation rates for particles experiencing anisotropic interactions. *J. Chem. Phys.*, 117:8540, 2002.

- [363] J. K. Cheung, V. K. Shen, J. R. Errington, and T. M. Truskett. Coarse-grained strategy for modeling protein stability in concentrated solutions. III: directional protein interactions. *Biophys. J.*, 92:4316, 2007.
- [364] R. P. Sear. Phase behavior of a simple model of globular proteins. *J. Chem. Phys.*, 111:4800, 1999.
- [365] A. Shiryayev, X. Li, and J. D. Gunton. Simple model of sickle hemoglobin. *J. Chem. Phys.*, 125:024902, 2006.
- [366] N. Wentzel and J. D. Gunton. Effect of Solvent on the Phase Diagram of a Simple Anisotropic Model of Globular Proteins. *J. Phys. Chem. B*, 112:7803, 2008.
- [367] G. Pellicane, G. Smith, and L. Sarkisov. Molecular Dynamics Characterization of Protein Crystal Contacts in Aqueous Solutions. *Phys. Rev. Lett.*, 101:248102, 2008.
- [368] E. Bianchi, R. Blaak, and C. N. Likos. Patchy colloids: state of the art and perspectives. *Phys. Chem. Chem. Phys.*, 13:6397, 2011.
- [369] T. Neuhaus, A. Härtel, M. Marechal, M. Schmiedeberg, and H. Löwen. Density functional theory of heterogeneous crystallization. *Eur. Phys. J. Spec. Top.*, 223:373, 2014.
- [370] K. R. Elder, M. Katakowski, M. Haataja, and M. Grant. Modeling Elasticity in Crystal Growth. *Phys. Rev. Lett.*, 88:245701, 2002.
- [371] K. R. Elder and M. Grant. Modeling elastic and plastic deformations in nonequilibrium processing using phase field crystals. *Phys. Rev. E*, 70:051605, 2004.
- [372] J. Rottler, M. Greenwood, and B. Ziebarth. Morphology of monolayer films on quasicrystalline surfaces from the phase field crystal model. *J. Phys. Condens. Matter*, 24:135002, 2012.
- [373] M. Schmiedeberg, J. Roth, and H. Stark. Freezing and Melting of a Colloidal Adsorbate on a 1D Quasicrystalline Substrate. *Phys. Rev. Lett.*, 97:158304, 2006.
- [374] S. Savitz, M. Babadi, and R. Lifshitz. Multiple-scale structures: from Faraday waves to soft-matter quasicrystals. *IUCrJ*, 5:247, 2018.
- [375] A. S. Keys and S. C. Glotzer. How do Quasicrystals Grow? *Phys. Rev. Lett.*, 99:235503, 2007.

- [376] H. Pattabhiraman, A. P. Gantapara, and M. Dijkstra. On the stability of a quasicrystal and its crystalline approximant in a system of hard disks with a soft corona. *J. Chem. Phys.*, 143:164905, 2015.
- [377] R. Ryltsev and N. Chtchelkatchev. Universal self-assembly of one-component three-dimensional dodecagonal quasicrystals. *Soft Matter*, 13:5076, 2017.
- [378] M. Zu, P. Tan, and N. Xu. Forming quasicrystals by monodisperse soft core particles. *Nat. Commun.*, 8:2089, 2017.
- [379] K. Nagao, T. Inuzuka, K. Nishimoto, and K. Edagawa. Experimental Observation of Quasicrystal Growth. *Phys. Rev. Lett.*, 115:075501, 2015.
- [380] S. Förster, K. Meinel, R. Hammer, M. Trautmann, and W. Widdra. Quasicrystalline structure formation in a classical crystalline thin-film system. *Nature*, 502:215, 2013.
- [381] S. Förster, J. I. Flege, E. M. Zollner, F. O. Schumann, R. Hammer, A. Bayat, K.-M. Schindler, J. Falta, and W. Widdra. Growth and decay of a two-dimensional oxide quasicrystal: High-temperature in situ microscopy. *Ann. Phys.*, 529:1600250, 2017.
- [382] C. T. Hann, J. E. S. Socolar, and P. J. Steinhardt. Local growth of icosahedral quasicrystalline tilings. *Phys. Rev. B*, 94:014113, 2016.
- [383] J. Hermisson, C. Richard, and M. Baake. A Guide to the Symmetry Structure of Quasiperiodic Tiling Classes. *J. Phys. I (France)*, 7:1003, 1997.
- [384] Jr. Witten, T. A. and L. M. Sander. Diffusion-Limited Aggregation, a Kinetic Critical Phenomenon. *Phys. Rev. Lett.*, 47:1400, 1981.
- [385] M. Oxborrow and C. L. Henley. Random square-triangle tilings: A model for twelfefold-symmetric quasicrystals. *Phys. Rev. B*, 48:6966, 1993.
- [386] E. Tondl, M. Ramsay, P. Harrowell, and A. Widmer-Cooper. Defect-mediated relaxation in the random tiling phase of a binary mixture: Birth, death and mobility of an atomic zipper. *J. Chem. Phys.*, 140:104503, 2014.
- [387] N. D. Mermin and H. Wagner. Absence of Ferromagnetism or Antiferromagnetism in One- or Two-Dimensional Isotropic Heisenberg Models. *Phys. Rev. Lett.*, 17:1133, 1966.
- [388] P. De and R. A. Pelcovits. Defect-mediated melting of pentagonal quasicrystals. *J. Phys. A*, 22:1167, 1989.

- [389] W. G. Hoover and F. H. Ree. Melting Transition and Communal Entropy for Hard Spheres. *J. Chem. Phys.*, 49:3609, 1968.
- [390] N. D. Mermin. Crystalline Order in Two Dimensions. *Phys. Rev.*, 176:250, 1968.
- [391] C. A. Murray and D. H. Van Winkle. Experimental observation of two-stage melting in a classical two-dimensional screened Coulomb system. *Phys. Rev. Lett.*, 58:1200, 1987.
- [392] P. Keim, G. Maret, and H.-H. von Grünberg. Frank's constant in the hexatic phase. *Phys. Rev. E*, 75:031402, 2007.
- [393] B.-J. Lin and L.-J. Chen. Phase transitions in two-dimensional colloidal particles at oil/water interfaces. *J. Chem. Phys.*, 126:034706, 2007.
- [394] S. Lee and S. J. Lee. Effect of the range of the potential on two-dimensional melting. *Phys. Rev. E*, 78:041504, 2008.
- [395] H. Shiba, A. Onuki, and T. Araki. Structural and dynamical heterogeneities in two-dimensional melting. *Europhys. Lett.*, 86:66004, 2009.
- [396] W.-K. Qi, Z. Wang, Y. Han, and Y. Chen. Melting in two-dimensional yukawa systems: A brownian dynamics simulation. *J. Chem. Phys.*, 133:234508, 2010.
- [397] S. Prestipino, F. Saija, and P. V. Giaquinta. Hexatic phase and water-like anomalies in a two-dimensional fluid of particles with a weakly softened core. *J. Chem. Phys.*, 137:104503, 2012.
- [398] M. Engel, J. A. Anderson, S. C. Glotzer, M. Isobe, E. P. Bernard, and W. Krauth. Hard-disk equation of state: First-order liquid-hexatic transition in two dimensions with three simulation methods. *Phys. Rev. E*, 87:042134, 2013.
- [399] W. Qi, A. P. Gantapara, and M. Dijkstra. Two-stage melting induced by dislocations and grain boundaries in monolayers of hard spheres. *Soft Matter*, 10:5449, 2014.
- [400] A. L. Thorneywork, J. L. Abbott, D. G. A. L. Aarts, and R. P. A. Dullens. Two-Dimensional melting of Colloidal Hard Spheres. *Phys. Rev. Lett.*, 118:158001, 2017.

- [401] M. Zu, J. Liu, H. Tong, and N. Xu. Density Affects the Nature of the Hexatic-Liquid Transition in Two-Dimensional Melting of Soft-Core Systems. *Phys. Rev. Lett.*, 117:085702, 2016.
- [402] K. J. Strandburg. Two-dimensional melting. *Rev. Mod. Phys.*, 60:161, 1988.
- [403] C. Alba-Simionesco, B. Coasne, G. Dosseh, G. Dudziak, K. E. Gubbins, R. Radhakrishnan, and M. Sliwinska-Bartkowiak. Effects of confinement on freezing and melting. *J. Phys. Condens. Matter*, 18:R15, 2006.
- [404] D. S. Fisher, B. I. Halperin, and R. Morf. Defects in the two-dimensional electron solid and implications for melting. *Phys. Rev. B*, 20:4692, 1979.
- [405] S. T. Chui. Grain-Boundary Theory of Melting in Two Dimensions. *Phys. Rev. Lett.*, 48:933, 1982.
- [406] S. T. Chui. Grain-boundary theory of melting in two dimensions. *Phys. Rev. B*, 28:178, 1983.
- [407] H. Kleinert. Disclinations and first order transitions in 2D melting. *Phys. Lett. A*, 95:381, 1983.
- [408] B. Joos and M. S. Duesbery. Dislocation Energies in Rare-Gas Monolayers on Graphite. *Phys. Rev. Lett.*, 55:1997, 1985.
- [409] P. De and R. A. Pelcovits. Linear elasticity theory of pentagonal quasicrystals. *Phys. Rev. B*, 35:8609, 1987.
- [410] P. De and R. A. Pelcovits. Disclinations in pentagonal quasicrystals. *Phys. Rev. B*, 36:9304, 1987.
- [411] P. De and R. A. Pelcovits. Interaction energy of disclinations in pentagonal quasicrystals. *Phys. Rev. B*, 38:5042, 1988.
- [412] P. A. Kalugin. Phason disorder in 2D quasicrystals. *JETP Lett.*, 49:467, 1989.
- [413] J. Hielscher, M. Martinsons, M. Schmiedeberg, and S. C. Kapfer. Phasonic Diffusion and Self-confinement of Decagonal Quasicrystals in Hyperspace. Submitted to: *J. Phys. Conf. Ser.*, 2019.
- [414] A. R. Denton and H. Löwen. Stability of Colloidal Quasicrystals. *Phys. Rev. Lett.*, 81:469, 1998.

- 
- [415] A. Gemeinhardt, M. Martinsons, and M. Schmiedeberg. Stabilizing quasicrystals composed of patchy colloids by narrowing the patch width. *Europhys. Lett.*, 126:38001, 2019.
- [416] D. Joseph, S. Ritsch, and C. Beeli. Distinguishing quasiperiodic from random order in high-resolution TEM images. *Phys. Rev. B*, 55:8175, 1997.
- [417] R. Hory, C. Pohla, and P. L. Ryder. Determination of the tiling type and phason strain analysis of decagonal quasicrystals in Al-Ni-Co alloys. *Philos. Mag. A*, 79:549, 1999.
- [418] T. Ishimasa, S. Iwami, N. Sakaguchi, R. Oota, and M. Mihalkovič. Phason space analysis and structure modelling of 100 Å-scale dodecagonal quasicrystal in Mn-based alloy. *Philos. Mag. A*, 95:3745, 2015.
- [419] K. Edagawa, P. Mandal, K. Hosono, K. Suzuki, and S. Takeuchi. *In situ* high-resolution transmission electron microscopy observation of the phason-strain relaxation process in an Al-Cu-Co-Si decagonal quasicrystal. *Phys. Rev. B*, 70:184202, 2004.
- [420] M. Senechal. *Quasicrystals and Geometry*. Cambridge: Cambridge University Press, 1995.
- [421] J. A. Nelder and R. Mead. A Simplex Method for Function Minimization. *Comput. J.*, 7:308, 1965.

# Danksagung

An dieser Stelle möchte ich mich bei allen Leuten bedanken, die zum Entstehen dieser Arbeit beigetragen haben.

Mein besonderer Dank gilt meinem Betreuer Prof. Dr. Michael Schmiedeberg, der mir die Promotion am Lehrstuhl ermöglicht hat, mich während der gesamten Arbeit unterstützt und sich immer Zeit für meine Fragen genommen hat. Vielen Dank außerdem für die Möglichkeit, viele interessante Konferenzen zu besuchen und die Gruppe der Quasikristaller kennenzulernen.

Ein weiterer Dank gilt meinen Kollegen und Freunden in Düsseldorf, wo ich die Promotion begonnen habe. Vielen Dank an alle Mitglieder der Theorie II, die für eine angenehme Arbeitsatmosphäre gesorgt haben. Danke außerdem an alle, die auch neben der Arbeit für eine lustige Zeit gesorgt haben. Insbesondere möchte ich mich bedanken bei Karo, Lara, Christian, sowie Alena, Flo, Frithjof, Isi, Julian, Laura, Laura, Manu und Olli für gemeinsame Treffen, Spieleabende und sonstige Aktivitäten.

Des Weiteren bedanke ich mich bei allen Menschen, die ich in Erlangen kennengelernt habe, wo der Großteil dieser Arbeit entstanden ist. Vielen Dank an die gesamte Theorie I für die entspannte Arbeitsatmosphäre sowie gemeinsame Unternehmungen. Insbesondere bedanke ich mich bei Johannes, Sebastian und Anja für die gute Zusammenarbeit, durch die Teile dieser Arbeit entstanden sind. Ein weiterer großer Dank gilt besonders Johannes, Robert, Benedikt, Moumita, Caro und Anja für das Korrekturlesen dieser Arbeit (oder Teilen davon) und für hilfreiche Anmerkungen und Verbesserungsvorschläge. Herzlichen Dank außerdem an Julia und die weiteren Menschen, mit denen es auch außerhalb der Uni nicht langweilig wurde. Mein ganz besonderer Dank gilt Oli sowohl für viele interessante physikalische Diskussionen als auch für alles darüber hinaus.

Und zum Schluss bedanke ich mich bei meinen Eltern und meiner Schwester Julia und Familie, dass ihr immer da seid. Danke für alles.